

Advances in Polymer Science 281

Werner Pauer *Editor*

Polymer Reaction Engineering of Dispersed Systems

Volume II

 Springer

Editorial Board Member:

- A. Abe, Yokohama, Kanagawa, Japan
- A.-C. Albertsson, Stockholm, Sweden
- G.W. Coates, Ithaca, NY, USA
- J. Genzer, Raleigh, NC, USA
- S. Kobayashi, Kyoto, Japan
- K.-S. Lee, Daejeon, South Korea
- L. Leibler, Paris, France
- T.E. Long, Blacksburg, VA, USA
- M. Möller, Aachen, Germany
- O. Okay, Istanbul, Turkey
- V. Percec, Philadelphia, PA, USA
- B.Z. Tang, Hong Kong, China
- E.M. Terentjev, Cambridge, UK
- P. Theato, Karlsruhe, Germany
- M.J. Vicent, Valencia, Spain
- B. Voit, Dresden, Germany
- U. Wiesner, Ithaca, NY, USA
- X. Zhang, Beijing, China

Aims and Scope

The series *Advances in Polymer Science* presents critical reviews of the present and future trends in polymer and biopolymer science. It covers all areas of research in polymer and biopolymer science including chemistry, physical chemistry, physics, and material science.

The thematic volumes are addressed to scientists, whether at universities or in industry, who wish to keep abreast of the important advances in the covered topics.

Advances in Polymer Science enjoys a longstanding tradition and good reputation in its community. Each volume is dedicated to a current topic, and each review critically surveys one aspect of that topic, to place it within the context of the volume. The volumes typically summarize the significant developments of the last 5 to 10 years and discuss them critically, presenting selected examples, explaining and illustrating the important principles, and bringing together many important references of primary literature. On that basis, future research directions in the area can be discussed. *Advances in Polymer Science* volumes thus are important references for every polymer scientist, as well as for other scientists interested in polymer science - as an introduction to a neighboring field, or as a compilation of detailed information for the specialist.

Review articles for the individual volumes are invited by the volume editors. Single contributions can be specially commissioned.

Readership: Polymer scientists, or scientists in related fields interested in polymer and biopolymer science, at universities or in industry, graduate students.

Special offer:

For all clients with a standing order we offer the electronic form of *Advances in Polymer Science* free of charge.

More information about this series at <http://www.springer.com/series/12>

Werner Pauer
Editor

Polymer Reaction Engineering of Dispersed Systems

Volume II

With contributions by

J. M. Asua · M. Babar · L. I. Costa · M. F. Cunningham ·
A. Darabi · E. Frauendorfer · S. Hamzehlou · W.-D. Hergeth ·
P. G. Jessop · O. Kiryutina · J. Kosek · M. Kroupa ·
J. R. Leiza · T. Melchin · M. Morbidelli · M. Soos · G. Storti ·
K. Tauer · A. Tripathi · M. Vonka · C. Wei · D. Wei · H. Wu



Springer

Editor

Werner Pauer
Institute for Technical and Macromolecular Chemistry
University of Hamburg
Hamburg, Germany

ISSN 0065-3195

ISSN 1436-5030 (electronic)

Advances in Polymer Science

ISBN 978-3-319-96435-5

ISBN 978-3-319-96436-2 (eBook)

<https://doi.org/10.1007/978-3-319-96436-2>

Library of Congress Control Number: 2018957453

© Springer Nature Switzerland AG 2018

This work is subject to copyright. All rights are reserved by the Publisher, whether the whole or part of the material is concerned, specifically the rights of translation, reprinting, reuse of illustrations, recitation, broadcasting, reproduction on microfilms or in any other physical way, and transmission or information storage and retrieval, electronic adaptation, computer software, or by similar or dissimilar methodology now known or hereafter developed.

The use of general descriptive names, registered names, trademarks, service marks, etc. in this publication does not imply, even in the absence of a specific statement, that such names are exempt from the relevant protective laws and regulations and therefore free for general use.

The publisher, the authors, and the editors are safe to assume that the advice and information in this book are believed to be true and accurate at the date of publication. Neither the publisher nor the authors or the editors give a warranty, express or implied, with respect to the material contained herein or for any errors or omissions that may have been made. The publisher remains neutral with regard to jurisdictional claims in published maps and institutional affiliations.

This Springer imprint is published by the registered company Springer Nature Switzerland AG
The registered company address is: Gewerbestrasse 11, 6330 Cham, Switzerland

Prof. Dr. H.-U. Moritz



Prof. Dr. Hans-Ulrich Moritz is a chemist and full professor at the University of Hamburg, and Chair of Technical Macromolecular Chemistry at the University Institute for Technical and Macromolecular Chemistry. He was born in West Berlin on June 30, 1952. His scientific life started in the research group of Prof. Dr. Karl-Heinz Reichert, with a PhD thesis on “Continuous Bead

Polymerization of Vinyl Acetate in a Stirred Tubular Reactor,” and has since then focused on polymer reaction engineering.

Consequently, he defended a postdoctoral thesis on “Computer-Assisted Laboratory Reactor for Emulsion Polymerization of Vinyl Acetate” in 1988.

After a short industrial intermezzo, he received his first full professorship in Technical Chemistry and Chemical Process Engineering at the University of Paderborn in 1990. During his scientific career, he published numerous articles and is documented as an inventor in many patents.

Besides his scientific life, Prof. Moritz is active as the chairman of the DECHEMA Education Committee for Technical Chemistry (since 2008), the chairman of the DECHEMA Working Committee for Reaction Technology on processes presenting difficulties from a safety perspective (since 2002), an appointed member of the DECHEMA Working Committee on Polyreactions (since 2000), and a member of the Board of Directors and Trustees of the Jung Foundation for Science and Research (since 2011).

Preface

Polymer reaction engineering of dispersed systems is a dynamic and broad research field with a high impact on everyday life. This is particularly obvious for dispersion paints but has many more aspects. Consequentially, the present volume of Springer's *Advances in Polymer Science* is intended to provide a review recognizing relevant research in both academic and industry labs.

The occasion to start work on this volume was the upcoming 65th birthday of Prof. Dr. Hans-Ulrich Moritz, to whom the authors dedicate this edition. Prof. Moritz's scientific work covers manifold aspects with a major focus on dispersed systems and reactor design, such as Couette–Taylor reactors and bent tubular reactors for continuous emulsion polymerization. The industrial realization of spray polymerization has relied on the research and development in his labs. Additionally, his interests include special research fields such as chemical safety engineering and online analytics.

José M. Asua opens the present volume with a description of the current knowledge of emulsion polymerization and moves on to the challenges of the unknown in this multiphase system.

A special chapter on mass transport in complex mixtures is contributed by Klaus Tauer, Chunxiang Wei, Amit Tripathi, and Olga Kiryutina. The mechanism of mass transport is one of the key processes of emulsion polymerization and is currently being controversially discussed. The authors do not just give a literature overview; rather, they dispute the various aspects of mass transport. The field of precipitation polymerization is presented by Liborio Ivano Costa and Giuseppe Storti, with a main emphasis on modeling. They summarize the most relevant aspects of the process, focusing on the free-radical polymerization mechanism, with an emphasis on the key role of radical interphase transport.

Despite an incomplete theoretical description and perhaps a lack of comprehensive understanding, polymerization in dispersed systems is a solid base for economically successful industrial products. There is a high level of empirically elaborated know-how, especially in industry, that may have been condensed into accurate but unpublished theoretical models.

A key factor for success is process monitoring and control. Hence, Eric Frauendorfer, Muhammad Babar, Timo Melchin, and Wolf-Dieter Hergeth

summarize and discuss the latest process-monitoring technologies, focusing on their applicability.

Facing the challenges of the unknown, an overview on stimuli-responsive latexes is given by Michael F. Cunningham, Philip G. Jessop, and Ali Darabi. The field of stimuli-responsive latexes opens new application fields with switchable stabilization/destabilization. Therefore, coagulation and stability modeling is presented by Martin Kroupa, Michal Vonka, Miroslav Soos, and Juraj Kosek, as well as by Hua Wu, Dan Wei, and Massimo Morbidelli. Stabilization by Pickering emulsion and development of novel materials therefrom are reviewed by He Zhu, Lei Lei, Bo-Geng Li, and Shiping Zhu. Klaus-Dieter Hungenberg and Ekkehard Jahns take a look at the future of emulsion polymerization processes from an industrial perspective.

Shaghayegh Hamzehlou and Jose Ramon Leiza review the field of composite polymer latexes. They elaborate on recent developments in the synthesis and application of composite (hybrid) latex particles, including polymer–polymer and polymer–inorganic latex systems and modeling efforts to simulate the development of particle morphology.

New products with novel characteristics are to be expected as further monomer resources become available, preferably from renewable sources. This emerging research field is reviewed by Yujie Zhang and Marc A. Dubé. They give a comprehensive overview of the technology and show the variety of substance classes from sustainable sources. General aspects of continuous emulsion polymerization are summarized by Werner Pauer, and the field of polyolefin production is discussed by M. Ahsan Bashir and Timothy F. L. McKenna.

PVC is one of the large-scale polymers produced by dispersion polymerization processes. However, in the currently accessible scientific literature, reports on PVC do not nearly have the corresponding volume. Costas Kiparissides thus gives a rare review, gathering knowledge on modeling of the dynamic evolution of the polymerization rate, concomitant average molecular weights, and morphological properties of dispersion PVC.

I am confident that this digest on dispersed systems provides a sound compilation of the current state of the art, which can be consulted by both young researchers and experienced practitioners.

I would like to express my very sincere thanks to the authors for their support and timely responses, to the reviewers for their important feedback, and to the whole editorial team of *Advances in Polymer Science* for their valuable assistance.

Special thanks from the editor go to the Hamburg Institute of Technical and Macromolecular Chemistry for its continuous support in completing this volume – in particular, to Prof. Dr. Dr. hc. mult. Walter Kaminsky, Prof. Dr. Patrick Théato, Prof. Dr. G. A. Luinstra, and Mrs. Christina Khenkhar.

Hamburg, Germany
1 June 2017

Werner Pauer

Contents

| | |
|---|------------|
| Challenges in Polymerization in Dispersed Media | 1 |
| José M. Asua | |
| Experiments and Thoughts on Mass Transfer During Emulsification . . . | 23 |
| Klaus Tauer, Chunxiang Wei, Amit Tripathi, and Olga Kiryutina | |
| Kinetic Modeling of Precipitation and Dispersion Polymerizations | 45 |
| L. Ivano Costa and G. Storti | |
| The Generalized Stability Model and Its Applications in Polymer Colloids | 79 |
| Hua Wu, Dan Wei, and Massimo Morbidelli | |
| Morphology of Composite Polymer Latexes: An Update on Synthesis and Applications, Modeling, and Characterization | 105 |
| Shaghayegh Hamzehlou and Jose Ramon Leizaola | |
| Stimuli-Responsive Latexes Stabilized by Carbon Dioxide Switchable Groups | 143 |
| Michael F. Cunningham, Philip G. Jessop, and Ali Darabi | |
| Probing Coagulation and Fouling in Colloidal Dispersions with Viscosity Measurements: In Silico Proof of Concept | 161 |
| Martin Kroupa, Michal Vonka, Miroslav Soos, and Juraj Kosek | |
| Monitoring of Vinyl Acetate–Ethylene Processes: An Industrial Perspective | 183 |
| Eric Frauendorfer, Muhammad Babar, Timo Melchin, and Wolf-Dieter Hergeth | |
| Index | 215 |

Challenges in Polymerization in Dispersed Media



José M. Asua

Abstract Polymerization in dispersed media is commercially employed to fabricate a wide range of specialty polymers. Thus, a deep understanding of the process is instrumental in improving the performance of these materials in current applications and in the development of new applications. This article gives a personal view of the fundamental knowledge available, pointing out aspects that are open to discussion, need improvement, or simply missing.

Keywords (Mini)emulsion polymerization • Mathematical modeling • Mechanisms • Particle morphology • Process efficiency • Radical entry and exit

Contents

| | | |
|-----|--|----|
| 1 | Introduction | 2 |
| 2 | Understanding the Characteristic Mechanisms of Polymerization in Dispersed Media | 3 |
| 2.1 | Radical Entry | 3 |
| 2.2 | Radical Exit | 5 |
| 2.3 | Radical Concentration Profile and Termination | 5 |
| 3 | Achieving the Desired Polymer/Dispersion Characteristics | 6 |
| 3.1 | Polymer Composition and Chain Architecture | 6 |
| 3.2 | Particle Morphology | 6 |
| 3.3 | Particle Size Distribution | 7 |
| 3.4 | Residual Monomer | 8 |
| 4 | Process Efficiency | 9 |
| 5 | Expanding the Polymerization Techniques and Types of Monomer | 10 |
| 6 | Overcoming the Drawbacks Associated with Film Formation and the Presence of Surfactant | 11 |

J.M. Asua (✉)
POLYMAT, University of the Basque Country UPV/EHU, Donostia-San Sebastian, Spain
e-mail: jm.asua@ehu.es

| | | |
|---|-----------------------------|----|
| 7 | Mathematical Modeling | 13 |
| 8 | Formulated Products | 13 |
| 9 | Conclusions | 14 |
| | References | 15 |

1 Introduction

Polymerization in dispersed media is commercially used to synthesize a wide range of specialty polymers such as adhesives, paints and coatings, paper and paperboard, carpet backing, inks, additives for leather and textiles, tires, redispersible powders, and impact modifiers for plastics and flocculants [1–4]. They are also used in chromatography packing materials [5] as well as in biological [6–8], biomedical [7, 9–18], and pharmaceutical applications [19–21]. Potential applications include anticounterfeiting [22], chemosensors [23–26], catalyst supports [27], enzymatic polymerization [28], photoswitchable fluorescent particles [29], polymeric photoresists [30], light-emitting diodes [31], night-vision displays [32], multicolor optical coding [33], ultrabright fluorescent polymer nanoparticles [34], single photon emission quantum dots [35], energy storage [36–40], surface-enhanced Raman scattering substrates [41], dielectric elastomer actuators [42], and solar cells [43, 44].

Polymer dispersions are produced by a series of closely related polymerization methods, including emulsion polymerization (accounting for the majority of polymer dispersions), microemulsion polymerization, miniemulsion polymerization, and dispersion polymerization. The first three methods use water as a continuous medium. When organic solvents are used, the process is referred to as inverse (mini/micro) emulsion polymerization. In dispersion polymerization, solvents or mixtures of water and solvents are used as continuous medium. The similarities and differences between these methods are well known and are not discussed here. The interested reader is referred to general books on this subject [1–4, 45]. Strictly speaking, suspension polymerization, which is the main process in the production of poly(vinyl chloride), should be included as a method for polymerization in dispersed media; however, it is not discussed in this article because it is kinetically more similar to bulk polymerization, and the polymer produced is not used as a dispersion.

The performance of dispersed polymers is determined by multiple characteristics (copolymer composition, monomer sequence distribution, molecular weight distribution (MWD), polymer architecture, particle morphology, particle surface composition, etc.). Furthermore, because dispersed polymers are product-by-process materials that cannot be transformed after the reaction, all the required characteristics should be achieved in the reactor (Fig. 1). Therefore, the big challenge is to develop an optimal process strategy that, in addition to achieving the required properties, ensures the cost efficiency, consistency, and safety of the production. Because a deep understanding of the process is key to development of such a process strategy, this article gives a personal view of the fundamental knowledge available, pointing out aspects that are open to discussion, need improvement, or simply missing.

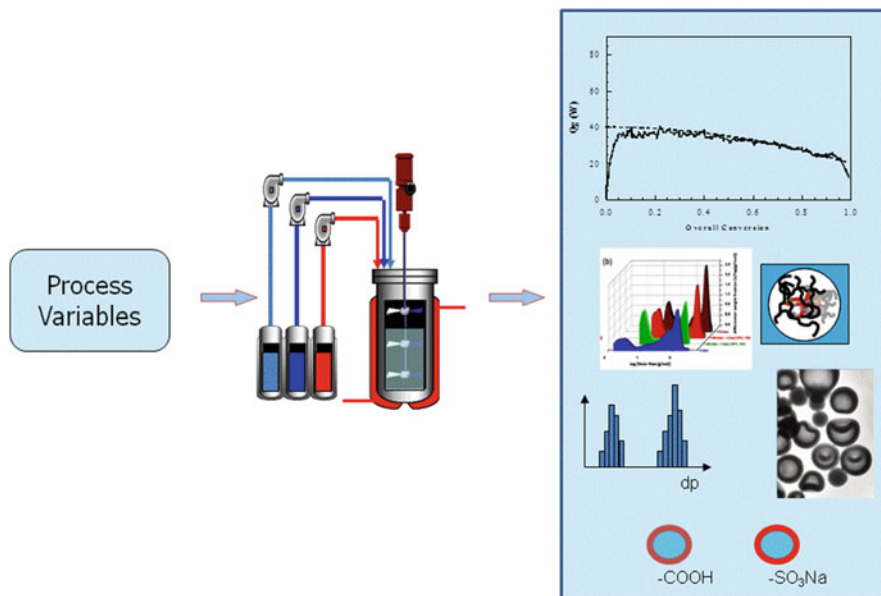


Fig. 1 Challenges in the production of dispersed polymers

2 Understanding the Characteristic Mechanisms of Polymerization in Dispersed Media

Free-radical polymerization (FRP) accounts for most of the polymer produced in dispersed media and its most relevant kinetic characteristic is radical compartmentalization. Radical compartmentalization refers to the fact that radicals in different particles cannot undergo bimolecular termination. Under these conditions, key aspects such as polymerization rate, MWD, and polymer architecture depend on the number of radicals in each particle, which, in turn, is determined by the rates of radical entry and exit to and from the particles and termination inside the particles (Fig. 2). The importance of these mechanisms has prompted research aimed at understanding the mechanisms involved. Several reviews on these mechanisms have been published recently [46–48]. Here, the discussion is centered on the predictive value of the rate coefficients obtained from these mechanisms.

2.1 Radical Entry

The basic mechanisms are relatively well understood. Radicals appear in the continuous phase either from the initiator or by radical desorption from polymer particles. If they are lyophobic (hydrophobic when the continuous phase is water),

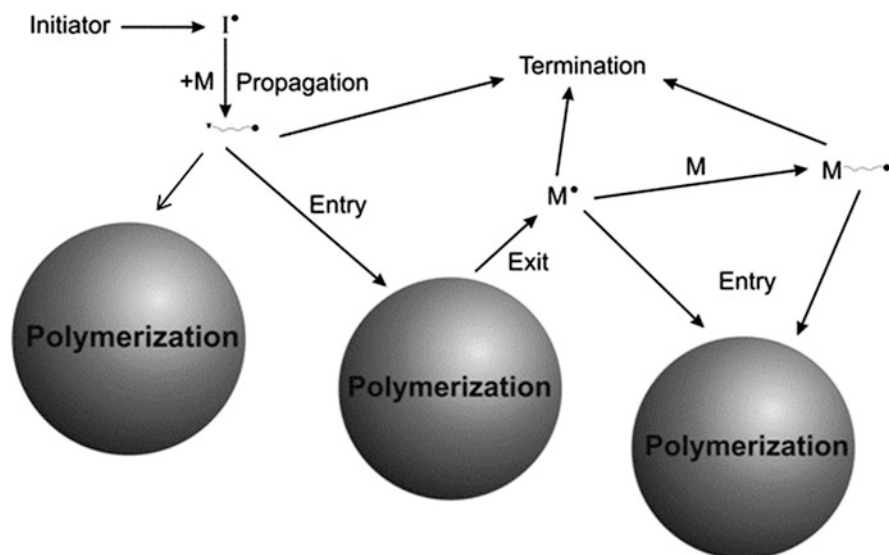


Fig. 2 Characteristic mechanisms of polymerization in dispersed media

they can enter directly into the polymer particles. Otherwise, to be able to enter into polymer particles, they must react with the monomer dissolved in the continuous medium to become either surface active or hydrophobic. The entry of these surface active/hydrophobic radicals has been treated as a collisional [49], diffusional [50], or colloidal [51] process. Furthermore, it has been proposed that the rate-determining step is propagation in the aqueous phase [52]. A lot of effort has been devoted to clarifying these mechanisms, mostly using the dependency of the entry rate coefficient with respect to particle size as a criterion for distinguishing between mechanisms [53–60]. There is general agreement that the propagational model fits the data well for systems in which the aqueous solubility of the growing oligoradical varies sharply upon addition of a monomeric unit (e.g., in the polymerization of styrene). On the other hand, the usefulness of this model for more hydrophilic monomers is open to discussion. It is worth pointing out that these studies were carried out using “academic” systems, namely, homopolymerizations in systems with low solids content. However, industrial systems include at least two main monomers and at least one functional monomer, often containing a carboxyl group. In such systems, there is a wide variety of oligoradicals in the aqueous phase and each of them undergoes entry at a different rate [61, 62]. This is complicated by the fact that radical entry can be affected by the surfactant used [63–65]. Currently, there is no reliable way to predict the average radical entry rate.

2.2 *Radical Exit*

Exit of radicals requires the formation of a small radical that presents some solubility in the continuous phase. A small radical is most often formed through chain transfer to monomer and, once formed, may desorb to the aqueous phase if it does not undergo either propagation or termination in the polymer particle. Once in the aqueous phase, a small radical may react there or reenter a polymer particle. In the latter case, the net desorption rate is zero. Comprehensive models accounting for these mechanisms have been developed [66, 67]. These models predict that the exit rate coefficient decreases with the solids content for particles of the same size and increases with the concentration of radicals in the aqueous phase, because of the, respectively, higher and lower probability of re-entry. In addition, for a constant solids content, the exit rate coefficient is not significantly affected by the particle size because of the counteracting effects of decreasing particle size and increasing number of particles. Nevertheless, for a constant number of particles, the exit rate coefficient decreases as the particle size increases [66]. These effects may be larger than predicted by the models because the models consider that the particles are surrounded by a stagnant layer of water of a thickness larger than the size of the particle. However, this is not the case for commercial latexes, where the distance between particles is around 10–15 nm. This close packing can affect the predictions [60]. A practical consequence of the dependency of the exit rate coefficient on operational variables such as the number of polymer particles and the initiator concentration is that the desorption-rate coefficients determined under some experimental conditions cannot be used directly to predict the behavior of emulsion polymerization systems under different conditions [46].

2.3 *Radical Concentration Profile and Termination*

The number of radicals per particle is determined by the interplay between radical entry, exit, and termination. If these parameters are available, the distribution of radicals among polymer particles can be calculated by solving the Smith–Ewart [68] population balance for particles with n radicals [69]. Analytical solutions for the average number of radicals are available [70]. An assumption in these balances is that all radicals in the same particle can participate in bimolecular termination with the same probability. However, this assumption can be challenged. More than 40 years ago, Williams and coworkers [71, 72] reported experimental evidence that, in the emulsion polymerization of styrene, the new polymer was located in the outer shell of the particles. These data were interpreted by Vanderhof in terms of a radical concentration profile caused by anchoring of the entering radicals to the particle surface [73]. This interpretation has been supported by theoretical modeling [74–76] and experimental evidence [77, 78]. For the sake of the discussion, if we simplify the radical concentration profile to a core–shell structure, where radicals

are at the shell, it seems unlikely that radicals located on opposite sides of the particle can undergo bimolecular termination. The result would be a significantly lower termination rate. However, this effect is not taken into account when modeling emulsion polymerization.

3 Achieving the Desired Polymer/Dispersion Characteristics

The performance of dispersed polymers is generally determined by multiple characteristics (copolymer composition, monomer sequence distribution, MWD, polymer architecture, particle morphology, etc.) and their relative importance depends on the application. In this section, the feasibility of controlling each of these properties is discussed.

3.1 Polymer Composition and Chain Architecture

Fine control of polymer chains is the most difficult challenge in polymer science [79]. In conventional FRP, control of the average copolymer composition can be carried out using starved conditions [80, 81], optimal trajectories [82–85], and on-line control [86–88]. On-line control also enables the desired MWD for linear polymers to be achieved [89–92], but on-line control of branched polymers has not yet been attained [93, 94].

Simultaneous control of the monomer sequence distribution and MWD can be partially achieved for gradient and block copolymers using controlled radical polymerization [95–102]. This technique produces well-defined polymer architectures (comb, star, etc.) and leads to crosslinked networks that differ from those traditionally obtained by conventional FRP [103]. Destarac [104] discussed reasons for the limited implementation of controlled radical polymerization in commercial practice, but recent developments such as sulfur-free reversible addition–fragmentation chain transfer (RAFT) polymerization [105, 106], photoinduced atom transfer radical polymerization (ATRP) with catalyst at the parts per million level [107], photoinduced metal-free ATRP [108], and nitroxide-mediated polymerization of methacrylates [109–113] are removing the obstacles to its wide commercial use.

3.2 Particle Morphology

The portfolio of properties of dispersed polymers can be expanded by including different materials (e.g., polymers, inorganic materials) in the same particle. The

properties of these hybrids are determined by the particle morphology achieved during synthesis. Reviews on this topic are available [114–117], including a recent review of available fundamental knowledge and information needed to develop an optimal production strategy [117]. The subject is also discussed in this issue by Leiza et al. [118]. During polymerization, the morphology of particles evolves toward the equilibrium morphology, which is determined by the minimum surface energy of the system [119–125]. Viscous drag opposes this evolution and the final morphology depends on the interplay between kinetics and thermodynamics.

Morphology maps allow prediction of equilibrium morphologies in terms of interfacial tensions and are available for two-phase polymer–polymer [124] and polymer–inorganic [125] systems. For multiphase systems, analytical prediction of the equilibrium morphology is much more difficult because the number of possible morphologies is high [126]. Monte Carlo approaches have been used for these systems [127, 128].

Kinetically controlled morphologies are formed when the viscosity of the polymer particles is high [129, 130]. Models for the development of the morphology of two-phase and multiphase polymer–polymer systems are available [131–135]. An important limitation of most of these dynamic models is that they provide the morphology of a single particle, whereas a broad distribution of morphologies is observed experimentally. In addition, they are computationally demanding. For polymer–polymer systems, these limitations have been recently overcome [135] with a model that calculates the distribution of morphologies for the whole population of polymer particles, with much less computational effort than that needed by previous models to calculate the morphology of a single particle. A similar model for polymer–inorganic systems is still needed.

3.3 *Particle Size Distribution*

Particle size distribution (PSD) affects both the rheology of the latex [136–146] and film formation [147]. Equations linking PSD and viscosity are available [136–138, 145, 146] and have been used to determine the target PSD for dispersions with high solids content, low viscosity, and limited maximum particle size [144, 148–150]. From a general point of view, to achieve control of the PSD, both particle nucleation and growth should be mastered, but the difficulties of the task can be substantially reduced by using seeded polymerizations, which overcome the need to control the uncertain nucleation step. Under these conditions, the key information is the competitive growth of particles of different sizes. A nice example is provided by Mariz et al. [148–150], who were able to obtain latexes with 70 wt% solids content, modest viscosity, and a maximum particle size of 300 nm. It is worth pointing out that the authors were not able to fit the competitive growth of particles of different sizes to theoretical values using available theories for radical entry and exit.

3.4 Residual Monomer

Health and environmental considerations require that the amount of residual monomer in a final product should be very low. Because polymerization rate is proportional to monomer concentration, the time needed to convert the last fraction of monomer is long and the required monomer levels cannot be achieved in an affordable time when working under regular polymerization conditions. Therefore, two special strategies have been developed for monomer removal: postpolymerization and devolatilization. Postpolymerization consists of addition of redox initiators at the end of the process. Redox initiators yielding hydrophobic radicals in the aqueous phase (e.g., tertbutyl hydroperoxide/ascorbic acid; TBHP/AsAc) are more efficient than those yielding hydrophilic radicals (e.g., potassium persulfate/sodium metabisulfite) [151]. The reason is that, because monomer concentration is low, hydrophilic radicals undergo substantial termination in the aqueous phase. It takes a long time before enough monomer units are added for the radicals to become hydrophobic and enter the polymer particles [151] (Fig. 3). Redox systems have the advantage of being effective at low temperatures [152]. It is worth pointing out that TBHP/AsAc leads to the formation of volatile organic compounds (VOC, e.g., acetone, tertbutanol) [153]. On the other hand, the highly reactive tertbutoxyl radicals are prone to undergo transfer to polymer, which can modify the architecture of the polymer [154]. This represents an opportunity to extend the range of properties achievable with a given emulsion polymer.

Devolatilization can be used for VOC removal, but because evaporation of water cannot be avoided, the solids content may increase during the process. The use of steam and gas saturated with water can overcome this problem [155]. Mass transfer from the aqueous phase to the gas phase is the rate-controlling step in the process. Devolatilization is not efficient at removing highly hydrophilic and low volatile

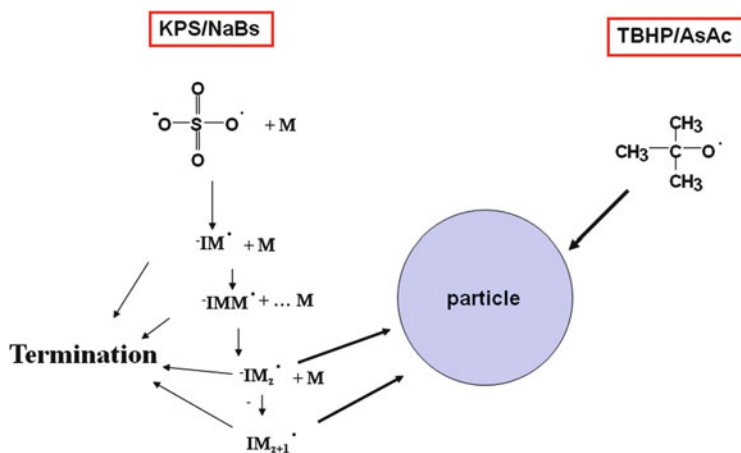


Fig. 3 Effect of the initiator on postpolymerization

compounds. Simultaneous application of postpolymerization and devolatilization enables efficient removal of both monomers and VOCs [156].

The problem of residual monomer is particularly acute for continuous stirred tank [157–159] and loop [160] reactors. In these cases, postpolymerization and/or devolatilization are applied in the holding tank.

4 Process Efficiency

To be commercially viable, polymerizations should be carried out in such a way that the consistency of the product quality is ensured and the production is safe and cost effective.

Consistency in production is a necessary condition in commercial practice because customers formulate their products based on the specific characteristics of the latexes. The main concerns are variation in the quality of raw materials and operator mistakes. Particularly important is accumulation of monomer in the reactor, which impacts safety and product properties. During polymerization, particle nucleation is the step that is most prone to variation. On-line monitoring [161–171] and control [86, 89, 90, 172–181] are instrumental in ensuring consistency in the production process. Nonresolved issues include on-line control of both MWD of nonlinear polymers and particle morphology.

In conventional FRP in dispersed media, the achievable production in semibatch reactors is limited by the heat removal capacity of the reactor. On the other hand, for many dispersed polymers, especially nonlinear polymers, characteristics such as polymer architecture depend on the process time. Furthermore, any variation in process variables leads to changes in several, if not all, polymer characteristics [156, 182, 183], and these changes affect the application properties in ways that are often conflicting. Therefore, the first challenge in process optimization is to specify a good objective function. There are very few articles dealing with optimization of emulsion polymerization reactors, and they are generally limited to discussion of only a few properties, mainly process time, copolymer composition, and MWD of linear polymers [184–189].

The approach used most often used to intensify polymerization in dispersed media is to substitute a semibatch reactor by a continuous reactor [157, 158, 160, 190–204] (Fig. 4). This topic is discussed in an article by Pauer in this issue [205] and in a recent review on continuous production of emulsion polymers [159].

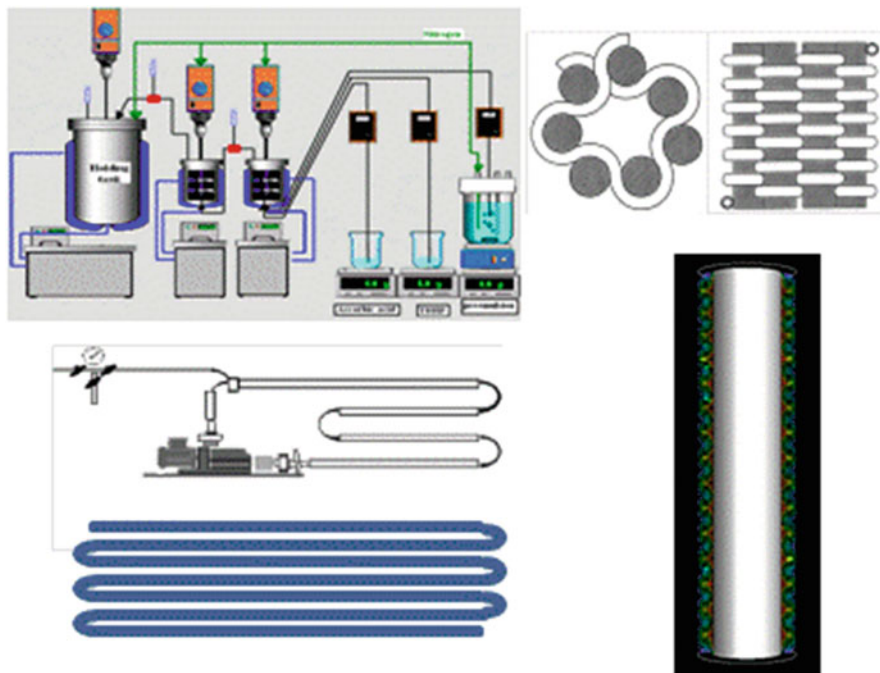


Fig. 4 Continuous reactors

5 Expanding the Polymerization Techniques and Types of Monomer

Emulsion polymerization is the workhorse for the production of dispersed polymers and mainly involves FRP. This process requires mass transfer of monomer through the aqueous phase, which makes use of highly water-insoluble monomers difficult, although cyclodextrins can help transport through the aqueous phase [206]. Miniemulsion polymerization overcomes this problem [207–213]. Commercial waterborne dispersions of polymers synthesized by step-growth polymerization are formed by first synthesizing the step-growth (pre)polymer and then dispersing it in water. The stability of these dispersions is provided by either polar moieties present in the polymer (e.g., DMTA in the case of polyurethanes) or surfactants (e.g., alkyd resins). Attempts to produce dispersed polymers directly by step-growth polymerization in water are rare and involve miniemulsion polymerization. Both polycondensation and polyaddition and have been implemented in miniemulsion. For polycondensation, the presence of water affects the equilibrium and limits the conversion and molecular weight of the polymer. Thus, limited esterification yields and low molecular weights were reported for synthesis of polyesters in miniemulsion [214]. Water does not affect the reaction equilibrium in polyaddition, enabling this technique to be used for production of epoxy [215], polyurethane

[216], and a broad range of waterborne hybrids such as alkyd–acrylics [217–221], polyurethane–acrylics [222–233], silicone–acrylics [234], and polyester–acrylics [235].

Polyolefins account for more than 50% of global polymer production. Both FRP (LDPE) and coordination polymerization (LLDPE, HDPE, PP) are used in polyolefin production, but these processes do not aim at waterborne dispersed polymers. The high pressure needed for the FRP of ethylene and the limited uses of polyethylene waterborne dispersions are barriers to more widespread use of FRP in water. Nevertheless, vinyl acetate–ethylene copolymer dispersions are produced by emulsion polymerization. Loop reactors are advantageously used in this case [236]. Micronized polyethylene wax dispersions (Glaswax[®] BASF) are used as additives for coatings to improve slip, antiblocking properties, sandability, and scratch and water resistance, but they are produced by dispersing the waxes in water.

Coordination polymerization is based on early transition metals (Ti, Zr, Cr, V) [237–244], which are oxophilic and, hence, very reactive with water. Therefore, they cannot be used in the presence of water. On the other hand, late transition metals (Ru, Co, Rh, Ni, Pd) are much less oxophilic and can be used in aqueous systems. Excellent reviews have been published on the use of late transition metal catalysts in the polymerization of olefins [245–250] and on the preparation of waterborne polymer dispersions [251, 252]. These reactions are usually carried out in miniemulsion. In this process, the water-insoluble catalyst is dissolved in an organic solvent and then miniemulsified. Addition of monomer triggers polymerization.

The range of polyolefin properties can be substantially increased by incorporating polar groups into the polymer. However, α -olefins cannot be efficiently polymerized by FRP because the radical formed is too stable and copolymerization with polar monomers is limited to vinyl acetate. Free-radical copolymerization with acrylic monomers is possible, but the reactivity ratios ($r_{\text{acrylate}} = 13.94$, $r_{\text{ethylene}} = 0.01$) make the incorporation of ethylene into the copolymer difficult. Attempts to copolymerize ethylene with acrylates in water using coordination polymerization have been reported [253, 254]. The polymerization rate, molecular weight, and crystallinity of the copolymer tend to decrease with the content of acrylate.

6 Overcoming the Drawbacks Associated with Film Formation and the Presence of Surfactant

Most of the applications of dispersed polymers involve formation of films and compete with solvent-borne products. Although the latter have the disadvantage of a higher environmental impact, their performance is often difficult to match. The main difference between solvent-borne and waterborne polymers is that, in the first

case, a homogeneous film is formed upon evaporation of the solvent, whereas, in the second case, the film is formed by agglomeration of particles, which deform and may or may not interpenetrate [147]. Particle deformation and interparticle polymer diffusion depend on the glass transition temperature [255] and molecular weight [256] of the polymer, crosslinking density [257], and particle morphology [258]. Interparticle diffusion is often hindered by the presence of surfactant and other functional moieties at the surface of the particles [259, 260]. In general, higher casting temperatures lead to better films and improved properties [261].

Surfactants are needed to provide stability to the otherwise thermodynamically unstable polymer dispersions. Migration of the physically attached surfactants during film formation negatively affects the performance (water sensitivity, poor gloss, and low adhesion). In addition, leak of surfactants from painted structures and buildings increases the environmental impact. Therefore, there have been attempts to develop polymer dispersions stabilized with nonmigratory moieties. Polymeric surfactants are high molecular weight surfactants that strongly adsorb to polymer particles and, hence, restrict migration during film formation [262–264]. However, the strong adsorption reduces their efficiency in particle nucleation [265]. Polymerizable surfactants (surfmers) are surfactants containing a double bond that can be incorporated into the polymer backbone during polymerization [266], avoiding the need for migration [262, 267]. In addition to the cost, the main drawback of surfmers is that they are system dependent and it is necessary to adapt the reactivity of their double bond to match the monomer system used. Very reactive surfmers become buried within the particles during polymerization, and those of low reactivity do not become attached to the polymer. Strategies for the optimal use of surfmers have been proposed [268, 269], but often the functionality of the surfmer must be adapted for the particular monomer system.

Functional monomers containing a charged moiety are an attractive alternative. Carboxyl [270–273], sulfate [274, 275], sulfonate [274, 276–279], phosphate [280, 281], phosphonate [282], and amine [283, 284] functionalities have been used, but most present serious drawbacks because they either can only be used in a limited pH range (carboxyl, amine, phosphate, phosphonate) or are prone to hydrolysis (sulfate, phosphate). Furthermore, some functionalities can lead to cationic stabilization, which is easily destabilized in contact with anionic natural surfaces (amine).

Among the sulfonates, sodium styrene sulfonate (NaSS) is particularly interesting because it is commercially available, has a styrenic double bond that reacts well with many of the monomers commonly used in emulsion polymerization, has a very low pK_a ($pK_a = 1$), and is highly stable over a wide range of temperatures. The use of NaSS in emulsion polymerization is challenging because it is completely soluble in water and tends to polymerize in the aqueous phase, giving polyelectrolytes. A two-stage shot-growth method has been used to increase the incorporation of NaSS into polymer particles, but the highest solids content attained without instability was 27 wt% [277].

It has been recently reported that the chemical incorporation of NaSS can be improved by increasing the concentration of comonomer in the aqueous phase

[285] and using initiators to give hydrophobic radicals in the aqueous phase [286]. The authors developed a polymerization strategy that led to high NaSS incorporation (up to 83.5%). Solids contents over 60 wt% were achieved with modest concentrations of NaSS (1.35 wt%), and a variety of monomers (acrylates, methacrylates, styrene) were efficiently polymerized. These latexes presented superior salt and freeze–thaw stability without compromising the water sensitivity of the films [286].

7 Mathematical Modeling

From the early days [68], mathematical modeling has played a central role in the understanding and development of emulsion polymerization. Due to the combination of high computing power and advanced mathematical methods, models are now available for simulation of most of the relevant characteristics of polymer dispersions, such as monomer conversion, polymer composition, nucleation, and particle size distribution [48, 287–293]; polymerizations using oil-soluble initiators [294, 295]; controlled radical polymerization [296–298]; MWD [62, 182, 299–306]; and particle morphology [135].

A general trend in these models is that they include more and more detailed mechanisms, which are accompanied by a higher number of parameters. Unfortunately, not enough effort has been devoted to achieving their unambiguous estimation. In addition, it seems that we have all the pieces of the puzzle for modeling the whole emulsion polymerization process, but we have not yet built the puzzle. For example, there are models that describe the evolution of particle morphology during polymerization. In these models, the movement of phases depends on the viscosity of the particle, which in turn depends on the MWD. However, the modeling of particle morphology has not been connected to that of the MWD. Furthermore, the models for particle morphology include the possibility of a radical concentration profile, but the models for MWD, which are needed to estimate particle viscosity, consider a homogeneous distribution of radicals in the particles.

8 Formulated Products

Commercial products are complex formulations, in which polymer dispersion is crucial. However, the final properties are affected by all the components of the formulation and the scientific bases of this influence are not well understood. The words “science” and “art” are often applied to formulation [307]. The current situation is that, even if all the components of a formulation are well characterized, prediction of the application properties of the formulated product is uncertain. The reverse path, namely, determination of the characteristics of a dispersion that can provide a set of desired properties, is not currently possible. Even if this reverse

path were possible, i.e., the desired characteristics of the polymer dispersion (polymer composition, MWD, polymer architecture, particle morphology, surface composition, PSD) were known, there is no example in the open literature in which all these characteristics have been controlled at the same time (although they have been controlled separately).

9 Conclusions

Polymerization in dispersed media is commercially employed to fabricate a wide range of specialty polymers and application of these materials is expected to expand tremendously in the future. A deep understanding of the process is key to fulfilling these expectations. This article is a personal view of the fundamental knowledge available, pointing out aspects that are open to discussion, need improvement, or simply missing.

Radical entry, exit, and termination control the average number of radicals per particle, which, in turn, determines the kinetics and polymer characteristics. However, there is currently no way to reliably predict the radical entry and exit rate coefficients for an industrial system. In addition, the effect of the radical concentration profile is not taken into account when modeling emulsion polymerization.

Great progress in on-line monitoring and control has been reported, but on-line control of nonlinear polymers and particle morphology has not yet been achieved. Controlled radical polymerization is not widely used in industry, but recent developments are removing the obstacles to wider commercial use of this technique.

There is plenty of information available on the formation of particle morphology for polymer–polymer systems, but polymer–inorganic hybrids still need further development. Examples of fantastic control of the PSD are available. The problem of removal of residual monomer has been solved.

A wide range of step-growth and free-radical hybrid polymers have been synthesized. Polyethylene and ethylene-acrylic copolymers have been prepared by coordination polymerization using late transition metals as catalysts. Alternatives to conventional surfactants are available (surfmers and functional monomers), opening the possibility of mitigating the problem of surfactant migration.

The combination of high computing power and advanced mathematical methods has boosted the development of mathematical models for different characteristics of the polymer dispersion. Unfortunately, not enough effort has been devoted to the unambiguous estimation of their parameters. In addition, there is a lack of connection between these models.

Commercial products are complex formulations in which polymer dispersion is crucial and the final properties are affected by all the components of the formulation; however, the scientific bases of this influence are not well understood.

Acknowledgements The Diputación Foral de Gipuzkoa, University of Basque Country UPV/EHU (UFI 11/56), Basque Government (GV IT999-16) and Spanish Government (CTQ2016-80886-R) are gratefully acknowledged for their financial support.

References

1. Asua JM (ed) (1997) Polymeric dispersions: principles and applications. Kluwer Academic, Dordrecht
2. Urban D, Takamura K (2002) Polymer dispersions and their industrial applications. Wiley VCH, Weinheim, Germany
3. Daniel JC, Pichot C (2006) Les Latex Synthétiques. Lavoisier, Paris
4. van Herk AM (2013) Chemistry and technology of emulsion polymerization. Wiley, Chichester
5. Lamprou A, Kose I, Storti G, Morbidelli M, Soos M (2014). *Langmuir* 30:6946–6953
6. Elaissari A, Rodriguez M, Meunier F, Herve C (2001). *J Magn Magn Mater* 225:127–133
7. Zhang J, Sun W, Bergman L, Rosenholm JM, Linden M, Wu G, Xu H, Gu HC (2012). *Mater Lett* 67:379–382
8. Shao D, Xia A, Hu J, Wang C, Yu W (2008). *Colloid Surf A: Physicochem Eng Aspects* 322:61–65
9. Han M, Gao X, Su JZ, Nie S (2001). *Nat Biotechnol* 18:631–635
10. Lorenz S, Hauser CP, Autenrieth B, Weiss CK, Landfester K, Mailander V (2010). *Macromol Biosci* 10:1034–1042
11. Tautzenberger A, Lorenz S, Kreja L, Zeller A, Musyanovych A, Schrezenmeier H, Landfester K, Mailander V, Ignatius A (2010). *Biomaterials* 31:2064–2071
12. Ramos J, Forcada J (2011). *Langmuir* 27:7222–7230
13. Baier G, Musyanovych A, Mailander V, Landfester K (2012). *Int J Artif Organs* 35:77–83
14. Fonseca LB, Nele M, Volpato NH, Seiceira RC, Pinto JC (2013). *Macromol React Eng* 7:54–63
15. Bencherif SA, Washburn NR, Matyjaszewski K (2009). *Biomacromolecules* 10:2499–2507
16. Bencherif SA, Siegwart DJ, Srinivasan A, Horkay F, Hollinger JO, Washburn NR, Matyjaszewski K (2009). *Biomaterials* 30:5270–5278
17. Sisson AL, Haag R (2010). *Soft Matter* 6:4968–4975
18. Schoeller K, Ethirajan A, Zeller A, Landfester K (2011). *Macromol Chem Phys* 212:1165–1175
19. Oh JK (2008). *J Polym Sci Part A: Polym Chem* 46:6983–7001
20. Oh JK, Dtumright R, Siewart DJ, Matyjaszewski K (2008). *Prog Polym Sci* 33:448–477
21. Sankarakumar N, Tong YW (2013). *J Mater Chem B* 1:2031–2032
22. Harun NA, Horrocks BR, Fulton DA (2011). *Nanoscale* 3:4733–4741
23. Sahiner N, Yu H, Tan G, He J, John VT, Blake DA (2012). *ACS Appl Mater Interfaces* 4:163–170
24. Li XG, Zhang JL, Huang MR (2012). *Chem A Eur J* 18:9877–9885
25. Zhang P, Chen J, Huang F, Zeng Z, Hu J, Yi P, Zeng F, Wu S (2013). *Polym Chem* 4:2325–2332
26. Zhu L, Yang X, Cao Y (2013). *Anal Lett* 46:982–998
27. Gichinga MG, Striegler S, Dunaway NA, Barnett JD (2010). *Polymer* 51:606–615
28. Kohri M, Kobayashi A, Fukushima H, Kojima T, Taniguchi T, Saito K, Nakahira T (2012). *Polym Chem* 3:900–906
29. Chen J, Zhang P, Fang G, Yi P, Yu X, Li X, Zeng F, Wu S (2011). *J Phys Chem B* 115:3354–3362
30. Klinger D, Landfester K (2011). *Macromol Rapid Commun* 32:1979–1985

31. Kim MS, Jin SM, Cho MY, Choi HY, Kim GS, Jeon SM, Yim KG, Kim HG, Shim KB, Kang BK, Kim Y, Lee DY, Kim JS, Kim JS, Leem JY (2011). *AIP Conf Proc* 1399:849–850
32. Meng X, Wen T, Quiang L, Ren J, Tang F (2013). *ACS Appl Mater Interfaces* 5:3638–3642
33. Wartenberg N, Raccurt O, Imbert D, Mazzanti M, Bourgeat-Lami E (2013). *J Mater Chem C Mater Opt Electron Devices* 1:2061–2068
34. Grazon C, Rieger J, Meallet-Renault R, Charleux B, Clavier G (2013). *Macromolecules* 46:5167–5176
35. Negele C, Haase J, Budweg A, Leitenstorfer A, Mecking S (2013). *Macromol Rapid Commun* 34:1145–1150
36. Froeschl T, Hoermann U, Kubiak P, Kucerova G, Pfanzelt M, Weiss CK, Behm RJ, Huesing N, Kaiser U, Landfester K, Wohlfahrt-Mehrens M (2012). *Chem Soc Rev* 41:5313–5360
37. Zhang GH, Bon SAF, Zhao CY (2012). *Sol Energy* 86:1149–1154
38. Chen ZH, Yu F, Zeng XR, Zhang ZG (2012). *Appl Energy* 91:7–12
39. Yang Z, Shen J, Jayaprakash N, Archer LA (2012). *Energ Environ Sci* 5:7025–7032
40. García de Cortazar M, Rodríguez R (2013). *J Appl Polym Sci* 127:5059–5064
41. Fateixa S, Girao AV, Nogueira HIS, Trindade T (2011). *J Mater Chem* 21:15629–15636
42. Molberg M, Crespy D, Rupper P, Nüesch F, Månson JAE, Löwe C, Opris DM (2010). *Adv Polym Mater* 20:3280–3291
43. Ge X, Wang M, Wang H, Yuan Q, Ge X, Liu H, Tang T (2010). *Langmuir* 26:1635–1641
44. Ha SJ, Lee SG, Ha JW, Moon JH (2016). *Langmuir* 32:7735–7740
45. Asua JM (ed) (2007) *Polymer reaction engineering*. Blackwell, Oxford
46. Asua JM (2004). *J Polym Sci Part A: Polym Chem* 42:1025–1104
47. Thickett SC, Gilbert RG (2007). *Polymer* 48:6965–6991
48. Sheibat-Othman N, Vale HM, Pohn JM, McKenna TFL (2017). *Macromol React Eng*. doi:10.1002/mren.201600059
49. Gardon JL (1968). *J Polym Sci Part A-1* 6:643–664
50. Ugelstad J, Hansen FK (1976). *Rubber Chem Technol* 49:536–609
51. Feeney PJ, Napper DH, Gilbert RG (1984). *Macromolecules* 17:2520–2529
52. Maxwell IA, Morrison BR, Napper DH, Gilbert RG (1991). *Macromolecules* 24:1629–1640
53. Asua JM, de la Cal JC (1991). *J Appl Polym Sci* 42:1869–1877
54. Coen EM, Lyons RA, Gilbert RG (1996). *Macromolecules* 29:5128–5135
55. van Berkel KY, Russell GT, Gilbert RG (2003). *Macromolecules* 36:3921–3931
56. De Bruyn H, Miller CM, Bassett DR, Gilbert RG (2002). *Macromolecules* 35:8371–8377
57. Liotta V, Georgakis C, Sudol ED, El-Aasser MS (1997). *Ind Eng Chem Res* 36:3252–3262
58. Lopez de Arbina L, Barandiaran MJ, Gugliotta LM, Asua JM (1996). *Polymer* 37:5907–5916
59. Asua JM, Adams ME, Sudol ED (1990). *J Appl Polym Sci* 39:1183–1213
60. Hernandez HF, Tauer K (2007). *Ind Eng Chem Res* 46:4480–4485
61. Zubitur M, Armitage PD, Ben Amor S, Leiza JR, Asua JM (2003). *Polym React Eng* 11:627–662
62. Calvo I, Hester K, Leiza JR, Asua JM (2014). *Macromol React Eng* 8:329–346
63. Yeliseyeva VI, Zuikov AV (1977). *Polym Sci USSR* 19:3021–3031
64. Vorwerg L, Gilbert RG (2000). *Macromolecules* 33:6693–6703
65. Caballero S, de la Cal JC, Asua JM (2009). *Macromolecules* 42:1913–1919
66. Asua JM (2003). *Macromolecules* 36:6245–6251
67. Ghielmi A, Cuccato D, Storti G (2014). *Ind Eng Chem Res* 53:9049–9057
68. Smith WV, Ewart RH (1948). *J Chem Phys* 16:592–599
69. Ballard MJ, Gilbert RG, Napper DH (1981). *J Polym Sci Polym Letters Ed* 19:533–537
70. Li BG, Brooks BW (1993). *J Polym Sci Part A: Polym Chem* 31:2397–2402
71. Grancio MR, Williams DJ (1970). *J Polym Sci A1* 8:2617–2629
72. Keuch P, Price J, Williams DJ (1973). *J Macromol Chem Chem A7:623–646*
73. Vanderhoff JW (1983) *Notes of the 14th annual short course on advances in emulsion polymerization and latex technology*. Lehigh University, Bethlehem

74. Chern CS, Poehlein GW (1987). *J Polym Sci Polym Chem Ed* 25:617–635
75. de la Cal JC, Urzay R, Zamora A, Forcada J, Asua JM (1990). *J Polym Chem Part A: Polym Chem* 28:1011–1031
76. Mills MF, Gilbert RG, Napper DH (1990). *Macromolecules* 23:4247–4257
77. Parker HY, Westmoreland DG, Chang HR (1996). *Macromolecules* 29:5119–5127
78. Blenner D, Stubbs J, Sundberg D (2017). *Polymer* 114:54–63
79. Ober CK, Cheng SZD, Hammond PT, Muthukumar M, Reichmanis E, Wooley KL, Lodge TP (2009). *Macromolecules* 42:465–471
80. Tang J, Ding T, Daniels ES, Dimonie V, Klein A, El Aasser MS (2003). *J Appl Polym Sci* 88:30–41
81. Trevino ME, Dube M (2013). *Macromol React Eng* 7:484–492
82. Arzamendi G, Asua JM (1989). *J Appl Polym Sci* 38:2019–2036
83. Arzamendi G, Asua JM (1990). *Makromol Chem Macromol Symp* 35–36:249–268
84. Arzamendi G, Asua JM (1991). *Ind Eng Chem Res* 30:1342–1350
85. Van Doremale GHJ, Schoonbrood HAS, Kurja J, German AL (1992). *J Appl Polym Sci* 45:957–966
86. Urretabizkaia A, Leiza JR, Asua JM (1994). *AIChEJ* 40:1850–1864
87. Othman N, Fevotte G, McKenna TF (2002). *Ind Eng Chem Res* 41:1261–1275
88. Sallares AC, Sayer C, Giudici R (2004). *DECHEMA Monogr* 138:231–237
89. Echevarria A, Leiza JR, de la Cal JC, Asua JM (1998). *AIChEJ* 44:1667–1679
90. Vicente M, BenAmor S, Gugliotta LM, Leiza JR, Asua JM (2001). *Ind Eng Chem Res* 40:218–227
91. Zeaiter J, Romagnoli JA, Gomes VG (2006). *AICHE J* 52:1770–1779
92. Sheibat-Othman N, Othman S, Boyron O, Alamir M (2011). *J Proc Control* 21:861–873
93. Sayer C, Lima EL, Pinto JC, Arzamendi G, Asua JM (2000). *J Polym Sci Part A: Polym Chem* 38:1100–1109
94. Sayer C, Arzamendi G, Asua JM, Lima EL, Pinto JC (2001). *Comp Chem Eng* 25:839–849
95. Qiu J, Charleux B, Matyjaszewski K (2001). *Prog Polym Sci* 26:2083–2134
96. Moad G, Rizzardi E, Thang SH (2008). *Acc Chem Res* 41:1133–1142
97. Nicolas J, Guillauneuf Y, Lefay C, Bertin D, Gigmes D, Charleux B (2013). *Prog Polym Sci* 38:63–235
98. Moad G (2015). *ACS Symp Ser* 1187:211–246
99. Matyjaszewski K (2015). *ACS Symp Ser* 1187:1–17
100. Zetterlund PB, Thickett SC, Perrier S, Bourgeat-Lami E, Lansalot M (2015). *Chem Rev* 115:9745–9800
101. Delaittre G (2016). *RSC Polym Chem Ser* 19:199–263
102. Cunningham M (ed) (2016) *Controlled radical polymerization in dispersed media*. *Polymer*, vol 106, pp 1–320
103. Wang R, Luo Y, Li BG, Zhu S (2009). *Macromolecules* 42:85–94
104. Destarac M (2010). *Macromol React Eng* 4:165–179
105. Engelis NG, Anastasaki A, Nurumbetov G, Truong NP, Nikolaou V, Shegiwal A, Whittaker MR, Davis TP, Haddleton DM (2017). *Nat Chem* 9:171–178
106. Nurumbetov G, Engelis N, Godfrey J, Hand R, Anastasaki A, Simula A, Nikolaou V, Haddleton DM (2017). *Polym Chem* 8:1084–1094
107. Pan X, Malhotra N, Simakova A, Wang Z, Konkolewicz D, Matyjaszewski K (2015). *J Am Chem Soc* 137:15430–15433
108. Pan X, Fang C, Fantin M, Malhotra N, So WY, Peteanu LA, Isse AA, Gennaro A, Liu P, Matyjaszewski K (2016). *J Am Chem Soc* 138:2411–2425
109. Ballard N, Aguirre M, Simula A, Agirre A, Leiza JR, Asua JM, van Es S (2016). *ACS Macro Lett* 5:1019–1022
110. Ballard N, Simula A, Aguirre M, Leiza JR, van Es S, Asua JM (2016). *Polym Chem* 7:6964–6972

111. Ballard N, Aguirre M, Simula A, Leiza JR, van Es S, Asua JM (2017). *Polym Chem* 8:1628–1635
112. Simula A, Aguirre M, Ballard N, Veloso A, Leiza JR, van Es S, Asua JM (2017). *Polym Chem* 8:1728–1736
113. Ballard N, Aguirre M, Simula A, Leiza JR, van Es S, Asua JM (2017). *Chem Eng J* 316:655–662
114. Sundberg DC, Durant YG (2003). *Polym React Eng* 11:379–432
115. Bourgeat-Lami E, Lansalot M (2010). *Adv Polym Sci* 233:53–123
116. Charleux B, D'Agosto F, Delaittre G (2010). *Adv Polym Sci* 233:125–183
117. Paulis M, Asua JM (2016). *Macromol React Eng* 10:8–21
118. Leiza et al. (2017) *Adv Polym Sci* doi: 10.1007/12_2017_25
119. Torza S, Mason SG (1970). *J Colloid Interface Sci* 33:6783
120. Sundberg DC, Casassa AP, Pantazopoulos J, Muscato MR, Kronberg B, Berg J (1990). *J Appl Polym Sci* 41:1425–1442
121. Chen YC, Dimonie V, El-Aasser MS (1991). *J Appl Polym Sci* 42:1049–1063
122. Chen YC, Dimonie V, El-Aasser MS (1992). *J Appl Polym Sci* 45:487–499
123. Chen YC, Dimonie V, Shaffer OL, El-Aasser MS (1993). *Polym Int* 30:185–189
124. González-Ortiz LJ, Asua JM (1995). *Macromolecules* 28:3135–3145
125. Asua JM (2014). *Macromol Chem Phys* 215:458–464
126. Sundberg EJ, Sundberg DC (1993). *J Appl Polym Sci* 47:1277–1294
127. Herrera V, Palmillas Z, Pirri R, Reyes Y, Leiza JR, Asua JM (2010). *Macromolecules* 43:1356–1363
128. Reyes Y, Asua JM (2010). *J Polym Sci Part A Polym Chem* 48:2579–2583
129. Luo Y, Zhou X (2004). *J Polym Sci Part A Polym Chem* 42:2145–2154
130. Li Y, Wang Z, Kong X, Xue G (2010). *Colloids Surf A* 363:141–145
131. González-Ortiz LJ, Asua JM (1996). *Macromolecules* 29:383–389
132. González-Ortiz LJ, Asua JM (1996). *Macromolecules* 29:4520–4527
133. Akhmatkaya E, Asua JM (2012). *J Polym Sci Part A Polym Chem* 50:1383–1393
134. Akhmatkaya E, Asua JM (2013). *Colloid Polym Sci* 291:87–98
135. Hamzehlou S, Leiza JR, Asua JM (2016). *Chem Eng J* 304:655–666
136. Krieger IM, Dougherty TJ (1959). *Trans Soc Rheology* 3:137–152
137. Mooney M (1951). *J Colloid Sci* 6:162–170
138. Sudduth RD (1993). *J Appl Polym Sci* 48:25–36
139. Sudduth RD (1993). *J Appl Polym Sci* 48:37–45
140. Sudduth RD (1993). *J Appl Polym Sci* 50:123–147
141. Sudduth RD (1994). *J Appl Polym Sci* 52:985–996
142. Guyot A, Chu F, Schneider M, Graillat C, McKenna TF (2002). *Prog Polym Sci* 27:1573–1615
143. Schneider M, Graillat C, Guyot G, Bétrémieux I, McKenna TF (2002). *J Appl Polym Sci* 84:1935–1948
144. do Amaral M, van Es S, Asua JM (2004). *J Polym Sci Part A: Polym Chem* 42:3936–3946
145. do Amaral M, van Es S, Asua JM (2004). *Macromol Theor Simul* 13:107–114
146. Arevalillo A, Do Amaral M, Asua JM (2006). *Ind Eng Chem Res* 45:3280–3286
147. Keddie JL, Routh AF (2010) *Fundamentals of latex film formation: processes and properties*. Springer, Dordrecht, The Netherlands
148. Mariz IFA, de la Cal JC, Leiza JR (2010). *Polymer* 51:4044–4052
149. Mariz IFA, de la Cal JC, Leiza JR (2011). *Chem Eng J* 168:938–946
150. Mariz IFA, de la Cal JC, Leiza JR (2011). *Macromol React Eng* 5:361–372
151. Ilundain P, Alvarez D, Da Cunha L, Salazar R, Barandiaran MJ, Asua JM (2002). *J Polym Sci Part A: Polym Chem* 40:4245–4249
152. Kohut-Svelko N, Pirri R, Asua JM, Leiza JR (2009). *J Polym Sci Part A: Polym Chem* 47:2917–2927

153. Da Cunha L, Ilundain P, Salazar R, Alvarez D, Barandiaran MJ, Asua JM (2000). *Polymer* 42:391–395
154. Salazar R, Ilundain P, Alvarez D, Da Cunha L, Barandiaran MJ, Asua JM (2005). *Ind Eng Chem Res* 44:4042–4050
155. Salazar R, Alvarez D, Ilundain P, Da Cunha L, Barandiaran MJ, Asua JM (2004). *Progr Colloid Polym Sci* 124:116–120
156. Ilundain P, Alvarez D, Da Cunha L, Salazar R, Barandiaran MJ, Asua JM (2003). *J Polym Sci Part A: Polym Chem* 41:3744–3749
157. Alarcia F, de la Cal JC, Asua JM (2006). *Chem Eng J* 122:117–126
158. Agirre A, Weitzel HP, Hergeth WD, Asua JM (2015). *Chem Eng J* 266:34–47
159. Asua JM (2016). *Macromol React Eng* 10:311–323
160. Abad C, de La Cal JC, Asua JM (1994) *Chem Eng Sci* 49:5025–5037
161. Urretabizkaia A, Sudol ED, El-Aasser MS, Asua JM (1993). *J Polym Sci A Polym Chem* 31:2907–2913
162. Siani A, Apostolo M, Morbidelli M (1995). *DECHEMA Monographien* 131:149–157
163. Gugliotta LM, Arotcarena M, Leiza JR, Asua JM (1995). *Polymer* 36:2019–2023
164. Florenzano FH, Strelitzki R, Reed WF (1998). *Macromolecules* 31:7226–7238
165. Bauer C, Amram B, Agnely M, Charmot D, Sawatzki J, Dupuy N, Huvenne J-P (2000). *Appl Spectrosc* 54:528
166. Reed WF (2000). *Macromolecules* 33:7165–7172
167. Elizalde O, Azpeitia M, Reis MM, Asua JM, Leiza JR (2005). *Ind Eng Chem Res* 44:7200–7207
168. Catalgil-Giz H, Giz A, Alb AM, Koc AO, Reed WF (2002). *Macromolecules* 35:6557–6571
169. Mignard E, Leblanc T, Bertin D, Guerret O, Reed WF (2004). *Macromolecules* 37:966–975
170. Alb AM, Enohnyaket P, Drenski MF, Head A, Reed AW, Reed WF (2006). *Macromolecules* 39:5705–5713
171. Reis MM, PHH A, Sayer C, Giudici R (2007). *Anal Chim Acta* 595:257–265
172. Urretabizkaia A, Leiza JR, Asua JM (1994). *AIChE J* 40:1850–1864
173. Gugliotta LM, Leiza JR, Arotcarena M, Armitage PD, Asua JM (1995). *Ind Eng Chem Res* 34:3899–3906
174. Saenz de Buruaga I, Echevarria A, Armitage PD, de la Cal JC, Leiza JR, Asua JM (1997). *AIChE J* 43:1069–1081
175. Liotta V, Sudol ED, El-Aasser MS, Georgakis C (1998). *J Polym Sci Part A: Polym Chem* 36:1553–1571
176. Vicente M, Leiza JR, Asua JM (2003). *Chem Eng Sci* 58:215–222
177. Edouard D, Sheibat-Othman N, Hammouri H (2005). *AIChE J* 51:3167–3185
178. Altarawneh IS, Gomes VG, Srour MH (2009). *Polym Intern* 58:1427–1434
179. Chicoma DL, Sayer C, Giudici R (2011). *Macromol React Eng* 5:150–162
180. Leonardi R, Natalie C, Montgomery RD, Siqueira J, McAfee T, Drenski MF, Reed WF (2017). *Macromol React Eng*. doi:[10.1002/mren.201600072](https://doi.org/10.1002/mren.201600072)
181. McAfee T, Leonardi R, Natalie C, Montgomery R, Siqueira J, Zekoski T, Drenski MF, Reed WF (2016). *Macromolecules* 49:7170–7183
182. Rossow K, Broege P, Lueth FG, Joy P, Mhamdi A, Mitsos A, Moritz HU, Pauer W (2016). *Macromol React Eng* 10:324–338
183. Agirre A, Calvo I, Weitzel HP, Hergeth WD, Asua JM (2014). *Ind Eng Chem Res* 53:9282–9295
184. Gentric C, Pla F, Latifi MA, Corriou JP (1999). *Chem Eng J* 75:31–46
185. Crowley TJ, Meadows ES, Kostoulas E, Doyle III FJ (2000). *J Process Contr* 10:419–432
186. Araujo PHH, Giudici R (2003). *Comput Chem Eng* 27(8–9):1345–1360
187. Srour MH, Gomes VG, Altarawneh IS (2008). *Chem Eng Sci* 63:4257–4268
188. Houben C, Peremezhney N, Zubov A, Kosek J, Lapkin AA (2015) *Org Process Res Dev* 19:1049–1053
189. Gil ID, Vargas JC, Corriou JP (2016). *Chem Eng Res Des* 111:63–82

190. Poehlein GW (1982). *Br Polym J* 14:153
191. Geddes RK (1983). *Chem Ind* 21:223
192. Imamura T, Saito K, Ishikura S (1993). *Polym Int* 30:203
193. Abad C, de la Cal JC, Asua JM (1995). *J Appl Polym Sci* 56:419
194. Araujo PHH, Abad C, de la Cal JC, Pinto JC, Asua JM (1999). *Polym React Eng* 7:303
195. Apostel M, Pauer W, Moritz HU, Kremeskötter J, Hungenberg KD (2001). *Chimia* 55:229
196. Conrad I, Kossak S, Moritz HU, Jung WA, Rink HP (2001). *DECHEMA Monogr* 137:117
197. Wei X, Yoshikawa K, Oshima A, Sato S, Nomura M (2002). *J Appl Polym Sci* 86:2755
198. Agnely M (2006) Les latex de styrène-butadiène. In: Daniel JC, Pichot C (eds) *Les latex synthétiques*, Lavoisier, Paris, p 417
199. Ruetters D, Negoita I, Pauer W, Moritz H-U (2007). *Macromol Symp* 259:26–31
200. de Castro BR, Adams D (2013) Vinyl ester/ethylene copolymer dispersions prepared by continuous tubular emulsion polymerization. Patent WO2013171584
201. Lueth FG, Pauer W, Moritz H-U (2013). *Macromol Symp* 333:69–79
202. Pokorný R, Zubov A, Matuska P, Lueth F, Pauer W, Moritz H-U, Kosek J (2016). *Ind Eng Chem Res* 55:472–484
203. Alarcia F, de la Cal JC, Asua JM (2006). *Ind Eng Chem Res* 45:3711
204. Alarcia F, de la Cal JC, Asua JM (2006). *Chem Eng J* 122:117
205. Pauer W (2017) *Adv Polym Sci* doi: 10.1007/12_2017_24
206. Lau W (2002). *Macromol Symp* 182:283–289
207. Ugelstad J, El-Aasser MS, Vanderhoff JW (1973). *J Polym Sci Polym Lett Ed* 11:503–513
208. Antonietti M, Landfester K (2002). *Prog Polym Sci* 27:689–757
209. Asua JM (2002). *Prog Polym Sci* 27:1283–1346
210. Schork FJ, Luo Y, Smulders W, Russum JP, Butte A, Fontenot K (2005). *Adv Polym Sci* 175:129–255
211. Landfester K (2009). *Angew Chem Int Ed* 48:4488–4507
212. Fauchau J, Gauthier C, Chazeau L, Cavaille JY, Mellon V, Bourgeat-Lami E (2010). *Polymer* 51:6–17
213. Asua JM (2014). *Prog Polym Sci* 39:1797–1826
214. Barrere M, Landfester K (2003) Polyester synthesis in aqueous miniemulsion. *Polymer* 44:2833–2841
215. Landfester K, Tiarks F, Hentze HP, Antonietti M (2000). *Macromol Chem Phys* 201:1–5
216. Tiarks F, Landfester K, Antonietti M (2001). *J Polym Sci Part A: Polym Chem* 39:2520–2524
217. Nabuurs T, Baijards RA, German AL (1996). *Prog Org Coat* 27:163–172
218. Reimers JL, Schork FJ (1996). *Polym React Eng* 4:135–152
219. Tsavalas JG, Luo Y, Schork FJ (2003). *J Appl Polym Chem* 87:1825–1836
220. Goikoetxea M, Minari RJ, Beristain I, Paulis M, Barandiaran MJ, Asua JM (2009). *J Polym Sci Part A: Polym Chem* 47:4871–4885
221. Goikoetxea M, Minari RJ, Beristain I, Paulis M, Barandiaran MJ, Asua JM (2010). *Polymer* 51:5313–5317
222. Barrere M, Landfester K (2003). *Macromolecules* 36:5119–5125
223. Li M, Daniels ES, Dimonie V, Sudol ED, El-Aasser MS (2005). *Macromolecules* 38:4183–4192
224. Erdem B, Debkumar B, Schrock AK (2005) US 6911487
225. Ballard N, Carretero P, Asua JM (2013). *Macromol React Eng* 7:504–514
226. Gooch JW, Dong H, Schork FJ (2000). *J Appl Polym Sci* 76:105–114
227. Lopez A, Degrandi-Contraires E, Canetta E, Creton C, Keddie JL, Asua JM (2011). *Langmuir* 27:3878–3888
228. Udagama R, Degrandi-Contraires E, Creton C, Graillat C, McKenna TL, Bourgeat-Lami E (2011). *Macromolecules* 44:2632–2642
229. Lopez A, Reyes Y, Degrandi-Contraires E, Canetta E, Creton C, Keddie JL, Asua JM (2013). *Macromol Mat Eng* 298:53–66

230. Lopez A, Reyes Y, Degrandi-Contraires E, Canetta E, Creton C, Asua JM (2013). *Eur Polym J* 49:1541–1552
231. Daniloska V, Tomovska R, Asua JM (2012). *Chem Eng J* 184:308–314
232. Lopez A, Degrandi E, Canetta E, Keddie JL, Creton C, Asua JM (2011). *Polymer* 52:3021–3030
233. Daniloska V, Carretero P, Tomovska R, Paulis M, Asua JM (2014). *ACS Appl Mater Interfaces* 6:3559–3567
234. Rodriguez R, de las Heras Alarcon C, Ekanayake P, McDonald PJ, Keddie, JL, Barandiaran MJ, Asua JM (2008) *Macromolecules* 41:8537–8546
235. Tsavalas JG, Gooch JW, Schork FJ (2000). *J Appl Polym Sci* 75:916–927
236. De Castro Lizandra BR, Adams D (2015) Patent U.S. 20150086746 A1 2015032
237. Natta G, Pino P, Corradini P, Danusso F, Mantica E, Mazzanti G, Moraglio G (1955). *J Am Chem Soc* 77:1708–1710
238. Ziegler K, Holzkamp E, Breil H, Martin H (1955). *Angew Chem Int Ed* 67:541–547
239. Hogan JP, Banks RL (1958) Patent US 2825721
240. Kaminsky W (2004). *J Polym Sci A Polym Chem* 42:3911–3921
241. Piers WE, Chivers T (1997). *Chem Soc Rev* 26:345–354
242. von Andresen A, Cordes HG, Herwig J, Kaminsky W, Merck A, Mottweiler R, Pein J, Sinn H, Vollmer HJ (1976). *Angew Chem Int Ed Engl* 15:630–632
243. Resconi L, Bossi S, Abis L (1990). *Macromolecules* 23:4489–4491
244. Alt HG, Palackal SG, Milius W (1994). *J Organomet Chem* 472:113–118
245. Ittel SD, Johnson LK (2000). *Chem Rev* 100:1169–1203
246. Goodall BL (2009). *Topics Organomet Chem* 26:159–178
247. Guan Z, Popeney CS (2009). *Topics Organomet Chem* 26:179–220
248. Mecking S (2001). *Angew Chem Int Ed* 40:534–540
249. Nakamura A, Ito S, Nozaki K (2009). *Chem Rev* 109:5215–5244
250. Bekerfeld A, Mecking S (2008). *Angew Chem Int Ed* 47:2538–2542
251. Claverie JP (2003) Catalytic copolymerization in aqueous medium. *Prog Polym Sci* 28:619–662
252. Mecking S (2007). *Colloid Polym Sci* 285:605–619
253. Skupov KM, Piche L, Claverie JP (2008). *Macromolecules* 41:2309–2310
254. Skupov KM, Marella PR, Simard M, Yap GPA, Allen N, Conner D, Goodall BL, Claverie JP (2007). *Macromol Rapid Commun* 28:2033–2038
255. Zhao CL, Wang Y, Hruska Z, Winnik MA (1990). *Macromolecules* 23:4082–4087
256. Soleimani M, Khan S, Mendenhall D, Lau W, Winnik MA (2012) *Polymer* 53:2652–2663
257. Pinenq P, Winnik MA, Ernst B, Juhue D (2000) *J Coating Technol* 72:45–61
258. Goikoetxea M, Reyes Y, de las Heras Alarcon CM, Minari RJ, Beristain I, Paulis M, Barandiaran MJ, Keddie JL, Asua JM (2012) *Polymer* 53:1098–1108
259. Rosenbauer E-M, Triftaridou AI, Karpati S, Tournilhac F, Leibler L, Auguste S, Pernot J-M (2012) *Polymer Chem* 3:2178–2185
260. Gonzalez-Matheus K, Leal GP, Asua JM (2015) *Polymer* 69:73–82
261. Gonzalez E, Tollan C, Chuvilin A, Paulis M, Barandiaran MJ (2015) *Colloid Polymer Sci* 293:2419–2427
262. Aramendia E, Barandiaran MJ, Grade J, Blease T, Asua JM (2005) *Langmuir* 21:1428–1435
263. Morizur J-F, Irvine DJ, Rawlins JJ, Mathias LJ (2007) *Macromolecules* 40:8938–8946
264. Shirakbari N, Ebrahimi M, Salehi-Mobarakeh H, Khorasani M (2014). *J Macromol Sci Part B Phys* 53:1286–1292
265. Ballard N, Urrutia J, Eizagirre S, Schafer T, Diaconu G, de la Cal JC, Asua JM (2014). *Langmuir* 30:9053–9062
266. Asua JM, Schoonbrood HAS (1998). *Acta Polym* 49:671–686
267. Aramendia E, Mallegol J, Jaynes C, Barandiaran MJ, Keddie JL, Asua JM (2003). *Langmuir* 19:3212–3221
268. Schoonbrood HAS, Asua JM (1997). *Macromolecules* 30:6034–6041

269. Aramendia E, Barandiaran MJ, Asua JM (2003). *Compt Rendus Chem* 6:1313–1317
270. Ceska GW (1974). *J Appl Polym Sci* 18:427–437
271. Guillaume JL, Pichot C, Guillot J (1988). *J Polym Sci A Polym Chem* 26:1937–1959
272. Kang K, Kan CY, Du Y, Liu DS (2004). *J Appl Polym Sci* 92:433–438
273. Abdollahi M (2007). *Polym J* 39:802–812
274. Guillaume JL, Pichot C, Guillot J (1990). *J Polym Sci A Polym Chem* 28:119–136
275. Goodall AR, Wilkinson MC, Hearn J (1997). *J Polym Sci Polym Chem Ed* 15:2193–2218
276. Juang MSD, Krieger IM (1976). *J Polym Sci Polym Chem Ed* 14:2089–2107
277. Kim JH, Chainey M, El-Aasser MS, Vanderhoff JW (1989). *J Polym Sci A Polym Chem* 27:3187–3199
278. Chang HS, Chen SA (1988). *J Polym Sci A Polym Chem* 26:1207–1229
279. Kim JH, Chainey M, El-Aasser MS, Vanderhoff JW (1992). *J Polym Sci Part A: Polym Chem* 30:171–183
280. Aguirreurreta Z, Dimmer JA, Willerich I, de la Cal JC, Leiza JR (2015). *Macromol Mater Eng* 300:925–936
281. Gonzalez I, Mestlaz D, Leiza JR, Asua JM (2008). *Prog Org Coat* 61:38–44
282. Gaboyard M, Jeanmaire T, Pichot C, Hervaud Y, Boutevin B (2003). *J Polym Sci Part A Polym Chem* 41:2469–2480
283. Ganachaud F, Sauzedde F, Elaissari A, Pichot C (1997). *J Appl Polym Sci* 65:2315–2330
284. Charreyre MT, Razafindrakoto V, Veron L, Delair T, Pichot C (1994). *Macromol Chem Phys* 195:2153–2167
285. Bilgin S, Tomovska R, Asua JM (2016). *RSC Adv* 6:63754–63760
286. Bilgin S, Tomovska R, Asua JM (2017). *Polymer* 117:64–75
287. Hansen FK, Ugelstad J (1978). *J Polymer Sci Polymer Chem Ed* 16:1953–1979
288. Rawlings JB, Ray WH (1988). *Polym Eng Sci* 28:237–256
289. Rawlings JB, Ray WH (1988). *Polym Eng Sci* 28:257–274
290. Sajjadi S, Yianneskis M (2003). *Polymer React Eng* 11:715–736
291. Vale HM, McKenna TF (2005). *Prog Polym Sci* 30:1019–1048
292. Vale HM, McKenna TF (2009). *Ind Eng Chem Res* 48:5193–5210
293. D’hooge DR, Steenberge V, Paul HM, Reyniers M-F, Marin GB (2016). *Prog Polym Sci* 58:59–89
294. Autran C, de la Cal JC, Asua JM (2007). *Macromolecules* 40:6233–6238
295. Capeletto CA, Costa C, Sayer C, Araujo PHH (2017). *AIChEJ* 63:2128–2140
296. Van Steenberge PHM, D’hooge DR, Reyniers M-F, Marin GB, Cunningham MF (2014). *Macromolecules* 47:7732–7741
297. D’hooge DR, Van Steenberge PHM, Derboven P, Reyniers MF, Marin GB (2015). *Polym Chem* 6:7081–7096
298. Mastan E, Li X, Zhu S (2015). *Prog Polym Sci* 45:1–101
299. Tobita H (1994). *Polymer* 35:3023–3031
300. Tobita H, Takada Y, Nomura M (1994). *Macromolecules* 27:3804–3811
301. Arzamendi G, Asua JM (1995). *Macromolecules* 28:7479–7490
302. Ghielmi A, Florentino S, Storti G, Mazzotti M, Morbidelli M (1997). *J Polym Sci A Polym Chem* 35:827–858
303. Plessis C, Arzamendi G, Leiza JR, Schoonbrood HAS, Charmot D, Asua JM (2001). *Ind Eng Chem Res* 40:3883–3894
304. Butte A, Storti G, Morbidelli M (2002). *Macromol Theor Simul* 11:37–52
305. Hamzehlou S, Ballard N, Carretero P, Paulis M, Asua JM, Reyes Y, Leiza JR (2014). *Polymer* 55:4801–4811
306. Hamzehlou S, Reyes Y, Leiza JR (2016). *Eur Polym J* 85:244–255
307. Marrion A, Guy A (2004) The science and art of paint formulation. In: Marrion AR (ed) *The chemistry and physics of coatings*, 2nd edn. RSC, Cambridge

Experiments and Thoughts on Mass Transfer During Emulsification



Klaus Tauer, Chunxiang Wei, Amit Tripathi, and Olga Kiryutina

This paper is dedicated to Prof. Dr. H. U. Moritz on the occasion of his 65th birthday.

Abstract The traditional way of making emulsions is via the input of extra mechanical energy, but there is another mechanism of emulsification that is entirely thermodynamically controlled. Experimental results are presented elucidating the consequences of this spontaneous emulsification for heterogeneous reaction systems. Special emphasis is placed on aqueous heterophase polymerization. We present the results of unusual experiments in oil–water systems that fundamentally changed our view of the mechanism of emulsion polymerization.

Keywords Droplet formation • Emulsion polymerization • Thermodynamics

Contents

| | | |
|---|---|----|
| 1 | Introduction | 24 |
| 2 | Forced Droplet Formation | 25 |
| 3 | Spontaneous Droplet Formation | 30 |
| 4 | Spontaneous Emulsification and Heterophase Polymerization | 38 |
| 5 | Summary | 40 |
| | References | 41 |

1 Introduction

Mass transfer is an important issue in any kind of heterogeneous chemical and physical transformation, regardless of the nature of the dispersed and continuous phase, which can be gaseous, liquid, or solid. Fundamentally, thermodynamics controls mass transfer, that is, it determines whether or not it is long lasting or even possible at all. Note that colloidal systems may be composed of any kind of material in an arbitrary state of matter, except for the gas–gas combination. The context of dispersity and heterogeneity requires that the material forming the dispersed phase is insoluble/immiscible in the continuous phase.

Mixing, which is the combination of matter via the input of mechanical energy, is a basic chemical unit operation [1]. If the mixture is stirred, mixing competes with thermodynamics, particularly during heterogeneous reactions where mixing enhances mass transfer, increases reaction rate, and contributes to unify product quality. However, heterogeneous reactions are also possible in the quiescent state (i.e., without any mechanical power input). Interestingly, even solid state reactions can be conducted in the quiescent state and, surprisingly, some continue until complete conversion [2–5]. Study of reactions that are commonly carried out in stirred reactors under quiescent conditions (e.g., heterophase polymerizations) allows a different and deeper insight into the mechanism.

Input of mechanical energy (i.e., forced mixing) increases the energy content in the system and, consequently, the changes introduced while stirring do not last when stirring is stopped. In other words, a stirred system is not in an equilibrium state and the application of equilibrium thermodynamics is not straightforward. Moreover, a considerable portion of the mechanical energy used for mixing is wasted as heat [6].

In contrast, changes in the quiescent state (i.e., simply by contact between two components) happen spontaneously and are almost entirely driven by thermodynamics. These changes last forever, provided the system is closed and properly sealed.

This paper aims to deliver an insightful, perceptive, and in some aspects an “out of the box” way of looking at various phenomena and issues of mass transfer that are more or less directly related to aqueous heterophase polymerization. We present a combination of experiments, thoughts, and theoretical considerations on the behavior of colloidal objects (particles and droplets) subjected to conditions allowing mass transfer.

Figure 1 sets the scene and schematically explains key aspects of our ideas for a heterogeneous fluid system. The equilibrium between both phases is established across the interface and, so, it seems reasonable to take a closer look at the interface. The interface between fluid phases, here water and an organic liquid, is not smooth or sharply defined down to the molecular level. Moreover, fluctuations lead to roughness of the interface with changing curvature, which, in turn, causes pressure according to the Laplace equation. The crucial consequence of this scenario is that the concentration profile is not a vertical step function but a more or less

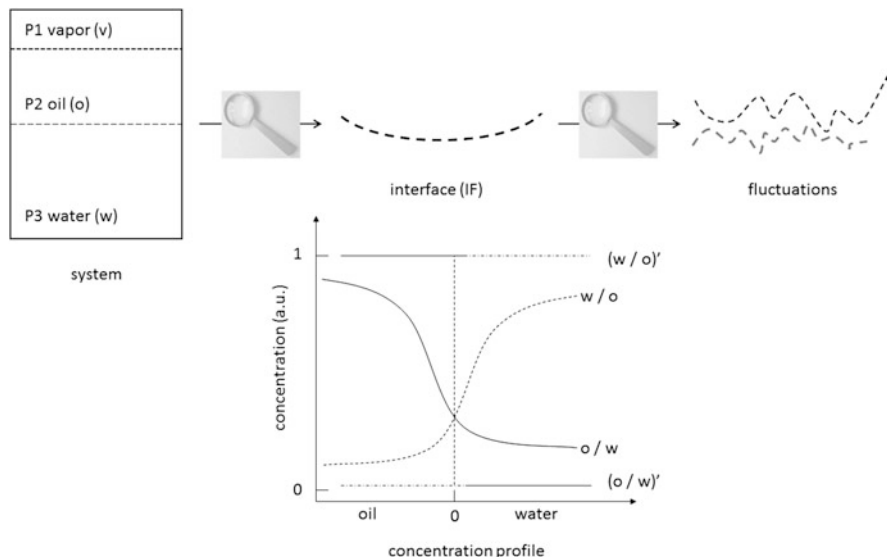


Fig. 1 Sketch of the scene at the interface between two fluids; the system is closed with respect to mass transfer with the environment. Fluid phases are ordered with decreasing density from bottom to top including the vapor phase, which is present in almost all real cases. The interface is typically not flat but curved, where the curvature is determined by the interfacial tension and characterized by fluctuations that are not constant with respect to frequency and intensity. The *lower graph* illustrates the concentration in a region close to the interface, showing that the concentration might be higher nearer the interface than farther away, where the concentration approaches the formal overall solubility

continuously decreasing/increasing profile with gradual changes in the concentration of both water and oil on the opposite sides of the interface. In this “thought experiment,” the concentration close to the interface is higher than the overall mutual solubility of both liquids in each other; hence, a supersaturation is defined in this region. This scenario should hold for any interface between two fluids and is useful for describing the transfer of matter, as explained below. These ideas are not restricted to pure fluids; they are also applicable to solutions and, in some cases, to solid–fluid interfaces. Examples of mass transfer in solid–fluid systems are the dissolution of solid polymers [7, 8], swelling of solid polymers such as hydrogels [9–11], and decomposable salts such as ammonium carbonate salt [12, 13].

2 Forced Droplet Formation

Stirring is used to facilitate and accelerate mixing, homogenization, and/or dissolution during chemical or physical processes. In addition, the state of mixing in a reaction vessel (or the hydrodynamic force field) can influence the result of a

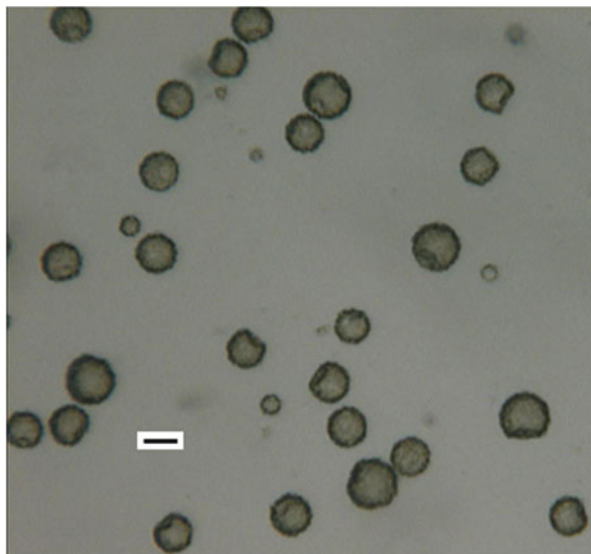
chemical reaction. Homogenization can occur with respect to the spatial distribution of heat and matter; that is, it ensures distribution of temperature and concentration evenly across the reaction volume. Because of the increase in overall interface, the exchange of matter and heat is increased. During mixing, the distribution, dispersion, and diffusion of matter are important partial steps, which take place consecutively [6, 14]. The distribution of matter along the streamlines of the mixing device is superimposed by turbulent erratic motion of larger eddies (roughly of the size of the stirrer diameter), which break into smaller eddies by dispersion. These small eddies spin and facilitate the transfer of matter, whereby their size limits the homogeneity of the reaction mixture. The size of the smallest eddies is, according to Kolmogorov, given by the power input related to the reaction mass and is called the Kolmogorov length, $\lambda = \left(\frac{\nu^3}{P_m}\right)^{\frac{1}{4}}$, where ν is the kinematic viscosity and λ the size of the turbulence element [15]. Mixing on a length scale below λ requires mutual diffusion of the components. Typically, for λ between 30 and 100 μm , the time for achieve micromixing is given by $\tau_m = \frac{\lambda^2}{\tilde{D}}$, with \tilde{D} being the diffusion coefficient; the time needed is in the order of seconds.

Cutting of matter during comminution strongly depends on the reactor volume-related power input (P/V) and is not very dependent on the stirring rate. The stirring rate needed to attain a given P/V value varies with the size of the reactor [6].

The hydrodynamic force acting on particles during stirring in reaction vessels is, in many cases, of paramount importance. Here, “particle” is used in the very general sense as colloidal object, in either a gaseous, liquid, or solid state of matter, dispersed in a fluid, preferentially a liquid continuous phase. Stirring can lead to formation of the intended dispersions (gas in liquid, liquid in liquid, or solid in liquid). In a system as sketched in Fig. 1, the distribution, dispersion, and diffusion occur not only between the two liquid phases but also in the vapor phase. Vapor is distributed within the liquids by the action of the stirrer. Depending on the composition of the vapor phase, the presence of gas in the liquid can influence the outcome of polymerization [16]. Also, during chemical reactions, different degrees of mixing can lead to different reaction products, particularly for autocatalytic, consecutive, and parallel reactions [17, 18].

Shear forces cause mechanical stress in matter, which might be crucial for dispersing solid particles. According to Isaac Newton “*Quantitas motus est mensura ejusdem orta ex velocitate et quantitate materiae conjunctim*” (definition II in [19]), “the magnitude of the motion (i.e., the impact) is measured by the velocity and the size of the matter interplaying.” Clearly, this is important for emulsions and suspensions because the momentum (product of mass and velocity) between eddies and/or particles of the dispersed matter can be quite high and possibly result in physical action (destruction). There are many examples known where solid particles and even dissolved polymers are damaged during intense stirring. Figure 2 shows an example of polystyrene particles damaged by stirring.

Fig. 2 Damaged polystyrene particles after being magnetically stirred in water during redispersion after centrifugational cleaning of the suspension obtained during dispersion polymerization in a toluene–butanol mixture with poly(vinyl pyrrolidone) as steric stabilizer; the *scale bar* indicates 10 μm



There are many examples of how the input of mechanical energy during chemical engineering operations affects the molecular weight distribution of dissolved polymers. Scission of polymer chains (poly(methyl methacrylate), poly(iso-butylene), polystyrene) occurs in stirred solution [20, 21]. For a given polymer, the scission rate is higher and the final chain length shorter in good solvents (where polymers possess higher hydrodynamic volume) than in poor solvents [22, 23]. This clearly points to the influence of the momentum transfer (momentum flow) from the stirrer during encounters between eddies and polymer coils [24]. Degradation of linear poly(acryl amide) was observed when the polymer solution was injected into electrophoretic channels at flow rates as low as 1 $\mu\text{L}/\text{min}$ [25]. Moreover, molecular weight degradation of polymers is a crucial issue in a variety of practical situations such as turbulent drag reduction [26, 27], the use of polymers during secondary oil recovery [28], characterization of polymers (rheology measurements at high shear rates and even size-exclusion chromatography) [29], microfluidic application of polymer solutions [28], and sonication [30].

However, stirring of suspensions can also lead to unexpected and exciting results. A prominent example is the observed symmetry-breaking in stirred crystallization experiments. Non-stirred nucleation of sodium chlorate from aqueous solutions leads to statistically equal fractions of both enantiomers. However, stirring during crystallization leads to the result that 99% of the crystals have the same handedness, although dominance of the L- or D-enantiomer is random [31–33]. The reason for this effect is mechanical damage to early-formed crystals and the action of the debris as seed particles for secondary nucleation [34].

During heterophase polymerization, transition from emulsion to suspension occurs and each state may have a different stirring requirement (see Fig. 2, showing damage to large polystyrene particles). In recent studies, we have investigated the

particular role of stirring during emulsion polymerization [35–37]. Experimental data evidence the occurrence of direct encounters between particles and monomer drop during polymerization. These encounters are enabled and facilitated by stirring and are crucial for fast replenishment of the consumed monomer in polymerizing particles. Diffusion of molecularly dissolved monomer in the water phase from the droplets to the particles is much too slow to compete with the fast consumption of monomer. Diffusion alone cannot maintain a high monomer concentration in the particles during the course of polymerization [38]. The impact between polymer particles and monomer phase can be so strong that the particles are pushed into the monomer, provided that the stabilizer layer is dilute enough and unable to prevent the uptake of polymer particles, which is thermodynamically favored [37]. The uptake of polymer particles by the monomer phase is thermodynamically favored in cases where the monomer is a solvent for the polymer.

These findings challenge the state-of-the-art view that, during emulsion polymerization, the monomer drops only have a passive role as monomer storehouse and that the monomer concentration within the polymerizing particles is kept constant simply by diffusion of monomer molecules through the water phase from the monomer droplets [39, 40]. The idea of a passive role for monomer drops dates back to the pioneering paper by Harkins on the mechanism of emulsion polymerization [41]. Our experimental results support the idea of shear-induced mass transfer of monomer from the droplets to the particles during emulsion polymerization. Accordingly, the transfer takes place via droplet–particle collisions, driven by the impact of the stirring energy, in a kind of momentum flow [24, 42].

We now consider another aspect that is particularly important for emulsification. The homogenization of fluid mixtures by stirring is a process that requires a certain length of time to reach steady state with respect to a minimum average droplet size. The steady state is characterized by a dynamic equilibrium between re-breaking of larger drops, in the vicinity of the stirrer, and re-coalescence of smaller droplets farther away from the stirrer [43, 44].

The question should be asked: What happens after switching off the stirrer? As the additional energy input ends, the system relaxes and returns to the state illustrated in Fig. 1, just before starting the comminution. However, for a given oil phase, what and how fast it happens depends on whether a stabilizer is present and, if present, its properties and concentration (Figs. 3 and 4). In these experiments, ethyl benzene was the oil phase, the aqueous phase contained either a surfactant or no surfactant, and stirring was performed by shaking the properly sealed glass vials for about 30 s.

Macroscopic observation of this simple experiment with the naked eye reveals surprising results. Phase separation is not complete, even after a resting time of more than 200 days, particularly for samples containing SDS, CTAB, and IGP as surfactant. It should be stressed, again, that the systems is nonreactive and closed with respect to exchange of matter with the environment; that is, the vials are sealed and exchange of matter is only possible between water, ethylbenzene, and vapor. Interestingly, the upper oil phase shows the whitish appearance of an emulsion, but

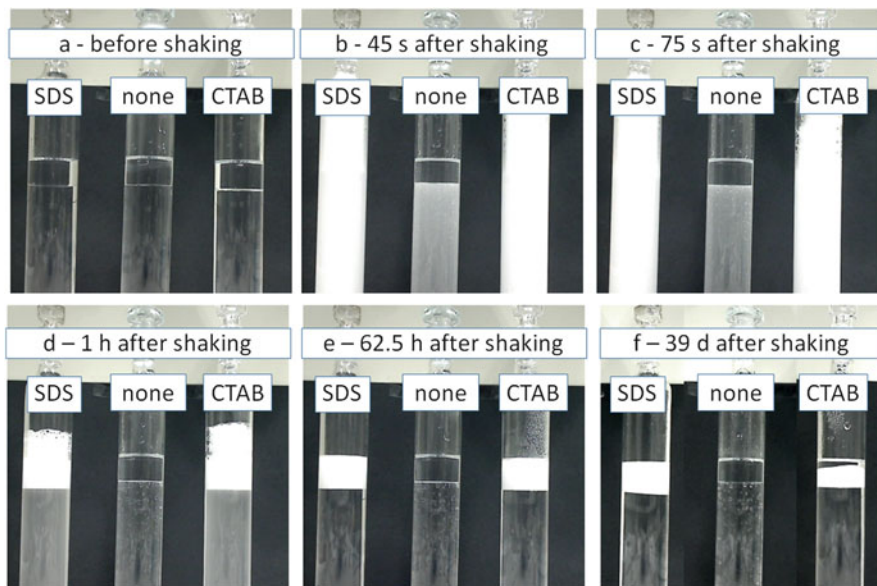


Fig. 3 Time sequence of the relaxation of an ethyl benzene-in-water emulsion after comminution: (a) the starting situation, with ethyl benzene on top of the aqueous phase containing 1% sodium dodecylsulfate (SDS, *left vial*), no surfactant (*middle vial*), or 1% cetyltrimethylammonium bromide (CTAB, *right vial*); (b–f) after resting time of (b) 45 s, (c) 75 s, (d) 1 h, (e) 62.5 h, and (f) 39 days

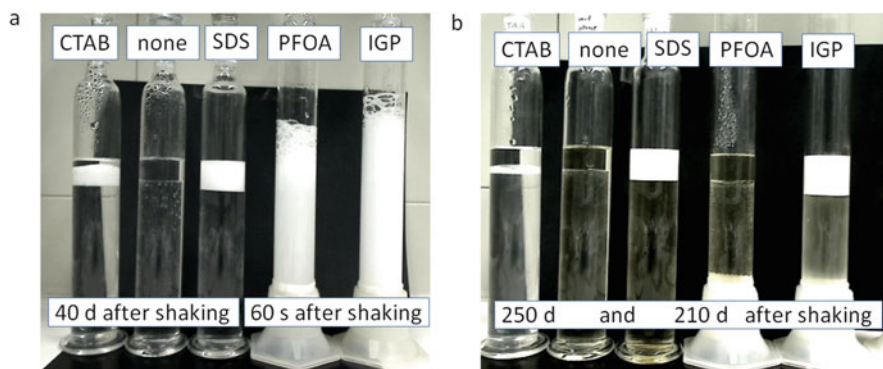


Fig. 4 Time sequence of the relaxation of ethyl benzene-in-water emulsions after comminution. Vials contained the following additives: (a) 1% CTAB (*left vial*), no surfactant (second vial from *left*), or 1% SDS (third vial from *left*), all three after 40 days of resting time; 0.5% sodium perfluorooctanoic acid (PFOA, fourth vial from *left*), or 0.1% of a nonionic surfactant (nonylphenol ether with 15 ethylene oxide groups condensed at the *para* position, IGP), these two after 60 s of resting time; (b) the vials 210 days later

not the lower water phase. Comparing the thickness of the oil layers proves that the whitish appearance is due to a water-in-oil emulsion. Figure 4b shows that the thickness of the oil layer increases from the surfactant-free sample over the sample with CTAB to the sample with SDS in accordance with amount of emulsion phase in the layer. The thickness of the emulsion layer in the oily phase for the sample with CTAB decreases slowly with time (Figs. 3e, f and 4a, b), which indicates that the system has not yet reached thermodynamic equilibrium.

The long-lasting existence of an emulsion in the oil phase, probably a water-in-oil emulsion, is surprising because it is in contradiction to Bancroft's rule, which states that "the liquid in which the stabilizer has a higher solubility forms the continuous phase" [45].

The surfactant-free system and the system containing perfluorooctanoic acid (PFOA) eventually lead to apparent macroscopic phase separation. Interestingly, both samples phase-separate within about 1 h. This is a result of the facts that both water and ethyl benzene are not fluorophilic and that, apparently, PFOA likes water more than ethyl benzene.

Notably, observation of the supposed formation of a water-in-oil emulsion in the oil phase with SDS, CTAB, and IGB is not possible during the emulsification process but only during de-emulsification under quiescent conditions with respect to stirring. However, we can assume that it might also happen during the emulsification stage in larger monomer drops.

3 Spontaneous Droplet Formation

Besides the input of mechanical energy to a system (as sketched in Fig. 1), droplet formation can also be driven entirely by thermodynamics. This process is called spontaneous emulsification and was discovered during studies of particle nucleation using multi-angle laser light scattering (MALLS) [46]. This finding was absolutely unexpected and did not result from careful planning, but rather arose serendipitously. In essence, we used MALLS to observe the styrene concentration in water during the equilibration period. We slowly and carefully placed styrene on top of water in the MALLS cuvette, in a thermostat at 25°C, and increased scattering intensity over several hours. Evaluation of the MALLS data showed that the droplet size distribution was very broad and that the average size increased with time before it leveled off after about 1,000 min, for the particular conditions during the MALLS experiments [46]. It is important to emphasize that the drop formation takes place before polymerization, just after carefully layering styrene on water to allow concentration-wise equilibration between both liquids via diffusion. The average drop diameter was greater than 1 μm (Fig. 5) and, thus, direct observation with optical microscopy was possible.

We observed spontaneous emulsification in the interfacial region for all combinations of not completely miscible liquid pairs. Moreover, the interface between two immiscible liquids is not static but highly dynamic, with fluctuations occurring

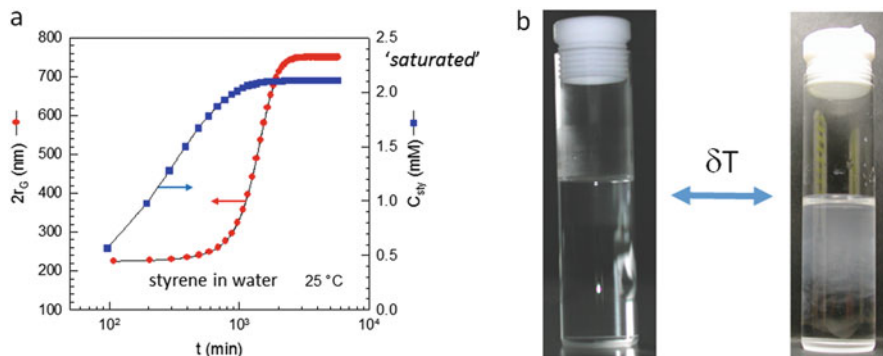


Fig. 5 (a) Spontaneous emulsification at the styrene–water interface, as observed during the equilibration period investigated by MAALS (squares $2r_G$, scattering volume focused in the water phase), and the styrene concentration in water (C_{STY} , obtained by gas chromatography of the water phase). (b) Images of the aqueous phase at the end of the experiment subjected to small temperature fluctuations (δT): *left* fluctuations below the equilibrium temperature, *right* fluctuations above the equilibrium temperature

as sketched in Fig. 1. Droplet formation occurs on both sides of the interface and the shape of the interface changes with time. Moreover, changes in drop size distribution and drop number take place over long periods of time. Interestingly, the scattering intensity observed during the equilibration period depends on the gas content in the system, such that degassed liquids give higher scattering intensity than gassed solutions [46].

The styrene droplet size (expressed as $2r_G$) in water, as determined by MALLS, and the gross styrene content in water (C_{STY}), as determined by gas chromatography, show an interesting correlation [46, 47]. The averaged time-dependent data sets are depicted in Fig. 5a and show that the average droplet size increases sharply in the vicinity of the saturation concentration. Over the entire concentration range, $d(2r_G)/dC_{STY}$ (not shown) increases by a factor of about 1,000. This behavior strongly resembles critical phenomena in the vicinity of phase transition points [48].

Figure 5b illustrates the behavior of the saturated aqueous phase when the temperature fluctuates slightly below and above the equilibration temperature. This behavior shows that a styrene-in-water solution (or any other solution) close to saturation with respect to concentration is in a critical state and that macroscopic phase separation can be triggered by minor temperature fluctuations. One should be aware that a saturated solution of A in B is thermodynamically on the edge of the stability–instability limit and, hence, small changes in the thermodynamic parameters may cause phase transitions. Because the white light of an optical microscope is able to initiate polymerization (cf. Sect. 4) and the chemical changes drastically influence distribution with respect to dynamics and equilibrium state, observation of spontaneous emulsification with nonpolymerizable oils and water is much more revealing.

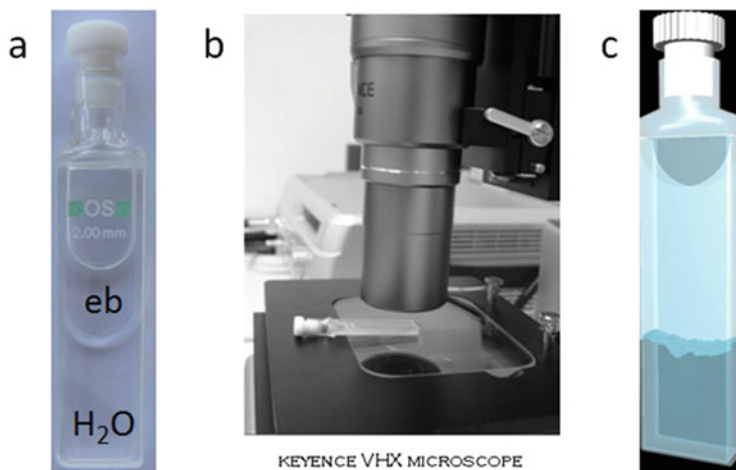


Fig. 6 Investigation of spontaneous emulsification using optical microscopy: (a) optical cuvette filled with water and ethyl benzene (*eb*); (b) cuvette placed under the objective of the optical microscope; note that the cuvette is slightly inclined from the stopper toward the bottom; (c) drawing of the ruffled interface between water and oil (not to scale)

Investigations with optical microscopy were carried out as illustrated in Fig. 6. Both liquids were placed in optical cuvettes (1–10 mm thick), with decreasing density from bottom to top. The cuvettes were closed with plastic stoppers for short-term investigations but with glass stoppers and glued glass caps for permanent storage of the samples.

Figure 7 shows optical microscopy images illustrating spontaneous emulsification in *ter*-butylstyrene (TBS) and cyclodecane–water systems. The images were taken about 65 h and 6 years after establishing contact between the oil and water. The sample with TBS started to polymerize after a few days and the transparent system turned into a milky-white latex. Drop formation happened quite fast, particularly for the cyclodecane–water combination. Moreover, the time scale up to years indicates that the drops are surprisingly stable.

Droplet formation occurs on both sides of the interface, as shown in Fig. 7b. Cyclodecane drops are visible in the water phase and water drops in oil phase. If one of the liquids is water, the larger water drops adopt a nonspherical shape and adhere to the glass wall of the cuvette. The oil drops in the water phase are spherical and show, depending on the drop size, Brownian motion. There is another observation worth mentioning: Droplets are concentrated in the vicinity of the interface, but do not re-enter the corresponding mother phase, at least we have no experimental indication that this process occurs. The droplets on both sides of the interface are stable (for up to 9 years) and one might cautiously conclude that the situation shown in Fig. 7b represents a snapshot of the equilibrium state. The droplets, once formed, exist in a closed system seemingly endlessly.

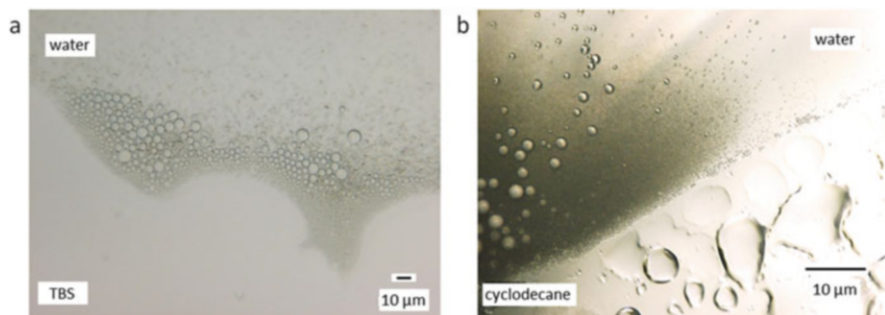


Fig. 7 Optical microscopy images proving spontaneous emulsification for (a) *ter*-butylstyrene (taken 65 h after contact) and (b) cyclodecane–water system (taken 6 years after contact); note that the cuvette is inclined toward the water phase

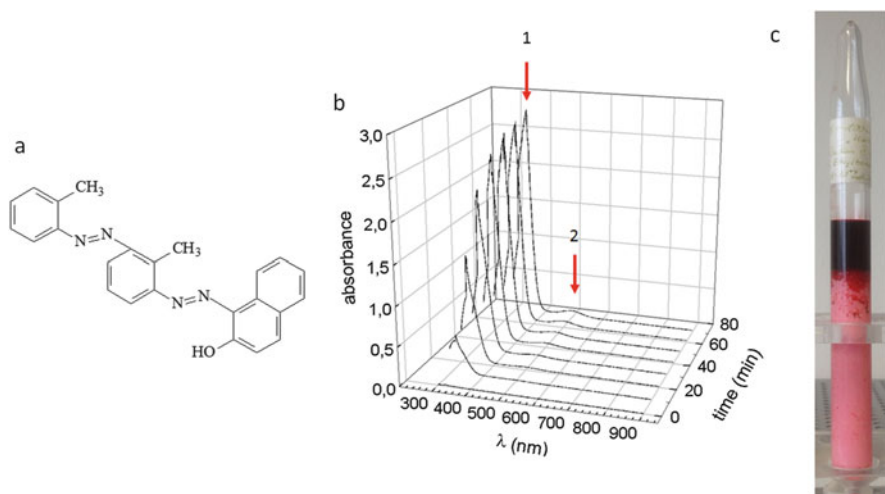


Fig. 8 Tinting polystyrene latex particles *red* with Sudan IV (a) dissolved in ethyl benzene and placed on top of the latex. (b) Dye uptake was monitored with a UV-vis immersion probe in diluted latex. The latex phase was gently stirred without generating oil drops, as described and discussed [50]. Arrows indicate the absorption of ethyl benzene (1) and the dye (2) at about 310 and 480 nm, respectively. (c) Image of latex overlaid with the dye solution confined in a sealed glass vial, taken some years after establishing the contact

The extent of spontaneous emulsification without any chemical transformation leads to emulsions with low volume fractions on either side. The volume fraction of the emulsion depends on the mutual solubility of the components and, for the combination styrene–water, is clearly below 1%. However, the situation changes if polymerization takes place [49].

Spontaneous emulsification also takes place with immiscible solutions, meaning that solutes from the organic phase are transferred into the water phase (and vice versa). This is demonstrated in Fig. 8, which shows that polystyrene particles are

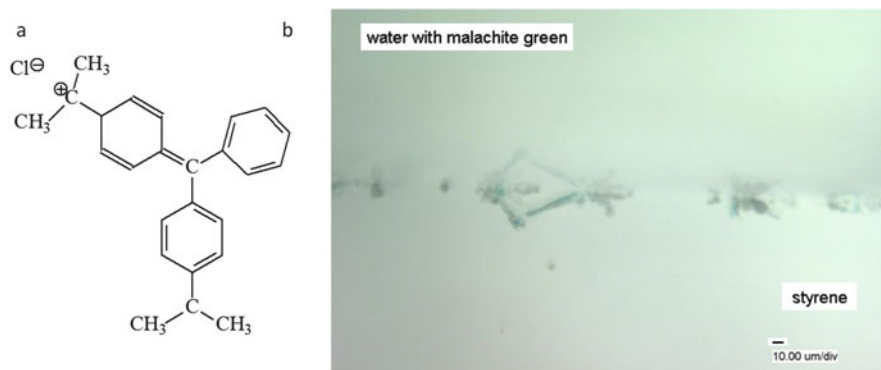


Fig. 9 Light microscopy image (true colors) of malachite green crystals at the interface between the dye-in-water solution and styrene; the crystals are in the organic phase close to the water side and mirrored at the interface; *scale bar* marks 10 μm

slowly tinted red over a long period of time when a solution of Sudan IV (hydrophobic dye) is placed on top of the latex.

If the water phase contains surfactants, the formation of oil drops is faster and their size decreases with increasing surfactant concentration [49]. However, if just a simple (i.e., not surface active) salt is dissolved in water, the compound precipitates at the water–oil interface. In some cases, the resulting structure, together with the mirror images reflected from the interface, looks quite fancy (Fig. 9). The fact that precipitation occurs in a region close to the interface supports the sketch of Fig. 1 with respect to the distribution of the concentrations in the interfacial layer.

Another important point concerning the mechanism of emulsion polymerization should be mentioned. The occurrence of spontaneous emulsification directly touches the issue of monomer-swollen micelles and leads, at least in our understanding, to a modified interpretation of solubilization.

According to the data given in Fig. 10, we should not consider monomer-swollen micelles as being in a thermodynamically well-defined state (i.e., with a given size and amount of imbibed monomer molecules). To justify this conclusion, consider an aqueous surfactant solution with a concentration of about the critical micelle concentration (CMC). The addition of some monomer drops to this solution pushes the free surfactant concentration below the CMC. Thermodynamics requires an adsorption equilibrium of the surfactant at all interfaces. Hence, because of the broad size distribution of monomer drops with a high number concentration in the size range below 1 μm (Fig. 5a) [46, 49, 51], “swollen micelles” with a saturated surfactant layer disappear and transform into small monomer drops. The situation is similar to Ostwald ripening, where larger particles grow at the expense of smaller ones. This idea is supported by the data summarized in Fig. 10, which prove the spontaneous transfer of toluene into the aqueous phase. Persisting swollen micelles would lead to saturation of the absorption after the time needed for equilibration, as indicated by the dashed line. However, the experimental data do not support this

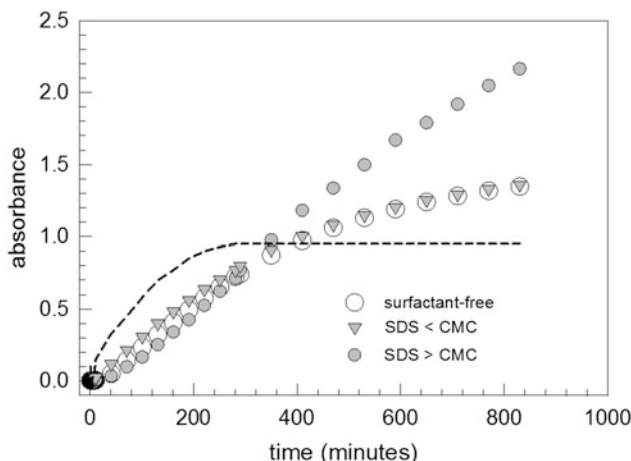


Fig. 10 Increase in absorption of the aqueous phase (measured at $\lambda = 260$ nm, the long-wave absorption maximum of toluene) during sorption of toluene in pure water (*open circles*), in SDS solution with concentration below the critical micelle concentration (CMC) (0.43 g/L, which is about 1/6 CMC, *grey circles*), and above the CMC (5.3 g/L, which is about twice the CMC, *grey downward triangles*). The *dashed line* indicates the expected course, assuming swollen micelles with both fixed size and fixed imbibed amount of toluene. Measurements were carried out at a temperature of 23°C in 1-cm UV cuvettes containing aqueous phase and a carefully placed toluene layer on top. The water layer in the cuvette was much higher than the optical path of the Uvikon 931 spectrometer (Kontron Instruments, UK)

idea but, instead, show increasing absorption in all cases, which means ongoing oil transport to the aqueous phase. In addition, the data prove the facilitating action of high surfactant concentration on spontaneous emulsification.

The experimental facts are quite clear, but a satisfying understanding of what causes spontaneous emulsification and of its driving force is still lacking. To achieve this, one has to distinguish between the thermodynamic driving force for droplet formation and the formation mechanism itself. A thermodynamic justification of spontaneous emulsification seems possible, as follows: Immediately after contact between the oil phase (o) and water (w), mass transfer of oil molecules into water and of water molecules into oil starts. The chemical equilibrium of the system, as sketched in Fig. 1 (no mass transfer with the environment and neglecting the vapor phase), is reached when the chemical potential (μ) for a given liquid is the same in each of the liquid phases. In the following equations, the subscript letter denotes the liquid and the superscript letter denotes the phase. For example, μ_o^w and μ_w^o represent the chemical potential of oil in the water phase and of water in the oil phase, respectively. Zero after a subscript letter indicates the concentration of pure liquid (i.e.; the reciprocal of molar volume v_m). In Eq. (1), the chemical potential (μ) for a given liquid is the same in each of the liquid phases, indicating chemical equilibrium.

$$\mu_o^o = \mu_o^w, \mu_w^o = \mu_w^w \quad (1)$$

Applying standard thermodynamics and considering homogenous phases after equilibration, equalities (2a) and (2b) are obtained for the oil and water, respectively.

$$\mu_o^o = \mu_o^w = \mu_{o,0} + RT \ln \frac{C_o^o}{C_{o,0}} = \mu_{o,0} + RT \ln \frac{C_o^w}{C_{o,0}} \quad (2a)$$

$$\mu_w^o = \mu_w^w = \mu_{w,0} + RT \ln \frac{C_w^o}{C_{w,0}} = \mu_{w,0} + RT \ln \frac{C_w^w}{C_{w,0}} \quad (2b)$$

Considering the experimental values for the mutual solubilities of styrene and water, $C_w^o = 4 \times 10^{-2}$ M, $C_o^w = 3 \times 10^{-3}$ M [52], we get the values $C_w^w = 55.32$ M, $C_o^o = 9.993$ M. Here, we assume that the molar volumes of water and oil are 18.07 and 100 mL/mol, respectively. The estimated concentrations C_w^w and C_o^o take into account the presence of the corresponding solute. Applying these values in (2a) and (2b) shows that the equilibrium conditions (1) are not fulfilled because the chemical potentials of the mother phases are much higher than those of the complementary phases. A way out of this dilemma is to consider heterogeneity, that is, formation of an emulsion on either side instead of formation of a homogeneous solution. The key is that emulsion drops lead to a size-dependent increase in chemical potential [35, 53, 54]. With this, the chemical potentials can be expressed as shown in (3a–3d).

$$\mu_o^o = \mu_{o,0} + RT \ln \frac{C_o^o}{C_{o,0}} + RT \frac{k_{1,o}^o}{d_{d,w}^o} \quad (3a)$$

$$\mu_o^w = \mu_{o,0} + RT \ln \frac{C_o^w}{C_{o,0}} + RT \frac{k_{1,o}^w}{d_{d,o}^w} \quad (3b)$$

$$\mu_w^w = \mu_{w,0} + RT \ln \frac{C_w^w}{C_{w,0}} + RT \frac{k_{1,w}^w}{d_{d,o}^w} \quad (3c)$$

$$\mu_w^o = \mu_{w,0} + RT \ln \frac{C_w^o}{C_{w,0}} + RT \frac{k_{1,w}^o}{d_{d,o}^o} \quad (3d)$$

The constants k_1 derive from the corresponding Laplace relations (4a–4d), where σ is the interfacial tension, R the gas constant, and T the temperature. The interfacial tensions for the oil drops in water and the water drops in oil phase are assumed identical.

$$k_{1,o}^o = \frac{4\sigma \times v_{m,w}}{RT} \quad (4a)$$

$$k_{I,o}^w = \frac{4\sigma \times v_{m,o}}{RT} \quad (4b)$$

$$k_{I,w}^w = \frac{4\sigma \times v_{m,o}}{RT} \quad (4c)$$

$$k_{I,w}^o = \frac{4\sigma \times v_{m,w}}{RT} \quad (4d)$$

The equilibrium conditions for the oil and the water lead to the inequalities (5a, 5b), which allows derivation of a relation between the size of oil drops in the water phase and water drops in the oil phase (6).

$$\ln \frac{C_o^o}{C_o^w} = \left(\frac{k_{I,o}^w}{d_{d,o}^w} - \frac{k_{I,o}^o}{d_{d,w}^o} \right) > 0 \quad (5a)$$

$$\ln \frac{C_w^w}{C_w^o} = \left(\frac{k_{I,w}^o}{d_{d,w}^o} - \frac{k_{I,w}^w}{d_{d,o}^w} \right) > 0 \quad (5b)$$

$$d_{d,o}^w \approx \frac{v_{m,w}}{v_{m,o}} d_{d,w}^o \quad (6)$$

Assuming the data for water and styrene, Eq. (6) suggests that the water drops are about 1.8 times larger than the oil drops in water. Because the drops in both phases possess a very broad size distribution, the average drop size is only a very rough measure. Nevertheless, the largest water drops are bigger than the largest oil drops (Fig. 7b), which supports the above thermodynamic argument with respect to the driving force of spontaneous emulsification. The nucleation of drops takes place close to the interface, which supports the idea that classical nucleation theory can be applied to describe the droplet formation mechanism.

A way to prove these ideas experimentally is a swelling experiment, as described next. The experiment also supports the idea that monomer droplets play a major role in latex particle swelling. A method for measuring swelling pressure has recently been developed in our laboratory [55] and was applied here. A crosslinked bulk polystyrene sample was placed in a confinement (ensuring almost isochoric conditions) with porous walls, allowing contact with an outer liquid phase, which is inside a container placed on a balance. The confinement containing the sample has contact with the container bottom and, hence, any action on or of the sample is transferred directly to the balance, easily allowing monitoring of an apparent mass change (m_{app}). We emphasize that the method measures the “desire” to establish direct contact between the sample and the fluid surrounding the confinement. Figure 11 shows the development of the balance readout over the whole duration of the experiment. This particular experiment was designed on the basis of Okubo’s dynamic swelling method, with changing composition of the continuous phase [56, 57].

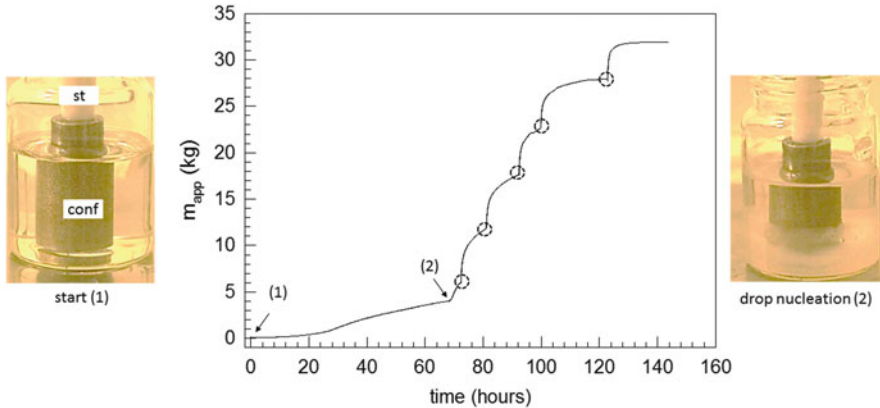


Fig. 11 Changes in the balance readout during a swelling pressure experiment. Crosslinked polystyrene was placed in the confinement (*conf*) with a stamp (*st*); (1) marks the time when a mixture of toluene and ethanol (30/70 vol%) was added; (2) indicates when water was added (after about 70 h), which caused the transition from solution to emulsion. The *left* images show the setup at (1) and the *right* image after (2), when water drops are clearly recognizable in the lower part of the liquid. *Circles* mark the time when the limit of the balance was reached and the load was manually relaxed (the curve is the sum of individual sections after each relaxation)

The data in Fig. 11 show only a slight increase in the balance readout in the presence of toluene/ethanol solution. However, after water addition and the formation of toluene droplets, the swelling pressure increased sharply due to the presence of toluene drops, which have a higher toluene concentration than the solution. These droplets cause a stronger “desire” for the polystyrene in the confinement. This is in accordance with the swelling results obtained with forced swelling [36].

4 Spontaneous Emulsification and Heterophase Polymerization

Knowing that spontaneous emulsification takes place, it is straightforward to check what happens when the oil phase is a polymerizable monomer such as styrene. The use of styrene allows initiator-free photoinitiation, which happens inside monomer drops because more than one styrene molecule is necessary to initiate the polymerization [58]. Of course, the setup as shown in Fig. 12a also leads to initiation in the styrene phase.

Figure 12 shows the time sequence of such polymerizations under different stabilizing conditions, leading to significant differences in the appearance of the reaction system. The common result for all systems is formation of polymer particles in the aqueous phase (latex formation) and a polymerized monomer layer. Astonishingly, the appearance of the monomer phase during polymerization strongly depends on the stabilizer. At the end of the polymerization, only for

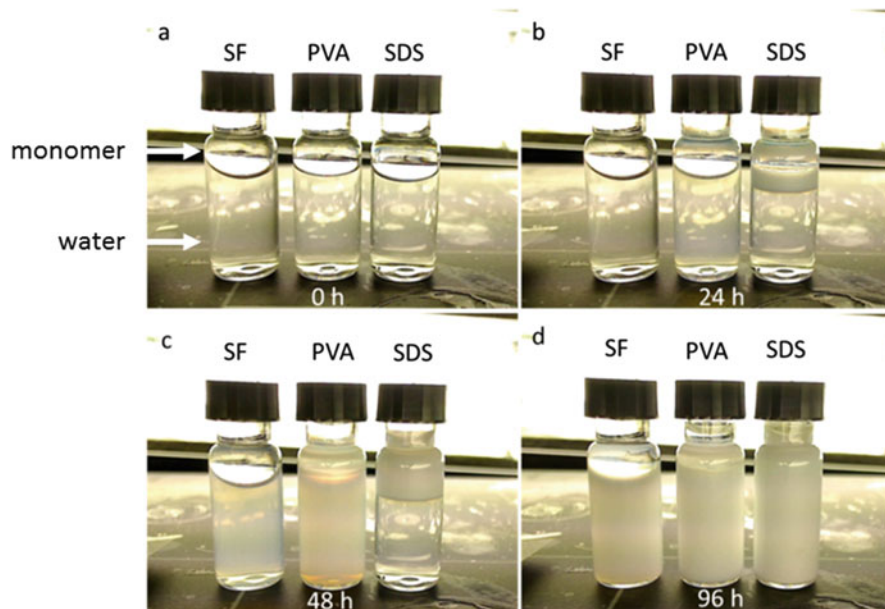


Fig. 12 Time sequence of images illustrating self-photoinitiated styrene polymerization after (a) placing the monomer phase on top of the water phase and (b) 24 h, (c) 48 h, and (d) 96 h later; *SF* surfactant-free, *PVA* poly(vinyl alcohol), *SDS* sodium dodecylsulfate as stabilizer (1% by weight in the aqueous phase). The photopolymerizations were carried out at room temperature by placing the reaction vials in front of normal fluorescence tubes used for laboratory illumination (Osram L 18 W, light color 840, lumilux, cool white)

surfactant-free polymerization, the monomer phase resembles that of a bulk polymerization (i.e., a transparent glassy state).

In our opinion, this is the most interesting result. The styrene phase is almost completely transparent during the entire duration of the reaction in the absence of stabilizer. However, in the presence of SDS, a typical stabilizer for emulsion polymerization, the polymerization starts in the monomer phase with formation of an emulsion phase visible by its turbidity (Fig. 13). With poly(vinyl alcohol) (PVA) as stabilizer, appearance of the monomer phase is between that of the other cases. After 48 h of polymerization time, the aqueous phase of the polymerization with PVA is much more turbid than in the other cases. Particularly for the polymerization with SDS, the latex phase appears to be concentrated in the oil phase, as indicated by its increasing thickness compared with the other system (Fig. 12c). The images in Fig. 13 for polymerization with SDS elucidate this behavior, particularly the shift in turbidity from the oil toward the water phase.

The sequence of snapshots in Fig. 13 shows how the main locus of polymerization, evaluated by the turbidity of both phases, shifts from the oil toward the water phase. A turbid region in the monomer phase appears about 6 h after exposing the vial to the light source. It appears as if the “pressure of the latex” in the oil phase

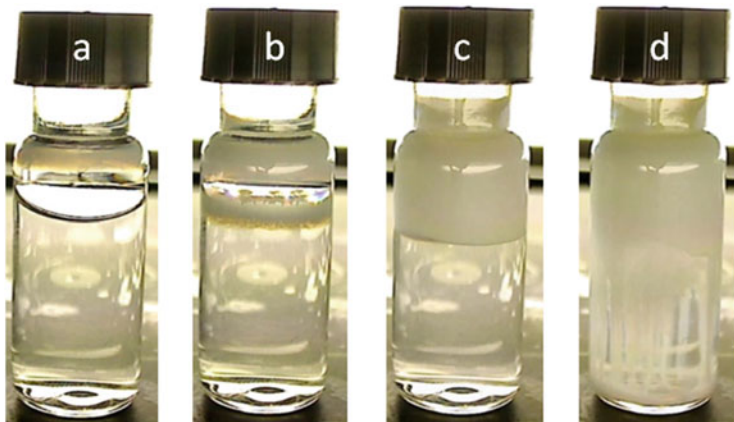


Fig. 13 Transition of turbidity from the oil to the water phase during self-photoinitiated polymerization of styrene placed on top of an aqueous SDS solution (for details see Fig. 12). The vial was illuminated for (a) 10 h 40 min, (b) 13 h 50 min, (c) 53 h 10 min, and (d) 56 h 40 min

increases with time until it breaks through the interface into the aqueous phase. However, this is a prosaic description, rather than scientific. Admittedly, a sound scientific explanation for this effect is not possible at present. It appears reasonable to assume that this behavior is related to spontaneous emulsification and, particularly, to that of water in the oil phase, supported by the action of SDS surfactant. Further investigations are necessary to reveal more details of this process.

The experimental data in Fig. 12, labeled “SF,” were obtained with pure styrene on top of pure water (i.e., the simplest possible recipe for heterophase polymerization). At this point, questions arise regarding the stabilization mechanism of the spontaneously formed drops or particles. Zeta potential measurements revealed that the particles obtained in the absence of any stabilizer had a potential of -47.1 ± 1.9 mV. This value is comparable with that measured for particles stabilized with SDS (-50.6 ± 3.1 mV) [59], but much more negative than that observed for the particles stabilized with PVA (-14.0 ± 3.7 mV). Regarding the origin of this potential, two hypotheses can be discussed. The first hypothesis, that it is a kind of contact potential, can be traced back to Alfred Coehn [60]. The second explanation is based on preferential adsorption of hydroxyl anions at the droplet-water interface, which was also observed for other nonpolar oil-in-water emulsions [61–67].

5 Summary

In this contribution, we look at mass transfer in heterogeneous systems, mainly from the perspective of colloid science rather than chemical engineering. Our main goal is to combine various experimental observations from study of

nonpolymerizing systems, which are all related to heterophase polymerization. Because studying these effects was only possible under experimental conditions very different from those applied in technical heterophase polymerization, direct experimental proof of their relevance and importance for technical polymerizations is not possible at this time. However, we are convinced of the importance of the results for a deeper mechanistic understanding, principally because the observed effects connect heterophase polymerization with the general context of physical and colloid chemistry. Hopefully, this discussion will initiate new studies in the future.

We focus on spontaneous emulsification as thermodynamically driven emulsion formation at a colloidal scale, which should take place under all experimental conditions, including forced emulsification processes. However, this can only be reasonably supposed and is hard to verify experimentally, because forced emulsification is always able to emulsify larger volumes.

The key aspect of our discussion with respect to mass transfer between two liquid phases is that it takes place in both directions across the interface. For the oil–water combination, this means that an oil-in-water emulsion on the aqueous side and a water-in-oil emulsion on the oily side are formed. A number of experimental results are presented that prove spontaneous emulsification.

The implications of these results for the mechanism of heterophase polymerization, particularly emulsion polymerization, will be treated in an upcoming paper dealing with simulations of mass transfer into polymerizing latex particles.

Acknowledgements O.K. acknowledges a scholarship from the DAAD (German Academic Exchange Service) in the year 2011. Financial support of the MPI of Colloids and Interfaces is gratefully acknowledged. The authors are obliged to Mrs. Ursula Lubahn and Mrs. Sylvia Pirok for technical assistance. The authors are particularly thankful for fruitful discussions with Markus Antonietti, the head of the Colloid Chemistry Department.

References

1. Danckwerts PV (1958). *Chem Eng Sci* 8:93
2. Cohn G (1948). *Chem Rev* 42:527
3. Tammann G (1925). *Z Allg Anorg Chem* 149:21
4. van't Hoff JH (1884) *Etudes de Dynamique Chimique*. Frederik Muller., Amsterdam
5. van't Hoff JH, van Deventer CM (1887). *Z Phys Chem* 1:165
6. Zlokarnik M (1999) *Rührtechnik*. Springer, Berlin
7. Miller-Chou BA, Koenig JL (2003). *Prog Polym Sci* 28:1223
8. Narasimhan B, Peppas NA (1997). *Polym Anal Polym Phys* 128:157
9. Hirose H, Shibayama M (1998). *Macromolecules* 31:5336
10. Holtus G, Borchard W (1989). *Colloid Polym Sci* 267:1133
11. Lee WF, Hsu CH (1998). *J Appl Polym Sci* 69:1793
12. House JE (1980). *Inorg Nucl Chem Lett* 16:185
13. House JE (1980). *Thermochim Acta* 40:225
14. Walas SM (1990) 10 mixing and agitation. *Chemical process equipment: selection and design*. Butterworth–Heinemann, Newton
15. Kolmogorov AN (1949). *Dokl Akad Nauk SSSR* 66:825

16. Höhne P, Krüger K, Tauer K (2013). *Colloid Polym Sci* 291:483
17. Metcalfe G, Ottino JM (1994). *Phys Rev Lett* 72:2875
18. Epstein IR (1995). *Nature* 374:321
19. Newton I (1726) *Philosophiae Naturalis Principia Mathematica*. London
20. Nakano A, Minoura Y (1972). *J Appl Polym Sci* 16:627
21. Nakano A, Minoura Y (1977). *J Appl Polym Sci* 21:2877
22. Nakano A, Minoura Y (1975). *Macromolecules* 8:677
23. Nakano A, Minoura Y (1975). *J Appl Polym Sci* 19:2119
24. di Sessa AA (1980). *Am J Phys* 48:365
25. Vazquez M, Schmalzing D, Matsudaira P, Ehrlich D, McKinley G (2001). *Anal Chem* 73:3035
26. Izzat N, Slaiman IN, Al-Qamaje HM, Abdul-Jabbar MF, Al-shiffee HS (2011). *J Eng* 17:1143
27. Shanshool J, Abdul Jabbar MF, Slaiman IN (2011). *Pet Coal* 53:218
28. Nghe P, Tabeling P, Ajdari A (2010). *J Non-Newtonian Fluid* 165:313
29. Kai Kang K, Lee LJ, Koelling KW (2005). *Exp Fluids* 38:222
30. Kean ZS, Ramirez ALB, Craig SL (2012). *J Polym Sci Polym Chem* 50:3481
31. Kondepudi DK, Kaufman RJ, Singh N (1990). *Science* 250:975
32. Kondepudi DK, Hall JK (1992). *Physica A* 188:113
33. Kondepudi DK, Bullock KL, Digits JA, Hall JK, Miller JM (1993). *J Am Chem Soc* 115:10211
34. Martin B, Tharrington A, Wu XL (1996). *Phys Rev Lett* 77:2826
35. Krüger K, Wei CX, Nuasaen S, Höhne P, Tangboriboonrat P, Tauer K (2015). *Colloid Polym Sci* 293:761
36. Wei C, Tauer K (2016). *Macromol Symp* 370:99
37. Wei C, Plucinski A, Nuasaen S, Tripathi A, Tangboriboonrat P, Tauer K (2017). *Macromolecules* 50:349
38. Tripathi A, Wei C, Tauer K (2017). *Colloid Polym Sci* 295:189
39. van Herk A, Gilbert B (2005) Emulsion polymerisation. In: van Herk A (ed) *Chemistry and technology of emulsion polymerisation*. Blackwell, Hoboken, pp 46–78
40. van Herk A (2013) *Chemistry and technology of emulsion polymerisation*. Wiley, Chichester
41. Harkins WD (1947). *J Am Chem Soc* 69:1428
42. Mason SG (1973). *Chem Can* 25:29
43. Ludwig A, Flechtner U, Prüss J, Warnecke H-J (1997). *Chem Eng Technol* 20:149
44. Polat H, Polat M, Chander S (1999). *AIChE J* 45:1866
45. Bancroft WD (1912). *J Phys Chem* 16:177
46. Kozempel S, Tauer K, Rother G (2005). *Polymer* 46:1169
47. Kozempel S (2005) *Emulgatorfreie emulsionspolymerisation - Monomerlösungszustand und Teilchenbildung*. PhD, University of Potsdam, Potsdam
48. Pelissetto A, Vicari E (2002). *Physics Rep Rev Sect Phys Lett* 368(6):549–727
49. Tauer K, Kozempel S, Rother G (2007). *J Colloid Interface Sci* 312:432
50. Tauer K, Nozari S, Ali AMI, Kozempel S (2005). *Macromol Rapid Commun* 26:1228
51. Tauer K, Hernandez H, Kozempel S, Lazareva O, Nazaran P (2008). *Colloid Polym Sci* 286:499
52. Lane WH (1946). *Ind Eng Chem Anal Ed* 18:295
53. Kabalnov A (2001). *J Dispers Sci Technol* 22:1
54. Kabalnov AS, Pertzov AV, Shchukin ED (1987). *Colloid Surf* 24:19
55. Höhne P, Tauer K (2014). *Colloid Polym Sci* 292:2983
56. Okubo M, Ise E, Yamashita T (1998). *J Polym Sci Part A: Polym Chem* 36:2513
57. Okubo M, Shiozaki M, Tsujihira M, Tsukuda Y (1991). *Colloid Polym Sci* 269:222
58. Krüger K, Tauer K, Yagci Y, Moszner N (2011). *Macromolecules* 44:9539
59. Wei C (2017) *On the role of monomer drops and swelling in aqueous heterophase polymerization*. University of Potsdam, Potsdam
60. Coehn A (1898). *Ann Phys* 300:217
61. Beattie JK, Djerdjev AM (2004). *Angew Chem Int Ed* 43:3568
62. Beattie JK, Djerdjev AM, Warr GG (2009). *Faraday Discuss* 141:31

63. Creux P, Lachaise J, Graciaa A, Beattie JK, Djerdjev AM (2009). *J Phys Chem B* 113:14146
64. Leunissen ME, Van Blaaderen A, Hollingsworth AD, Sullivan MT, Chaikin PM (2007). *Proc Natl Acad Sci* 104:2585
65. Marinova K, Alargova R, Denkov N, Velev O, Petsev D, Ivanov I, Borwankar R (1996). *Langmuir* 12:2045
66. Siretanu I, Chapel JP, Drummond C (2011). *ACS Nano* 5:2939
67. Stachurski J, MichaŁek M (1996). *J Colloid Interface Sci* 184:433

Kinetic Modeling of Precipitation and Dispersion Polymerizations



L. Ivano Costa and G. Storti

Abstract Dispersion and precipitation polymerizations represent a simple and attractive synthetic platform for the production of a large variety of polymers and micron-sized particles. Although the main qualitative features of these processes have been known for a long time, obtaining quantitative descriptions of the polymerization kinetics and, especially, the full molecular weight distributions, is still a major challenge because of the heterogeneous nature of the reactions. This review summarizes the most relevant aspects of the processes involved, focusing on the free-radical polymerization mechanism, with special emphasis on the key role of radical interphase transport. We describe a unified mathematical modeling framework that has enabled accurate description of reaction rates and evolution of molecular weight distributions in a number of cases. Examples of copolymerization reactions carried out in organic and supercritical fluids are discussed to demonstrate the reliability and capabilities of the modeling approach.

Keywords Diffusion • Dispersed systems • Dispersion polymerization • Modeling • Precipitation polymerization • Radical polymerization

Contents

| | | |
|---|--|----|
| 1 | Introduction | 46 |
| 2 | Mechanism of Reaction and Polymerization Locus | 49 |
| 3 | Model Framework | 52 |
| | 3.1 Key Assumptions | 52 |

L.I. Costa
Etzbergstrasse 19c, 8405 Winterthur, Switzerland
e-mail: liborio78@gmail.com

G. Storti (✉)
Institute for Chemical and Bioengineering, ETH Zürich, Vladimir-Prelog-Weg 1-5/10, 8093
Zürich, Switzerland
e-mail: giuseppe.storti@chem.ethz.ch

| | | |
|-----|---|----|
| 3.2 | Material and Population Balance Equations | 53 |
| 3.3 | Kinetic Rate Constants | 56 |
| 3.4 | Transport Parameters | 58 |
| 4 | Applications | 61 |
| 4.1 | Precipitation Polymerization in Organic Solvent | 61 |
| 4.2 | Precipitation and Dispersion Copolymerizations in Supercritical Carbon Dioxide .. | 65 |
| 4.3 | Precipitation Polymerization of Vinyl Chloride | 69 |
| 5 | Conclusions | 72 |
| | References | 73 |

1 Introduction

Dispersion polymerization is a heterogeneous polymerization process enabling the production of micron-sized polymer particles with narrow size distributions [1–3]. Even though different polymerization mechanisms can be applied [4], free-radical polymerization is by far the most popular and it is the only one considered here. Dispersion polymerization can be considered an evolution of precipitation polymerization. In precipitation polymerization, the initial system is a homogeneous solution of monomer and initiator in a solvent in which the polymer is insoluble. As the polymerization proceeds, the system undergoes phase separation. The polymer chains nucleate first in the form of unstable nuclei, which then aggregate and/or coalesce to eventually form large polymer aggregates, as sketched in Fig. 1. In dispersion polymerization, a suitable stabilizer (or simply “surfactant”) is initially added to the system. The stabilizer adsorbs or anchors to the surface of the polymer particles and hinders their aggregation/coalescence, thus leading to a stable colloidal dispersion. Ionic, nonionic, steric, and polymeric stabilizers can be used, the choice depending on the nature of the system [1–5].

In precipitation polymerization, the irregular aggregates produced in the absence of surfactant have sizes in the range 1–100 μm . In dispersion polymerization, roughly spherical particles of 0.1–10 μm are formed in the presence of sufficient effective surfactant. In both cases, the polymerization occurs under heterogeneous conditions in the presence of a continuous solvent-rich phase and a dispersed monomer-swollen and polymer-rich phase. For this reason, we refer to such systems in general as “dispersed systems”, even when dealing with precipitations.

Dispersion polymerization was initially developed with the aim of producing coating formulations with high polymer content and low viscosity, and many of the early reports on dispersion polymerizations are in fact patents from the chemical industry for such applications [6–9]. For the same reason, most early studies focused on reactions carried out in nonpolar organic solvents such as low molecular weight hydrocarbons, which, being highly volatile, are ideal candidates for coating formulations [10, 11]. Nevertheless, this technique is not limited to the use of nonpolar solvents, and reactions carried out in polar solvents have been reported since the 1980s [2, 3, 5]. The range of suitable solvents was further extended to the use of nonconventional solvents such as supercritical carbon dioxide (scCO_2) with

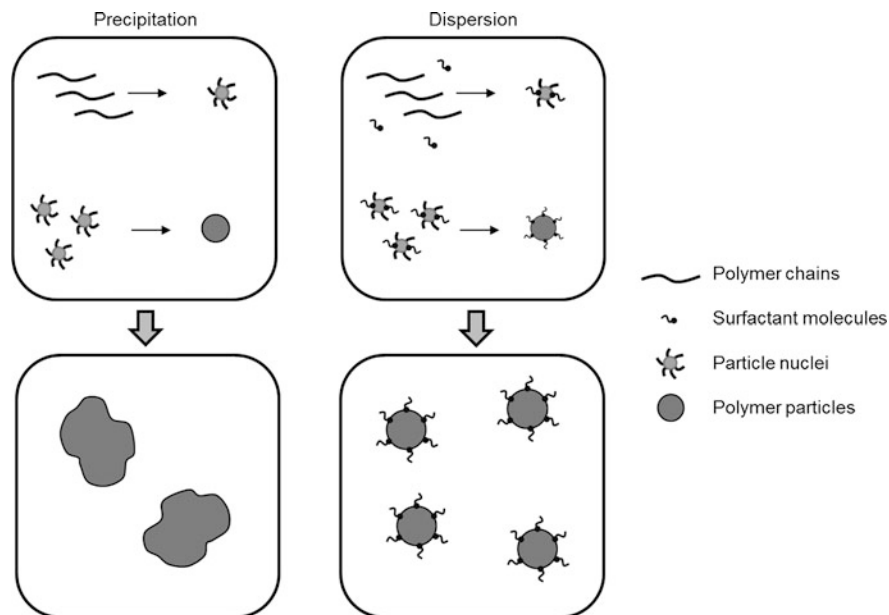


Fig. 1 Time evolution of precipitation/dispersion free-radical polymerization processes. *Top*: Starting from a single homogenous phase, insoluble polymer chains are formed, which nucleate in unstable particle nuclei that aggregate/coalesce into polymer particles. *Bottom*: Without surfactant (precipitation), large irregularly shaped particles are formed; with surfactant (dispersion), smaller more regular particles are produced

the aim of replacing the more typical, but often hazardous and/or toxic, organic solvents [12]. Because many common low molecular weight monomers are easily soluble in scCO_2 , but most high molecular weight polymers are not [13, 14], heterogeneous polymerizations in scCO_2 under precipitation or dispersion conditions are relatively straightforward to accomplish, at least on a laboratory scale [15–24].

More recently, it has been realized that precipitation and dispersion polymerizations are relatively simple and effective techniques for production of micron-sized particles with advanced structures and functionalities. Extensive and updated reviews cover this topic; for example, Li et al. [25] and Pich and Richtering [26] report the use of precipitation polymerization for the preparation of hollow structures and aqueous microgels, while Zhang [27] and Sun et al. [28] review the emerging field of controlled heterogeneous polymerization techniques for the synthesis of “living” functionalizable nano-objects and supramolecular objects ranging from micelles to vesicles and worms. Thus, although precipitations and dispersions are mature techniques for the production of a large variety of polymers and colloidal microspheres for conventional applications, at the same time they represent a simple and versatile platform for the synthesis of advanced nanomaterials.

Compared with the large amount of experimental activity in the field [4], the number of works that focus on quantitative modeling of polymerization kinetics in dispersed systems is relatively low. The reason for this can be attributed to the complexity of such systems when reliable quantification of the physical and chemical phenomena involved is required. As mentioned above, a fully detailed kinetic description requires the modeling of particle nucleation and of surfactant partitioning between the phases, which in turn dictates the final number of particles and their stability behavior (i.e., the rate at which they aggregate). In parallel, the monomer often swells the polymer particles and, hence, the polymerization reaction may occur in both the continuous and dispersed phases, making the identification of the predominant locus of polymerization a nontrivial task [24, 29–31]. This is due to the fact that the relative contribution of the polymerization rate in the two phases is affected by many system parameters, as Jiang et al. [32] and Saenz and Asua [33] have shown through their experimental investigation of the kinetics of dispersion homopolymerization of methyl methacrylate in methanol/water mixtures, and of dispersion copolymerization of styrene and butyl acrylate in ethanol/water.

In view of this complexity, the first proposed kinetic models for dispersed systems were quite empirical and aimed to describe reaction rate and average molecular weight, rather than the full polymer molecular weight distribution (MWD) or aspects related to particle nucleation and particle size distribution. In this respect, the works of Barrett and Thomas on the dispersion polymerization of methyl methacrylate [10], of Crosato-Arnaldi et al. and Olay on the heterogeneous polymerization of vinyl chloride [34, 35], and of Avela et al. on the precipitation polymerization of acrylic acid [36] deserve special mention. One of the first attempts to model the full MWD was made by Abdel-Alim and Hamielec [37] and was followed by more comprehensive, two-phase models [38–45]. It was realized that the radical interphase transport between the continuous and dispersed phases is one of the most crucial aspects for reliable modeling of precipitations and dispersions [43–45]. By properly accounting for such transport process, a common modeling framework was developed for these complex processes and found to be successful in modeling both homopolymerizations [43–46] and copolymerizations [47, 48].

It is the aim of this contribution to review such modeling framework that enables the prediction of reaction rates and MWDs for this type of heterogeneous polymerizations. The model accounts for all the most relevant reactions taking place in both phases (continuous and dispersed) as well as for the partitioning of the different species between the phases. Namely, while all low molecular weight species are assumed to be partitioned according to thermodynamic equilibrium, the transport rate of active chains (or radicals) is accounted for explicitly as the key factor determining the relative contribution of each phase to the polymer buildup (i.e., as reaction locus). Notably, the model does not include population balances for the particle size distribution of the dispersed phase, thus relying on simpler, ordinary differential equations. The only particle-related property needed as model input is the total interphase surface area. Different approaches have been suggested for its reliable evaluation, depending upon particle morphology or experimentally

observable parameters, without relying on complex particle population balances that require inclusion of additional mechanisms (e.g., particle nucleation and aggregation/breakage terms) into the model [38–40, 49, 50]. Once a model for the specific system under examination has been validated and all parameters evaluated, the (particle) population balances can be integrated into the model equations if information about the particle size distribution are of relevance. This separation between kinetics and particle size distribution is convenient for facilitating an understanding of the mechanistic behavior of the system and improving the reliability of the estimated model parameters.

The polymerization mechanism is discussed in Sect. 2 and the possible operating regimes are rationalized in terms of dimensionless quantities correlating transport properties and termination rates. In Sect. 3, the main model equations are presented and suitable strategies and correlations for evaluating the parameters are provided. In Sect. 4, three case studies illustrate the capabilities of the proposed modeling approach in predicting conversion and evolution of MWD.

2 Mechanism of Reaction and Polymerization Locus

The polymerization starts in a single-phase, homogeneous system (the solvent-rich phase). Accordingly, in the early stages of polymerization, all the kinetic steps typical of free-radical polymerization (initiation, propagation, and terminations) occur in this phase, as schematically shown in Fig. 1. However, as soon as insoluble polymer chains are formed, they phase-separate and aggregate into unstable primary nuclei, which eventually coalesce into stable particles. From this moment on, the system becomes heterogeneous and two phases are present: the continuous, solvent-rich phase and the newly formed dispersed, polymer-rich phase. The generation of polymer particles proceeds until the overall surface area of the polymer phase is so large that all polymer chains formed in the continuous phase are “captured” by the particles; that is, the process of diffusion into existing particles becomes much faster than their aggregation into primary nuclei [1, 49, 51]. When present, surfactant molecules absorb or anchor on the surface of the particles and prevent further coalescence and/or aggregation.

Experimental and theoretical evidences indicate that the nucleation phase generally occurs in the first few seconds to minutes of the reaction and is already complete after few percent of monomer conversion [49, 52–54]. Subsequently, the concentration of particles remains constant provided that an effective surfactant is present in the system. When the surfactant is not effective enough or absent (as in precipitation polymerization), polymer particles may coalesce and/or aggregate, which leads to a decrease in their concentration. This can result in a longer nucleation phase, because capture by pre-formed particles is less efficient in view of the reduced overall surface area.

As already mentioned, once the system evolves from homogeneous to heterogeneous, the reaction proceeds in both phases provided that the monomer is at least partly solubilized in the dispersed phase. Identification of the relative contribution

of the reaction in each phase is crucial for reliable prediction of the evolution of polymer buildup. The relevance of each reaction locus can be conveniently rationalized in terms of the dimensionless “second Damköhler number,” or equivalently from its reciprocal, the so-called Ω parameter [45, 55]. Let us assume that, at a given instant in time, the total volumes of the continuous and dispersed phases are V_1 and V_2 , respectively, and that the total interphase area (i.e. the total particle surface area) is A_p . For each phase j the quantity Ω_j is defined as the ratio between the rate of diffusion of radicals from that phase to the other phase and the rate of termination of the radicals in the same phase j :

$$\Omega_1 = \frac{KA_p}{V_1 k_{t,1} [R_1]} \quad (1)$$

$$\Omega_2 = \frac{\alpha KA_p}{V_2 k_{t,2} [R_2]} \quad (2)$$

where K is the overall mass transfer coefficient for phase 1, $[R_j]$ is the overall concentration of active chains in phase j and α is the partition coefficient of the radicals between the two phases at thermodynamic equilibrium:

$$\alpha = \frac{[R_1]_{\text{eq}}}{[R_2]_{\text{eq}}} \quad (3)$$

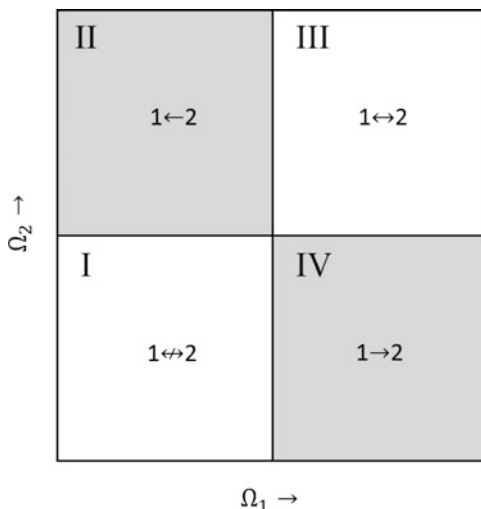
where $[R_j]_{\text{eq}}$ indicates the equilibrium concentration of active chains in phase j .

In general, parameters such as α , $k_{t,j}$, and K are dependent on composition and chain length and, therefore, Ω_j is also dependent on these parameters (a detailed discussion about their meaning and evaluation is provided in the following sections). However, for the sake of simplicity, let us neglect such dependencies here and assume constant Ω_j values. According to Eqs. 1 and 2, a value of Ω_j much larger than 1 means that the rate at which radicals in phase j diffuse out of that phase is much larger than the rate at which they terminate in the same phase. On the other hand, the opposite is true when Ω_j is much smaller than 1 (i.e., the rate of termination of the radicals in phase j is much larger than the rate at which they diffuse to the other phase). It follows that four limiting operating regimes can be readily identified according to the Ω values, as represented in the master plot in Fig. 2:

(I) $\Omega_1 \ll 1$ and $\Omega_2 \ll 1$: The termination rate is higher than that of diffusion out for both phases. This implies that radicals predominantly terminate in their original phase and the system can be considered segregated with respect to radical partitioning, in view of their limited transfer from one phase to the other.

(II) $\Omega_1 \ll 1$ and $\Omega_2 \gg 1$: The termination rate is higher than that of diffusion out only for the continuous phase, whereas the opposite is true for the dispersed phase. Accordingly, radicals generated in the dispersed phase diffuse out and eventually terminate in phase 1 (from where they cannot diffuse out because $\Omega_1 \ll 1$), and the continuous phase is the main reaction locus.

Fig. 2 Ω Master plot showing the four operating regions in terms of radical distribution: *I* segregated system, *II* phase 1 favored, *III* equilibrated distribution, and *IV* phase 2 favored



(III) $\Omega_1 \gg 1$ and $\Omega_2 \gg 1$: The rate of diffusion out of one phase is larger than the termination rate for both phases. Therefore, radicals are exchanged between the two phases very rapidly and, on average, each radical crosses the boundary from one phase to the other many times before terminating in one of the two phases. Under such conditions, the radicals achieve thermodynamic equilibrium between the two phases.

(IV) $\Omega_1 \gg 1$ and $\Omega_2 \ll 1$: This case is the opposite of case II. Radicals generated in the continuous phase ($j=1$) diffuse to the dispersed phase ($j=2$) much faster than they terminate in their original phase. By contrast, radicals in the dispersed phase terminate there before diffusing out to the continuous phase. Irrespective of where the radicals are generated, they predominantly terminate in the dispersed phase, which therefore represents the main reaction locus.

The four sectors in Fig. 2 correspond to the four operating regions identified above. Given the Ω values for each phase, the location of a given system in this plane can be found and the corresponding picture in terms of radical interphase transport readily assessed, from which the predominant reaction locus (if any) can be quickly identified. On the other hand, even if very short oligomers are partly soluble in the continuous phase, the continuous phase is a poor solvent for the polymer and the partition coefficient is expected to decay rapidly as the length of the chains increases. Therefore, because the partition coefficient α is usually very small, the case $\Omega_2 \ll 1$ occurs frequently. This means that the operating conditions for dispersed systems are determined by the value of Ω_1 alone, and regimes I and IV are the only feasible limiting regimes.

Given the key relevance of the Ω value of the continuous phase, the next question is how to control its value and, therefore, how to determine the operating regime of a given polymerization system. Because reaction rate constants and transport coefficients are given once the specific chemistry of a system is selected,

the most relevant tunable parameter is the interphase area, A_p . Specifically, a system is radical-segregated for extremely low values of the particle surface area, whereas the dispersed phase is the dominant reaction locus for very large values. Accordingly, this particle property becomes very important in determining not only the particle size and colloidal stability, which is expected, but also the two main aspects of the overall polymerization kinetics, reaction rate, and MWD. This interplay is described in more detail in the following sections.

3 Model Framework

In this section, the main constitutive model equations, as well as the correlations required to estimate the most relevant parameters, are reported and discussed. For the sake of clarity, the equations are written for a single monomer case (homopolymerization) and a basic radical polymerization scheme, but the same approach can be easily extended to the case of multiple monomers and more complex kinetic schemes, including chain transfer and crosslinking reactions [43, 45, 47, 48].

3.1 Key Assumptions

According to the phenomenological picture described above, the following key assumptions are considered:

- (1) Particle nucleation is instantaneous and not accounted for in the model. As previously noted, this assumption is justified by the observation that the nucleation period in dispersion polymerization systems is much shorter than the overall polymerization time [49, 53, 54, 56]. Therefore, the role of the stabilizer in determining the particle concentration is not explicitly considered and a constant number of polymer particles (small enough to correspond to a negligible polymer amount at the end of the nucleation phase) is assumed to be present since the early phase of the reaction. This assumption is also considered valid for the case of precipitation polymerization. From a practical viewpoint, this implies that, in the absence of seeds (pre-formed particles), one can consider the system as homogeneous until a critical percentage conversion, X_{cr} , is reached. At $X = X_{cr}$, polymer particles form instantaneously and the reaction proceeds under heterogeneous conditions with a constant particle concentration. The value of X_{cr} is typically below 1%. The corresponding initial value of the particle size is readily evaluated given the particle number.
- (2) Low molecular weight species (solvent, initiator, monomer) are in thermodynamic equilibrium between the continuous solvent-rich phase and the dispersed

Table 1 Kinetic scheme

| Reaction step | Reaction scheme | Rate [mol L ⁻¹ s ⁻¹] |
|----------------------|--|--|
| Initiation | $I_j \xrightarrow{k_{d,j}} 2I_j^*$ | $k_{d,j}I_j$ |
| | $I_j^* + M_j \xrightarrow{k_{I,j}} R_{1,j}^*$ | $2f_j k_{d,j} I_j$ (for $k_{I,j} \gg k_{d,j}$) |
| Propagation | $R_{n,j}^* + M_j \xrightarrow{k_{p,j}} R_{n+1,j}^*$ | $k_{p,j} R_{n,j}^* M_j$ |
| Termination | $R_{n,j}^* + R_{m,j}^* \xrightarrow{k_{tc,j}} P_{n+m,j}$ | $k_{tc,j} R_{n,j}^* R_{m,j}^*$ |
| | $R_{n,j}^* + R_{m,j}^* \xrightarrow{k_{td,j}} P_{n,j} + P_{m,j}$ | $k_{td,j} R_{n,j}^* R_{m,j}^*$ |
| Interphase transport | $R_{n,1}^* \rightleftharpoons R_{n,2}^*$ | $\frac{K_n A_p}{V_j} ([R_{n,1}^*] - \alpha_n [R_{n,2}^*])$ |

Where I_j , M_j , $R_{n,j}^*$, and $P_{n,j}$ represent initiator, monomer, and active and terminated polymer chains of length n in phase j , respectively

polymer-rich phase. Their partitioning is independent of particle size and there are no concentration gradients within the particles.

- (3) Both phases are considered as potential reaction loci (for $X > X_{cr}$), and the interphase mass transfer for the radicals is accounted for explicitly. The polymer particles are considered as a single pseudo-phase with homogeneous radical concentration.
- (4) Dead polymer is fully insoluble in the continuous phase and is considered instantaneously accumulated in the dispersed phase.

Given these general premises, the mathematical framework required to evaluate the system kinetics is detailed in the following subsections, with reference to the basic free-radical polymerization kinetic scheme detailed in Table 1. Note that the rate of radical diffusion between the two phases is also included in Table 1.

3.2 Material and Population Balance Equations

The mass balances for low molecular weight species and population balances for active and dead polymer chains are reported below. Subscripts 1 and 2 indicate continuous and dispersed phases, respectively, and the rates of all the kinetic events listed in Table 1 are considered.

$$\frac{dS}{dt} = 0 \quad (4)$$

$$\frac{dI}{dt} = -k_{d,1}[I_1]V_1 - k_{d,2}[I_2]V_2 \quad (5)$$

$$\begin{aligned} \frac{dM}{dt} = & -2f_1k_{d,1}[I_1]V_1 - 2f_2k_{d,2}[I_2]V_2 - k_{p,1}[M_1]V_1 \sum_{n=1}^{\infty} [R_{n,1}^*] \\ & - k_{p,2}[M_2]V_2 \sum_{n=1}^{\infty} [R_{n,2}^*] \end{aligned} \quad (6)$$

$$\begin{aligned} \frac{dR_{n,1}^*}{dt} = & \delta_{(n,1)}2f_1k_{d,1}[I_1]V_1 + k_{p,1}[M_1]V_1([R_{n-1,1}^*](1 - \delta_{(n,1)}) - [R_{n,1}^*]) + \\ & - [R_{n,1}^*]V_1 \sum_{m=1}^{\infty} (k_{tc,1} + k_{td,1})[R_{m,1}^*] - K_nA_p([R_{n,1}^*] - \alpha_n[R_{n,2}^*]) \end{aligned} \quad (7)$$

$$\begin{aligned} \frac{dR_{n,2}^*}{dt} = & \delta_{(n,1)}2f_2k_{d,2}[I_2]V_2 + k_{p,2}[M_2]V_2([R_{n-1,2}^*](1 - \delta_{(n,1)}) - [R_{n,2}^*]) + \\ & - [R_{n,2}^*]V_2 \sum_{m=1}^{\infty} (k_{tc,2} + k_{td,2})[R_{m,2}^*] + K_nA_p([R_{n,1}^*] - \alpha_n[R_{n,2}^*]) \end{aligned} \quad (8)$$

$$\frac{dP_{n,1}}{dt} = \frac{1}{2}V_1 \sum_{m=1}^{n-1} k_{tc,1}[R_{m,1}^*][R_{n-m,1}^*] + V_1[R_{n,1}^*] \sum_{m=1}^{\infty} k_{td,1}[R_{m,1}^*] \quad (9)$$

$$\frac{dP_{n,2}}{dt} = \frac{1}{2}V_2 \sum_{m=1}^{n-1} k_{tc,1}[R_{m,2}^*][R_{n-m,2}^*] + V_2[R_{n,2}^*] \sum_{m=1}^{\infty} k_{td,2}[R_{m,2}^*] \quad (10)$$

where f_j is the initiator efficiency, V_j the volume of phase j , K_nA_p the product of an overall radical transport coefficient and the total surface area of the particles, α_n the chain-length dependent partition coefficient for the radicals, and $\delta_{(n,1)}$ the delta Dirac function, which is equal to 1 when $n = 1$ and equal to 0 otherwise. While Eqs. 4–6 are written in terms of total number of moles of solvent, initiator, and monomer (S , I , and M) in both phases, the population balance equations (Eqs. 7–10) are the phase-specific, standard equations for free-radical polymerization systems. The only notable difference is the presence of the radical interphase transport (last term in Eqs. 7 and 8), which provides a coupling between the radical concentrations in the two phases. Note that the radical transport rate is expressed using the two-film theory [57] as the product of an overall transport coefficient and a driving force evaluated as the difference between the radical concentration in the continuous phase and the one in the same phase in equilibrium with the particle phase.

From the solution of the population balance equations, the moments of the first, leading orders of the polymer chain length distribution can be readily evaluated (e.g., $\lambda_i = \sum_{n=1}^{\infty} n^i (P_{n,1} + P_{n,2})$ for the i th order). Given the moments, calculation of the main average molecular weights follows from their definition. The overall mass of produced polymer, m , assumed to be completely in phase 2 (assumption 4) is readily evaluated as $m = \lambda_1 MW$, where MW is the molecular mass of the monomer repeating units.

To solve Eqs. 4–10, additional equations are needed to characterize the equilibrium partitioning of the low molecular weight species. At each instant of time, given the total amounts of solvent, initiator, monomer, and polymer (as calculated from Eqs. 4–10), the following equalities apply:

$$S = [S_1]V_1 + [S_2]V_2 \quad (11)$$

$$I = [I_1]V_1 + [I_2]V_2 \quad (12)$$

$$M = [M_1]V_1 + [M_2]V_2 \quad (13)$$

Moreover, the concentrations of solvent, initiator, and monomer in the two phases at equilibrium are constrained by the equality of the chemical potentials in the two phases:

$$\mu_{S,1} = \mu_{S,2} \quad (14)$$

$$\mu_{I,1} = \mu_{I,2} \quad (15)$$

$$\mu_{M,1} = \mu_{M,2} \quad (16)$$

Thus, by complementing the six equations Eqs. 11–16 with suitable correlations for the chemical potentials and the specific volumes of the two phases as a function of state variables, the equilibrium concentrations of the low molecular weight species can be determined at each time point by solving the corresponding set of nonlinear algebraic equations by standard numerical methods.

Different approaches are available for evaluating the thermodynamic properties of the different phases. Cubic equations of state such as the Peng–Robinson equations [58–60] can be used, or more comprehensive approaches suitable for polymeric systems, such as the statistical associating fluid theory [61, 62], the perturbed hard-sphere chain model [63], the Simha–Somcynski lattice-hole theory [64, 65], and the lattice theory of Sanchez and Lacombe [66]. Moreover, when dealing with compressible systems (gaseous continuous phase), the system pressure is also unknown and can be evaluated by imposing the following additional constraint:

$$V_R = V_1 + V_2 \quad (17)$$

where V_R is the reactor volume. In this context, the Sanchez–Lacombe equation of state is widely used for its ability to correlate pressure, volume, and temperature (PVT) data [23, 42, 43] and the equilibrium of multicomponent polymeric systems [67].

On the other hand, although equations of state provide both the volumes of the two phases and the chemical potentials of the species in a single theoretical framework, they are quite demanding in terms of computational effort. When such a detailed thermodynamic description is not required, the complexity of the mathematical treatment can be reduced by using simplistic equations such as the

volume additivity rule and expressing the equilibrium conditions using oversimplified, constant partition coefficients [47]. Accordingly, Eqs. 14–16 simplify to:

$$\frac{[S_1]}{[S_2]} = K_S \quad (18)$$

$$\frac{[I_1]}{[I_2]} = K_I \quad (19)$$

$$\frac{[M_1]}{[M_2]} = K_M \quad (20)$$

Whatever the selected approach, accurate prediction of the interphase partitioning at equilibrium is a prerequisite for any reliable model of polymerization in heterogeneous systems. Therefore, the parameters of the chosen thermodynamic model should always be determined from independent equilibrium data [47, 67, 68].

For high molecular weight species (active chains), the corresponding partition coefficients α_n are also needed to evaluate the driving force in the interphase transport in terms of Eqs. 7 and 8. Such evaluation is less established than in the case of low molecular weight species and is discussed separately in Sect. 3.4.

3.3 Kinetic Rate Constants

As is always the case in polymerization modeling, reliable evaluation of kinetic parameters is a difficult task, but crucial for ensuring that the model has good predictive ability. This is even more problematic in heterogeneous systems such as found in precipitation and dispersion polymerizations, where the values of such rate constants are needed for both phases.

For the continuous phase, the rate constants of initiator decomposition, propagation, and termination are generally expressed using Arrhenius-type expressions that account for the temperature and pressure effect:

$$k(T, p) = A \exp\left(-\frac{E + \Delta V^\#(p - p_{\text{ref}})}{RT}\right) \quad (21)$$

where A is a constant pre-exponential factor, E the thermal activation energy, $\Delta V^\#$ the activation volume, and p_{ref} a reference pressure. The rate constants calculated according to Eq. 21 are the intrinsic rate constants that reflect the chemistry of the system. Because the continuous phase is often characterized by low viscosity, in most cases these values apply throughout the polymerization reaction so that chain-length and conversion dependencies can be neglected.

For the dispersed phase, at the high polymer loadings typical of the particles (>50% by weight) the rate parameters become diffusion controlled, with values several orders of magnitude smaller than found in polymer-free systems [69–71]. Among the many approaches reported in the literature for the evaluation of diffusion-controlled kinetic constants [71, 72], a very convenient approach was developed in the frame of the collision theory of chemical reactions in liquids [73] together with a Fickian description of the diffusion process. Accordingly, considering two reacting species A and B, the effective rate constant, k_{eff} , can be estimated as [71, 74]:

$$\frac{1}{k_{\text{eff}}} = \frac{1}{k} + \frac{1}{4\pi r_{\text{AB}} D_{\text{AB}} N_{\text{A}}} \quad (22)$$

where k is the intrinsic rate constant, r_{AB} is the radius of collision of the two considered reacting species (i.e., the distance at which A and B react instantaneously), and D_{AB} is the mutual diffusion coefficient.

For propagation, a reasonable estimate of the radius of collision is given by the monomer molecular diameter σ . The mutual diffusion coefficient between radical and monomer is assumed equal to the sum of the respective self-diffusion coefficients. Under diffusion-controlled regimes, the monomer diffuses much faster than long radicals (i.e., $D_{\text{M}} \gg D_{\text{R}}$), therefore it follows that:

$$D_{\text{AB}} = D_{\text{MR}} = D_{\text{M}} + D_{\text{R}} \cong D_{\text{M}} \quad (23)$$

and the propagation rate constant in the dispersed phase can be expressed as:

$$\frac{1}{k_{p,2}} = \frac{1}{k_{p,1}} + \frac{1}{4\pi\sigma D_{\text{M},2} N_{\text{A}}} \quad (24)$$

where the intrinsic rate constant of propagation has been set equal to the value in the continuous phase, $k_{p,1}$.

For the termination reaction between two radicals of length n and m , the mutual diffusion coefficient is the sum of different contributions, that is, the center of mass diffusion coefficients of the two radicals, D_n and D_m , and the diffusion due to chain growth (the so-called propagation diffusion). Accordingly, the rate constant for the termination reaction in the dispersed phase, $k_{t,nm,2}$, is given by [43, 48]:

$$\frac{1}{k_{t,nm,2}} = \frac{1}{k_{t,1}} + \frac{1}{4\pi r_{nm} N_{\text{A}} (D_{n,2} + D_{m,2} + \frac{a^2}{3} k_{p,2} [M]_2)} \quad (25)$$

where the intrinsic rate constant of termination is again set equal to the value in the continuous phase, $k_{t,1}$ and a is the root-mean end-to-end distance divided by the square root of the number of monomer units in the chain. In their analysis of diffusion-controlled termination, Russell et al. [69] estimated the parameters

a and σ for three different polymerization systems, finding in all cases that their numerical values were quite similar. Accordingly, one can conveniently approximate a as equal to the monomer diameter σ [48]. The radius of collision for the radicals, r_{nm} , ranges from the lower bound $r_{nm} = \sigma$ to the upper bound $r_{nm} = 2aj_c^{1/2}$, with $j_c^{1/2}$ being the entanglement spacing [69, 71].

For the initiation reaction, the corresponding rate constant is frequently set to the same value for both phases (i.e., $k_{d,1} = k_{d,2}$). This assumption is substantiated by the observation that the medium composition has a major impact on efficiency and much less impact on the dissociation rate constant itself [70]. Accordingly, all diffusion limitation effects on the initiation step, relevant for the polymer-rich phase, can be accounted for in terms of reduced efficiency, which is expressed as a function of the diffusion coefficient of the initiator, D_1 , as:

$$f_2 = \left[1 - \frac{D_{1,0}}{D_1} \left(1 - \frac{1}{f_{2,0}} \right) \right]^{-1} \quad (26)$$

where $D_{1,0}$ and $f_{2,0}$ represent the diffusion coefficient and efficiency in the polymer-free system, respectively, with the latter value being equal to that for the continuous phase ($f_{2,0} = f_1$).

3.4 Transport Parameters

As anticipated, the rate of radical interphase transport can be expressed as the product of the overall transport coefficient, the particle surface area, and a driving force (difference in radical concentrations). Given the impact of this transport rate on the model results, its evaluation deserves special attention.

The simplest approach is to neglect all dependencies of the two parameters K_n and A_p (mainly upon chain length and particle size) while using their product $K_n A_p$ as a single, constant parameter to be evaluated by direct fitting to the experimental data. Focusing on the cases of major practical interest (small α values), this approach is particularly convenient when full separability between particle morphology and polymerization kinetics can be assumed and an accurate value of this parameter is not strictly required. This is the case for systems exhibiting limiting segregated behavior ($K_n A_p \ll 1$; quadrant I in Fig. 2) or when the dispersed phase is the dominant reaction locus ($K_n A_p \gg 1$; quadrant IV in Fig. 2). On the other hand, for all intermediate cases, a more detailed evaluation is required. Let us therefore consider the evaluation of K_n and A_p separately.

The overall mass transport coefficient of radicals between the continuous and dispersed phases is conveniently evaluated using the two-film theory as [57]:

$$\frac{1}{K_n} = \frac{\delta}{D_{n,1}} + \frac{\delta\alpha_n}{D_{n,2}} \quad (27)$$

where δ is the thickness of the diffusive boundary layer, which can be approximated as the particle radius; $D_{n,j}$ is the diffusion coefficient of the radicals of length n in phase j ; and α_n is the equilibrium partition coefficient as given by Eq. 3 for the radicals of length n . The diffusion coefficient of a radical of length n can be expressed as a function of the diffusion coefficient of the monomer, D_M , through the empirical correlation proposed by Griffiths et al. [75], where the scaling coefficient of the diffusion coefficient with the number of repeating units is an explicit function of the polymer weight fraction ω_P :

$$D_n = D_M n^{-(0.664+2.02\omega_P)} \quad (28)$$

Several models can be applied to evaluate the diffusion coefficient of the monomer, D_M , in a polymer rich-phase [76]. Those based on the free-volume concept, and especially those based on the formulation of Vrentas and Duda [77], are some of the more powerful for application in polymer reactions [38, 41, 42, 70, 71]. According to Vrentas and Duda [77], the diffusion coefficient of the monomer is given by:

$$D_M = D_{M,0} \exp\left(-\frac{E}{RT}\right) \exp\left(-\frac{\gamma(\omega_M V_M^* + \xi_{MS}\omega_S V_S^* + \xi_{MP}\omega_P V_P^*)}{V_{FH}}\right) \quad (29)$$

where $D_{M,0}$ is a constant, pre-exponential coefficient, E is the activation energy for the jump process of the diffusing molecule, γ is the overlap factor, V_i^* is the critical hole free volume required for molecule i to “jump” into, ξ_{Mj} is the ratio between the molar volumes of monomer and molecule j , and V_{FH} is the total system free volume. Despite the large success of this formulation, its main drawback is that a large number of parameters are involved whose determination is not always trivial. To overcome this issue, Zielinski and Duda [78] and Vrentas and Vrentas [79] proposed general procedures and guidelines for independent determination of most of the required parameters. More recently, Costa and Storti [80] proposed an alternative formulation of the free-volume theory in which the self-diffusion coefficient of the monomer is expressed as:

$$D_M = D_{M,0} \exp\left(-\gamma \frac{(\omega_M/\rho_M^* + \xi_{MS}\omega_S/\rho_S^* + \xi_{MP}\omega_P/\rho_P^*)}{1/\rho - 1/\rho_{\text{mix}}}\right) \quad (30)$$

where ρ_i^* and ρ_{mix}^* are the close-packed density of species i and of the mixture, respectively, and ρ is the density of the system. The main advantage of Eq. 30 over Eq. 29 is the use of the Sanchez–Lacombe lattice theory to estimate most of the required parameters, thus simplifying the parameter evaluation problem associated with the evaluation of D_M .

The partition coefficient for the radicals, α_n , can be expressed as a function of the chain length n through semi-empirical correlations, such as that proposed by Kumar et al. [81]:

$$\log \alpha_n = \log \alpha_x + \beta(n - n_x) \quad (31)$$

where the scaling coefficient β and the parameters α_x and n_x are determined by fitting experimental data [81, 82].

Finally, let us consider the evaluation of the parameter A_p , the link between particle morphology and polymerization kinetics. Having assumed a constant number of particles, N_p , one can estimate its value through the following equation:

$$N_p = \frac{3m_f}{4\pi\rho r_f^3} \quad (32)$$

where m_f is the mass of polymer of density ρ in the reactor at the end of the reaction and r_f is the final radius of the particles. Once the number of particles is known, the overall interphase area at the generic reaction time is easily evaluated as:

$$A_p = N_p 4\pi r_p^2 \quad (33)$$

where the actual radius of the particles, r_p , is given by:

$$r_p = \left(\frac{3 V_2}{4\pi N_p} \right)^{1/3} \quad (34)$$

Note that Eqs. 32–34 imply the assumption of monodisperse spherical particles. Although quite crude, this assumption was accurate enough to predict the effect of A_p on the system kinetics in several instances, as shown in the next section. Additionally, it has the advantage of providing a simple way of estimating A_p through accessible experimental quantities such as the polymer mass at the reaction end and the final particle radius. Finally, for systems leading to fully amorphous morphologies where no average particle radius can be easily defined (typically precipitation polymerizations), one can still use Eqs. 33 and 34 to account for the change in overall area during the reaction by treating N_p as a fitting parameter [44, 46].

4 Applications

Three case studies are presented to illustrate the general reliability of the modeling approach for widely different systems: the precipitation copolymerization of vinyl-imidazole (VI) and vinyl-pyrrolidone (VP) in an organic solvent, the precipitation/dispersion copolymerization of vinylidene fluoride (VDF) and hexafluoropropylene (HFP) in scCO_2 , and the precipitation polymerization of vinyl chloride carried out in suspension.

4.1 Precipitation Polymerization in Organic Solvent

The precipitation copolymerization of VI and VP in butylacetate was investigated experimentally by Arosio et al. [83]. Let us first briefly summarize the experimental evidence concerning the impact of particle morphology on the polymerization kinetics, which is the key to identification of the relative contribution of the two phases to the polymerization and their possible interplay in the overall kinetics. A representative SEM image of the copolymer collected at the end of the reaction is shown in Fig. 3. Although the primary particles do not coalesce completely and keep their identity during the whole reaction, they aggregate in large clusters.

Analysis of the impact of mixing rate on the size distribution of clusters has shown that the combination of aggregation and breakage induced by shear leads to

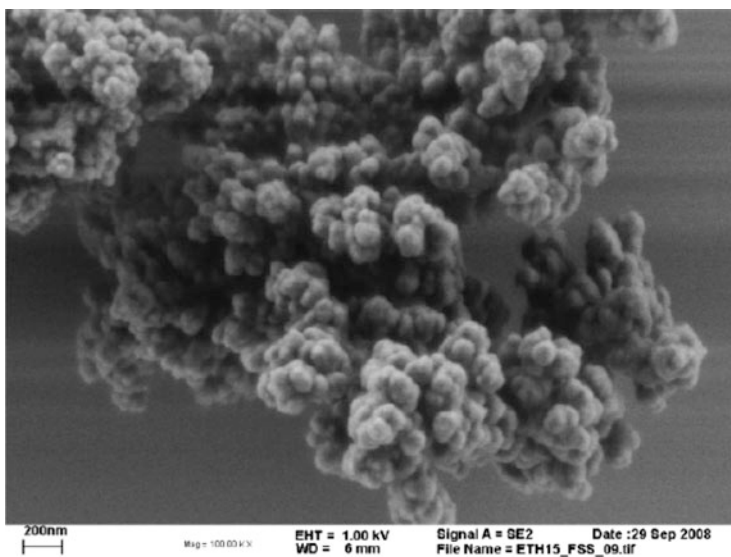


Fig. 3 SEM picture of polymer aggregates obtained at the end of VI/VP precipitation reactions. (Reprinted with permission from Arosio et al. [83]. Copyright 2011 Wiley)

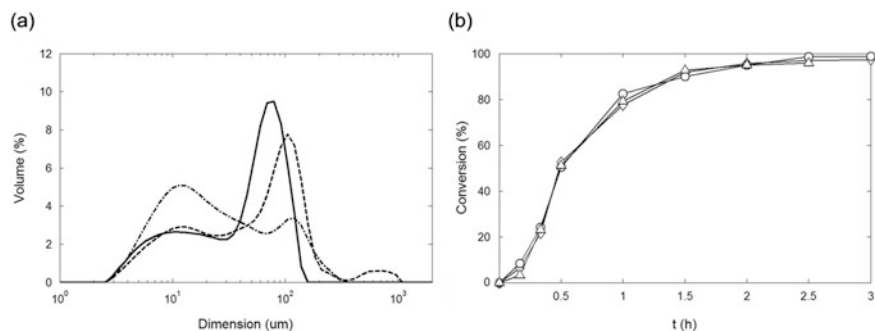


Fig. 4 Precipitation copolymerization of VI/VP (75/25 w/w). (a) Effect of stirring rate on the final particle size distribution: 100 (dash-dotted line), 200 (dashed line), and 300 rpm (continuous line). (b) Effect of stirring rate on monomer conversion: 100 (triangle), 200 (circle), and 300 rpm (diamond). (Adapted with permission from [83]. Copyright 2011 Wiley)

polydisperse aggregates covering a wide range of sizes (1–1,000 μm), with particle size distribution heavily affected by the mixing rate (Fig. 4a). In contrast, the reaction rate is not affected by the shear rate (Fig. 4b). Because the overall interphase area is a function of the average size of the particles and does not seem to affect the kinetics, the experimental evidence implies that the rate of radical interphase transport does not play a relevant role in the polymerization kinetics. More explicitly, evolution of the polymerization reaction and evolution of particle size can be fully separated and viewed as two independent processes.

In terms of Ω parameters, for $\Omega_2 \ll 1$, because the copolymer is fully insoluble in the continuous phase, the “separation” mentioned above corresponds to two possible limiting cases: (1) negligible transport of the radicals, leading to a segregated system ($\Omega_1 \ll 1$), or (2) very fast and irreversible transport of the radicals from the continuous to the dispersed phase ($\Omega_1 \gg 1$). From the model perspective, these two options correspond to setting negligible or extremely high values for the product KA_p , respectively, in both cases safely neglecting all functional dependencies of the same parameters. Accordingly, the rate of transport can be modeled assuming negligible solubility of radical oligomers in the solvent-rich phase ($\alpha = 0$) and a single lumped parameter, the product KA_p [47].

Using an additional series of simplifying assumptions (monomer partitioning in terms of constant partition coefficients; conversion-independent values of the rate parameters for the reactions of initiation, propagation, and termination; diffusion limitations on the termination rate constant simplistically accounted for by using a parameter value for the polymer-rich phase two orders of magnitude smaller than that for the solvent-rich phase), the number of fitting parameters can be reduced to three: the lumped transport parameter, KA_p ; the partition coefficient of the initiator, K_i ; and the rate constant of the crosslinking reactions taking place in the dispersed phase (these reactions need to be considered because of the presence of VI in the polymer backbone [84, 85]).

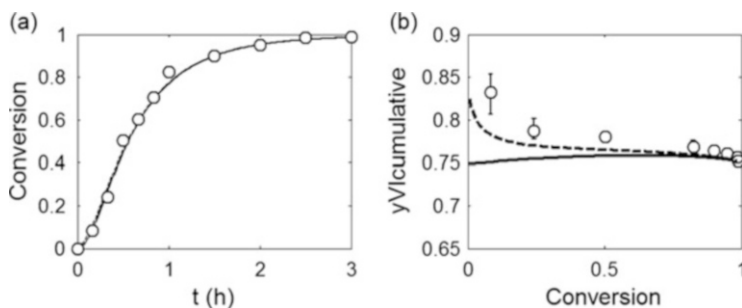


Fig. 5 Comparison between model and experimental data: (a) conversion versus time and (b) copolymer composition in terms of cumulative VI fraction. Model simulations correspond to initiator preferentially partitioned in the polymer phase, $K_I = 0.01$, and negligible transport leading to a segregated system (*dashed line*), or to $K_I = 0.01$ and extremely fast transport with the reaction occurring predominantly in the polymer phase (*continuous line*). Experimental data (*circle*) for VI/VP = 75/25. (Adapted with permission from Arosio et al. [47]. Copyright 2011 Wiley)

The last parameter only affects the polymer molecular weight, therefore a set of parametric simulations were initially carried out neglecting this specific reaction at different values of KA_p and K_I to elucidate the contribution of each reaction locus and the specific operative situation (segregation with two loci or irreversible transport with a dominant locus). Four limiting cases were considered: complete segregation ($KA_p = 0$), with preferential initiator partitioning in the continuous ($K_I = 100$) or dispersed phase ($K_I = 0.01$), and extremely fast transport ($KA_p \gg 0$) again with the same two extreme values of K_I . The model results clearly indicated that initiator partitioning in the dispersed phase is dominant. The effect of transport rate is shown in terms of conversion versus time in Fig. 5a and of copolymer composition versus conversion in Fig. 5b. Even though the reaction rate is practically identical whatever the KA_p value, it is interesting that the copolymer composition is quite different and closer to the experimental case when radical segregation is operative. This is because the compositions of the chains formed in the two phases are quite different: VI-richer chains are formed in the continuous phase rather than in the dispersed phase and, during the reaction, the increasing relevance of the particle phase is reflected by the corresponding change in copolymer composition. Although such a transition is almost complete at around 20% conversion, the copolymer is produced in both phases throughout the reaction, with a final contribution of the continuous phase of about 10%.

The model results in terms of MWD are compared with experimental data in Fig. 6, which also shows the contribution of the polymer produced in each phase as predicted by the model. The general agreement is quite good. Both overall distributions exhibit a clear shoulder in the high molecular weight region as a result of the crosslinking reactions mentioned above. Most of the chains are produced in the dispersed phase and all crosslinked chains are part of this population (i.e., they are

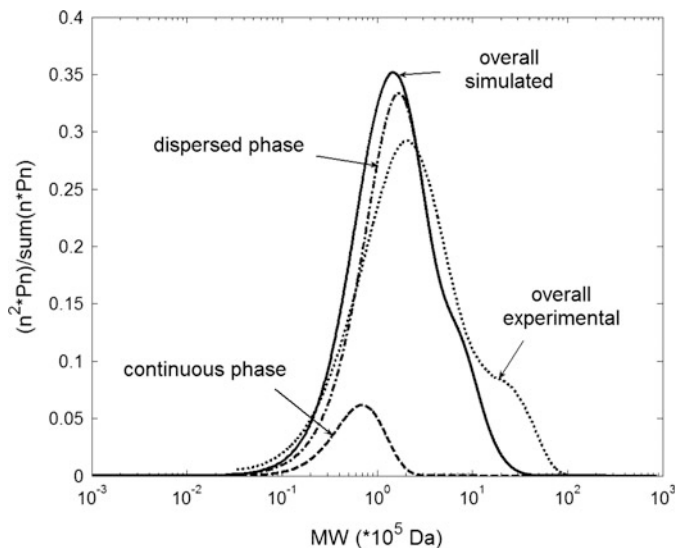


Fig. 6 Precipitation copolymerization of VI/VP (75/25 w/w). Final molecular weight distributions: experimental (*dotted line*), overall simulated (*continuous line*), contribution of the continuous phase (*dashed line*), and contribution of the dispersed phase (*dash-dotted line*). (Reprinted with permission from Arosio et al. [47]. Copyright 2011 Wiley)

formed in the particles). The continuous phase contributes to the overall MWD with only a small fraction of chains in the low molecular weight region, thus resulting in further broadening of the overall distribution. Most of these chains are produced in the early phases of the reaction, when the amount of polymer-rich phase is negligible. As the reaction proceeds, and the volume of the polymer particles increases, the initiator is mainly present within the polymer aggregates ($K_I = 0.01$) and the dominant reaction locus shifts from the continuous to the dispersed phase, which, eventually, contributes the most to polymer formation.

Finally, model and estimated parameter values were conclusively validated by the set of predictive simulations of conversion versus time compared with the experimental results (see Fig. 7). The impacts of monomer composition (Fig. 7a) and initiator concentration (Fig. 7b) are well captured by the model.

To conclude, the developed model – although very simplified – provides a reliable description of the reaction kinetics and enables sound interpretation of the experimental results. Additionally, a preliminary analysis in terms of Ω parameters, supported by some experimental evidence, provides effective conceptual understanding of the main process features, thus enabling identification of reasonable assumptions to be applied in model development without significantly affecting the predictive capabilities of the model.

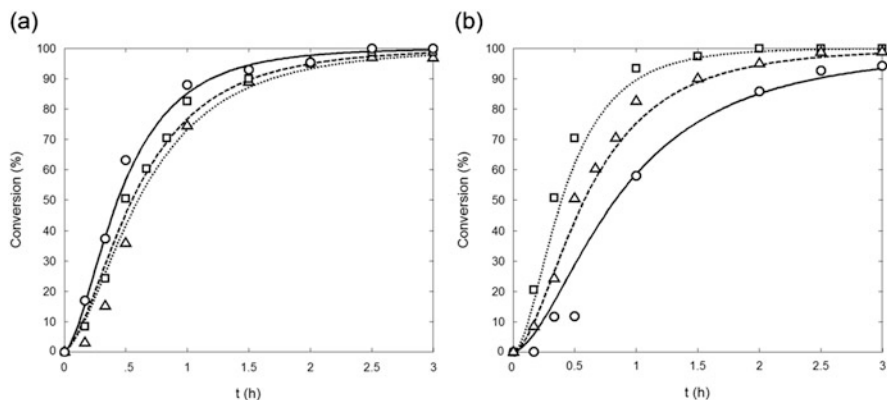


Fig. 7 Precipitation copolymerization of VI/VP. (a) Effect of monomer composition on conversion for VI/VP (w/w) ratios of 90:10 (*triangle*), 75:25 (*square*), and 50:50 (*circle*). (b) Effect of percentage initiator concentration on conversion (VI/VP w/w = 75:25) for 0.3 (*circle*), 0.6 (*triangle*), and 1.2% (*square*) initiator. (Adapted with permission from Arosio et al. [47]. Copyright 2011 Wiley)

4.2 Precipitation and Dispersion Copolymerizations in Supercritical Carbon Dioxide

We now focus on a different system, specifically on the binary system VDF-HFP polymerized in sCO_2 , a fluorinated material of industrial relevance usually produced in emulsion [86]. The impact of the interphase area on the copolymer MWD was investigated by comparing experiments carried out at different amounts of a perfluoropolyether surfactant [24], which was found especially effective for producing narrowly distributed spherical particles in VDF homopolymerization [23, 87]. SEM pictures of the copolymer particles produced in batch at an initial monomer mole fraction $f_{\text{HFP}} = 0.2$ without and with stabilizer (precipitation and dispersion) are shown in Fig. 8. The images reveal that microparticles are clearly formed in both cases. Given the plasticizing effect of the supercritical medium, coalesced particles do not retain their identity. Without stabilizer (Fig. 8a), the extent of coalescence is significant, resulting in a copolymer matrix composed of irregularly shaped particles with broad size distribution. With stabilizer (Fig. 8b), the particles are still partly coalesced but more spherical and, most importantly, better segregated, with an average diameter two to three times smaller than in the precipitation case. Accordingly, a value of A_p two to three times larger (the particle number is larger in the dispersion case) under otherwise identical conditions was estimated in the dispersion case.

Although the difference in interphase areas is small, a striking difference between the two processes is found when looking at the corresponding MWDs (see Fig. 9). A bimodal distribution is obtained by precipitation polymerization, with clearly distinct lower and higher molecular weight modes, whereas a broad but monomodal distribution is found under dispersion conditions. These experimental results indicate a major impact of radical transport (i.e., of interphase area A_p) on

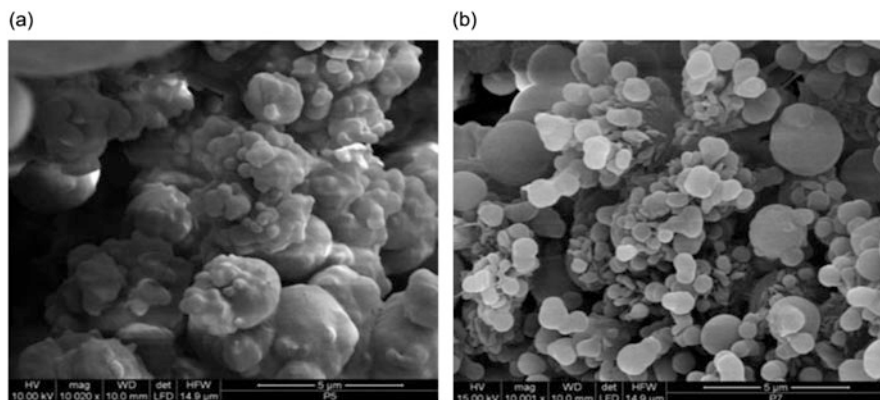


Fig. 8 SEM pictures of VDF-HFP copolymer produced in scCO_2 by (a) precipitation and (b) dispersion. (Adapted with permission from Costa et al. [24]. Copyright 2010 American Chemical Society)

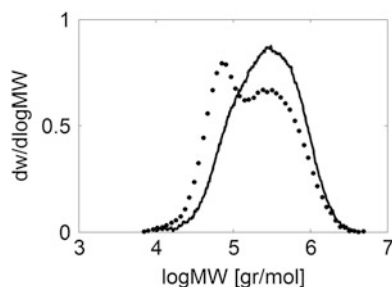


Fig. 9 Experimental molecular weight distributions of VDF-HFP copolymers produced by precipitation (*symbols*) and dispersion (*continuous line*); $T = 50^\circ\text{C}$, $t = 6$ h, $[M] = 5.5$ mol L^{-1} , $f_{\text{HFP}} = 0.2$. (Reprinted with permission from Costa et al. [24]. Copyright 2010 American Chemical Society)

the reaction kinetics. Again, given the negligible value of Ω_2 , parameter Ω_1 regulates the process and its value is expected to be close to 1, so that a small increase in the interphase area can horizontally shift the position of the operating point in Fig. 2 from the first to fourth quadrant, that is, from segregated (two loci) to dominant reaction in the polymer-rich phase (one locus). As a consequence, the system requires a more detailed description of radical interphase transport than in the VI/VP case. Accordingly, diffusion limitations and chain-length dependencies were taken into account for all the rate parameters, as well as for the overall transport coefficient, by using the correlations previously described in Sect. 3 (cf. [48]). With respect to the partitioning of low molecular weight species, the Sanchez-Lacombe equation of state was used for the monomers and for CO_2 , whereas equipartitioning (in mass) was assumed for the initiator.

The predictions of a model of this type in terms of time evolution of the MWD are compared with experimental results in Fig. 10a, c for precipitation and in

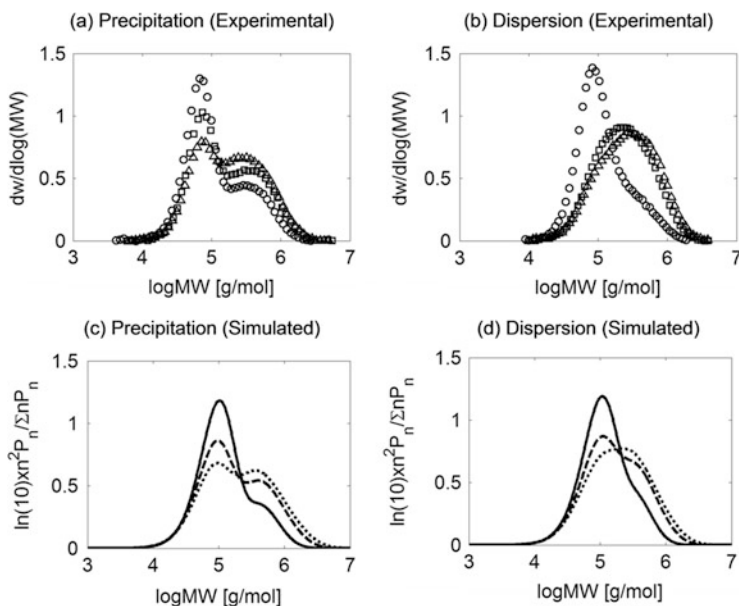


Fig. 10 Time evolution of molecular weight distribution of VDF-HFP copolymerization in scCO_2 for precipitation (*left*) and dispersion (*right*). *Top*: Experimental data after a reaction time of 60 (*circle*), 180 (*square*), and 360 min (*triangle*). *Bottom*: Calculated MWD after 60 (*continuous line*), 180 (*dashed line*), and 360 min (*dotted line*). (Adapted with permission from Costa et al. [48]. Copyright 2012 Wiley)

Fig. 10b, d for dispersion. In all cases, the agreement between model and experiments is quite remarkable, thus enabling a sound mechanistic interpretation of the results. The two MWD modes formed during the precipitation reactions are representative of copolymer chains produced in the continuous phase (lower MW mode) and in the dispersed phase (higher MW mode), respectively. The lower MW mode initially prevails, indicating that in the early phases of the reaction the continuous phase is the dominant reaction locus, which is always the case in unseeded batch reactions. However, as the reaction proceeds, the interphase area increases because of the increasing amount of polymer, and, in turn, the dispersed phase progressively becomes the dominant reaction locus. As a result, the relative contribution of the higher molecular weight mode to the overall MWD increases with time, as is clearly shown in Fig. 10 by both the experimental data and the model results. For dispersion reactions, a similar transition of the dominant reaction locus is observed. Nevertheless, because the particles are smaller than in the precipitation case, the resulting A_p is larger and the rate at which the radicals generated in the continuous phase are transported to the particles is enhanced, which makes the transition of the dominant locus of reaction occur more quickly. Eventually, most of the chains are terminated in the dispersed phase, and a broader but monomodal distribution is obtained.

Changing the monomer composition has a similar effect on the final MWD, as shown in Fig. 11 for dispersion copolymerization. A high molecular weight,

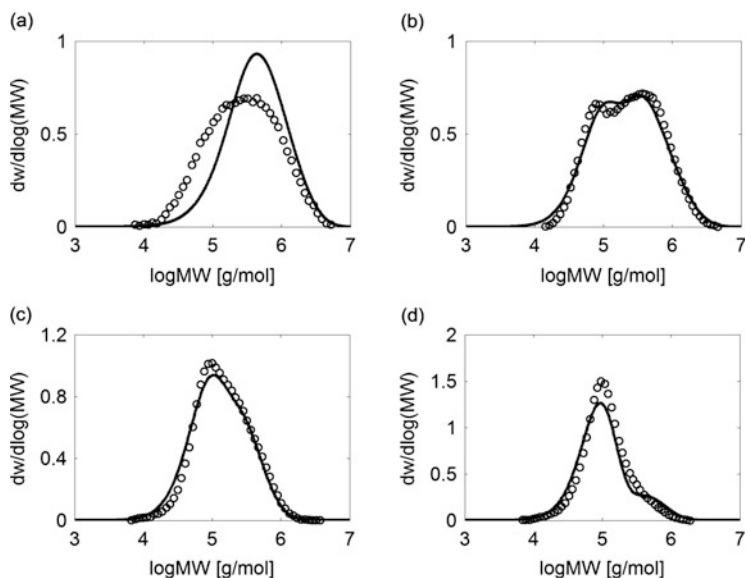


Fig. 11 Experimental (*circle*) and calculated (*line*) molecular weight distributions for VDF-HFP dispersion copolymerization; $T = 50^{\circ}\text{C}$, $t = 3\text{ h}$, $[\text{M}] = 5.5\text{ mol L}^{-1}$. Initial monomer mole fraction f_{HFP} is (a) 0, (b) 0.15, (c) 0.3, and (d) 0.4. (Adapted with permission from Costa et al. [48]. Copyright 2012 Wiley)

monomodal distribution is obtained when VDF alone is fed to the reactor (Fig. 11a). As the amount of HFP in the recipe increases, the distribution gradually shifts toward lower molecular weights: the MWD is clearly bimodal at intermediate HFP content (Fig. 11b), and the lower molecular weight peak becomes dominant at higher HFP content (Fig. 11c, d). The model captures all distributions and their transition remarkably well. From the model perspective, several factors contribute to the shift in distribution toward the lower MW mode as f_{HFP} increases [48]. First, HFP is significantly less reactive than VDF. Therefore, for the same reaction time, the amount of produced copolymer, and therefore the interphase area A_p , decreases with increasing HFP content. Additionally, the richer the system is in HFP, the lower the transport parameters of the growing radicals and the lower the monomer concentration in the polymer particles, which is a result of the composition-dependent partitioning of these monomers. Furthermore, the effectiveness of the surfactant deteriorates progressively as the content of HFP in the system increases [24], resulting in a reduction in the overall number of particles and, again, in the specific interphase area. Thus, VDF homopolymer dispersions are characterized by faster radical transport rates (larger Ω_1 values) and higher reactivity in the polymer-rich phase. This is the main reaction locus and a monomodal high MWD is obtained (Fig. 11a). In contrast, dispersion reactions carried out at high HFP concentrations (Fig. 11d) are characterized by slower radical transport rates and low reactivity in the polymer phase. Under these conditions, the continuous phase (where shorter

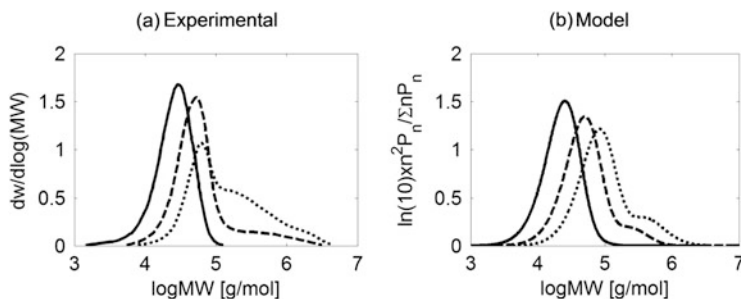


Fig. 12 Effect of total monomer concentration on molecular weight distribution produced in a continuous stirred tank reactor under precipitation conditions. Experimental data from Ahmed et al. 2007 (left) and model predictions (right). Operative conditions: $T = 40^\circ\text{C}$, $f_{\text{HFP}} = 0.265$, residence time $\tau = 20$ min. Monomer feed concentrations are 1.96 (solid curves), 3.92 (dashed curves), and 6.53 mol L^{-1} (dotted curves). (Adapted with permission from Costa et al. [48]. Copyright 2012 Wiley)

chains are produced) prevails as reaction locus, whereas the small fraction of chains terminating inside the particles results in MWD tailing at high molecular weights.

The predictive capabilities of the same kinetic model were further verified using independent data obtained in a continuous stirred tank reactor [88]. The effect of increasing monomer concentration for precipitation copolymerization at $f_{\text{HFP}} = 0.27$ is shown in Fig. 12, together with the corresponding model predictions. At low monomer concentration, the small amount of polymer particles present in the system captures a negligible amount of radicals, and the continuous phase is practically the only reaction locus. The distribution is therefore narrow and monomodal. As total monomer content increases, more radicals are captured because of the larger interphase area of the polymer particles and the contribution of the particle phase to the kinetics progressively increases, leading to the formation of high molecular weight tails. Although the comparison between model results and experimental data is not as good as in the previous examples, the model still captures the relevant features of the distributions and allows straightforward interpretation of the appearance of the high molecular weight tailing at increasing monomer concentration. This result appears especially significant when considering that, in this case, the model was used in a fully predictive way.

4.3 Precipitation Polymerization of Vinyl Chloride

Poly(vinyl chloride) (PVC) is a commodity polymers with one of the largest production capacities and is mostly produced by suspension polymerization [41, 89]. In suspension polymerization, the monomer is initially dispersed in water as 50–500 μm droplets by the combined effects of mechanical agitation and surfactant stabilization. Monomer-soluble initiators are used, so the entire

polymerization reaction takes place inside these droplets and each droplet can be considered a small, bulk polymerization reactor. However, PVC is insoluble in its monomer and precipitates as soon as it is formed. Therefore, a precipitation polymerization regime is established within each monomer droplet. The droplet is finally converted into a PVC grain composed of a porous network of packed polymer particles [89, 90]. In view of the industrial relevance of this process, the mechanism of formation and evolution of the internal morphology of the grain with the reaction progress has been studied extensively, both experimentally and through modeling [90–94]. After a short nucleation phase, completed within the first few percent of monomer conversion, primary polymer particles of 0.2–1.5 μm are formed. The particles then grow by polymerization of the absorbed monomer and by further precipitation of polymer formed in the monomer phase. Additionally, the particles aggregate and coalesce as the reaction proceeds. The interplay between growth, aggregation, and coalescence finally determines the internal morphology and porosity of the grains. The extent of aggregation and coalescence of the primary particles in this system is influenced by many parameters (temperature, mixing, nature of the suspending medium, nature and concentration of stabilizers, etc.), meaning that the estimation of the interphase area between the polymer and the monomer phases is a challenging task. On the other hand, it has been observed that aggregation is significant even at low conversions, giving rise to a densely packed morphology similar to that observed for VI/VP precipitation (see Fig. 3 with SEM images reported by Smallwood for PVC [90]). Accordingly, as for the VI/VP case, one can expect that the total effective amount of interphase area available for radical interphase transport is also quite small in this system. The assumption of a segregated system (regime I in Fig. 2) for PVC precipitation polymerization thus appears reasonable and has often been applied. As representative examples, Crosato-Arnaldi et al. [34], Abdel-Alim et al. [37], and Kiparissides et al. [41] successfully applied two-phases models without interphase transport (segregated models) to describe the kinetics of PVC suspension polymerization.

More recently, the validity of the assumption of a fully segregated system was evaluated by Wieme et al. [45], who also included a term for radical interphase transport in the two-phase model. The authors used the two-film theory for the overall mass transfer coefficient (Eq. 27), and, to take into account the decrease in particle concentration as a result of coalescence, they did not assume constant particle concentration and assumed the following empirical relationship:

$$n_p = n_p^0 \exp(-\gamma X) \quad (35)$$

where $n_p = N_p/(V_1 + V_2)$, and the two adjustable parameters n_p^0 and γ represent the initial volumetric concentration of polymer particles and the decay parameter, respectively. Thus, the evolution of the overall interphase area and the rate of radical interphase transport throughout the reaction can be calculated using Eqs. 33–35. In particular, in agreement with experimental observations [90], n_p^0 increases with decreasing temperature, implying that A_p , and thus the flow of radicals precipitating

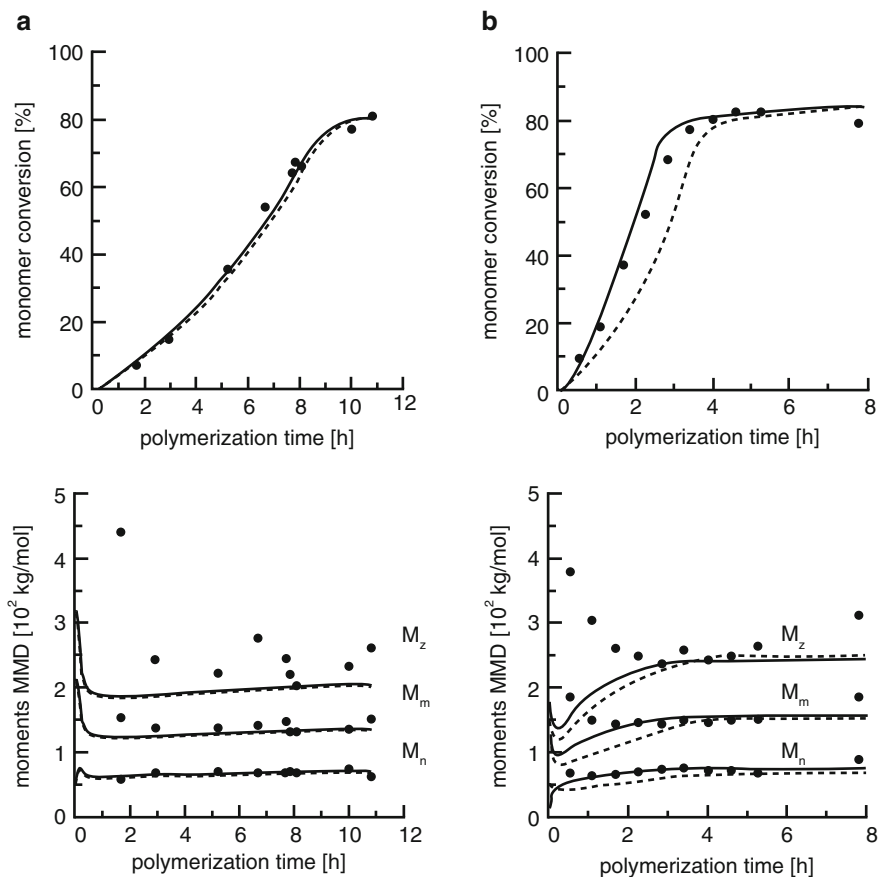


Fig. 13 Effect of temperature on conversion (*top*) and average molecular weights (*bottom*) for PVC suspension polymerization at (a) $T = 318$ K with 0.02354 wt% of *tert*-butyl peroxyneodecanoate initiator, (b) $T = 308$ K with 3.02 wt% of *tert*-butyl peroxyneodecanoate initiator. Model simulations are shown as *dashed lines* for the segregated, two-loci model (without radical transfer) and as *continuous lines* for the complete two-loci model (with radical transfer). (Adapted with permission from Wieme et al. [45]. Copyright 2009 Wiley)

from phase 1 to phase 2, increases with decreasing temperature. Note that this model reduces to the segregated case by setting $n_p = 0$ (i.e., no interphase area available for radical transport). Wieme et al. evaluated the unknown model parameters (including the intrinsic rate constants for propagation and termination in the monomer phase) for both cases (segregated and nonsegregated) by regression of conversion and average molecular weight data from experiments carried out at different temperatures [45]. Comparison of the predictions of both models with the experimental results is shown in Fig. 13 for the reactions at 318 K and 308 K. At the highest temperature (Fig. 13a), the two models provide almost identical results, indicating that the role of the radical interphase transport in this

case is negligible. The polymerization occurs independently in each phase but, as the reaction proceeds and the volume of the polymer phase increases at the expenses of the monomer phase, the main reaction locus shifts from the monomer to the polymer phase, resulting in an evident auto-acceleration effect. By contrast, at the lowest temperature (Fig. 13b), the difference between the two model results is appreciable, and the complete model performs better than the segregated one, especially in terms of conversion versus time. This finding can be attributed to the enhanced rate of radical interphase transport resulting from the increased number of particles at the lower reaction temperature. The steeper conversion profile obtained from the full model with respect to the segregated one indicates that the transfer of radicals, at least partly, accelerates the shift of the main reaction locus from the continuous to the dispersed phase. It is worth noting that, as shown in Fig. 13 (lower images), the two models do not differ significantly in terms of molecular weight evolution, the final average molecular weight being mainly dictated by chain transfer to monomer. Notably, this makes the discrimination of different models (with or without radical transfer) more difficult as they are based on conversion data only.

Thus, two loci models that account for the reaction occurring in both phases can provide a fairly accurate description of the system kinetics. Even though PVC suspension and precipitation polymerizations can be considered in most cases as fully segregated, given the high degree of aggregation and coalescence of the polymer particles, accounting for the interphase radical transport broadens the range of model applicability to experimental conditions that favor the formation of a larger interphase area.

5 Conclusions

The presence of more than one reaction locus, coupled with the complex interactions between particle morphology and polymerization kinetics, makes the kinetic modeling of dispersed polymerization systems particularly challenging. On the other hand, judicious selection of meaningful and reliable assumptions enables the separation of the mathematical descriptions of kinetics and particle size distribution in many cases, the overall interphase area being the only parameter connecting kinetics and particle morphology.

The impact of the interphase area on the polymerization kinetics can be rationalized in terms of dimensionless phase-specific quantities, the Ω parameters, defined as the ratios between the rate of radicals diffusing out of a phase and the rate of termination in the same phase. Based on the values of the Ω parameters for the two phases, different limiting regimes and the role of radical interphase transport can be readily identified. Because the solubility of high molecular weight species in the continuous phase is negligible in most cases of practical interest, the Ω parameter for the continuous phase is decisive. Its value determines the operating regime, ranging from complete radical segregation to complete transport of radicals

to the dispersed phase. Notably, the main reaction locus, and therefore the overall MWD, can be controlled by tuning the interphase area. Such tuning can be achieved by varying the hydrodynamics of the system (enhancing or reducing particle aggregation through shear) or its colloidal stability (reducing or increasing the amount of an effective stabilizer).

A modeling framework suitable for capturing all the main features mentioned above and representing a good compromise between the requirement for a detailed description and the need to keep the number of adjustable parameters to a minimum has been reviewed in this contribution. Moreover, some of the theoretical approaches and correlations commonly used in the field of polymer reaction engineering to estimate the model parameters have also been reported.

The proposed modeling approach has been validated through selected applications to homo- and copolymerizations in organic solvents and in supercritical media. Accurate predictions of the time evolution of conversion, copolymer composition, and MWD can be achieved with limited computational effort when a meaningful mechanistic picture is selected. In the examined case of precipitation copolymerization of VI and VP in organic solvent, the time evolution of the cumulative composition directly reflects the different copolymerization behaviors in the different phases. On the other hand, with reference to the production of VDF-based fluorinated copolymers in scCO_2 , control of the final MWD from monomodal to bimodal is obtained by tuning the stabilizer amount (i.e., by shifting the polymerization from dispersion to precipitation conditions). Each MWD mode represents the contribution of the polymer produced in a specific phase. In the case of precipitation polymerization of vinyl chloride, carried out either in bulk or in suspension, the high degree of aggregation and coalescence of the polymer particles allows segregated models to be applied in most cases. On the other hand, accounting for radical interphase transport expands the model applicability to all cases in which the experimental conditions favor the formation of a larger number of particles.

To conclude, the proposed approach represents a powerful tool for understanding the reaction mechanisms. In turn, the reliable quantitative description of process kinetics is a decisive tool for the design of optimal reaction paths and careful quality control of the final product. Although only free-radical polymerization has been considered, the general concepts and strategies presented here can be effectively applied to other polymerization mechanisms.

Acknowledgements The financial support of Swiss National Science Foundation (SNF Project 200021.153403/1) is gratefully acknowledged.

References

1. Barrett KEJ (1975) Dispersion polymerization in organic media. Wiley, London

2. Ober CK, Lok KP, Hair ML (1985) Monodispersed, micron-sized polystyrene particles by dispersion polymerization. *J Polym Sci Polym Lett Ed* 23:103–108
3. Tseng CM, YY Lu, El-Aasser MS, Vanderhoff JW (1986) Uniform polymer particles by dispersion polymerization in alcohol. *J Polym Sci A Polym Chem* 24:2995–3007
4. Richez AP, Yow HN, Biggs S, Cayre OJ (2013) Dispersion polymerization in non-polar solvent: evolution toward emerging applications. *Prog Polym Sci* 38:897–931
5. Almog Y, Reich S, Levy M (1982) Monodisperse polymeric spheres in the micron size range by a single step process. *Br Polym J* 14:131–136
6. IG Farbenindustrie AG (1933) GB Patent 434,783
7. Osmond DWJ, Thompson HH (1957) GB Patent 893,429
8. Osmond DWJ (1963) GB Patent 893,429
9. Rohm & Haas (1963) GB Patent 934,038
10. Barrett KEJ, Thomas HR (1969) Kinetics of dispersion polymerization of soluble monomers. I Methyl methacrylate. *J Polym Sci A-1* 7:2621–2650
11. Barrett KEJ (1973) Dispersion polymerization in organic media. *Br Polym J* 5:249–332
12. Cooper AI (2000) Polymer synthesis and processing using supercritical carbon dioxide. *J Mater Chem* 10:207–234
13. Byun HS, McHugh MA (2000) Impact of free monomer concentration on the phase behavior of supercritical carbon dioxide-polymer mixtures. *Ind Eng Chem Res* 39:4658–4662
14. Dinoia TP, Conway SE, Lim JS, McHugh MA (2000) Solubility of vinylidene fluoride polymers in supercritical CO₂ and halogenated solvents. *J Polym Sci B Polym Phys* 38:2832–2840
15. Hsiao YL, Maury EE, DeSimone JM (1995) Dispersion polymerization of methyl methacrylate stabilized with poly(1,1-dihydroperfluorooctyl acrylate) in supercritical carbon dioxide. *Macromolecules* 28:8159–8166
16. Romack TJ, Maury EE, DeSimone JM (1995) Precipitation polymerization of acrylic acid in supercritical carbon dioxide. *Macromolecules* 28:912–915
17. Berger T, McGhee B, Scherf U, Steffen W (2000) Polymerization of vinylpyrrolidone in supercritical carbon dioxide with a diblock copolymer stabilizer. *Macromolecules* 33:3505–3507
18. Carson T, Lizotte J, Desimone JM (2000) Dispersion polymerization of 1-vinyl-2-pyrrolidone in supercritical carbon dioxide. *Macromolecules* 33:1917–1920
19. Charpentier PA, DeSimone JM, Roberts GW (2000) Continuous precipitation polymerization of vinylidene fluoride in supercritical carbon dioxide: modeling the rate of polymerization. *Ind Eng Chem Res* 39:4588–4596
20. Galia A, Giaconia A, Iaia V, Filardo G (2004) Synthesis of hydrophilic polymers in supercritical carbon dioxide in the presence of a siloxane-based macromonomer surfactant: heterogeneous polymerization of 1-vinyl-2 pyrrolidone. *J Polym Chem A Polym Chem* 42:173–185
21. Tai H, Wang W, Howdle SM (2005) Dispersion polymerization of vinylidene fluoride in supercritical carbon dioxide using a fluorinated graft maleic anhydride copolymer stabilizer. *Macromolecules* 38:1542–1545
22. Beginn U, Najjar R, Ellmann J, Vinokur R, Martin R, Möller M (2006) Copolymerization of vinylidene difluoride with hexafluoropropene in supercritical carbon dioxide. *J Polym Chem A Polym Chem* 44:1299–1316
23. Mueller PA, Storti G, Morbidelli M, Costa I, Galia A, Scialdone S, Filardo G (2006) Dispersion polymerization of vinylidene fluoride in supercritical carbon dioxide. *Macromolecules* 39:6483–6488
24. Costa LI, Storti G, Morbidelli M, Ferro L, Scialdone O, Filardo G, Galia A (2010) Copolymerization of VDF and HFP in supercritical carbon dioxide: experimental analysis of the reaction loci. *Macromolecules* 43:9714–9723
25. Li GL, Möhwald H, Shchukin DG (2013) Precipitation polymerization for fabrication of complex core-shell hybrid particles and hollow structures. *Chem Soc Rev* 42:3628–3646
26. Pich A, Richtering W (2010) Microgels by precipitation polymerization: synthesis, characterization and functionalization. *Adv Polym Sci* 234:1–37

27. Zhang H (2013) Controlled/"living" radical precipitation polymerization: a versatile polymerization technique for advanced functional polymers. *Eur Polym J* 49:579–600
28. Sun JT, Hong CY, Pan CY (2013) Recent advances in RAFT dispersion polymerization for preparation of block copolymer aggregates. *Polym Chem* 4:873–881
29. Paine AJ, Luymes W, McNulty J (1990) Dispersion polymerization of styrene in polar solvents. 6. Influence of reaction parameters on particle size and molecular weight in poly (N-vinylpyrrolidone)-stabilized reactions. *Macromolecules* 23:3104–3109
30. Liu T, DeSimone JM, Roberts GW (2006) Kinetics of the precipitation polymerization of acrylic acid in supercritical carbon dioxide: the locus of polymerization. *Chem Eng Sci* 61:3129–3139
31. Costa LI, Storti G, Morbidelli M, Galia A, Filardo G (2011) The rate of polymerization in two loci reaction systems: VDF-HFP precipitation copolymerization in supercritical carbon dioxide. *Polym Eng Sci* 51:2093–2012
32. Jiang S, Sudol ED, Dimonie VL, El-Aasser MS (2008) Kinetics of dispersion polymerization: effect of medium composition. *J Polym Chem A Polym Chem* 46:3638–3647
33. Saenz JM, Asua JM (1998) Kinetics of the dispersion copolymerization of styrene and butyl acrylate. *Macromolecules* 31:5215–5222
34. Crosato-Arnaldi A, Gasparini P, Talamini G (1968) The bulk and suspension polymerization of vinyl chloride. *Makromol Chem* 117:140–152
35. Olay OF (1975) Ein einaches modell zur beschreibung der kinetic der vinylchlorid-polymerisation in substanz und in anderen fällungssystemen bei temperaturen um 50°C. *Angew Makromol Chem* 47:1–14
36. Avela A, Poersch HG, Reichert KH (1990) Modelling the kinetics of the precipitation polymerization of acrylic acid. *Angew Makromol Chem* 175:107–116
37. Abdel-Alim AH, Hamielec AE (1972) Bulk polymerization of vinyl chloride. *J Appl Polym Sci* 16:783–779
38. Saenz JM, Asua JM (1999) Mathematical modeling of dispersion copolymerization. *Colloids Surf A Physiochem Eng Asp* 153:61–74
39. Ahmed SF, Poehlein GW (1997) Kinetics of dispersion polymerization of styrene in ethanol. 1. Model development. *Ind Eng Chem Res* 36:2597–2604
40. Ahmed SF, Poehlein GW (1997) Kinetics of dispersion polymerization of styrene in ethanol. 2. Model validation. *Ind Eng Chem Res* 36:2605–2615
41. Kiparissides C, Daskalakis G, Achilias DS, Sidiropoulou E (1997) Dynamic simulation of industrial poly(vinyl chloride) batch suspension polymerization reactors. *Ind Eng Chem Res* 36:1253–1267
42. Chatzidoukas C, Pladis P, Kiparissides C (2003) Mathematical modeling of dispersion polymerization of methyl methacrylate in supercritical carbon dioxide. *Ind Eng Chem Res* 42:743–751
43. Mueller PA, Storti G, Morbidelli M (2005) Detailed modeling of MMA dispersion polymerization in supercritical carbon dioxide. *Chem Eng Sci* 60:1911–1925
44. Mueller PA, Storti G, Morbidelli M, Apostolo M, Martin R (2005) Modeling of vinylidene fluoride heterogeneous polymerization in supercritical carbon dioxide. *Macromolecules* 38:7150–7163
45. Wieme J, D'hooge DR, Reyniers MF, Marin GB (2009) Importance of radical transfer in precipitation polymerization of vinyl chloride suspension polymerization. *Macromol React Eng* 3:16–35
46. Mueller PA, Storti G, Morbidelli M, Mantelis CA, Meyer T (2007) Dispersion polymerization of methyl methacrylate in supercritical carbon dioxide: control of molecular weight distribution by adjusting particle surface area. *Macromol Symp* 259:218–225
47. Arosio P, Mosconi M, Storti G, Banaszak B, Hungenberg KD, Morbidelli M (2011) Precipitation copolymerization of vinyl-imidazole and vinyl-pyrrolidone, 2 – kinetic model. *Macromol React Eng* 5:501–517

48. Costa LI, Storti G, Morbidelli M, Ferro L, Galia A, Scialdone O, Filardo G (2012) Copolymerization of VDF and HFP in supercritical carbon dioxide: a robust approach for modeling precipitation and dispersion kinetics. *Macromol React Eng* 6:24–44
49. Paine AJ (1990) Dispersion polymerization of styrene in polar solvents. 7. A simple mechanistic model to predict particle size. *Macromolecules* 23:3109–3117
50. Prochazka O, Stejskal J (1992) Spherical particles obtained by dispersion polymerization: model calculations. *Polymer* 33:3658–3663
51. Shen S, Sudol ED, El-Aasser MS (1994) Dispersion polymerization of methyl methacrylate: mechanism of particle formation. *J Polym Sci A Polym Chem* 32:1087–1100
52. O'Neill ML, Yates MZ, Johnston KP, Smith CD, Wilkinson SP (1998) Dispersion polymerization in supercritical CO₂ with siloxane-based macromonomer. 2. The particle formation regime. *Macromolecules* 31:2848–2856
53. Fehrenbacher U, Ballauff M (2002) Kinetics of the early stage of dispersion polymerization in supercritical CO₂ as monitored by turbidimetry. 2. Particle formation and locus of polymerization. *Macromolecules* 35:3653–3661
54. Cockburn RA, McKenna TFL, Hutchinson RA (2011) A study of particle nucleation in dispersion copolymerization of methyl methacrylate. *Macromol React Eng* 5:404–417
55. Mueller PA, Storti G, Morbidelli M (2005) The reaction locus in supercritical carbon dioxide dispersion polymerization. The case of poly(methyl methacrylate). *Chem Eng Sci* 60:377–397
56. Fehrenbacher U, Muth O, Hirth T, Ballauff M (2000) The kinetics of the early stage of dispersion polymerization in supercritical CO₂ as monitored by turbidimetric measurements, 1. *Macromol Chem Phys* 201:1532–1539
57. Sherwood TK, Pigford RL, Wilke CR (1975) *Mass transfer*. McGraw-Hill, New York
58. McHugh MA, Krukoni VJ (1994) *Supercritical fluid extraction: principles and practice*. Butterworth-Heinemann, Stoneham
59. Bae W, Kwon S, Byun HS, Kim H (2004) Phase behavior of the poly(vinyl pyrrolidone) + N-vinyl-2-pyrrolidone + carbon dioxide system. *J Supercrit Fluids* 30:127–137
60. Wenzel JE, Lanterman HB, Lee S (2005) Experimental *P-T-ρ* measurements of carbon dioxide and 1,1-difluoroethene mixtures. *J Chem Eng Data* 50:774–776
61. Chapman WG, Gubbins KE, Jackson G, Radosz M (1990) New reference equation of state for associating liquids. *Ind Eng Chem Res* 29:1709–1721
62. Müller EA, Gubbins KE (2001) Molecular-based equation of state for associating fluids: a review of SAFT and related approaches. *Ind Eng Chem Res* 40:2193–2211
63. Gupta RB, Prausnitz JM (1995) Vapor-liquid equilibria of copolymer + solvent and homopolymer + solvent binaries: new experimental data and their correlation. *J Chem Eng Data* 40:784–791
64. Simha R, Somcynsky T (1969) On the statistical thermodynamics of spherical and chain molecule fluids. *Macromolecules* 2:342–350
65. Utracki LA, Simha R (2001) Analytical representation of solutions to lattice-hole theory. *Macromol Theory Simul* 10:17–24
66. Sanchez IC, Lacombe RH (1978) Statistical thermodynamics of polymer solutions. *Macromolecules* 11:1145–1156
67. Galia A, Cipollina A, Scialdone O, Filardo G (2008) Investigation of multicomponent sorption in polymers from fluid mixtures at supercritical conditions: the case of the carbon dioxide/vinylidene fluoride/poly(vinylidene fluoride) system. *Macromolecules* 41:1521–1530
68. Cao K, Li BG, Pan ZR (1999) Micron-size uniform poly(methyl methacrylate) particles by dispersion polymerization in polar media. IV. Monomer partition and locus of polymerization. *Colloids Surf A Physicochem Eng Asp* 153:179–187
69. Russell GT, Napper DH, Gilbert RG (1988) Termination in free-radical polymerizing systems at high conversion. *Macromolecules* 21:2133–2140
70. Shen J, Tian Y, Wang G, Yang M (1991) Modelling and kinetic study on radical polymerization of methyl methacrylate in bulk, 1. Propagation and termination rate coefficients and initiation efficiency. *Makromol Chem* 192:2669–2685

71. Achilias DS (2007) A review of modeling of diffusion controlled polymerization reactions. *Macromol Theory Simul* 16:319–347
72. Soh SK, Sundberg DC (1982) Diffusion-controlled vinyl polymerization. II. Limitations on the gel effect. *J Polym Sci Polym Chem Ed* 20:1315–1329
73. North AM (1964) The collision theory of chemical reactions in liquids. Wiley, New York
74. Noyes RM (1961) Effects of diffusion rates on chemical kinetics. In: *Progress in reaction kinetics*, vol 1. Pergamon, New York, pp 131–158
75. Griffiths MC, Strauch J, Monteiro MJ, Gilbert RG (1998) Measurement of diffusion coefficients of oligomeric penetrants in rubbery polymer matrixes. *Macromolecules* 31:7835–7844
76. Masaro L, Zhu XX (1999) Physical models of diffusion for polymer solutions, gels and solids. *Prog Polym Sci* 24:731–775
77. Vrentas JS, Duda JL (1977) Diffusion in polymer-solvent systems. I. Reexamination of the free-volume theory. *J Polym Sci Polym Phys Ed* 15:403–416
78. Zielinski JM, Duda JL (1992) Predicting polymer/solvent diffusion coefficients using free-volume theory. *AIChE J* 38:405–415
79. Vrentas JS, Vrentas CM (1998) Predictive methods for self-diffusion and mutual diffusion coefficients in polymer-solvent systems. *Eur Polym J* 34:797–803
80. Costa LI, Storti G (2010) Self-diffusion of small molecules into rubbery polymers: a lattice free-volume theory. *J Polym Sci B Polym Phys* 48:529–540
81. Kumar SK, Chhabria SP, Reid RC, Suter UW (1987) Solubility of polystyrene in supercritical fluids. *Macromolecules* 20:2550–2557
82. Bonavoglia B, Storti G, Morbidelli M (2006) Modeling the partitioning of oligomers in supercritical CO₂. *Ind Eng Chem Res* 45:3335–3342
83. Arosio P, Mosconi M, Storti G, Morbidelli M (2011) Precipitation copolymerization of vinyl-imidazole and vinyl-pyrrolidone, 1 – experimental analysis. *Macromol React Eng* 5:490–500
84. Chapiro A, Mankowski Z (1988) Polymerisation du vinylimidazole en masse et en solution. *Eur Polym J* 24:1019–1028
85. Chapiro A (1992) Peculiar aspects of the free-radical polymerization of 1-vinylimidazole. *Int J Radiat Appl Instrum C Radiat Phys Chem* 40:89–93
86. Apostolo M, Arcella V, Storti G, Morbidelli M (1999) Kinetics of the emulsion polymerization of vinylidene fluoride and hexafluoropropylene. *Macromolecules* 32:989–1003
87. Galia A, Giaconia A, Scialdone O, Appostolo M, Filardo G (2006) Polymerization of vinylidene fluoride with perfluoropolyether surfactants in supercritical carbon dioxide as dispersing medium. *J Polym Chem A Polym Chem* 44:2406–2418
88. Ahmed TS, DeSimone JM, Roberts GW (2007) Continuous copolymerization of vinylidene fluoride with hexafluoropropylene in supercritical carbon dioxide: low hexafluoropropylene content semicrystalline copolymers. *Macromolecules* 40:9322–9331
89. Darvishi R, Esfahany MS, Bagheri R (2015) S-PVC grain morphology: a review. *Ind Eng Chem Res* 54:10953–10963
90. Smallwood PV (1986) The formation of grains in suspension poly(vinyl chloride). *Polymer* 27:1609–1618
91. Alexopoulos AH, Kiparissides C (2007) On the prediction of internal particle morphology in suspension polymerization of vinyl chloride. Part I: the effect of primary particle size distribution. *Chem Eng Sci* 62:3970–3983
92. Etesami N, Esfahany MN, Bagheri R (2008) Effect of the phase ratio on the particle properties of poly(vinyl chloride) resins produced by suspension polymerization. *J Appl Polym Sci* 110:2748–2755
93. Bao YZ, Brooks BW (2003) Particle features of poly(vinyl chloride) resins prepared by a new heterogeneous polymerization process. *J Appl Polym Sci* 90:954–958
94. Georgiadou S, Thomas NL, Gilbert M, Brooks BW (2009) Nonaqueous polymerization of vinyl chloride: an environmentally friendly process. *J Appl Polym Sci* 112:2472–2481

The Generalized Stability Model and Its Applications in Polymer Colloids



Hua Wu, Dan Wei, and Massimo Morbidelli

Abstract This chapter reviews the generalized stability model developed in recent years Jia et al. (J. Colloid Interface Sci. 302:187–202, 2006) and its application to different polymer colloids. The most important feature of this model is that it accounts simultaneously for the interplay between different physicochemical processes, such as surfactant adsorption equilibrium on the particle surface, association equilibria of surface charges with counterions involved in the system, and DLVO and non-DLVO colloidal interactions. Through its application to different polymer colloids produced from industrial polymerization processes, we demonstrate that the generalized stability model is powerful and capable of describing the stability of the most complicated colloidal systems. After the model has been established, it can be used to analyze how the interplay of the relevant processes affects the stability of colloids, which is not often feasible through experimental investigation.

Keywords Colloidal interaction • Counterion association • Fuchs stability ratio • Physicochemical process interplay • Stability model • Surfactant adsorption

H. Wu (✉) and M. Morbidelli (✉)

Department of Chemistry and Applied Biosciences, ETH Zurich, Institute for Chemical and Bioengineering, 8093 Zurich, Switzerland
e-mail: hua.wu@chem.ethz.ch; massimo.morbidelli@chem.ethz.ch

D. Wei

School of Chemistry and Chemical Engineering, Guangdong Pharmaceutical University, 528458 Zhongshan, Guangdong, China

Contents

| | | |
|-----|--|-----|
| 1 | Introduction | 80 |
| 2 | The Generalized Stability Model | 81 |
| 2.1 | Surfactant Adsorption Equilibrium | 81 |
| 2.2 | Electrolyte Dissociation Equilibrium | 82 |
| 2.3 | Colloidal Interactions | 83 |
| 2.4 | Computation of Key Quantities of the Generalized Stability Model | 85 |
| 3 | Applications of the Generalized Stability Model | 87 |
| 3.1 | Fluorinated Elastomer Latex with Only Mobile Charges [8] | 87 |
| 3.2 | Styrene–Acrylate Copolymer Latex with Both Mobile and Fixed Charges [37] ... | 91 |
| 3.3 | Butylacrylate–Methylmethacrylate–Acrylic Acid Copolymer Latexes | 95 |
| 4 | Concluding Remarks | 101 |
| | References | 102 |

1 Introduction

Latexes produced by emulsion polymerization are typical colloids, stabilized through adsorption of ionic surfactants on the particle surface. The electrical charges generate an electrical double layer (EDL), leading to electrostatic repulsion, which, when prevailing over the short-range van der Waals attraction, results in a repulsive barrier that kinetically stabilizes the particles. Quantification and control of the stability of polymer colloids are of great importance in industrial practice. Thus, it is essential to develop a stability model that can describe the stability of industrial polymer colloids, accounting for the effect of operating variables (e.g., type and concentration of electrolyte, system pH, etc.) on the stability.

The dominant theoretical studies describing colloidal stability focus on how to correctly describe colloidal interactions, but the effect on colloidal stability of interplay between various physicochemical processes is seldom accounted for. The centerpiece in describing colloidal interactions is the DLVO (Deryaguin–Landau–Verwey–Overbeek) theory [1, 2], which models the competition between van der Waals attraction and EDL repulsion. Additional non-DLVO forces (e.g., long-range dispersion forces, short-range hydration forces, steric forces, capillary condensation) are known to be important under specific conditions [3–7], but, unlike DLVO forces, such non-DLVO forces are difficult to measure experimentally or predict theoretically, particularly for industrial polymer colloids.

In practical applications, for a chosen colloid, one often first measures the surface charge or zeta-potential under well-defined conditions, and then uses the measured surface charge or potential in the DLVO model (accounting for the ionic strength) to compute the interaction energy barrier or the Fuchs stability ratio, W . Although this method can model the stability of a specific colloid under specific conditions (i.e., ionic strength, ion types, particle concentration, etc.), it cannot be applied to describe the stability of the same colloid at different ionic strengths, ion types, and particle concentrations by simply changing the ionic strength and ion valence in the DLVO model. This is because the above approach ignores the interplay between the various physicochemical processes (e.g., colloidal

interactions, counterion association equilibrium, surfactant adsorption equilibrium). As a result of such interplay, changes in the ionic strength and type lead to changes in the counterion association equilibria, and thus to changes in the surface charge and potential. Consequently, there are changes in the ion and surfactant distributions (the Boltzmann effect), thus coupled back with further changes in counterion association. The interplay becomes even more complex for industrial polymer colloids, where the surfactant systems are often very complex.

To account for the interplay mentioned above, our group has developed a generalized stability model to describe colloidal stability [8], where different physicochemical processes, such as surfactant adsorption equilibrium, counterion association equilibria, and DLVO and non-DLVO colloidal interactions, have been integrated in a single model so that their coupled interplays can be simultaneously accounted for and correctly described. In this review, we first briefly describe the developed generalized stability model and then discuss its successful application in modeling the stability of different polymer colloids.

2 The Generalized Stability Model

The interactions between charged particles and electrolytes in solution lead to ion distributions around the particles, which are governed by the Poisson–Boltzmann equation. When the ionic strength of the system is changed, redistribution of the ionic species occurs, leading to changes in the association equilibria between the ionic surfactant adsorbed on the particle surface and the counterions in the disperse medium. Consequently, this leads to changes in the surface charge density and colloidal stability. Here, we briefly describe how the generalized stability model accounts simultaneously for different processes, based on the theories available in the literature [2, 9–11].

2.1 Surfactant Adsorption Equilibrium

Ionic surfactants (denoted by E in the following) are commonly used in emulsion polymerization. They are adsorbed on the particle surface and their dissociation forms charges on the surface, stabilizing the particle. The charges generated from the surfactant molecules are referred to as mobile charges because of the reversibility of surfactant adsorption. As an equilibrium process, surfactant adsorption depends on the surfactant concentration in the disperse medium. Different adsorption isotherms are proposed in the literature to describe surfactant adsorption [12, 13], depending on the nature of the particle surface and surfactant type. The Langmuir-type adsorption isotherm is simple and probably the most commonly used:

$$bC_i^i = \frac{\Gamma/\Gamma_\infty}{1 - \Gamma/\Gamma_\infty} \quad (1)$$

where Γ is the surfactant surface coverage, Γ_∞ at saturation, and b the adsorption constant. It is particularly worth noting that C_i^i is the total surfactant concentration at the particle–liquid interface, which is different from the concentration in the bulk disperse medium, C_i^b .

On the particle surface there are also ionically dissociable polymer end groups, such as the sulfate head groups ($-\text{SO}_4^-$) from the initiator and potassium persulfate (KPS). These charges are covalently bound to the surface; they are denoted by L and referred to as fixed charges in t .

2.2 *Electrolyte Dissociation Equilibrium*

Apart from the ionic surfactant, different electrolytes may exist in polymer colloids. Thus, their dissociation equilibria should be taken into account. It should be pointed out that for each electrolyte, there are two different dissociation equilibria: one at the particle–liquid interface and another in the bulk disperse medium. The properties of the particle surface are computed on the basis of the equilibria at the particle–liquid interface, instead of the properties in the bulk disperse medium. This is one of the essential features of the generalized stability model.

In the description of the dissociation equilibria, we use E^- and L^- to denote the surfactant and fixed charge anions, M_m^+ and M_d^{2+} for the mono- and divalent cations, A_m^- and A_d^{2-} for the mono- and divalent anions, and H^+ for the proton. The divalent cation M_d^{2+} is assumed to combine with E^- and L^- only in the form of 1:1 complexes, M_dE^+ and M_dL^+ . This assumption is reasonable at the interface for aliphatic surfactants [11], because 1:2 complexes can be formed only when the surfactant hydrocarbon chains are oriented perpendicular to each other, facing the metal ions with their functional groups. Except for cases of extremely low surface coverage, this is not a preferred conformation for surfactant molecules adsorbed on a particle surface [14]. The association of M_d^{2+} with A_d^{2-} is also included, but all the weak associations of M_m^+ with anions, A_m^- and/or A_d^{2-} , are ignored. The associations of H^+ with both A_m^- and A_d^{2-} are accounted for to correctly predict the system pH. These associations are particularly important when carboxyl groups are the main source of the surface charges, which are very sensitive to the system pH. For the association between H^+ with A_d^{2-} , we consider only 1:1 association and the very weak 2:1 association is ignored. Note that all these assumptions are not strictly needed for the generalized stability model, and are only proposed treatments based on some general validity in the literature. In addition, we generally assume that the equilibrium constant K is independent of whether the association occurs at the interface or in the bulk disperse medium. The acidic surfactant, HE, is assumed to be water-soluble, regardless of whether it is associated or dissociated.

It should be pointed out that when both cationic surfactant and cationic fixed charges, E^+ and L^+ , are used, one should consider their associations with anions in the disperse medium. However, in the specific case of cationic surfactant and

anionic fixed charges, the applied surfactant first neutralizes the negative fixed charges. Beyond the charge compensation point, the particle surface progressively becomes positively charged [15]. In this case, such charge compensation has to be included in the electrolyte association equilibria.

2.3 Colloidal Interactions

The classical DLVO model accounting for electrostatic repulsive (U_R) and van der Waals attractive (U_A) potentials is considered here. As indicated by various studies [4, 6, 7, 16–19], in many polymer colloids there is often an additional short-range repulsive force that decays exponentially with distance. This force exhibits a specific electrolyte ion effect, which is related to the hydration strength of the ions, and this non-DLVO force is often referred to as “hydration force.” Thus, in addition to the DLVO interactions, we generally include this non-DLVO hydration force, referred to as the hydration interaction, U_{hyd} . Thus, the total interaction energy U is given as follows:

$$U = U_A + U_R + U_{\text{hyd}} \quad (2)$$

where the van der Waals attraction, U_A , is computed with the Hamaker relation [1]:

$$U_A = -\frac{A_H}{6} \left[\frac{2}{l^2 - 4} + \frac{2}{l^2} + \ln \left(1 - \frac{4}{l^2} \right) \right] \quad (3)$$

where A_H is the Hamaker constant and $l = r/a$, where r is the center-to-center distance between two particles and a is the particle radius. For the electrostatic repulsion, U_R , we use the modified Hogg–Healy–Fuersteneau expression [20]:

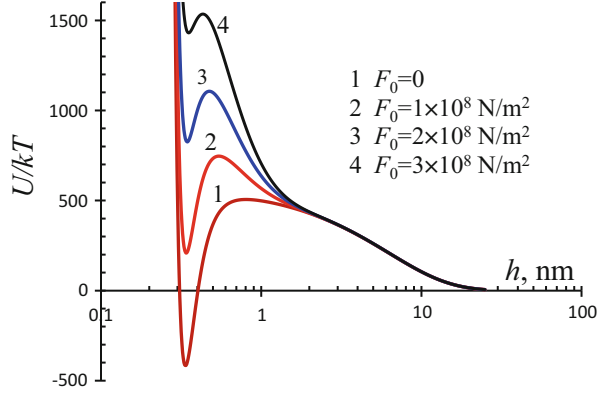
$$U_R = \frac{4\pi\epsilon_0\epsilon_r a \psi_0^2}{l} \ln \{1 + \exp[-\kappa a(l - 2)]\} \quad (4)$$

where ϵ_0 is the vacuum permittivity, ϵ_r the relative dielectric constant of the medium, and ψ_0 the surface potential. The Debye–Hückel parameter κ is given by:

$$\kappa = \sqrt{\left(e^2 N_A \sum_j z_j^2 C_j^b \right) / (\epsilon_0 \epsilon_r k T)} \quad (5)$$

with e being the electron charge, N_A the Avogadro constant, C_j^b and z_j the concentration and charge valence of the j -th ion in the bulk disperse medium, respectively; k is the Boltzmann constant and T the absolute temperature. The hydration force is modeled with an exponential decay function [9, 21]:

Fig. 1 Example of the typical effect of the presence of the hydration interaction on the total interaction energy [23]



$$F_{\text{hyd}} = F_0 \exp(-h/\delta_0) \quad (6)$$

where $h = r - 2a$ is the surface-to-surface distance between particles, F_0 is the hydration force constant, and δ_0 is the characteristic decay length. Applying the Deryaguin approximation leads to the corresponding hydration interaction energy between two spherical particles [22]:

$$U_{\text{hyd}} = \pi a F_0 \delta_0^2 \exp(-h/\delta_0) \quad (7)$$

Typical examples of the total interaction profiles in the presence of the hydration interaction are shown in Fig. 1 (cases 2, 3, and 4) and compared with the case in the absence of hydration (case 1). It can be seen that the hydration interaction not only increases the interaction barrier but also moves the primary minimum upward.

With the above total interaction energy U , one can compute the Fuchs stability ratio, W , based on its definition [24]:

$$W = 2 \int_2^{\infty} \frac{\exp(U/kT)}{Gl^2} dl \quad (8)$$

where G is a hydrodynamic function accounting for additional resistance caused by squeezing of the fluid during the approach of a particle [25]:

$$G = \frac{6l^2 - 20l + 16}{6l^2 - 11l} \quad (9)$$

2.4 Computation of Key Quantities of the Generalized Stability Model

One of the most important quantities related to the processes described above is the total effective charge density on the particle surface, with which one can directly compute the surface potential needed in colloidal interactions. As mentioned previously, there are two types of charge, mobile and fixed. Of the adsorbed species on the particle surface, HE, M_mE , M_dE^+ , and E^- , only the last two contribute to the surface charge. The net mobile charge density coming from the adsorbed surfactants, $\sigma_{0,E}$, is given by:

$$\sigma_{0,E} = F \left(C_{M_dE^+}^S - C_{E^-}^S \right) \frac{V_p}{A_p} = \frac{aF}{3} \left(K_{M_dE} C_{M_d^{2+}}^i - 1 \right) C_{E^-}^S \quad (10)$$

where the superscripts *s* and *i* denote quantities on the particle surface and at the interface, respectively. *F* is the Faraday constant and V_p and A_p are the volume and surface area of a particle, respectively. Note that the sign of the mobile charge density given by Eq. 10 depends on the difference in the concentrations of M_dE^+ and E^- on the surface. When the association between E^- and M_d^{2+} is very strong, or when the M_d^{2+} concentration in the bulk disperse medium is substantially high, the net mobile charge on the surface is positive and charge sign inversion occurs. The charge sign inversion is often used to explain the re-stabilization phenomenon observed at substantially high concentrations of divalent cation in the liquid phase [26–29].

For the net fixed charge, we can similarly write:

$$\sigma_{0,L} = \frac{aF}{3} \left(C_{M_dL^+}^S - C_{L^-}^S \right) = \frac{aF}{3} \left(K_{M_dL} C_{M_d^{2+}}^i - 1 \right) C_{L^-}^S \quad (11)$$

Therefore, the total surface charge density, σ_0 , is given by:

$$\sigma_0 = \sigma_{0,E} + \sigma_{0,L} \quad (12)$$

It should be noted again that the above equations for computation of charge are valid only when both the mobile and fixed charges are negative. When the mobile and/or fixed charges are positive, the above equations must be modified accordingly.

As mentioned above, the distribution of all the ionic species in the system is described by the Poisson–Boltzmann equation. For simplification of the description, we treat it in the frame of the classical Gouy–Chapman theory [2, 11]. Thus, we obtain the following expression to correlate between the surface charge density, σ_0 , the surface potential, ψ_0 , and the ionic strength in the bulk disperse medium, C_j^b :

$$\sigma_0 = -\left\{R_0 \sum C_j^b \left[\exp\left(-\frac{z_j e \psi_0}{kT}\right) - 1 \right]\right\}^{1/2} \quad (13)$$

where $R_0 = 2F\varepsilon_0\varepsilon_r kT/e$.

The other important quantities to be properly computed are the mass balances of each species distributed in the different phases. Let us use $C_{j,0}$ to represent the concentration of the j -th species initially added to the system. It is distributed on the particle surface and in the disperse medium at equilibrium according to:

$$C_{j,0} = \phi C_j^S + N_0 \int_0^{V_{l,p}} C_j(x) dV(x) \quad (14)$$

where ϕ is the particle volume fraction, N_0 the particle number concentration, and $V_{l,p}$ the liquid volume that on average can be assigned to each particle ($V_{l,p} = 1/N_0$). The first term on the right-hand side of Eq. (14) is the mass on the particle surface, and the second is the mass distributed in the entire disperse medium, which can be divided into two regions, the diffuse layer near the particle surface and the bulk disperse medium:

$$\begin{aligned} \int_0^{V_{l,p}} C_j(x) dV(x) &= \int_0^{V_d} C_j^d dV + \int_0^{V_{l,p}} C_j^b dV \\ &= \int_0^{V_d} C_j^d dV + (V_{l,p} - V_d) C_j^b \end{aligned} \quad (15)$$

where V_d is the liquid volume occupied by the diffuse layer, and C_j^d and C_j^b the concentrations of the j -th component in the diffuse layer and in the bulk disperse medium, respectively. To solve the material balance, it is necessary to estimate V_d . For a moderate or thin EDL (~ 2 nm) compared with the particle radius ($a > 30$ nm), the contribution of the diffuse layer (i.e., the first term on the right-hand side of Eq. 15) to the total material balance is relatively small, and the concentration in the diffuse layer can be simply replaced by the concentration in the bulk disperse medium (i.e., $C_j^d \approx C_j^b$), which should not result in significant error in the material balance. In this way, Eq. 14 reduces to:

$$C_{j,0} = \phi C_j^S + (1 - \phi) C_j^b \quad (16)$$

Note that such an approximation is only for the purpose of the material balance computation and is not applied in the calculation of association equilibria and surface charge density.

Therefore, in summary, once the surfactant adsorption parameters in Eq. (1) and all the electrolyte association constants are known, the set of equations described in Sect. 2 can be solved simultaneously to obtain the surface potential or charge density, the concentrations of all species on the particle surface and in the bulk disperse medium, and finally the Fuchs stability ratio W .

3 Applications of the Generalized Stability Model

To demonstrate the reliability of the generalized stability model, we have applied it to various polymer colloids stabilized in one of three ways: by purely mobile charges, by purely fixed charges, or by both mobile and fixed charges. The unknown model parameters were estimated using a few values of the Fuchs stability ratio, W , as determined experimentally for various salt types and concentrations. Application of the model allows one to monitor the dynamics of surfactant partitioning between particle surface and disperse medium, analyze the variation in surface charge density and potential as a function of the electrolyte type and concentration, and predict the critical coagulant concentration (CCC) for fast coagulation, which can be defined as the minimum coagulant (salt) concentration at which no repulsive barrier exists between colloidal particles.

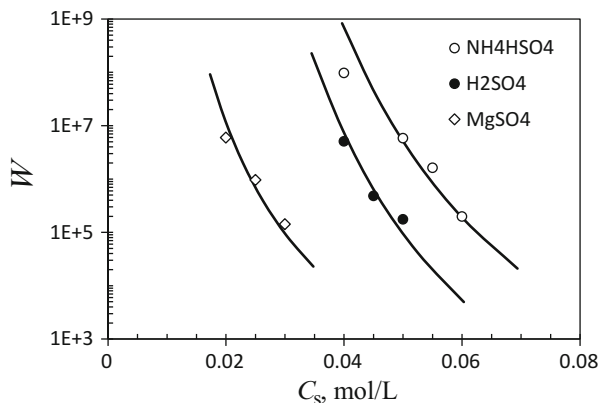
3.1 *Fluorinated Elastomer Latex with Only Mobile Charges* [8]

The first polymer colloid used to demonstrate the feasibility of the generalized stability model was a fluorinated elastomer latex, manufactured by Solvay (Italy) through emulsion polymerization. This colloid does not have fixed charges and is stabilized purely by the surfactant (E), a perfluoropolyether (PFPE)-based carboxylate. The particle radius is 60 nm, the surfactant concentration is 33.3 mol/m³ polymer, and the surfactant counterion is Na⁺. The original latex is acidic due to the presence of a small amount of HF, whose concentration at the particle volume fraction $\phi = 5.0 \times 10^{-3}$ is equal to 1.6×10^{-3} mol/L.

3.1.1 Estimation of the Model Parameters

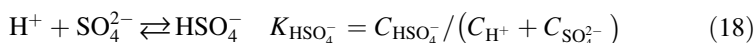
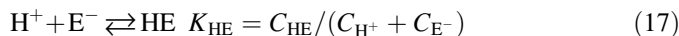
Application of the model involves knowing various parameters. Some can be found in the literature, but others have to be determined experimentally. The proposed approach is first to experimentally measure a few W values with different types of salts and then fit these data with the generalized stability model to obtain the unknown parameters. Figure 2 reproduces some W values measured using

Fig. 2 Values of the Fuchs stability ratio (W) of a fluorinated elastomer latex measured as a function of the salt concentration, for three types of salt, NH_4HSO_4 , H_2SO_4 , and MgSO_4 , at $\phi = 5.0 \times 10^{-3}$. The solid curves show fitting of the model [8]



NH_4HSO_4 , H_2SO_4 , and MgSO_4 . The details of how to measure W values can be found in the original paper [8].

Let us first consider the cases using H_2SO_4 and NH_4HSO_4 , both of which involve generation of protons in the solution that can associate with the carboxyl groups of E. There are two parameters (K_{HE} and $K_{\text{HSO}_4^-}$) for the associations of H^+ with the surfactant E and the anion SO_4^{2-} , respectively:



The $K_{\text{HSO}_4^-}$ value can be found in the literature and is equal to 97.0 L/mol [30]. There is also the constant, $K_{\text{NH}_4\text{E}}$, for the association of NH_4^+ with E:



The associations of NH_4^+ with the other anions are known to be very weak and can be ignored [31]. Thus, for H_2SO_4 and NH_4HSO_4 , two association parameters K_{HE} and $K_{\text{NH}_4\text{E}}$ need to be estimated.

For the adsorption of surfactant (E) on the particle surface, we consider the Langmuir isotherm (Eq. 1), which involves two parameters, Γ_∞ and b . The saturation coverage (Γ_∞) depends mainly on the affinity between the surfactant and the particle surface but not on the electrolyte. Thus, we take the value $\Gamma_\infty = 5.5 \times 10^{-6}$ mol/m², as reported elsewhere [32].

For colloidal interactions, we assume the presence of the hydration interaction, which involves two parameters, F_0 and δ_0 in Eq. (6). Literature information indicates that F_0 lies in the range between 1×10^6 and 5×10^8 N/m² and δ_0 in the range between 0.2 and 1.0 nm [33]. We consider here that $\delta_0 = 0.6$ nm, which is approximately twice the size of a water molecule and, instead, F_0 is to be fitted.

Table 1 Values of parameters for the generalized stability model in the case of fluorinated elastomer latex [8]

| Parameter | | Cation (M) | | |
|-----------------------|--|------------------------|------------------------------|-------------------|
| | | H ⁺ | NH ₄ ⁺ | Mg ²⁺ |
| Association constants | K_{ME} (L/mol) | 29.4 ^a (30) | 11.2 ^a | 7.8 ^a |
| | K_{MSO_4} (L/mol) | 97.0 | – | 28.8 |
| Hydration parameters | F_0 (10 ⁶ N/m ²) | 1.15 ^a | 1.25 ^a | 1.36 ^a |
| | δ_0 (nm) | 0.6 | 0.6 | 0.6 |
| Adsorption parameters | Γ_∞ (10 ⁻⁶ mol/m ²) | 5.1 (5.1) | | |
| | b (10 ³ L/mol) | 3.5 ^a (4.0) | | |

Values in parentheses are taken from the literature

^aFitted values

Another interaction parameter, the Hamaker constant, is assumed to be equal to that of a similar fluorinated polymer, PTFE, so that $A_H = 3.0 \times 10^{-21}$ J [34].

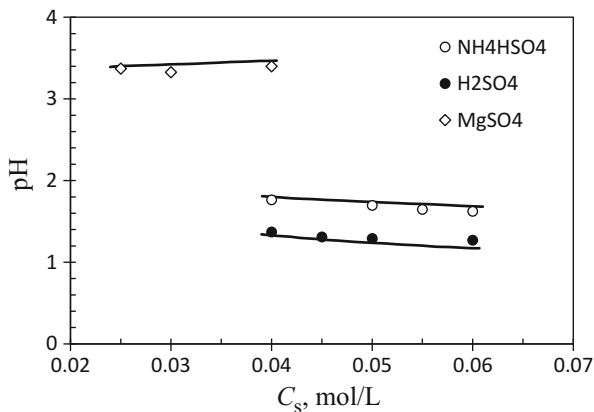
Therefore, there are four totally unknown parameters, K_{HE} , K_{NH_4E} , b , and F_0 . To obtain these unknown parameters, a proper set of initial values are chosen for each parameter to solve the set of nonlinear algebraic equations, Eqs. 1–16. Then, the best fit is obtained to the measured W values in the cases of H₂SO₄ and NH₄HSO₄, using a proper optimization algorithm. The values of the parameters obtained in the cases of H₂SO₄ and NH₄HSO₄ are given in Table 1, and the good agreement between simulated and experimental W values is shown in Fig. 2.

We next consider the case of MgSO₄. The surfactant adsorption parameters obtained previously are still valid. Association of the surfactant with H⁺ is also present in this system because the latex is acidic, and the association constant K_{HE} obtained above can be used directly. Thus, there are only two parameters to be determined, the association equilibrium constant, K_{MgE^+} , and the hydration constant, F_0 . The result of the fitting is also shown in Fig. 2, and the values of the parameters are reported in Table 1. It is interesting that the association constant of Mg²⁺ is slightly smaller than that of NH₄⁺. This could arise from the structure of NH₄⁺, which is different from that of the metal cations.

3.1.2 Model Predictions

With all the parameters available in Table 1, one can now use the generalized stability model to predict the desired quantities for the given latex. Let us first apply it to predict the system pH under various conditions, particularly as a function of the salt type and concentration. Figure 3 compares predictions with experimentally measured pH values. It is evident that the model predictions agree excellently with the experiment results in all three cases. In the cases of H₂SO₄ and NH₄HSO₄, because they produce H⁺ both measured and predicted values of pH in Fig. 3 decrease as the concentration of H₂SO₄ or NH₄HSO₄ increases. On the other hand, in the case of MgSO₄, because the anion SO₄²⁻, at equilibrium, can consume

Fig. 3 Comparison between the measured (symbols) and predicted (solid curves) pH values for a fluorinated elastomer latex as a function of the salt concentration, for three types of salt, NH_4HSO_4 , H_2SO_4 , and MgSO_4 , at particle volume fraction $\phi = 5.0 \times 10^{-3}$ [8]



H^+ to form HSO_4^- , the system pH increases slightly as the concentration of MgSO_4 increases. The capture of these slight variation trends confirms the reliability of the generalized stability model.

The second verification of model reliability is to predict the CCC value. This signifies using the generalized stability model, whose parameters were estimated at low salt concentrations, to extrapolate its application to substantially larger salt concentrations.

The CCC values are experimentally determined based on the fact that when diffusion-limited aggregation occurs at $\phi > 1 \times 10^{-3}$, clearly visible large pieces of clusters are formed immediately [35, 36]. Therefore, a given amount of latex was added to a series of salt concentrations to reach $\phi = 5 \times 10^{-3}$, and the time for the appearance of large clusters was recorded. The CCC value was obtained by extrapolation to the salt concentration at which the large clusters appear at time zero. Table 2 compares the measured CCC values of the three salts with the predicted values for three types of latexes. It should be mentioned that each predicted CCC value is reported with its significant error bar, because near the CCC the interaction energy barrier reduces asymptotically without a sharp change. It is clear that the model predictions are in good agreement with experimental results. Note that of the three latexes mentioned in Table 2, latex 1 is the one used above to define the generalized stability model; latexes 2 and 3 are similar to latex 1 but differ in the particle size and amount of surfactant. Thus, the model developed from latex 1 should be applicable to the other two cases. It is worth mentioning that since latexes 2 and 3 use less surfactant (i.e., smaller surface charge densities), both the measured and predicted CCC values are smaller than those of latex 1.

Table 2 Comparison between measured and predicted CCC values for three different salts used for fast coagulation of three latexes [8]

| Latex type | CCC (mol/L) | | | | | |
|------------|--------------------------------|-------------|----------------------------------|-------------|-------------------|-------------|
| | H ₂ SO ₄ | | NH ₄ HSO ₄ | | MgSO ₄ | |
| | Exp. | Model | Exp. | Model | Exp. | Model |
| Latex 1 | 0.4 | 0.35 ± 0.05 | 0.52 | 0.55 ± 0.05 | 0.6 | 0.45 ± 0.05 |
| Latex 2 | 0.3 | 0.25 ± 0.05 | 0.4 | 0.35 ± 0.05 | – | – |
| Latex 3 | 0.3 | 0.25 ± 0.05 | 0.4 | 0.35 ± 0.05 | – | – |

3.2 Styrene–Acrylate Copolymer Latex with Both Mobile and Fixed Charges [37]

The second polymer colloid used to verify the generalized stability model was a styrene-acrylate copolymer latex, manufactured by BASF SE (Ludwigshafen, Germany) through emulsion polymerization with a carboxylate surfactant. Unlike the previous latex, this latex possesses fixed charges, $-\text{SO}_4^-$, on the particle surface as a result of the use of a persulfate initiator. Because it is stabilized by both mobile and fixed charges, we can compare its stability behavior to that investigated above with only mobile charges. The radius of primary particles is $a = 52$ nm, and the stability behavior is investigated at a fixed particle volume fraction, $\phi = 0.02$.

3.2.1 Estimation of the Model Parameters

To estimate the model parameters, we used the measured CCC values as a function of the system pH, using a bivalent salt, MgSO₄. The data were obtained using a similar method to that described above and are reported in Fig. 4. Note that because the pH of the original latex was 8.3, the pH value is tuned by adding H₂SO₄.

Considering MgSO₄ and H₂SO₄ as well as the mobile and fixed charges, we have three anions in the system, SO_4^{2-} and $-\text{COO}^-$ from the surfactant (denoted by E^-), and $-\text{SO}_4^-$ from the fixed charges (denoted by L^-), and two cations, H^+ and Mg^{2+} . Thus, there are a total of six association equilibria. To reduce fitting parameters, we use association equilibrium constants for similar molecules but with shorter chain lengths. This does not introduce significant error because, for long carbon chain surfactants, the electronic effects are transferred through molecular bonds and are not felt beyond two to three carbon atoms [38]. Five of the six association constants were taken from the literature and are reported in Table 3 [30]. The only association constant of Mg^{2+} with fixed charge L^- ($-\text{SO}_4^-$), K_{MgL^+} , was used as a fitting parameter, because of unavailability in the literature. We again used the Langmuir isotherm for surfactant adsorption, and of the two parameters, Γ_∞ and b , we assumed that Γ_∞ is equal to that of stearic acid on butadiene-styrene polymer particles, a system very similar to the present one [39], while b was used as a fitting parameter. The Hamaker constant, A_{H} , was estimated using the Lifshitz theory

Fig. 4 CCC values (symbols) for $MgSO_4$ as a function of the system pH for a styrene-acrylate copolymer latex at $\phi=0.02$; the continuous curve is the model simulation [37]

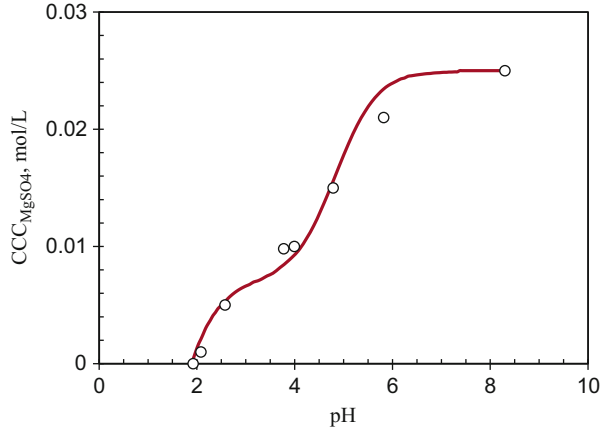


Table 3 Values of parameters for the generalized stability model in the case of styrene-acrylate copolymer latex [37]

| Parameter | | Cation (M) | |
|-----------------------|--|----------------------|------------------|
| | | H ⁺ | Mg ²⁺ |
| Association constants | K_{ME} (L/mol) | 6.3×10^{4b} | 3.5^b |
| | K_{ML} (L/mol) | 33.9^b | 2.5^a |
| | K_{MSO_4} (L/mol) | 97.0^b | 28.8^a |
| Fixed charge amount | C_L (mol/m ³ polymer) | 4.66^a | |
| Hamaker constant | A_H (10 ⁻²⁰ J) | 1.3^d | |
| Adsorption parameters | Γ_∞ (10 ⁻⁶ mol/m ²) | 7.1^c | |
| | b (10 ³ L/mol) | 0.88^a | |

^aFitted values

^bValue taken from [30]

^cValue taken from [39]

^dValue computed from Lifshitz theory

[16]. The concentration of fixed charge groups C_L on the particle surface was used as a fitting parameter. Therefore, in total, there were three fitting parameters, K_{MgL^+} , b , and C_L , which were determined by fitting the nine CCC values at different pH values, as shown in Fig. 4.

It should be noted that for a small radius of the particles and the computed separation distance at the potential barrier larger than or close to 1 nm, we use the classical DLVO model for colloidal interactions and ignore any short-range non-DLVO forces. The simulated CCC values are compared with the experimental values in Fig. 4, and it is seen that not only the trend but also the absolute values are in good agreement. The values of the three fitted parameters, together with the values of the other parameters, as taken from the literature, are listed in Table 3.

3.2.2 Model Predictions and Applications

Both the experimental and simulated CCC data in Fig. 4 show two distinct regimes: one for $\text{pH} > 4$ and another for $\text{pH} < 4$. This corresponds to two types of surface charge, mobile $-\text{COO}^-$ (E^-) and fixed $-\text{SO}_4^-$ (L^-), as a result of their substantially different association constants with H^+ , as reported in Table 3. Let us now manifest the system behavior by applying the generalized stability model to detail the surface charge concentrations on the particle surface as a function of pH.

Let us first consider the case in the absence of MgSO_4 . The computed concentrations of mobile and fixed charge groups on the particle surface as a function of pH are given in Fig. 5a, and the corresponding total surface charge density (σ_0) and potential (ψ_0) are shown in Fig. 5b. It can be seen that at the original pH of the latex (8.3), because $\text{E}^- = \text{E}_{\text{total}}$ on the surface and L^- is at plateau, all the mobile and fixed charge groups on the surface are in dissociated form (E^- and L^-). The σ_0 and ψ_0 values in Fig. 5b reach their maximum (in absolute value) corresponding to the highest colloidal stability of the latex. In this case, the total surfactant concentration (E_{total}) on the surface is only composed of the dissociated anions, E^- . It is particularly important to mention that the E_{total} values on the surface and in the disperse medium are 8.16×10^{-3} mol/L and 2.54×10^{-4} mol/L, respectively, and do not follow the partitioning computed by the adsorption isotherm. The latter gives E_{total} values on the surface and in the disperse medium of 1.11×10^{-1} and 4.2×10^{-4} mol/L, respectively. This arises because the ionized E^- follows the Boltzmann distribution, resulting in its concentration at the particle–liquid interface being smaller than that in the bulk disperse medium. Because, for the generalized stability model, the surfactant adsorption equilibrium is considered to establish at the particle–liquid interface, the Boltzmann distribution certainly changes the amount of surfactant adsorbed on the particle surface (in fact, it is reduced because the ionic surfactant species are dominated by E^-). For $\text{pH} > 7.0$, no significant changes occur, as shown in Fig. 5.

When the system pH is less than seven, the protonation process starts. Because $-\text{COO}^-$ (E^-) has a much larger association constant with H^+ than the fixed $-\text{SO}_4^-$ (L^-), its protonation initially dominates and follows that shown in Fig. 5a. The E^- concentration decreases sharply as pH decreases, while the fixed charge L^- concentration remains nearly constant. The decrease in σ_0 or ψ_0 with decreasing pH in Fig. 5b is a result of a reduction in the mobile charges E^- . In the pH range between 3 and 4, the system reaches another (almost) flat region, where the E^- protonation is close to completion but the H^+ concentration is still insufficient to significantly protonate L^- . When the pH is less than three, L^- starts to protonate and its concentration decreases as pH decreases, as shown in Fig. 5a. This leads to sharper decreases in σ_0 and ψ_0 with decreasing pH. In this region, basically all E is in the protonated form, HE, and because HE does not follow the Boltzmann distribution, the partitioning of HE on the surface and in the bulk disperse medium is exactly given by the surfactant adsorption isotherm. Therefore, E_{total} is equal to HE on the particle surface and reaches a plateau. Referring back to Fig. 4, showing the

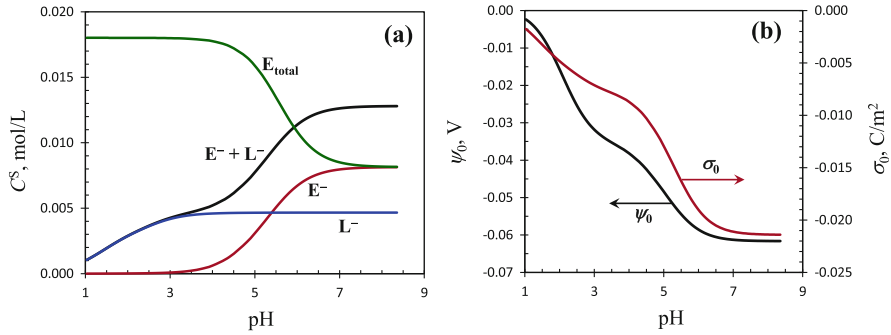


Fig. 5 Concentrations of charge groups E^- and L^- on the particle surface (a), and surface charge density σ_0 and potential ψ_0 (b), as a function of pH for the styrene-acrylate copolymer latex at $\phi = 0.02$ and $C_{MgSO_4} = 0$ [37]

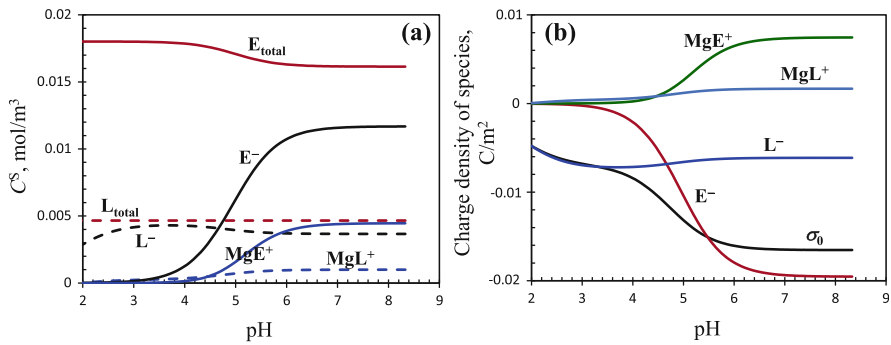


Fig. 6 (a) Concentrations of the surfactant, E, species (solid curves) and the fixed charge, L, (broken curves) groups on the particle surface, and (b) total and species charge densities as a function of the system pH, for the styrene-acrylate copolymer latex at $\phi = 0.02$ and $C_{MgSO_4} = 0.01$ mol/L [37]

behavior of CCC values for $MgSO_4$, it is clear that for $pH > 4$, the change in CCC value with pH is related to protonation of the mobile charges, E^- ; for $pH < 4$, it is due to protonation of the fixed charges, L^- .

For the presence of $MgSO_4$ at 0.01 mol/L, Fig. 6a shows the computed concentrations of the surfactant and fixed charge species on the particle surface as a function of pH. The total surface charge density (σ_0) and the contribution of each surface charge group are given in Fig. 6b.

Comparing Fig. 6a to Fig. 5a in the absence of Mg^{2+} , we see that the concentration variations of the surfactant species are very similar, but now the new species, MgE^+ , is present on the surface as a result of $E^- - Mg^{2+}$ association. In the presence of Mg^{2+} , the plateau value of the total surface charge density, σ_0 in Fig. 6c for $pH > 7$, is substantially smaller than that in Fig. 5b in the absence of Mg^{2+} . As the system pH decreases to less than seven, the surface concentrations of both E^- and MgE^+ species decrease. For E^- , this arises because of its protonation (as discussed

above), whereas for Mg^{2+} , we should consider that MgE^+ is progressively substituted by HE as pH decreases, because $-\text{COO}^-$ association with H^+ is much stronger than with Mg^{2+} .

For the species related to the fixed charge (L) groups, their concentration variations shown in Fig. 6a differ from those in Fig. 5a, as a result of the presence of Mg^{2+} . The L^- concentration in Fig. 6a increases as pH decreases, and then decreases after reaching a local maximum at around $\text{pH} \sim 3.5$. However, as shown in Fig. 5a, there is no such local maximum in the L^- concentration in the absence of Mg^{2+} . To explain this, we should recall that the total amount of fixed charge groups (L_{total}) is constant, which is a sum of L^- and MgL^+ in Fig. 6a. As pH decreases by adding H_2SO_4 , the ionic strength increases, leading to a decrease in the surface potential. The latter, through the effects of Boltzmann distribution, results in a shift of positive Mg^{2+} ions from the particle–liquid interface to the liquid phase, thus favoring the dissociation of MgL^+ on the surface and freeing more L^- . Consequently, the L^- concentration increases as pH decreases for $\text{pH} > 3.5$ (Fig. 6a). In the region of $\text{pH} < 3.5$, protonation of the L^- species becomes dominant, and it follows that the L^- concentration starts to decrease with decreasing pH.

3.3 *Butylacrylate-Methylmethacrylate-Acrylic Acid Copolymer Latexes*

The third type of polymer colloids used here for verifying the model feasibility is represented by two butylacrylate-methylmethacrylate-acrylic acid copolymer latexes, referred to as P1 and P2. They were supplied by BASF SE (Ludwigshafen, Germany), produced through emulsion polymerization with $\text{Na}_2\text{S}_2\text{O}_8$ as initiator and sodium dodecyl sulfate (SDS) as emulsifier. The radius of the particles is 80.0 and 81.0 nm, respectively, for P1 and P2. The main difference between them is the amount of acrylic acid (AA) used in the polymerization, which is 0% for P1 and 1% for P2. It follows that the particles of P1 possess only the fixed charges $-\text{SO}_4^-$ and those of P2 contain both $-\text{SO}_4^-$ and $-\text{COO}^-$ (fixed) charges. The SDS surfactant was removed completely using ion exchange resins [40]. Therefore, after cleaning, unlike the latexes described in Sects. 3.1 and 3.2, the P1 and P2 latexes possess only fixed charges. It should be pointed out that P1 and P2 latexes (after removing the surfactant used during polymerization) represent the simplest type of polymer colloid. Similar but different systems have also been used to successfully verify the generalized stability model [41].

3.3.1 P1 Latex with Only Sulfate Groups

For the P1 latex, the W values measured in the presence of NaCl and H_2SO_4 are reproduced from the literature [42] and shown in Fig. 7a. The corresponding pH

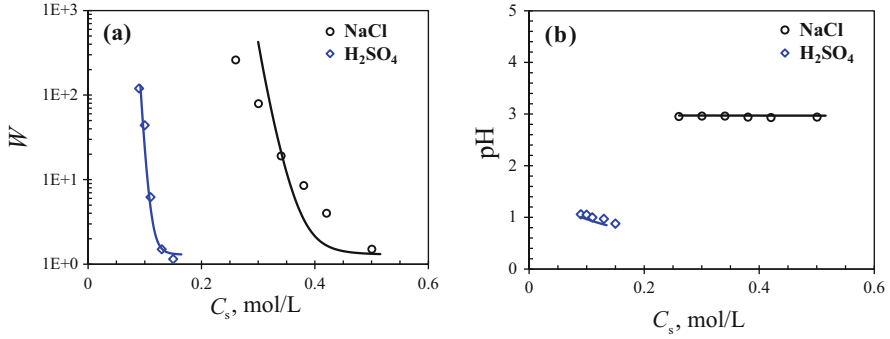


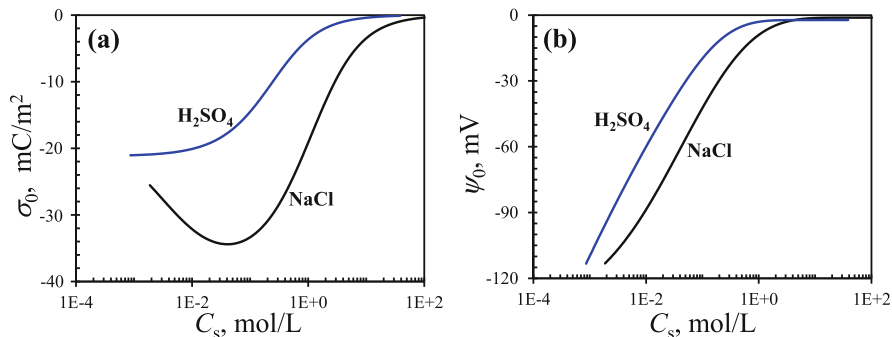
Fig. 7 Comparison between measured (*symbols*) and simulated (*solid curves*) values for (a) the Fuchs stability ratio W and (b) pH values, for P1 latex at $\phi = 2.0 \times 10^{-5}$, destabilized by NaCl and H_2SO_4

values are reported in Fig. 7b. Because P1 possesses only the fixed charges $-\text{SO}_4^-$ (denoted by I) on the particle surface, it is the simplest latex considered. For P1, we have a total of seven parameters: A_{H} , $C_{\text{I,T}}^{\text{S}}$, K_{HI} , K_{NaI} , $F_{0,\text{H}}$, $F_{0,\text{Na}}$, and δ_0 . Of these, values for A_{H} (1.0×10^{-20} J) and δ_0 (0.40 nm) are taken from the literature. For the total concentration of $-\text{SO}_4^-$ on the particle surface, $C_{\text{I,T}}^{\text{S}}$, we used the result obtained previously [37] (i.e., with respect to the total added initiator during the polymerization) that 33.1% $-\text{SO}_4^-$ groups remain on the particle surface. From the polymerization recipe, this corresponds to $C_{\text{I,T}}^{\text{S}} = 0.0235$ mol/kg polymer. The remaining four parameters, K_{HI} , K_{NaI} , $F_{0,\text{H}}$, and $F_{0,\text{Na}}$, are used as fitting parameters. In addition, because H_2SO_4 was used to destabilize the latex and tune pH, there are two associations of SO_4^{2-} in the bulk disperse medium with H^+ and Na^+ . Equilibrium constants $K_{\text{H}\text{SO}_4^-}$ and $K_{\text{Na}\text{SO}_4^-}$ were taken directly from the literature [30], being equal to 97.0 and 5.0 L/mol, respectively.

Following the same procedure as above, the simulated values of two sets of W values are shown in Fig. 7a, as well as the corresponding pH values in Fig. 7b. All the simulations are very satisfactory, but in the case of NaCl, the simulations show significantly sharper decrease in the W value with C_{S} than the experimental data. This could indicate that the hydration interaction increases as more Na^+ ions are associated on the surface. The obtained values for the unknown parameters are listed in Table 4 under P1. The obtained value for K_{HI} is about one order of magnitude larger than that for K_{NaI} , which follows the same trend as $K_{\text{H}\text{SO}_4^-}$ with respect to $K_{\text{Na}\text{SO}_4^-}$. Both K_{HI} and K_{NaI} values are substantially smaller than those of $K_{\text{H}\text{SO}_4^-}$ and $K_{\text{Na}\text{SO}_4^-}$. The obtained K_{HI} value is equal to 33.1 L/mol, which is comparable to the association constant of propyl sulfonate ($\text{C}_3\text{H}_7\text{SO}_3^-$) with H^+ [30], but smaller. In fact, the association constant of SO_4^{2-} with H^+ is also smaller than that of SO_3^{2-} with H^+ . The estimated values for the hydration force constants, $F_{0,\text{H}}$ and $F_{0,\text{Na}}$ for P1, are well within the range reported in the literature (1×10^6 – 5×10^8 N/m²). Note that $F_{0,\text{H}}$ and $F_{0,\text{Na}}$ were considered to be independent of the salt concentration. The $F_{0,\text{H}}$ value is smaller than the $F_{0,\text{Na}}$ value, indicating that the

Table 4 Values of the parameters for P1 and P2 latexes obtained from fitting the measured W values

| Latex | K_{HI} (L/mol) | K_{NaI} (L/mol) | $F_{0,\text{H}}$ (N/m ²) | $F_{0,\text{Na}}$ (N/m ²) | $C_{\text{L,T}}^s$ (mol/kg P) | K_{HL} (L/mol) | K_{NaL} (L/mol) |
|-------|----------------------------|-----------------------------|--------------------------------------|---------------------------------------|----------------------------------|-------------------------|-----------------------------|
| P1 | 16.0 | 1.80 | 7.77×10^6 | 8.80×10^6 | – | – | – |
| P2 | 16.0 | 1.80 | 12.1×10^6 | (in Fig. 10) | 0.0866 | 4.0×10^6 | 2.80 |

**Fig. 8** Surface charge density σ_0 and surface potential ψ_0 computed from the generalized stability model using the estimated parameters in Table 4, for P1 latex at $\phi = 2.0 \times 10^{-5}$, destabilized by NaCl and H_2SO_4

hydration force in the presence of H_2SO_4 is smaller than that in the presence of NaCl. Such a trend is consistent with those reported in the literature [8, 43].

With estimated values for all the model parameters, the generalized stability model has been well established for P1 latex and can be applied to analysis of the system stability. As examples, let us calculate the evolutions of the surface charge density (σ_0) and potential (ψ_0) with salt concentration, which in most cases are difficult to determine experimentally. Figure 8a, b shows the computed σ_0 and ψ_0 values as functions of the salt (NaCl or H_2SO_4) concentration. In the case of H_2SO_4 , both σ_0 and ψ_0 (absolute values) decrease as the H_2SO_4 concentration increases. For σ_0 , this arises because of association of added H^+ with the surface $-\text{SO}_4^-$ charge groups. For ψ_0 , the decrease is the result of two factors: (1) σ_0 reduction and (2) the screening effect of an increase in ionic strength.

For NaCl as destabilizer, the variation in surface charge density σ_0 with NaCl concentration C_s in Fig. 8a is rather peculiar. At low C_s , the absolute σ_0 value increases as C_s increases, instead of decreasing. Only when the σ_0 value reaches a local maximum at around $C_s = 0.04$ mol/L, does it start to decrease with C_s . It is worth pointing out that, without the generalized stability model, such behavior would be very difficult to observe experimentally. To explain the observed phenomenon, we should first consider that the surface charge results from the association equilibria between the surface $-\text{SO}_4^-$ groups and cations Na^+ and H^+ at the particle–liquid interface. As the NaCl concentration increases, the increased Na^+ ions at the interface in principle drive the equilibrium towards association, thus

decreasing the surface charge; however, the computed surface charge increases, which means that the increased Na^+ concentration in the bulk disperse medium leads to a decrease (rather than an increase) in the Na^+ concentration at the particle–liquid interface. The occurrence of this phenomenon is related to the Boltzmann equation:

$$C_j^i = C_j^b \exp\left(-\frac{z_j e \psi_0}{kT}\right) \quad (20)$$

Indeed, the concentration at the interface, C_j^i , increases as the concentration in the bulk disperse medium, C_j^b , increases (from Eq. 20), but the increase in C_j^b also leads to a decrease in the surface potential (ψ_0) as a result of the screening effect. Then, the exponent term in Eq. (20) decreases with C_j^b . Thus, whether C_j^i increases or decreases with C_j^b depends on the combined effect of C_j^b and the exponent term. As can be seen in Fig. 8a, at NaCl concentrations smaller than about 0.04 mol/L the absolute ψ_0 value is very large, and variations in ψ_0 result in substantial changes in the value of the exponent term. Thus, the effect of the exponent term overwhelms that of C_j^b , leading to C_j^i decreasing with C_j^b . It follows that σ_0 increases with the NaCl concentration. With further decrease in ψ_0 , because its value is small, the effect of the exponent term becomes smaller than that of C_j^b , and C_j^i increases with C_j^b , leading to a decrease in σ_0 .

3.3.2 P2 Latex with 1% PAA

On the particle surface of P2 latex, apart from the fixed $-\text{SO}_4^-$ groups, there are also carboxylic groups from PAA formed from 1% acrylic acid monomer, which when ionized ($-\text{COO}^-$) contribute to the surface charge. The measured W values at different pH values in the presence of NaCl and H_2SO_4 , respectively, are reproduced from previous work [42] and shown in Fig. 9a; the corresponding pH values are reported in Fig. 9b. The contributions of 1% PAA to the colloidal stability can be modeled by simulating the W and pH values using the generalized stability model. Except for 1% AA, the recipe for P2 is basically the same as that for P1. Thus, to reduce the fitting parameters, we assume that the total $-\text{SO}_4^-$ concentration on the particle surface is identical for P1 and P2. Then, the values for the parameters $C_{\text{I,T}}^{\text{S}}$, K_{HI} and K_{NaI} evaluated for P1 (Table 4) can be directly used for P2. Because of the presence of $-\text{COO}^-$ groups on the surface, whose properties depend strongly on pH, we expect that the hydration force constants, $F_{0,\text{H}}$ and $F_{0,\text{Na}}$, also vary with pH. Thus, they are still set as fitting parameters.

There are three parameters related to the $-\text{COO}^-$ groups: the total carboxylic group contraction on the surface, $C_{\text{L,T}}^{\text{S}}$, and two association constants of $-\text{COO}^-$ with H^+ and Na^+ , K_{HL} and K_{NaL} , respectively. The $C_{\text{L,T}}^{\text{S}}$ value has been determined by titration and is equal to 0.0866 mol/kgP, as given in Table 4 under P2. Therefore, for P2, we have a total of four fitting parameters, $F_{0,\text{H}}$, $F_{0,\text{Na}}$, K_{HL} , and K_{NaL} , to be

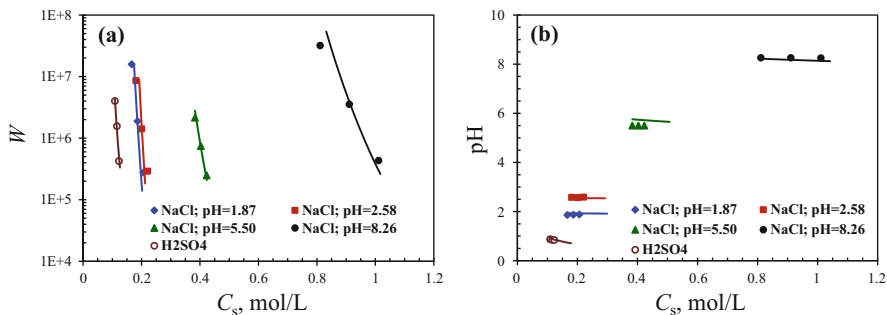


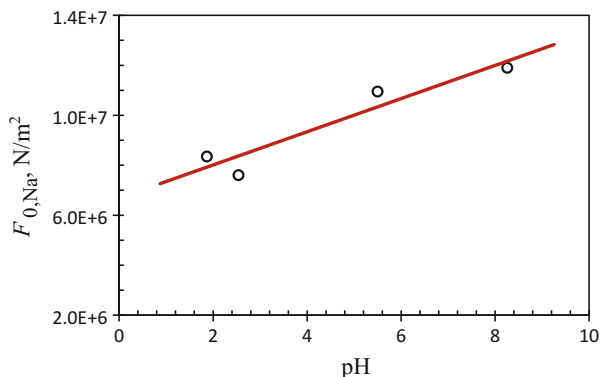
Fig. 9 Comparison between measured (*symbols*) and simulated (*solid curves*) values of (a) the Fuchs stability ratio W and (b) pH values, for P2 latex at $\phi = 5.0 \times 10^{-2}$, destabilized by NaCl and H_2SO_4

determined from simulations of W and pH values. The simulation results are shown in Fig. 9 a, b, and we can see that the agreement between experiments and simulations is very satisfactory. The obtained values for all the unknown parameters are reported in Table 4 under P2.

Let us first analyze the simulation results for W and pH corresponding to H_2SO_4 , which involve only two fitting parameters, K_{HL} and $F_{0,H}$. It is seen in Fig. 9 that the three W and three pH values have been excellently simulated. However, the obtained association constant of $-COO^-$ with H^+ (K_{HL} in Table 4), is unreasonably large, equal to 4.0×10^6 L/mol, which is almost two orders of magnitude larger than the typical value of 2×10^4 – 6.3×10^4 L/mol for the association of $-COO^-$ with H^+ when $-COO^-$ is present at the end of a polymer chain [30, 37, 41]. Such an extremely large K_{HL} value indicates that the consumption of H^+ ions is more than the association equilibrium requires. We believe that this is a consequence of the presence of PAA chains, which are in the collapsed state in the H_2SO_4 solution. The protonated carboxylic groups ($-COOH$) are buried in the collapsed layer and do not participate in the association equilibrium. Because this protonated “dead” $-COOH$ state consumes a lot of H^+ ions, one has to increase the K_{HL} value to compensate for the consumed H^+ in order to fit the measured pH values. The hydration force constant $F_{0,H}$ in the presence of H_2SO_4 is much larger for P2 than for P1 (as shown in Table 4), signifying that even in the collapsed state at such low pH, the PAA brushes lead to an increase in surface hydrophilicity as a result of the polar nature of carboxylic acid.

Using NaCl as destabilizer, because the W values in Fig. 9 were measured at different pH values (tuned using H_2SO_4), the association of $-COO^-$ with H^+ is also involved. In the simulations, we directly applied the value for the association constant of $-COO^-$ with H^+ , K_{HL} , obtained in the case where H_2SO_4 was used as destabilizer. Thus, we have only two fitting parameters, $F_{0,Na}$ and K_{NaL} . The obtained value for K_{NaL} , the association constant of $-COO^-$ with Na^+ , is equal to 2.80 L/mol (Table 4). This value is comparable with the value of 2.65 L/mol estimated for perfluoropolyether-based carboxylic groups in another work [8]. It

Fig. 10 Hydration force constant $F_{0,\text{Na}}$ for P2 latex as a function of pH, estimated from W simulations using NaCl as the destabilizer at $\phi = 5.0 \times 10^{-2}$



is interesting to see that the estimated value for the hydration force constant, $F_{0,\text{Na}}$ as shown in Fig. 10, increases as pH increases. This indicates that, as pH increases, more carboxylic groups are deprotonated and the surface becomes more polar (i.e., more hydrophilic). However, such an explanation is inconsistent with the results of previous work [41], where we simulated the W values of a colloidal system stabilized by fixed carboxylic groups, but not PAA (previously measured at pH 3–10 by Behrens et al. [44]). It was found that, using the generalized stability model accounting for only the DLVO colloidal interactions, we can describe the system stability behavior in the entire range of pH 3–10, without even introducing the hydration force. This means that carboxylic acid when deprotonated acts mainly as a charge group contributing to electrostatic repulsion, and that its contribution to the hydration force is not substantial. Thus, the increase in $F_{0,\text{Na}}$ with pH (Fig. 10) cannot be explained by the hydration force. Instead, we believe that this results from the steric force of the PAA chains, which, as pH increases, become more stretched and contribute more and more to particle stability. Because steric interactions are not included in our model, they are naturally lumped into the hydration force, leading to an increase in $F_{0,\text{Na}}$ with pH.

Based on the above discussion, we can explain why the $F_{0,\text{H}}$ value at very low pH (<1) in Table 4 is larger than the $F_{0,\text{Na}}$ values at pH ~ 2 in Fig. 10 by considering that the protonated $-\text{COOH}$ contributes to the hydration force, but the deprotonated $-\text{COO}^-$ does not. At pH 2, the amount of $-\text{COOH}$ is reduced and the hydration force is reduced. Of course, the increase in deprotonated $-\text{COO}^-$ (as well as $-\text{SO}_4^-$) groups contributes to electrostatic repulsion, which has a dominant effect on W . In fact, the W values in the case of NaCl at pH 1.87 and 2.58 are larger than those for H_2SO_4 at pH < 1 (Fig. 9a).

Using the established generalized stability model, we calculated the surface charge density and potential (σ_0 and ψ_0) as functions of the concentration of total added salts ($\text{H}_2\text{SO}_4 + \text{NaCl}$), C_s . The conditions corresponded to those for the five sets of experiments shown in Fig. 9a, b, and the results are shown in Fig. 11a, b. It is seen that for pH < 3, the variations in σ_0 and ψ_0 with C_s in Fig. 11b are very similar to those in Fig. 8a, b for P1 latex. This is because at low pH most of the $-\text{COO}^-$

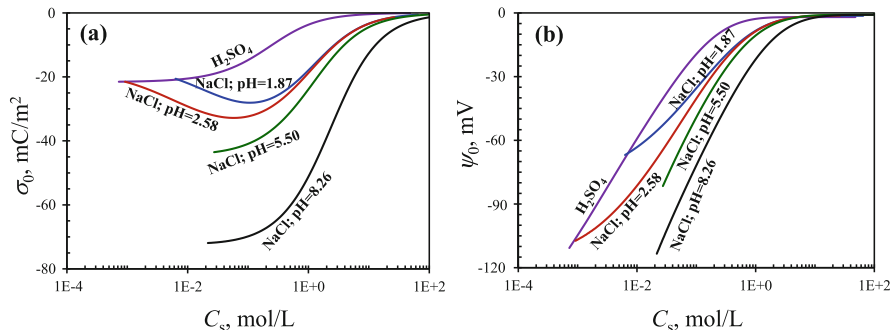


Fig. 11 Surface charge density σ_0 and surface potential ψ_0 computed from the generalized stability model using the estimated parameters in Table 4, for P2 latex at $\phi = 5.0 \times 10^{-2}$, destabilized by NaCl and H_2SO_4

groups are protonated and the surface charge mainly comes from $-SO_4^-$, which is practically the same for P1 and P2 latexes. As pH increases, the surface charge density and potential increase as a result of the increase in $-COO^-$ groups.

4 Concluding Remarks

We have reviewed the generalized stability model developed in recent years [8] and particularly its application to various polymer colloids. The stability of a colloidal system is not only determined by the DLVO colloidal interactions but is also affected by the interplay of other physicochemical processes such as surfactant adsorption equilibrium on the particle surface, association equilibria of the surface charges with counterions involved in the system, and non-DLVO colloidal interactions. The generalized stability model can account simultaneously for such complex interplay between different processes. The model has been successfully validated through its application to different polymer colloids produced from industrial polymerization processes, and its powerful capacity to describe the stability of complicated colloidal systems demonstrated.

Various processes are involved in the model and therefore the model parameters need to be defined. The values of some of the parameters are reported in the literature, and values for the remaining unknown parameters are required. We propose that their values be estimated through application of the model to fit ad hoc experiments, such as the value of the Fuchs stability ratio as a function of salt concentration, the CCC values of different types of salts, etc. Once all the parameters are defined, the established model can be used to analyze in detail how the interplay between different processes affects the stability of the system.

From application of the generalized stability model to different polymer colloids, we have demonstrated that the interplay between various physicochemical processes is substantial. Such interplay can result in very different (peaked or

monotonic) tendencies of the surface charge density and different surfactant partitioning between the particle surface and the bulk disperse medium, with respect to changes in the ionic strength, counterion type, pH, etc. Therefore, the generalized stability model can be used as a reliable tool for understanding and defining suitable conditions for obtaining the desired stability during the production and application of polymer colloids for both industrial practice and academic purpose.

Acknowledgements Financial support from the Swiss National Science Foundation (Grant No. 200020_165917) is gratefully acknowledged.

References

1. Israelachvili JN (1991) *Intermolecular and surface forces*, 2nd edn. Academic, London
2. Hunter RJ (2001) *Foundations of colloid science*. Oxford University Press, New York
3. Ninham BW, Yaminsky V (1997) Ion binding and ion specificity: the Hofmeister effect and Onsager and Lifshitz theories. *Langmuir* 13:2097–2108
4. Ruckenstein E, Manciu M (2003) Specific ion effects via ion hydration: II. Double layer interaction. *Adv Colloid Interf Sci* 105:177–200
5. Kunz W, Lo Nostro P, Ninham BW (2004) The present state of affairs with Hofmeister effects. *Curr Opin Colloid Interface Sci* 9:1
6. Manciu M, Ruckenstein E (2004) The polarization model for hydration/double layer interactions: the role of the electrolyte ions. *Adv Colloid Interf Sci* 112:109
7. Parsegian VA, Zemb T (2011) Hydration forces: observations, explanations, expectations, questions. *Curr Opin Colloid Interface Sci* 16:618–624
8. Jia ZC, Gauer C, Wu H, Morbidelli M, Chittofrati A, Apostolo M (2006) A generalized model for the stability of polymer colloids. *J Colloid Interface Sci* 302:187–202
9. Leikin S, Parsegian VA, Rau DC, Rand RP (1993) Hydration forces. *Annu Rev Phys Chem* 44:369–395
10. Grahame DC (1947) The electrical double layer and the theory of electrocapillarity. *Chem Rev* 41:441–501
11. Bloch JM, Yun W (1990) Condensation of monovalent and divalent metal ions on a Langmuir monolayer. *Phys Rev A* 41:844
12. Lucassen-Reynders EH (1981) *Anionic surfactants: physical chemistry of surfactant action*. Marcel Dekker, New York
13. Zhu B-Y, Gu T (1991) Surfactant adsorption at solid-liquid interfaces. *Adv Colloid Interf Sci* 37:1–32
14. Mclaughlin S, Mulrine N, Gresalfi T, Vaio G, Mclaughlin A (1981) Adsorption of divalent cations to bilayer membranes containing phosphatidylserine. *J Gen Physiol* 77:445–473
15. Koopal LK, Goloub T, De Keizer A, Sidorova MP (1999) The effect of cationic surfactants on wetting colloid stability and flotation of silica. *Colloid Surf A Physicochem Eng Asp* 151:15–25
16. Israelachvili JN (2011) *Intermolecular and surface forces*, 3rd edn. Academic Press, San Diego
17. Faraudo J, Bresme F (2005) Origin of the short-range, strong repulsive force between ionic surfactant layers. *Phys Rev Lett* 94:077802
18. Boström M, Williams DRM, Ninham BW (2001) Specific ion effects: why DLVO theory fails for biology and colloid systems. *Phys Rev Lett* 87:168103

19. Valle-Delgado JJ, Molina-Bolivar JA, Galisteo-Gonzalez F, Galvez-Ruiz MJ, Feiler A, Rutland MW (2005) Hydration forces between silica surfaces: experimental data and predictions from different theories. *J Chem Phys* 123(3):034708
20. Sader JE, Carnie SL, Chan DYC (1995) Accurate analytic formulas for the double-layer interaction between spheres. *J Colloid Interface Sci* 171:46–54
21. Runkana V, Somasundaran P, Kapur PC (2005) Reaction-limited aggregation in presence of short-range structural forces. *AIChE J* 51:1233–1245
22. Derjaguin VB (1934) Studies on friction and adhesion IV. Theory of adhering small particles. *Kolloid-Z* 69:155–164
23. Wu H, Tsoutsoura A, Lattuada M, Zaccone A, Morbidelli M (2010) Effect of temperature on high shear-induced gelation of charge-stabilized colloids without adding electrolytes. *Langmuir* 26:2761–2768
24. Spielman LA (1970) Viscous interactions in Brownian coagulation. *J Colloid Interface Sci* 33:562
25. Honig EP, Roeberson GJ, Wiersema PH (1971) Effect of hydrodynamic interaction on the coagulation rate of hydrophobic colloids. *J Colloid Interface Sci* 36:97
26. Manciu M, Ruckenstein E (2001) Role of the hydration force in the stability of colloids at high ionic strengths. *Langmuir* 17:7061–7070
27. Manciu M, Ruckenstein E (2003) Specific ion effects via ion hydration: I. Surface tension. *Adv Colloid Interf Sci* 105:63
28. Huang H, Manciu M, Ruckenstein E (2005) On the restabilization of protein-covered latex colloids at high ionic strengths. *Langmuir* 21:94–99
29. Sinha P, Szilagyí I, Montes Ruiz-Cabello FJ, Maroni P, Borkovec M (2013) Attractive forces between charged colloidal particles induced by multivalent ions revealed by confronting aggregation and direct force measurements. *J Phys Chem Lett* 4:648–652
30. Martell AE, Smith RM (1989) Critical stability constants. Plenum, New York
31. Maeda M, Iwata T (1997) Dissociation constants of ammonium ion and activity coefficients of ammonia in aqueous ammonium sulfate solutions. *J Chem Eng Data* 42:1216–1218
32. Chittofrati A (2005) Self-association of model perfluoropolyether carboxylic salts internal report. Solvay, Bollate
33. Thompson DW, Collins IR (1994) Electrolyte-induced aggregation of gold particles on solid surfaces. *J Colloid Interface Sci* 163:347–354
34. Evans DF, Wennerström H (1999) The colloidal domain: where physics, chemistry, biology, and technology meet, 2nd edn. Wiley-VCH, Weinheim
35. Lattuada M, Wu H, Sandkühler P, Sefcik J, Morbidelli M (2004) Modelling of aggregation kinetics of colloidal systems and its validation by light scattering measurements. *Chem Eng Sci* 59:1783
36. Wu H, Xie J-J, Morbidelli M (2005) Kinetics of cold-set diffusion-limited aggregations of denatured whey protein isolate colloids. *Biomacromolecules* 6:3189–3197
37. Jia ZC, Wu H, Morbidelli M (2007) Application of the generalized stability model to polymer colloids stabilized with both mobile and fixed charges. *Ind Eng Chem Res* 46:5357–5364
38. Fox MA, Whitesell JK (1997) Organic chemistry. Jones And Bartlett, Boston
39. Maron SH, Elder ME, Ulevitch IN (1954) Determination of surface area and particle size of synthetic latex by adsorption I. latices containing fatty acid soaps. *J Colloid Sci* 9:89
40. Zaccone A, Wu H, Lattuada M, Morbidelli M (2008) Correlation between colloidal stability and surfactant adsorption/association phenomena studied by light scattering. *J Phys Chem B* 112:1976–1986
41. Ehrl L, Jia ZC, Wu H, Lattuada M, Soos M, Morbidelli M (2009) Role of counterion association in colloidal stability. *Langmuir* 25:2696–2702
42. Jaquet B, Wei D, Reck B, Reinhold F, Zhang X, Wu H, Morbidelli M (2013) Stabilization of polymer colloid dispersions with pH-sensitive poly-acrylic acid brushes. *Colloid Polym Sci* 291:1659–1667

43. Pashley RM (1981) Hydration forces between mica surfaces in aqueous-electrolyte solutions. *J Colloid Interface Sci* 80:153–162
44. Behrens SH, Christl DI, Emmerzael R, Schurtenberger P, Borkovec M (2000) Charging and aggregation properties of carboxyl latex particles: experiments versus DLVO theory. *Langmuir* 16:2566–2575

Morphology of Composite Polymer Latexes: An Update on Synthesis and Applications, Modeling, and Characterization



Shaghayegh Hamzehlou and Jose Ramon Leiza

Abstract Polymer latexes are used in a wide range of technological and industrial products. Polymer–polymer and polymer–inorganic composite (hybrid) latexes have found specific applications in coatings, adhesives, impact modifiers, and medical diagnostics, among others. Control of latex particle morphology is a key factor to achieve a desired application in structured polymer latex particles. Fundamental knowledge of the effects of different synthetic routes and reaction parameters such as temperature, glass transition temperature, and functional groups is vital to obtain the required morphology of polymer–polymer and polymer–inorganic hybrids. Subsequently an unambiguous characterization of particle morphology is essential, which requires determining the shape of the particles, the surface composition, and the internal composition. In this review, we focus on the most recent developments (of the last 5 years) in the synthesis and application of composite (hybrid) latex particles, including polymer–polymer and polymer–inorganic latex systems. Furthermore, we discuss the most recent modeling efforts to simulate the development of particle morphology in composite polymer latexes synthesized by (mini)emulsion polymerization and the latest advances and improvements in characterization techniques to determine the morphology of composite polymer latexes.

Keywords Characterization • Composite • Emulsion • Latex • Mathematical model • Particle morphology • Polymer hybrid • Polymerization

S. Hamzehlou (✉) and J.R. Leiza (✉)
POLYMAT, Kimika Aplikatua saila, Kimika Zientzien Fakultatea, University of the Basque Country (UPV/EHU), Joxe Mari Korta Zentroa, Tolosa Hiribidea 72, 20018 Donostia/San Sebastián, Spain
e-mail: shaghayegh.hamzehlou@ehu.eus; jrleiza@ehu.eus

Contents

| | | |
|-----|--|-----|
| 1 | Introduction | 106 |
| 2 | Hybrid Polymer–Polymer Particles | 107 |
| 2.1 | Core–Shell Particles | 107 |
| 2.2 | Hollow Latex Particles | 109 |
| 2.3 | Nonequilibrium Morphologies | 111 |
| 3 | Hybrid Polymer–Inorganic Particles | 115 |
| 4 | Modeling the Morphology of Composite Latex Particles | 123 |
| 5 | Characterization Methods for Particle Morphology | 124 |
| 6 | Concluding Remarks | 134 |
| | References | 135 |

1 Introduction

Polymer latexes are used in a myriad of relevant technological and industrial products, such as synthetic rubber, coatings, paints, adhesives and sealants, additives in paper and textiles, impact modifiers for thermoplastic matrices, additives in concrete, drug delivery, cosmetics, and flocculants [1–3]. Polymer–polymer and polymer–inorganic composite (hybrid) latexes demonstrate the possibility of combining the positive properties of each phase and avoiding their drawbacks. Such hybrids have found applications in coatings, adhesives, impact modifiers, and medical diagnostics [4–14].

Many works have attempted to synthesize structured polymer latex particles with tailored particle morphologies to meet specific application requirements. Sundberg and Durant [12] and Reyes et al. [11] have summarized these works in two good reviews in 2003 and 2013, respectively. Sundberg and Durant reviewed the most important characterization techniques employed to determine the morphology of composite particles, as well as the most important considerations for producing equilibrium and nonequilibrium morphologies, analyzing the conditions and reaction parameters that lead to either type of morphology. They also discussed the effect of polar carboxylic acid comonomers on the morphology of particles obtained using emulsion polymerization and briefly reviewed works dealing with the morphologies achieved in polymer–polymer hybrid latexes.

Reyes et al. [11] presented the physical and chemical methods used to produce structured polymer particles, distinguishing two-phase polymer–polymer and polymer–inorganic latex systems. They also discussed multiphase polymer latexes and described a Monte Carlo model to predict the equilibrium morphology, and a stochastic dynamic simulation to predict the dynamic evolution of particle morphology for multiphase (polymer–polymer and polymer–inorganic) waterborne systems. The correlation between particle morphology and film morphology was also considered in this review paper.

More recently, Paulis and Asua [15] addressed the knowledge-based production of waterborne hybrid materials, with special emphasis on particle morphology because of the strong impact of this property on final application. They concluded

that mathematical models able to predict particle morphology are essential for implementation of an optimal strategy to produce composite latexes with a defined morphology, because there are no devices capable of on-line monitoring of particle morphology. The authors proposed use of mathematical models for the development of particle morphology as a soft sensor to guide and design advanced control strategies. They reviewed the state of the art of mathematical models for polymer–polymer and polymer–inorganic systems and critically analyzed the drawbacks and improvements required to enable these models to be used in the control strategies.

In this article, we aim to update the most recent developments (of the last 5 years) on the synthesis and application of composite (hybrid) latex particles, including polymer–polymer and polymer–inorganic latex systems. Furthermore, we discuss the most recent modeling efforts to simulate the development of particle morphology in composite polymer latexes synthesized by (mini)emulsion polymerization and the latest advances and improvements in characterization techniques to determine the morphology of composite polymer latexes.

2 Hybrid Polymer–Polymer Particles

Structured polymer particles with different morphologies can be synthesized by chemical methods such as seeded emulsion polymerization and miniemulsion polymerization or by physical methods such as heterocoagulation and solvent evaporation [11, 16]. The choice of a specific technique depends on the final properties of interest of the material. Seeded emulsion polymerization is suitable for synthesizing polymer–polymer particles. Miniemulsion polymerization is much more versatile than seeded emulsion polymerization and allows the synthesis of both polymer–polymer and polymer–inorganic hybrids with a great variety of morphologies [17, 18]. We present the most relevant works that report composite polymer–polymer particles, including core–shell, hollow, and nonequilibrium morphologies.

2.1 Core–Shell Particles

Core–shell particles are synthesized to combine the properties of the core and shell polymers to achieve a certain application. Often, core–shell morphologies of latex particles are claimed by the sole fact that a two-stage batch or semibatch emulsion polymerization is conducted. However, obtaining particles with core–shell morphologies (being strict in the consideration of the morphology) is difficult [19] because, normally, a substantial amount of interface material composed of the two polymeric phases is obtained, not a totally phase-separated morphology.

Core–shell particles with hard/soft, soft/hard, hydrophilic/hydrophobic, and hydrophobic/hydrophilic phases have been reported [11, 12]. These types of core–shell latexes have applications in high-performance coatings, impact modifiers for brittle polymers, photonic crystals, and electrical conductive films, to name a few.

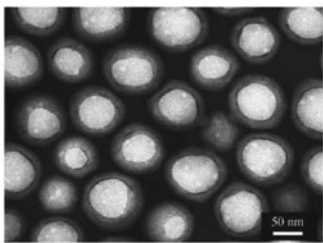
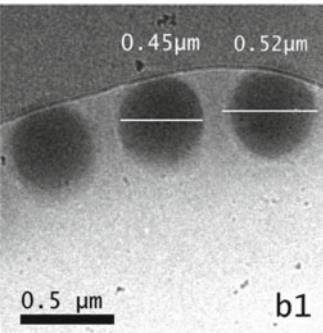
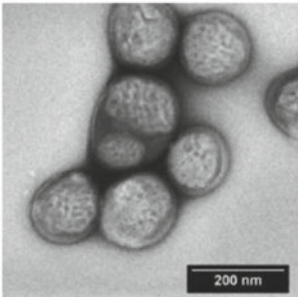
| Polymers | TEM Image/CryoTEM Image | Reference |
|---|--|-----------|
| Fluorinated polyacrylate/polyacrylate |  | 20 |
| Crosslinked poly(styrene-co-butyl acrylate)/poly(styrene-co-butyl acrylate) |  | 22 |
| Polyacrylate/PU |  | 27 |

Fig. 1 Representative TEM images of the core-shell morphologies discussed in the text (Images reproduced with permission from the references in the table)

Shells with specific properties can be used to meet specific application demands, such as water/oil repellence in fluorinated polymer coatings. Because fluorinated polymers are costly, it is desired that the fluorinated part forms a complete shell around the particle. Methylacryloyloxy-2-hydroxypropyl perfluorooctanoate (FGOA) monomer is a fluorinated acrylate monomer with both hydrophilic and hydrophobic groups, and has been used to copolymerize with acrylate monomers in a two-stage emulsion polymerization to synthesize the core-shell particles with fluorinated groups covalently bonded in the shell [20] (Fig. 1). Fluorinated polymers have also been used in photocatalytic paint formulations to improve the low resistance

of acrylic polymers to UV radiation and weathering. Core-shell latex particles with poly(vinylidene fluoride-*co*-hexafluoropropene) core and acrylate shell combine both UV and weathering resistance with low minimum film formation properties [21].

Acrylate emulsion-based adhesives have the disadvantage of low cohesive properties. Structured core-shell particles of poly(styrene-*co*-butyl acrylate) [P(S-*co*-BA)] with crosslinked and harder cores exhibit both high cohesive and high adhesive strength [22] (Fig. 1). The crosslinked core is responsible for the cohesive strength, whereas the softer shell maintains the adhesive properties. It has been shown that the ratio between core and shell has an important effect on the balance between adhesive and cohesive strengths. Another strategy to improve the adhesive properties of acrylate emulsion-based adhesives is to utilize the excellent properties of polyurethane (PU), such as high cohesive strength and solvent resistance by producing hybrid acrylic/PU composite latexes. Hybrid PU/acrylic latexes can be synthesized by miniemulsion polymerization following two different polymerization approaches. The first approach is simultaneous free-radical and addition polymerization in miniemulsion droplets that contain the main acrylic comonomers plus diisocyanate, chain extenders, and hydroxymethyl methacrylate (HEMA, which can participate in both free-radical and addition polymerizations grafting the acrylic and PU chains) [23–26]. The second approach is to produce PU in an acrylate mixture containing HEMA (to introduce double bonds into the PU to have a grafting degree equivalent to 10% of the NCO functions) and chain extender, and then miniemulsify this organic phase to yield miniemulsion droplets that polymerize [27]. The first approach yields particles of homogeneous morphology and enhanced adhesive properties for PU contents below 15 wt%. The second approach yields particle morphologies that evolve from homogenous particles to core-shell structures (with PU-rich occlusions in the acrylic core) by increasing the PU weight fraction from 5 to 50%. The core-shell morphology persists in the adhesive films, resulting in a percolating network of stiffer PU-rich shells [27] (Fig. 1).

2.2 *Hollow Latex Particles*

Hollow particles are generally synthesized from core-shell particles through removing the core material by dissolution or calcination [28]. Hollow particles have found applications as opacifiers in coatings. The hollow latex particles can be filled with a material to be released in a controlled manner [15]. This characteristic makes them especially suitable for drug delivery applications. Hollow latex particles were synthesized from poly(methacrylate-*co*-methacrylic acid)/poly(methacrylic acid-*co*-*N*-isopropylacrylamide) core-shell particles by heating the latex in the presence of ammonia solution. These particles showed thermo- and pH-sensitive behavior, with the ability to load a model drug [29] (Fig. 2).

The intermediate core-shell particle has a strong effect on the properties of the final hollow particle. Multilayer particles can also be used as intermediate particles

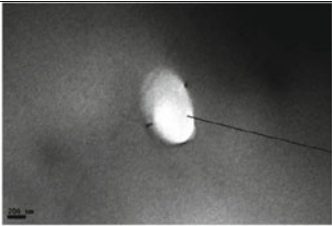
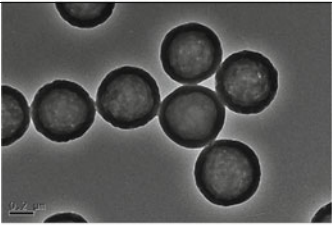
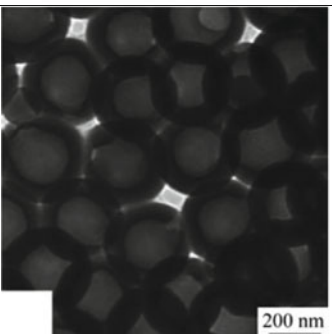
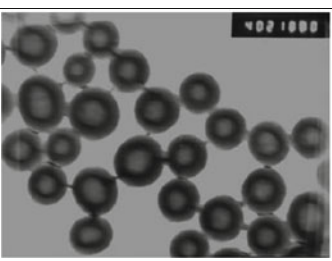
| Polymers | TEM Image/CryoTEM Image | Reference |
|--|---|-----------|
| Poly(methacrylic acid-co-N-isopropylacrylamide) |  | 29 |
| P(MMA-BA-MAA-EGDMA)/P(MMA-St-MAA)/P(St-DVB) |  | 31 |
| Polyacrylate/PS |  | 30 |
| Core(MMA/MAA)/Intermediate layer (MMA/BA/MAA)/Shell(Styrene) |  | 32 |

Fig. 2 Representative TEM images of the hollow particle morphologies discussed in the text (Images reproduced with permission from the references in the table)

to synthesize hollow particles in which the core, intermediate, and shell layer properties (such as shell crosslinking level [30] (Fig. 2)) control the function of the hollow particles. In attempts to synthesize hydrophilic core/hydrophobic shell particles as an intermediate particle, the type and ratio of the unsaturated acid

monomer was a key factor [31]. Deng et al. studied the effect of type of unsaturated acid monomer by using acrylic acid and methacrylic acid. They found that the hydrophilic core/hydrophobic shell particles could be easily formed using methacrylic acid (MAA) instead of acrylic acid (AA). For an MAA content of 12.2 wt% in the core latex preparation, only fine pores existed inside the alkali-treated particles. Increasing MAA content from 20.0 to 30.0 wt%, the alkali-treated particle morphology evolved from a porous hollow structure to a collapsed structure. Increasing MAA content to 40.0 wt% made it difficult to prepare uniform multistage particles. Distinct morphologies such as solid, deficient swelling, hollow, and collapsed structures were coexistent in the alkali-treated particles (Fig. 2). Yuan et al. [32] synthesized core–intermediate layer–shell particles using a three-stage emulsion polymerization. The latexes were exposed to alkali treatment to yield hollow particles. The authors studied the effect of the intermediate layer–core ratios on the morphology and opacity of the hollow latex particles. Interestingly, they showed that ratios in the range of 6–10 present differences in the swelling and opacities of films prepared by blending styrene/acrylic latexes and hollow particles. The best performance in terms of opacity of the films was achieved for an intermediate layer–core ratio of 8 (Fig. 2).

2.3 Nonequilibrium Morphologies

Nonequilibrium morphologies such as occluded particles, raspberry, and multilobed are the result of the hindered movement of clusters caused by the high internal viscosity of the matrix or the second polymer forming the lobes. Using a crosslinked matrix induces phase separation and leads to different nonequilibrium morphologies. The morphology of the nanoparticles depends on the crosslinking density of the phases. However, further processing of these latex particles is a problem because of the high crosslinking level.

In noncrosslinked seeds, specific conditions should be fulfilled to synthesize nonequilibrium morphologies (e.g., multilobed morphology). Recently, Blenner et al. summarized the key factors for achieving a multilobed morphology in polymer–polymer composite polymer latexes synthesized by seeded emulsion polymerization [33]. The first condition is that the second-stage polymer oligoradicals should not penetrate to the seed particles. On the other hand, the seed should be more hydrophilic than the second-stage polymer (i.e., the interfacial tension between water and first-stage polymer should be smaller than the interfacial tension of the second-stage polymer and water). In the case that these two conditions are fulfilled, the particle morphology is controlled by the difference between the glass transition temperature (T_g) of the seed and second-stage polymer and the reaction temperature. The authors examined these factors with a series of well-

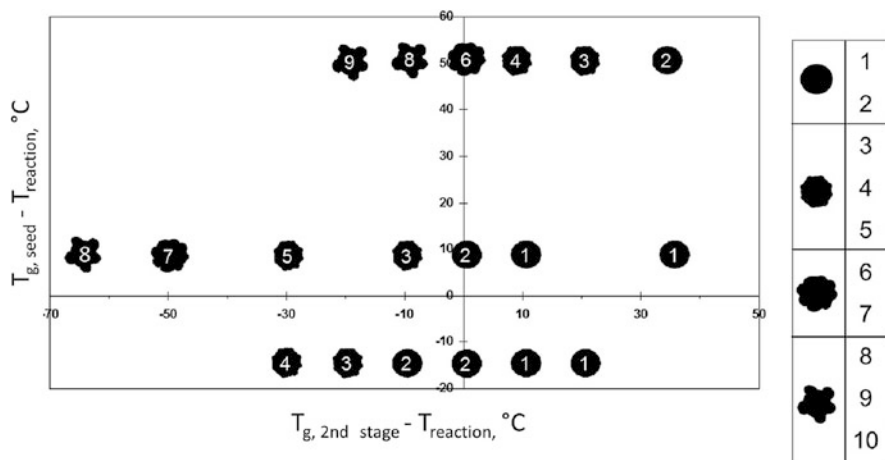


Fig. 3 Multilobed nature of composite particles with P(MMA-*co*-MA) seed polymers and P(styrene-*co*-HMA) second-stage polymer, at various T_g s as compared with reaction temperature. All representations are for stage ratios of 1:1. Nonspherical nature of the particle is ranked in the chart on the right (Reproduced with permission from [33])

defined experiments and summarized the findings in a guiding morphological map (Fig. 3). The map shows that if the second-stage polymer is soft at the reaction temperature (upper and lower left side of the map in Fig. 3), the resulting particle morphology is always multilobed and the size of the lobes changes according to the difference between the T_g of the seed and the reaction temperature. Because the second-stage polymer is soft, the particles can move to create bigger lobes to minimize the interfacial energy of the system. On the other hand, a glassy second-stage polymer stays where it forms and creates a uniform shell around the particles.

Niu et al. [34] synthesized multilobed particles (with low solids content of below 5 wt%) of P(VC-*co*-AAEM)/PS by seeded emulsion polymerization of styrene on a surfactant-free seed made out of vinyl chloride (VC) and acetoacetoxyethyl methacrylate (AAEM). According to the authors, the role of AAEM is to increase the hydrophilicity of the surface of the seed, which controls the nucleation and phase separation of the polystyrene (PS) domains during the seeded emulsion polymerization. The authors found that increasing the amount of AAEM in the seed preparation led to a substantial change in the morphology of the particles, as illustrated in Fig. 4 and the SEM images in Fig. 5. They attributed these differences to different swelling of styrene under low and high concentrations of AAEM on the surface of the particles. Interestingly, the authors followed the morphology of the particles with polymerization time and, for the two lowest AAEM loadings (6 and 12 g per 60 g of VC), the particles exhibited more lobes at early stages (30 min) than after 5 or 8 h of polymerization, and the number of lobes increased with AAEM concentration. However, at the highest concentration of AAEM, lobes were hardly seen during the polymerization. The authors

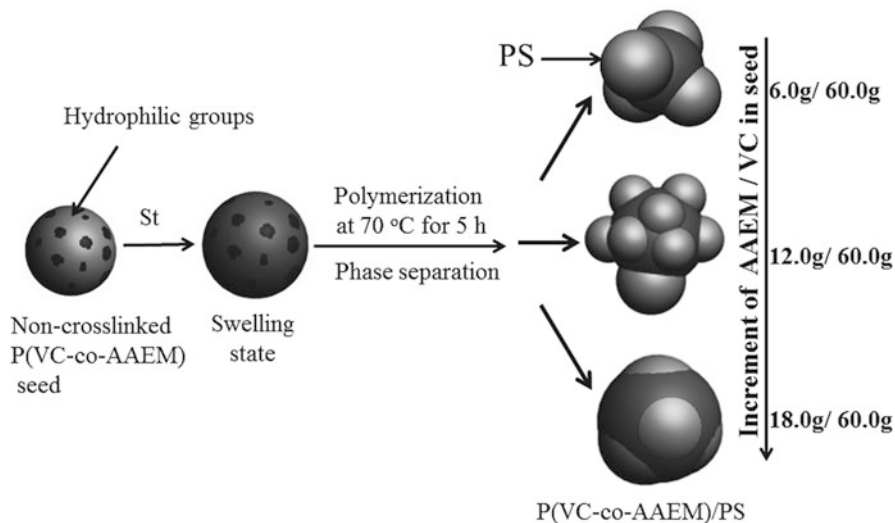


Fig. 4 Synthesis of multilobed P(VC-co-AAEM)/PS nanoparticles (Reproduced with permission from [34])

explained this finding by the formation of a hydrophilic AAEM layer covering the entire surface of the PVC-co-AAEM and swelling of styrene at the interface between the PVC surface and this layer, which phase-separated upon polymerization and led to almost spherical particles.

Li et al. [35] synthesized particles of P(BA-co-MMA)/P(BA-co-MMA-co-acrylate-dodecafluoroheptyl methacrylate-co-AA) with a multilobe (“plum blossom-like”) morphology by a two-stage seeded semibatch emulsion polymerization (see Fig. 5). It was shown that adding a hydrophilic monomer to the shell was responsible for the change in particle morphology from core-shell to multilobe. The authors claimed that acrylic acid shifts polymerization of the second-stage monomers from polymer particle to aqueous phase and that adsorption of oligomers to the surface of the seed particles creates lobed particles at the surface. A more plausible explanation is based on the glass transitions of the polymer phases. The reaction temperature for the morphology achieved is probably that provided by the morphology map proposed by Blenner et al. and depicted in Fig. 3.

Particles with flower-like morphology (see Fig. 5) were synthesized as intermediate particles in an attempt to synthesize phthalate-free flexible PVC. The particles were synthesized by seeded emulsion polymerization of VC, 3-(trimethoxysilyl) propyl methacrylate (MPS, 0–1.5 wt% VC), and allyl methacrylate (AMA, less than 1 wt% VC) in the presence of a crosslinked PBA seed stabilized by sodium dodecyl sulfate emulsifier (PBA/PVC ratio was 6.5:93.5 w/w) [36]. The second-stage polymerization did not use additional surfactant. However, MPS was prehydrolyzed at pH 10–11 and some of the SiOH groups formed could self-condense to form oligomers that might contain two or more methacrylate double

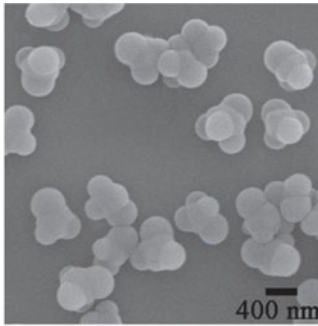
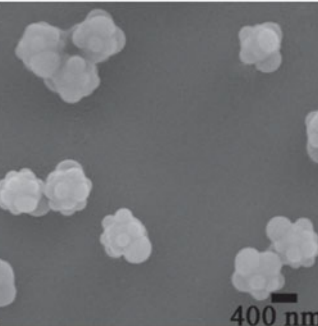
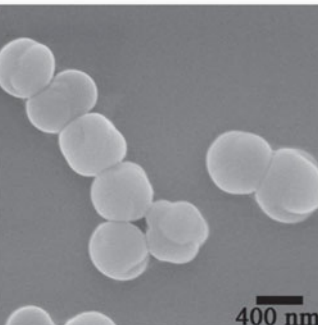
| Polymers | TEM Image/SEM Image | Reference |
|--|--|-----------|
| P(VC- <i>co</i> -AAEM)/PS 6gAAEM per 60 g PVC Reaction time=5 h |  | 34 |
| P(VC- <i>co</i> -AAEM)/PS 12gAAEM per 60 g PVC Reaction time=5 h |  | 34 |
| P(VC- <i>co</i> -AAEM)/PS 16gAAEM per 60 g PVC Reaction time=5 h |  | 34 |

Fig. 5 Representative TEM/SEM images of nonequilibrium morphologies of latexes discussed in the text (Images reproduced with permission from the references in the table)

bonds that could participate in the copolymerization with VC and AMA. The authors found that MPS loadings lower than 0.8 wt% produced spherical particles, but stability of the latex was poor and very large particles (800 nm) were produced. Above this concentration, the morphology of the composite particles showed some irregularities or roughness (the authors called this morphology “flower-like”). The stability of the latex improved with particle sizes in the range of 400 nm. The

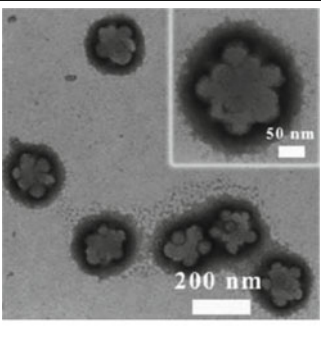
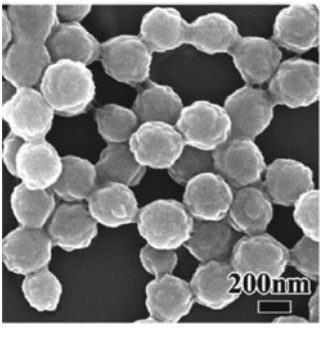
| | | |
|---|---|----|
| P(BA-co-MMA)/P(BA-co-MMA-co-DFMA-co-AA) |  | 35 |
| PBA/PVC |  | 36 |
| | | |

Fig. 5 (continued)

authors attributed formation of the flower-like structure to the adsorption of hydrophilic species derived from the base-catalyzed prehydrolyzed MPS molecules in the aqueous phase to the PBA core surface.

3 Hybrid Polymer–Inorganic Particles

Hybrid polymer–inorganic particles can be synthesized by conventional emulsion, surface-initiated emulsion polymerization, miniemulsion, and suspension polymerization, among other techniques [15, 37–41]. The morphologies of the hybrid polymer–inorganic particles that can be achieved depend not only of the type of polymerization method employed, but also on the aspect ratio of the inorganic material. For instance, encapsulation of high aspect ratio clays (like natural montmorillonite) is elusive and has hardly ever been achieved [42–46].

Two main morphologies are sought for polymer–inorganic composite latexes. On the one hand, encapsulation of the inorganic material inside the polymer particles is important for several applications because it yields a better distribution of the inorganic material, thus reducing aggregation/agglomeration and the amount of inorganic material needed to achieve the same properties (e.g., metal oxides in paint and coating formulations [47–53]). Furthermore, because of its small particle size and potential toxicity, the inorganic material should be protected from the environment. Encapsulation achieves this and makes manipulation and application of the inorganic material (e.g., quantum dots [54–56]) easier.

The second main morphology sought has the inorganic particles at the surface of the polymer particle. This morphology is appropriate for applications where the hybrid polymer particles are used in dispersed form and the inorganic material provides stability to the system (e.g., pollutant degradation in wastewater treatments), and also for applications where the functionality provided by the inorganic material is required at either an air–film or film–substrate interface (e.g., photocatalytic coatings [57, 58]).

Miniemulsion polymerization and surface-initiated emulsion polymerization are the most suitable techniques for producing polymer–inorganic hybrids with an encapsulated morphology [50, 59–62]. The former does not allow the encapsulation of a single inorganic nanoparticle in each polymer particle because of the low probability of efficiently producing monomer miniemulsions with one inorganic particle per monomer droplet. The latter technique is better suited for this purpose and requires inorganic particles to be appropriately modified to initiate polymerization from the surface (reactive groups such as double bonds, thermal initiators, and oligomers end-capped with controlled radical polymerization agents) and to be homogeneously and individually distributed (in the case of layered clays, ideally exfoliated in single layers) in the aqueous phase.

For inorganic particles with high aspect ratios, Reyes et al. [63] and Mballa Mballa et al. [64] were able to encapsulate natural montmorillonite (MMT) clay in a two-stage seeded semibatch emulsion polymerization. In both cases, the seed was prepared in the presence of MMT clay. In the first case, the seed was made by miniemulsion polymerization of VAc stabilized by polyvinyl alcohol with organically modified clay. In the second case, the seed was produced using pristine MMT and MMA monomer by conventional emulsion polymerization. In both cases, only a small fraction of the polymer particles produced contained encapsulated clay, and were of nonspherical shape (see Fig. 6).

Several research groups have used surface-initiated emulsion polymerization to attempt encapsulation of other clays, such as Gibbsite and layered double hydroxide (LDH), following the strategy originally developed by Hawket and coworkers for encapsulating metal oxides [50], multiwalled carbon nanotubes [65], and graphene oxide [66]. Thus, Ali et al. [61] and Loiko et al. [67, 68] adsorbed $(BA)_x-co-(AA)_y$ charged anionic oligomers produced either by RAFT or ATRP polymerization on the surface of the clays. The modified clays were then used as seeds on starved feed

| Polymer-inorganic | TEM Image | Reference |
|--|-----------|-----------|
| PVAc/PVOH/MMT Two stage seeded semibatch EP Seed: Miniemulsion PVAc/PVOH/MMT Feed: VAc | | 63 |
| PMMA/PS/MMT Two stage seeded semibatch EP Seed. PMMA/MMT conventional EP Feed: Styrene | | 64 |
| P(MMA-co-BA)/Gibbsite/(AA-co-BA) Surface initiated EP ATRP oligomers: AA-co-BA | | 68 |
| P(MA-co-BA)/LDH Surface initiated EP RAFT oligomers: AA-co-BA | | 69 |

Fig. 6 Representative TEM morphologies of composite polymer–inorganic latexes with encapsulation of the inorganic material in the polymer particle, as discussed in the text (Images reproduced with permission from references in the table)

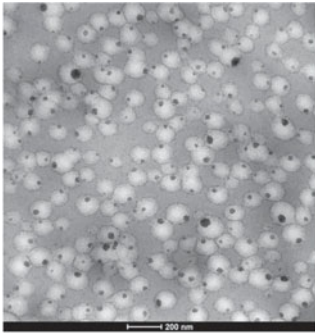
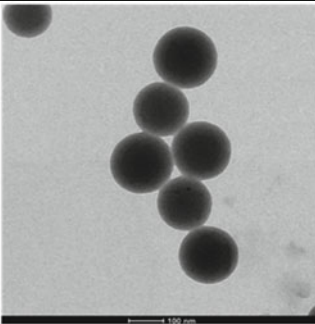
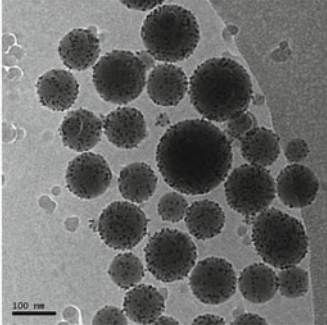
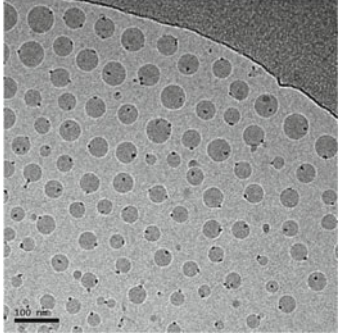
| | | |
|---|---|-------|
| <p>P(MMA-co-BA-AA)/CeO₂</p> <p>Two stage seeded semibatch EP</p> <p>Seed: Miniemulsion P(MMA-co-BA-AA)/ CeO₂</p> <p>Feed: MMA/BA/AA</p> |  | 70 |
| <p>P(S-co-DVB)/P(MMA-co-DVB)/CdSe/CdS</p> <p>Seed: Miniemulsion P(S-co-DVB)/ CdSe/CdS</p> <p>Feed: MMA/DVB</p> |  | 54 |
| <p>P(VDF-co-MA)/CeO₂</p> <p>Surface initiated EP.</p> <p>CeO₂ nanoparticles modified with RAFT oligomers of vinylbenzyl phosphonyl diethyl ester and styrene</p> <p>-----</p> |  | 73,74 |
| <p>P(S-co-MA)/ CeO₂</p> <p>Surface initiated EP.</p> <p>CeO₂ nanoparticles modified with RAFT oligomers of BA-co-AA, BA-co-AMPS, and BA-co-AA-co-AMPS</p> |  | |

Fig. 6 (continued)

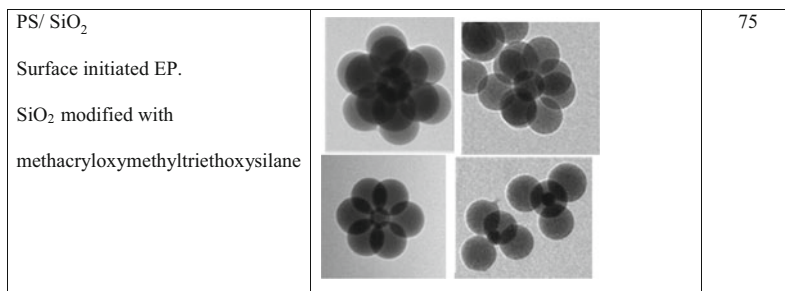


Fig. 6 (continued)

semibatch polymerizations and, depending on the lengths of the hydrophilic and hydrophobic monomers of the oligomers, muffin-like (clay at the polymer particle–aqueous phase interface) or encapsulated morphologies were obtained. In the most recent work of this series [68], the authors demonstrated that using co-oligomer concentrations below the critical micelle concentration, but higher than those required to stabilize the Gibbsite platelets, led to efficient encapsulation of the clay. Every latex particle contained a single Gibbsite platelet, independent of the investigated anionic co-oligomer composition or chain length (see Fig. 6).

Following the same approach described above, Cenacchi Perreira et al. [69] synthesized nanocomposite latex particles containing cationic LDH using BA and AA random oligomers synthesized by RAFT. The oligomers were adsorbed on the clay platelets, then MA and BA were starve-fed to the reactor. Encapsulation of the LDH layers was achieved, but the efficiency was low (a substantial number of the particles did not contain platelets, as seen in Fig. 6) and polymerization could only reach high conversions when hydrolytically stable cationic initiator was used.

Low aspect ratio inorganic nanoparticles (spherical in most cases) have been encapsulated using the two polymerization approaches described above. Aguirre et al. [49, 51, 70–72] encapsulated CeO₂ and ZnO nanoparticles by a two-stage seeded semibatch emulsion polymerization to produce waterborne binders for UV-blocking clear coats. In the first stage, a hybrid seed was produced by batch miniemulsion polymerization using organically modified CeO₂ nanoparticles compatible with the MMA/BA/AA comonomer mixture. The resulting latexes had encapsulated morphologies (a single CeO₂ aggregate per particle), but with the aggregate at the edge of the polymer particle–aqueous phase interface. In the semibatch stage, the seed latex was grown to reach latexes with high solids content (up to 50 wt% solids and up to 5 wt% inorganic material). The CeO₂ aggregates were more centered in the interior of the polymer particle (Fig. 6). A similar approach was used by de San Luis et al. [54] to encapsulate octadecylamine-modified CdSe/ZnS quantum dots (QDs) in a two-stage seeded semibatch emulsion polymerization. In this case, the seed was prepared by miniemulsion polymerization of styrene/divinyl benzene (DVB) because it was more compatible with the octadecylamine used to modify the surface of the QDs.

In the seed, the QDs were at the edge of the polymer particles. The fluorescence of the seed particles substantially decreased with time because the QDs migrated to the surface and degraded when in contact with water. The semibatch process was carried out using a polymer that was less compatible with the QDs (MMA), with DVB as crosslinker. The morphology of the final hybrid composite particles demonstrated that the QDs were well encapsulated, and the fluorescence of the latexes remained constant for several months, demonstrating that the QDs did not come into contact with water (Fig. 6).

Surface-initiated emulsion polymerization has been used to produce hybrid waterborne latexes with CeO₂ [73, 74]. In the first work by Garnier et al. [73], BA-co-AA, BA-co-AMPS (2-acrylamido-2-methyl propane sulfonic acid) and BA-co-AA-co-AMPS RAFT oligomers were adsorbed on the surface of CeO₂ nanoparticles dispersed in water. Then, starved feed semibatch emulsion polymerization of S/MA was carried out to produce hybrid latexes. The best compromise, considering the high efficiency of hybrid particle formation and a good distribution of CeO₂ nanoclusters between latex particles, was a combination of BA, AA, and AMPS units in the RAFT oligomer. Snowman-like hybrid particles with a cluster of several CeO₂ nanoparticles at the edge of the polymer particle were produced. In the second work [74], the authors used the same surface-initiated strategy for P(VDF-co-MA) latexes, employing RAFT oligomers made of vinylbenzyl phosphonyl diethyl ester and styrene. The 25 wt% solids hybrid latex particles contained a large number of CeO₂ nanoparticles sitting on the surface of the polymer particles or partly engulfed, which differed substantially from the morphologies of the first work (see Fig. 6).

Desert et al. [75] also used surface-initiated polymerization to produce PS/SiO₂ hybrid latexes. The surface of the SiO₂ nanoparticles was first modified with methacryloxymethyltriethoxysilane (MMS) and then styrene was polymerized on the SiO₂ modified seeds. Interestingly, tuning the diameter and concentration of the silica seeds gave homogeneous batches of tetrapods, hexapods, octapods, nonapods, and dodecapods with yields as high as 80% (Fig. 6). The PS/SiO₂ hybrid latexes with tetrapod morphology were used to produce robust clusters of gold satellites positioned with tetrahedral symmetry on the surface of a patchy silica core by adsorption and growth of gold on the patches [76].

The inorganic particles can be attached to the surface of the polymer particle using either emulsion or miniemulsion polymerization. It is important to favor the affinity of the inorganic particle to the polymer particle. This can be achieved by increasing the ionic strength of the medium or by using monomers that can specifically interact with the surface of the inorganic particle. As discussed above, surface location of the inorganic particles is interesting because an additional functionality can be provided to the polymer particles or resulting films. Additionally, the inorganic nanoparticles can provide colloidal stability (Pickering stabilization) to the system and, hence, avoid (or substantially reduce) the use of conventional surfactants, which are responsible for undesired film properties such as water sensitivity and water uptake. The most common inorganic materials used for Pickering stabilization are clays and silica, but other inorganic

nanoparticles such as ZnO, magnetite, CeO₂, TiO₂, and graphene oxide have been used [77–84]. Here, only some recent representative examples are discussed. Bonnefond et al. [85] successfully synthesized low solids content surfactant-free Pickering-stabilized S/BA/MMT hybrid latexes (see Fig. 7) using a functional comonomer [a phosphate ester of poly(ethyleneglycol) monomethacrylate] to improve the interaction between polymer and clay, thus allowing the clay platelets to adhere to the surface of the polymer particles. The films made out these latexes showed lower water absorption and water vapor permeation rates than their counterparts synthesized in absence of the functional monomer.

González et al. [57] synthesized photoactive self-cleaning polymer coatings made of hybrid latexes Pickering-stabilized with TiO₂ nanoparticles. Miniemulsion polymerization, using hydrophobically modified TiO₂ as the sole stabilizer, was used to produce hybrid latexes made of MMA/BA. The hybrid latexes were used to coat concrete specimens and it was shown that the coated films were able to degrade Rhodamine B under UV light. Gonzalez-Matheus et al. [86] synthesized Pickering-stabilized PVAc latexes using hydrophobically modified SiO₂ as the sole stabilizer by miniemulsion polymerization. They obtained coagulum-free latexes with 50 wt % solid content, with over 90 wt% incorporation of silica and better salt tolerance than latexes stabilized with conventional emulsifiers.

More recently, polymer–inorganic multifunctional hybrid particles with more than one type of inorganic material incorporated into the polymer particles have been synthesized. One of the inorganic materials is located at the surface (as in the Pickering-stabilized systems) and the other is encapsulated in the polymer particle.

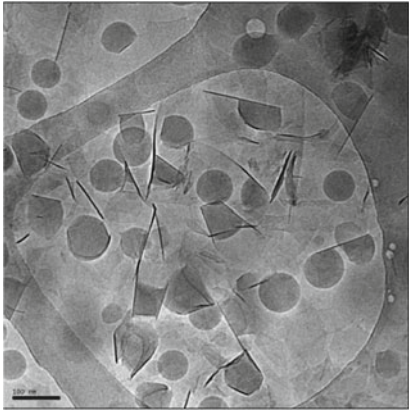
| Polymer-inorganic | TEM/STEM Image | Reference |
|--|---|-----------|
| P(BA-co-S)/NaMMT Surfactant free emulsion polymerization using SIPOMER PAM100 as comonomer |  | 85 |

Fig. 7 Representative TEM/STEM morphologies of polymer–inorganic composite latexes with the inorganic material in the surface of the polymer particles as discussed in the text (Images reproduced with permission from references in the table)

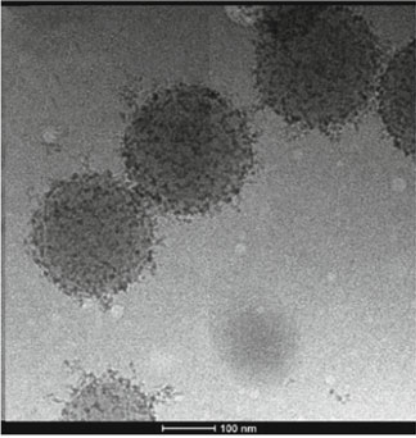
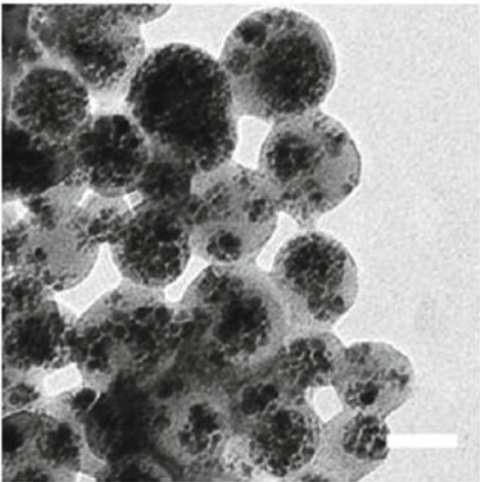
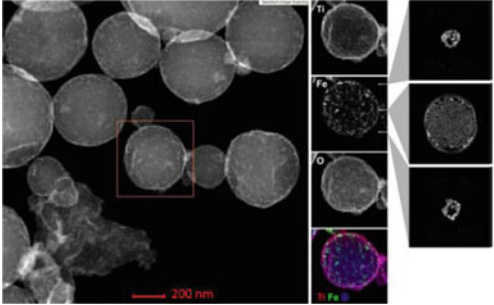
| | | |
|---|---|----|
| <p>P(MMA-co-BA-co-SA)/TiO₂</p> <p>Miniemulsion polymerization</p> |  | 57 |
| <p>PS/Magnetite/CdS</p> <p>Two step process:</p> <p>1. Miniemulsion polymerization</p> <p>S/magnetite using a phosphonate based surfmer</p> <p>2. Crystallization on surface to produce CdS</p> |  | 87 |
| <p>PS/TiO₂/magnetite</p> <p>Miniemulsion polymerization</p> |  | 88 |

Fig. 7 (continued)

Fischer et al. [87] synthesized luminescent and magnetoresponseive multifunctional chalcogenide/polymer hybrid nanoparticles in a two-stage process (see Fig. 7). In the first step, the authors encapsulated oleic acid-modified magnetite nanoparticles in PS particles with phosphonate functionalization, using a phosphonate surfmer in the polymerization. Subsequently, the magnetic and phosphonate-functionalized latex was used to grow cadmium sulfide (CdS) in the surface of the polymer particles to create CdS crystals on the surface of the magnetic PS particles. After three purification steps using solvents or magnetic separation, particles with magnetic and luminescent properties were obtained.

Bonnefond et al. [88] synthesized photocatalytic and magnetic TiO_2 /PS/magnetite hybrid polymer latex particles by one-step Pickering miniemulsion polymerization. The multifunctional composite polymer latex particles can be employed as wastewater decontaminating material to remove harmful compounds from drinking water. TEM images showed that the magnetite nanoparticles were embedded in the polymer particles, whereas the TiO_2 nanoparticles were located on the surface of the particles as Pickering stabilizers. This well-defined morphology guarantees the required contact of photocatalyst with contaminants in the water, minimizes migration of magnetite to the water, and enables easy collection of the particles after the purification process.

4 Modeling the Morphology of Composite Latex Particles

Particle morphology is determined by the interplay between thermodynamics and kinetics, and the underlying fundamental principles are similar for polymer–polymer and polymer–inorganic hybrids. Recently, Paulis and Asua [15] analyzed the most important requirements for the development of knowledge-based strategies for the production of hybrid waterborne polymer dispersions targeting a specific particle morphology. They concluded that the implementation of knowledge-based control strategies requires mathematical models to predict particle morphology to be used as soft sensors. The authors critically reviewed the existing models for polymer–polymer and polymer–inorganic hybrid particles and underlined some of the limitations of these models and the challenges to be overcome in order to use the models in advanced control strategies.

The output of all the existing models developed so far is a very detailed description of the morphology of a single particle, with extremely time-consuming simulations [89–96]. For better statistics, many particles should be simulated but this makes the simulation even longer. Hamzehlou et al. introduced an innovative and fast approach for the prediction of particle morphology of two-phase polymer–polymer hybrids synthesized by seeded emulsion or miniemulsion polymerization [97]. The model can also be easily extended for polymer–inorganic hybrid particles synthesized by miniemulsion polymerization. The advantage of this new method over the existing methodologies is prediction of the dynamics of particle

morphology during the reaction for the whole population of polymer hybrid nanoparticles, in substantially shorter times.

The particle morphology in this approach is described by two cluster size distributions, one for the clusters at the equilibrium positions and another for clusters at nonequilibrium positions. The equilibrium position varies according to the equilibrium morphology. In the case of hemispherical equilibrium morphology, the equilibrium position is the surface of the particles and the nonequilibrium position is within the polymer matrix. The model takes into account relevant kinetic and thermodynamic effects, such as growth of clusters by propagation, diffusion of polymer from the polymer matrix to clusters, cluster coalescence, movement of clusters to the equilibrium position, and nucleation by phase separation. The model also takes into account changes in viscosity and T_g of the reaction medium during polymerization, which affect the evolution of particle morphology. The output of the model is the distribution of the two cluster populations. These distributions can be transformed by a random sampling algorithm to 2D or 3D particle morphology representative images. Because a TEM image is a 2D projection of a 3D image, the contrast that is seen at each coordinate is dependent on the relative amount of each phase. Following this concept, the 3D images from the model were converted to TEM-like images. Figure 8 shows an example of the model output for the evolution of particle morphology during the simulation of a standard seeded semibatch emulsion polymerization with a hemispherical equilibrium morphology. The output of the model consists of a weighted size distribution of equilibrium and nonequilibrium clusters, together with their relevant 3D, 2D, and TEM-like morphology images for six randomly selected particles.

The model was validated by comparison with the experimental results reported by Chen et al. [98] for the polymerization of MMA on a PS seed at 70°C (Fig. 9). The equilibrium morphology predicted upon measuring/calculating the interfacial tensions was hemispherical [98]. The authors reported evolution of the morphology during the reaction, as measured by TEM. Figure 9 presents a comparison of the predicted morphologies and the experimentally observed morphologies. The model was able to predict the glass effect at high conversions of the mentioned polymerization system, which led to insignificant evolution of particle morphology at high reaction conversions.

5 Characterization Methods for Particle Morphology

As described in the previous sections, composite latex particles (either polymer–polymer or polymer–inorganic) can be produced with a wide range of particle morphologies. The resulting particle morphology is a consequence of a number of complex interactions between the chemical and physical characteristic of the heterogeneous polymerization process used for the production of the composite latex (generally, a two-stage semibatch (mini)emulsion polymerization). Unambiguous determination of the morphology achieved at the end of the process is

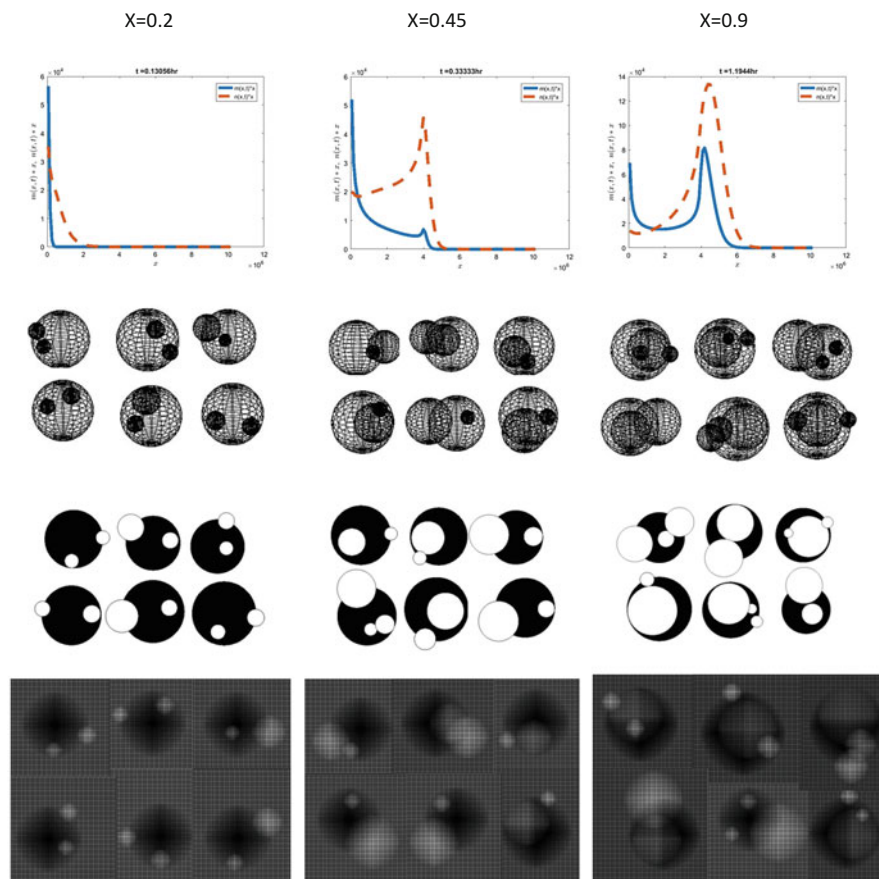


Fig. 8 Conversion evolution of the weighted distribution for equilibrium and nonequilibrium clusters and relevant 3D, 2D, and TEM-like morphology images related to each distribution for six randomly selected particles (Reproduced with permission from [97])

challenging and an accurate determination of the particle morphology is often elusive.

For polymer–polymer composite latexes produced in two-stage semibatch emulsion polymerization processes, Stubbs and Sundberg, in collaboration with other universities and latex producers [19, 99], concluded that, in order to fully specify particle morphology, one need to assess (1) the overall shape of the composite particle, (2) the composition of the polymer present at the particle–water interface (i.e., the surface composition), and (3) the internal structure of the particle. No single experimental technique can provide this full characterization and, hence, several techniques must be combined to achieve a comprehensive understanding of the particle morphology. Artefacts resulting from sample preparation (i.e., staining) or damage during measurement can lead to erroneous interpretation of the

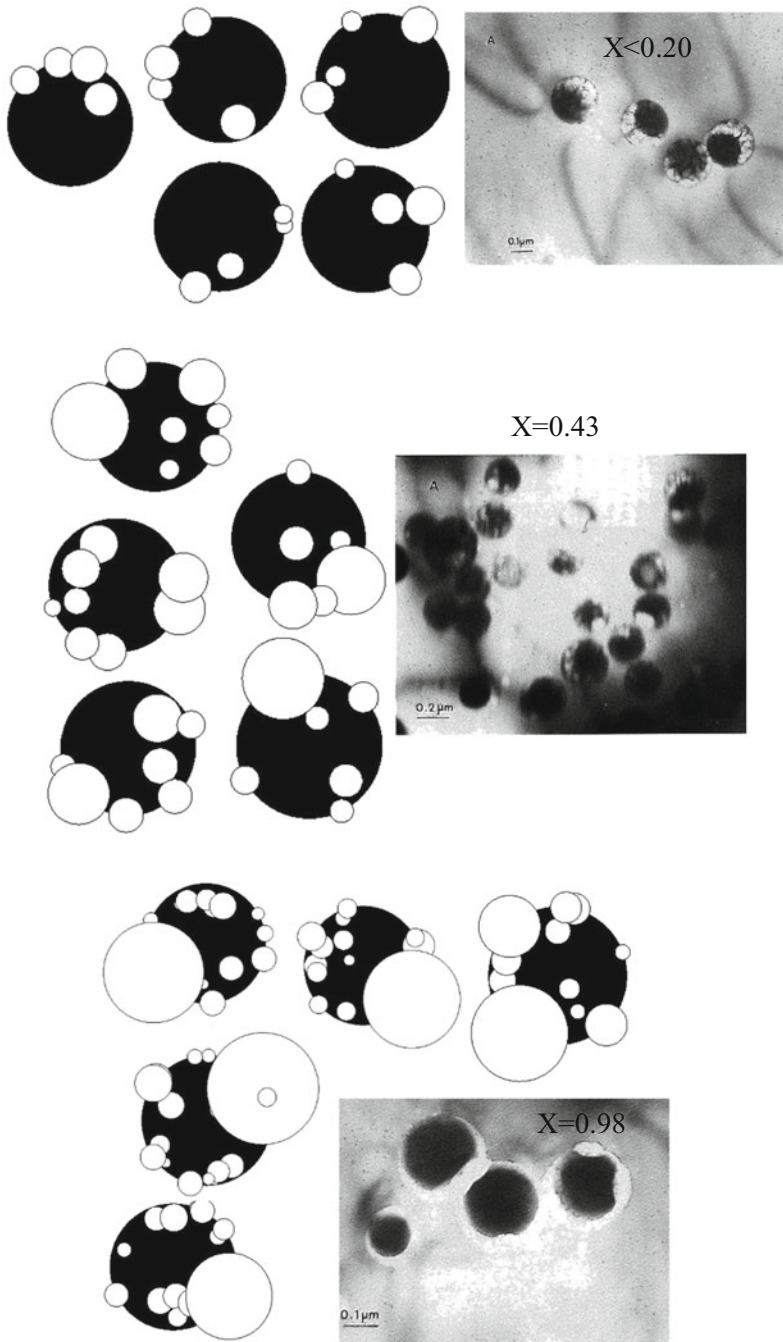


Fig. 9 Comparison of the evolution of particle morphology predicted by the model and the experimental morphology observed by Chen et al. [98] (Reproduced with permission from [97])

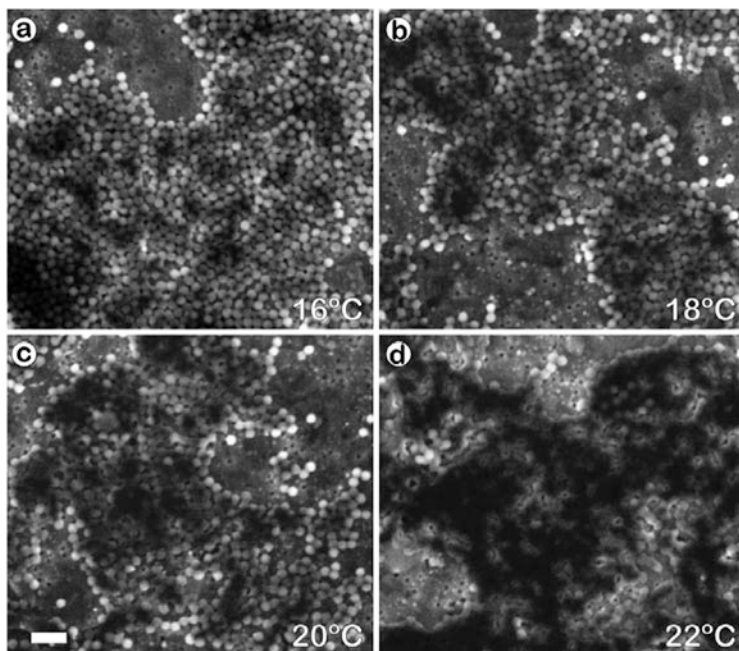
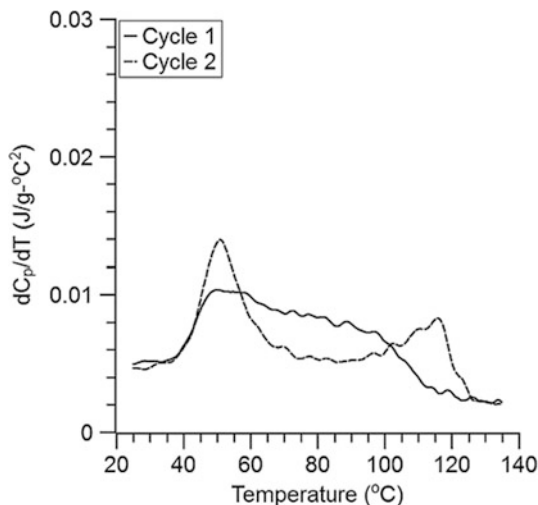


Fig. 10 ESEM images for a latex obtained at different temperatures: (a) 16, (b) 18, (c) 20, and (d) 22°C. In all cases, the pressure was 270 Pa. The length of the *scale bar* is 1 μm (Reproduced with permission from [100])

morphology. In the round-robin study carried out by Stubbs and Sundberg for three different composite particles (with (meth)acrylic and styrene polymers in each phase), the overall shape of the polymer particles was well captured by AFM, SEM, and whole-particle conventional TEM measurements. The particle surface was indirectly determined by the minimum film formation temperature and by surfactant titration, with the advantage that the latter can provide quantitative information on the percentage of each type of polymer phase at the interface. However, the surfactant titration method is not free of uncertainty when the particles are not spherical, because the surface area of the particles is very uncertain (e.g., in particles with lobes). Recently, environmental SEM (ESEM) has been used to quantify the temperature at which the coalescence between polymer particles in latexes occurs during film formation [100]. The temperature at which the particles start to coalesce was in good agreement with the T_g measurements. Thus, ESEM can be used to determine the surface composition of composite polymer latexes indirectly (Fig. 10).

The internal structure of the particle was determined directly by conventional TEM and/or TEM of microtomed and stained samples and indirectly by differential scanning calorimetry (DSC). As shown in the round-robin study, microtomed TEM provided the best insight into the internal structure of the polymer particle. However, this technique also presented more artefacts and was affected by the sample

Fig. 11 dC_p/dT versus T for poly(methyl acrylate-*co*-methyl methacrylate)/poly(10% acrylic acid-*co*-styrene). Cycle 1 (solid line) is the first pass. After cycle 1, the sample was annealed at 150°C for 60 min prior to cycle 2 (dashed line). The data are smoothed by 3°C (Reproduced with permission from [104])



preparation method (the type of epoxy resin used to embed the polymer particles modified the morphology of the particles; plasticization of the polymer by some of the epoxy resins used was sometimes observed). DSC detects T_g s and crystalline melting points routinely, but can also be used to quantify the amount of interfacial material between two polymers in blends and latex films [101–103]. In a composite polymer particle containing two polymer phases, two T_g s are expected in the DSC, provided that the T_g s of each phase are substantially different. However, in many cases, the DSC traces for composite polymer latex films present distinctive shapes where the positions of the T_g s are shifted or broadened; in other words, the ΔC_{ps} of each polymer phase in the composite particle DSC differ from the ΔC_{ps} found in the DSC of the pure polymer phase. The difference between the ΔC_{ps} is attributed to polymer that is in the interface regions. It is worth noting that these differences are always seen in the first heating cycle during the DSC experiment. After the second heating cycle (if the temperature is increased above the T_g of the polymer phase with the highest T_g), phase separation occurs and two peaks corresponding to the pure phases are obtained. As reported by Tripathi et al. [104], the information from the first heating cycle should be analyzed to obtain information about the morphology of the composite polymer particle as obtained from the reactor (Fig. 11).

Microtomy of embedded and stained composite polymer latex is not free of uncertainty, as discussed above. Development of cryogenic SEM [105] and cryo-TEM [106] techniques have enabled rapid freezing of the sample and observation of the preserved morphology under cryogenic conditions. Although the shape is well preserved, the contrast of the polymer phases is not always enough in polymer–polymer systems (this might not be the case for polymer–inorganic systems). In view of these drawbacks, some authors have recently explored the use of scanning TEM (STEM) to determine the internal structure of composite polymer latexes. Because the operation energy of STEM (15–20 kV) is lower than that of TEM, the

technique is thought to be more suitable for analysis of samples with beam-sensitive characteristics (e.g., soft polymer phases). Thus, Geng et al. [107] reported sample preparation methods for STEM analysis of a composite latex composed of a soft PBA matrix with occluded PS domains. Because of the soft composition of the matrix (PBA), they attempted to preserve the shape of the particles by dispersing them in other colloidal materials that, upon casting, lead to a matrix with dispersed (embedded) composite polymer particles. The colloidal materials used were solutions of a low- T_g acrylic latex resin (ACS261 Dow), hydroxy-ethyl cellulose (HEC, QP 4400 H, Dow), polyethylene oxide (POLYOX WSR 301, AMERCHOL), and carboxymethyl cellulose (CRT 100, Dow). The authors concluded that the latex particles embedded in HEC best preserved the contour of the PBA particles and also presented the strongest contrast between the PS and PBA phases, making determination of the internal structure easier.

It is clear from the electron transmission microscopy results that the main difficulty in correctly determining the internal structure and morphology of composite polymer latexes is the lack of sufficient contrast between the different polymeric phases. Libera and Egerton [108] have recently reviewed the TEM of polymers and, more specifically, the contrast mechanisms available. They explained that some soft materials exhibit spatial variations in crystallinity, crystal orientation, and density due to the presence of heavy elements (e.g., added by staining). Crystallinity gives Bragg diffraction and heavy elements induce Rutherford scattering. In both cases, some incident electrons are scattered to relatively high angles, where they can be blocked by an objective aperture to produce dark images in the final image. This is the main strategy used to determine the morphology of composite polymer latexes. On the other hand, the authors pointed out that amorphous soft materials do not exhibit significant spatial variations in density and, hence, scattering is primarily in the forward direction, and an objective aperture provides little or no contrast unless the sample is appropriately stained [109–111]. Nevertheless, the rich valence electron structure of soft materials can introduce spatial modulations in the phase or energy of an incident electron wave and thus provide two sources of contrast for imaging soft-material morphology. Most of the research in the last two decades in this field has been concentrated on the development of phase contrast and spectroscopic imaging methods. Libera and Egerton [108] reviewed the most important developments in these two approaches and concluded that converting the phase information into amplitude information (using techniques such as defocusing, holography and Zernike phase plate methods) produces images with adequate contrast between the two polymer phases [112], but pointed out that the technique does not determine which phase corresponds to which polymer.

Fortunately, spectroscopic contrast developments seem to be more promising. The inelastic interaction between the energetic electrons and materials provide an alternative source of contrast for quantitative determination of chemical composition and phase distribution, without the need for heavy-element stains. These interactions can be analyzed by electron energy-loss spectroscopy (EELS). EELS is particularly suitable for analyzing energy losses in the sub-kiloelectron-volt

regime (e.g., K-shell core excitations from carbon 284 eV, oxygen 532 eV, and nitrogen 401 eV). Most soft materials have high concentration of C, N, O, and H, and the electronic structure associated with macromolecular compounds of these elements leads to a distinctive fine structure in the ionization edges. Thus, different polymer phases can be distinguished from each other based on their relative compositions. The multiple hybrid bonding states characteristic of carbon provides a rich valence-electron fine structure in soft materials. Low-loss TEM mode spectra (losses between a few electron-volts and 50 eV) provide a second type of characteristic fingerprint that can be used to differentiate between different polymer phases based on different polymer compositions.

Imaging based on spectroscopic contrast can be performed in either STEM mode using spectrum imaging or using energy-filtering (EFTEM) techniques. During the last few decades, there has been steady interest in using these techniques to study several aspects of multiphase polymer morphology in polymer–polymer and polymer–inorganic systems [113–121]. This technique combined with cryo-TEM can overcome the uncertainties observed in determining the morphology of complex composite polymer latexes using microtomed and stained samples in conventional TEM analysis. An example of the potential of this technique to analyze the internal structure of a composite polymer latex was reported by Libera and coworkers [122–124]. In this work, the authors used seeded emulsion polymerization to synthesize a biphasic colloid composed of PDMS (seed) and a copolymer made of MA, MMA, and VAc. Figure 12 shows the high-angle annular dark field (HAADF) cryo-STEM image, the low-loss EELS spectra for the pure components, and the composition map of one lobed particle of the latex (each phase is identified by a different color). According to the authors, it was possible to determine the exact composition of the lobed particles from the low-loss EELS mapping. They found that the acrylate-rich lobe consisted of almost pure organic copolymer, whereas the PDMS-rich lobe was partly mixed with the copolymer. They used the composition distribution graphs to conclude that the interface between the PDMS-rich lobe and the acrylate lobe was highly diffuse. According to the authors, this information could not be obtained by HAADF-STEM alone, which predicted the transition from light (PDMS) to dark (acrylate) contrast occurred in approximately 10 nm, whereas the low-loss EELS predicted that the acrylate copolymer remained entrapped in the PDMS lobe over a length scale of many tens of nanometers.

Although low-loss EELS is a promising technique for determining the composition distribution of composite polymer particles, there are very few reports of its successful implementation. In the authors' experience, there are still some aspects, such as the thickness of the samples (particle sizes) and the treatment of the EELS spectra of each phase (especially when the compositions of the phases are not pure), that need to be improved for extended use of this technique.

For correct characterization of the morphology of polymer–inorganic composite polymer latexes, the criterion provided by Stubbs and Sundberg for polymer–polymer systems should be a good roadmap. Although the shape and interface composition of the composite particles can be obtained by the same methods

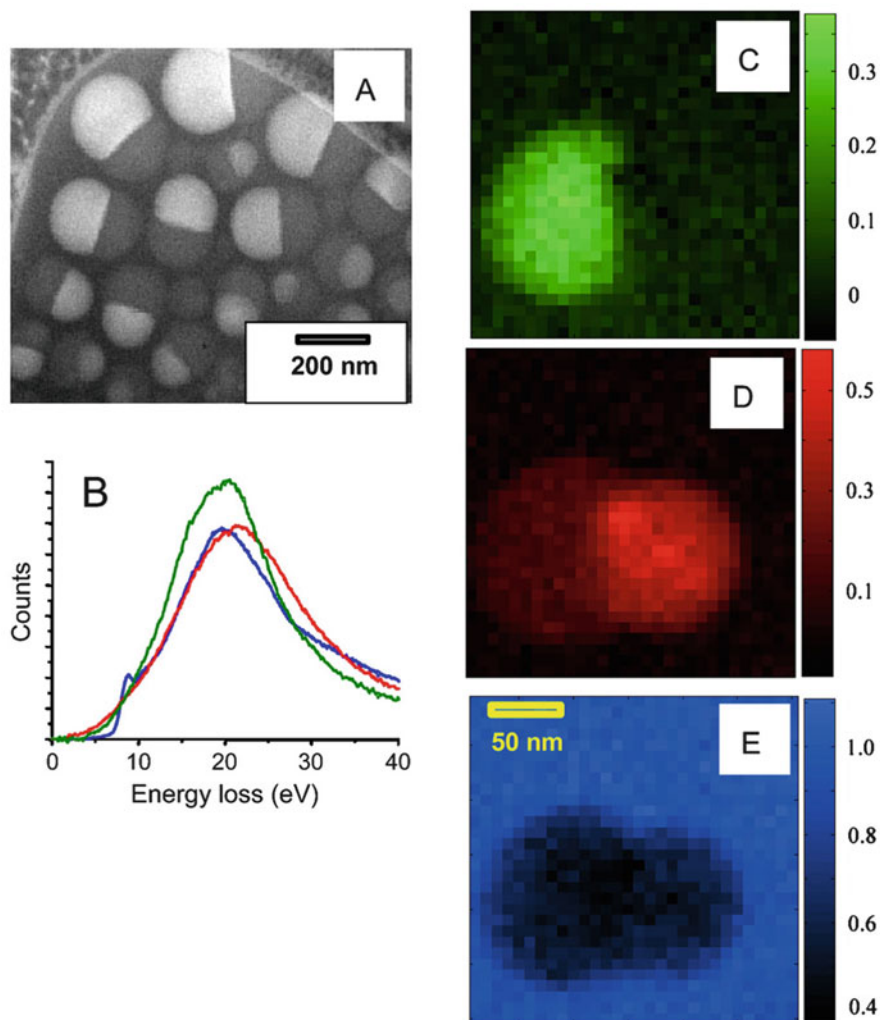


Fig. 12 (a) HAADF STEM image of a two-phase nanocolloid consisting of PDMS-rich (*dark contrast*) and acrylate-rich (*light contrast*) phases in amorphous ice carried by a holey carbon support film. (b) Normalized low-loss EELS reference spectra of the PDMS (*green*), acrylate copolymer (*red*), and amorphous ice (*blue*) (Reproduced with permission from [124])

discussed for the polymer–polymer systems, determination of the internal structure of polymer–inorganic composite polymer latexes presents inherent advantages. This is related to the relatively higher density of the inorganic material (nanoparticles), which enhances the contrast between the polymer phase and the inorganic material without the need for any additional staining elements (as shown by TEM micrographs in Sect. 3). However, there are also some uncertainties in

analyzing polymer–inorganic composite particles using TEM, which are briefly discussed next.

One of the aims of producing hybrid polymer–inorganic latexes is encapsulation of the inorganic nanoparticles within the polymer particles. In the literature on hybrid polymer/metal oxide (and other inorganic nanoparticles) latexes, encapsulation of the inorganic moieties is always assessed by TEM images of the hybrid particles. However, TEM images are not always conclusive with respect to the location of the inorganic nanoparticles, even when they are seen in the middle or centered in the polymer particle. The uncertainty comes from the fact that TEM images of polymer particles with encapsulated inorganic nanoparticles and images with nanoparticles located at the surface of the particle might look the same [125]. Further proof can be obtained by taking TEM micrographs after tilting the sample at positive and negative angles and following the potential displacement of the nanoparticles within the polymer particle [51, 126]. For some cases, TEM gives sufficient proof of location of the nanoparticle within the polymer particle, but conclusive proof can only be obtained by electron tomography or 3D-TEM that provides resolution at the nanometer range [127, 128]. Literature reports on the morphology of hybrid polymer–inorganic latexes measured by 3D-TEM are scarce [44, 62, 66, 119]. Mori and Kawaguchi [129] reported the morphology of PS/iron oxide hybrid latexes synthesized by miniemulsion polymerization to illustrate the effect of the type of initiators used in the miniemulsion polymerization process (potassium persulfate, azobisisobutyronitrile, or both) on the morphology of the hybrid latexes. Aguirre et al. [49, 70] demonstrated that a two-stage seeded miniemulsion polymerization ensured encapsulation of metal oxide (CeO_2 and ZnO) nanoparticles in waterborne acrylic coatings to be used as binders for UV-protection clear coats. Figure 13 illustrates the tomographic reconstruction of a hybrid acrylic/ ZnO polymer particle

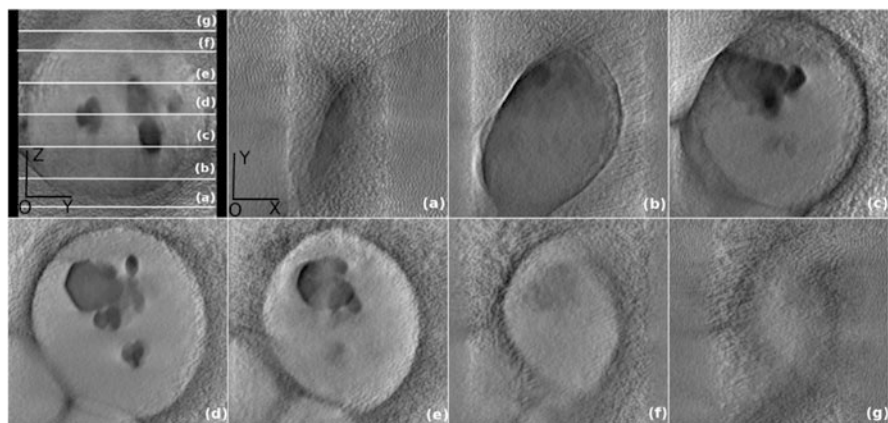


Fig. 13 Orthogonal sections of a reconstructed single particle. OXY sections corresponding to the planes indicated in the OYZ section with *white lines*: (a) $Z = 26$ nm, (b) $Z = 86$ nm, (c) $Z = 156$ nm, (d) $Z = 229$ nm, (e) $Z = 298$ nm, (f) $Z = 367$ nm, and (g) $Z = 420$ nm (Reproduced with permission from [49])

and presents how the ZnO nanoparticle aggregates are unambiguously located in the interior of the polymer particles (i.e., encapsulated).

In the same vein, Desert et al. [75] presented 3D reconstructions by cryo-electron tomography of multipod-like clusters composed of a silica core and PS satellites, prepared by seeded growth emulsion polymerization of styrene in the presence of size-monodisperse silica particles previously surface-modified with methacryloxymethyltriethoxysilane. The 3D reconstruction shows the high symmetry and regularity of the clusters, demonstrating good control of the synthesis process (Fig. 14).

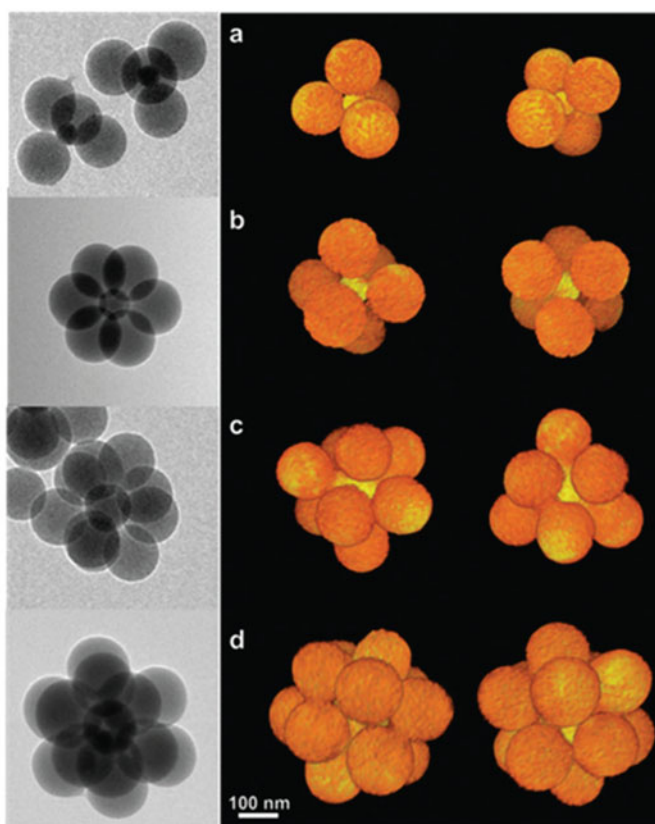


Fig. 14 Cryo-electron microscopy and cryo-electron tomography images of multipod clusters: (a) tetrapods, (b) hexapods, (c) nonapods, and (d) dodecapods. Each row presents from left to right a cryo-TEM image of such clusters and two different orientations of the 3D-reconstructed multipod (Reproduced with permission from [75])

6 Concluding Remarks

We present an update on the synthetic routes and applications claimed for polymer–polymer and polymer–inorganic composite latexes. Two-stage semibatch emulsion polymerization is the most commonly used route for the production of polymer–polymer composite latexes. The first stage is, in most of the cases, a seed latex that often contains functional or reactive groups at the surface to influence the location of the second-stage polymer. The temperature at which the second-stage polymerization is carried out and the T_g s of the first-stage and second-stage polymers are key to the final morphologies achieved. For the polymer–inorganic composite latexes, two-stage polymerizations are preferred for encapsulating the inorganic material. The first stage can be either miniemulsion polymerization in the presence of the inorganic material or adsorption of amphiphatic reactive oligomers on the surface of individual nanoparticles of the inorganic material. The second stage is a starved feed semibatch emulsion polymerization. For the surface location of the inorganic material, Pickering emulsion or miniemulsion are chosen.

Mathematical modeling of the development of particle morphology has also been reviewed and updated. A recently developed model differs from existing models in the speed of the calculation and in the fact that it predicts the morphology of all the particles (instead of simulating a single particle) by calculating the distribution of equilibrium and nonequilibrium clusters. The model can be used in advanced control strategies as a soft sensor to control polymer microstructure and particle morphology simultaneously.

In addition, we have revisited the characterization techniques frequently used to determine the morphology of composite particles. An unambiguous characterization of particle morphology requires determination of the shape of particles, surface composition, and internal composition. There is no single technique capable of provide this information. For polymer–polymer systems, electron microscopy techniques that provide a direct view and are the most appropriate, but suffer from the lack of contrast between the phases. The advent of low-loss EELS STEM and EFTEM allows characterization of the composition distribution of the different phases in composite polymer particles. However, the technique is not yet mature in the field and substantial advances are expected in the near future.

For polymer–inorganic composite latexes, the main concern in the characterization is not the contrast, but the exact location of the inorganic material on the polymer particles. 3D TEM or electron tomography and 3D reconstruction have shown to be conclusive, although their implementation can be time-consuming and challenging when cryo conditions are needed.

Acknowledgements The financial support of MINECO (grant CTQ2014-59016-P) and Basque Government (IT 999-16) is gratefully acknowledged.

References

1. Asua JM (2007) Polymer reaction engineering. Blackwell, Oxford
2. Asua JM (ed) (1997) Polymeric dispersions: principles and applications 1st edn. Springer Netherlands, Dordrecht
3. Urban D, Takamura K (2002) Polymer dispersions and their industrial applications. Wiley-VCH, Weinheim
4. Schork FJ, Tsavalas J (2004) The morphology of alkyd/acrylate latexes produced via hybrid miniemulsion polymerization: grafting mechanisms. *Colloid Polym Sci* 124:126–130
5. Tsavalas JG, Schork FJ, Landfester K (2004) Particle morphology development in hybrid miniemulsion polymerization. *J Coat Technol Res* 1:53–63
6. Herrera V, Pirri R, Asua JM, Leiza JR (2007) Morphology control in polystyrene/pol(methyl methacrylate) composite latex particles. *J Polym Sci A Polym Chem* 45:2484–2493
7. Goikoetxea M, Minari RJ, Beristain I, Paulis M, Barandiaran MJ, Asua JM (2009) Polymerization kinetics and microstructure of waterborne acrylic/alkyde nanocomposites synthesized by miniemulsion. *J Polym Sci A Polym Chem* 47:4871–4885
8. Li CY, Chiu WY, Don TM (2007) Morphology of PU/PMMA hybrid particles from miniemulsion polymerization: thermodynamic consideration. *J Polym Sci A Polym Chem* 45:3359–3369
9. Erdem B, Sudol ED, Dimonie VL, El-Aasser MS (2000) Encapsulation of inorganic particles via miniemulsion polymerization. I. Dispersion of titanium dioxide particles in organic media using OLOA 370 as stabilizer. *J Polym Sci A Polym Chem* 38:4419–4430
10. Chu HH, Ou ED (2000) Emulsion polymerization of 2-hydroxyethyl methacrylate and partition of monomer between particles and water phase. *Polym Bull* 44:337–344
11. Reyes Y, Akhmatkaya E, Leiza JR, Asua JM (2013) Particle morphology. In: van Herk AM (ed) Chemistry and technology of emulsion polymerization 2nd edn. Wiley, Singapore
12. Sundberg DC, Durant YG (2003) Latex particle morphology, fundamental aspects: a review. *Polym React Eng* 11:379–432
13. Schuler B, Baumstark R, Kirsch S, Pfau A, Sandor M, Zosel A (2000) Structure and properties of multiphase particles and their impact on the performance of architectural coatings. *Prog Org Coat* 40:139–150
14. Goikoetxea M, Reyes Y, de las Heras Alarcón CM, Minari RJ, Beristain I, Paulis M, Barandiaran MJ, Keddie JL, Asua JM (2012) Transformation of waterborne hybrid polymer particles into films: morphology development and Modeling. *Polymer* 53:1098–1108
15. Paulis M, Asua JM (2016) Knowledge-based production of waterborne hybrid polymer materials. *Macromol React Eng* 10:8–21
16. van Herk AM, Landfester K (eds) (2010) Hybrid latex particles: preparation with (mini) emulsion polymerization. Springer, Berlin
17. Asua JM (2002) Miniemulsion polymerization. *Prog Polym Sci* 27:1283–1346
18. Asua JM (2014) Challenges for industrialization of miniemulsion polymerization. *Prog Polym Sci* 39:1797–1826
19. Stubbs JM, Sundberg DC (2008) Core-shell and other multiphase latex particles-confirming their morphologies and relating those to synthesis variables. *J Coat Technol Res* 5:169–180
20. Cheng Y, Wang Z (2013) Fluorinated poly(isobornyl methacrylate-co-butyl acrylate) core-shell latex nanoparticles: synthesis, morphology and wettability of films. *Polymer* 54:3047–3054
21. Bonfond, A.; González, E.; Asua, J. M.; Leiza, J. R.; Ieva, E.; Brinati, G.; Carella, S.; Marrani, A.; Veneroni, A.; Kiwi, J.; et al. Stable photocatalytic paints prepared from hybrid core-shell fluorinated/acrylic/TiO₂ waterborne dispersions. *Crystals* 2016, 6(10), 136 doi:[10.3390/cryst6100136](https://doi.org/10.3390/cryst6100136).
22. Tan C, Tirri T, Wilen C-E (2016) The effect of core-shell particle morphology on adhesive properties of poly(styrene-co-butyl acrylate). *Int J Adhes Adhes* 66:104–113

23. Lopez A, Degrandi-Contraires E, Canetta E, Creton C, Keddie JL, Asua JM (2011) Waterborne polyurethane-acrylic hybrid nanoparticles by miniemulsion polymerization: applications in pressure-sensitive adhesives. *Langmuir* 27:3878–3788
24. Lopez A, Degrandi E, Canetta E, Keddie JL, Creton C, Asua JM (2011) Simultaneous free radical and addition miniemulsion polymerization: effect of the diol on the microstructure of polyurethane-acrylic pressure-sensitive adhesives. *Polymer* 52:3021–3030
25. Lopez A, Reyes Y, Degrandi-Contraires E, Canetta E, Creton C, Asua JM (2013) Waterborne hybrid polymer particles: tuning of the adhesive performance by controlling the hybrid microstructure. *Eur Polym J* 49:1541–1552
26. Hamzehlou S, Ballard N, Carretero P, Paulis M, Asua JM, Reyes Y, Leiza JR (2014) Mechanistic investigation of the simultaneous addition and free-radical polymerization in batch miniemulsion droplets: Monte Carlo simulation versus experimental data in polyurethane/acrylic systems. *Polymer* 55:4801–4811
27. Degrandi-Contraires E, Udagama R, McKenna T, Bourgeat-Lami E, Plummer CJG, Creton C (2014) Influence of composition on the morphology of polyurethane/acrylic latex particles and adhesive films. *Int J Adhes Adhes* 50:176–182
28. Bourgeat-Lami E (2003) Hollow particles: synthetic pathways and potential applications. In: Elaissari A (ed) *Colloidal polymers. Surfactant science series*. Marcel Dekker, New York, pp 189–223
29. Pan TY, Lee CF, Chu CH (2013) Synthesis and characteristics of poly(methacrylic acid-co-N-isopropylacrylamide) thermosensitive composite hollow latex particles and their application as drug carriers. *J Polym Sci A Polym Chem* 51:5203–5214
30. Jiang YM, Li BT, Wang WJ, Xu M, Kan CY (2014) Effect of the shell crosslinking level and core/shell ratio on the morphology of latex particles in the preparation of hollow latexes. *Chin J Polym Sci* 32:177–186
31. Deng W, Ji W, Jiang Y, Kan C (2013) Influence of unsaturated acid monomer on the morphology of latex particles in the preparation of hollow latex via the alkali post-treatment. *J Appl Polym Sci* 127:651–658
32. Yuan T, Shao Q, Hu J, Wang F, Tu W (2015) Effect of the intermediate layer-core ratio on the morphology and opacity ability of hollow latex particles. *J Appl Polym Sci* 132:1–7
33. Blenner D, Stubbs J, Sundberg D (2017) Multi-lobed composite polymer nanoparticles prepared by conventional emulsion polymerization. *Polymer* 114:54–63
34. Niu Q, Pan M, Yuan J, Liu X, Wang X, Yu H (2013) Anisotropic nanoparticles with controllable morphologies from non-cross-linked seeded emulsion polymerization. *Macromol Rapid Commun* 34:1363–1367
35. Li K, Zeng X, Li H, Lai X (2015) Role of acrylic acid in the synthesis of core-shell fluorine-containing polyacrylate latex with spherical and plum blossom-like morphology. *J Appl Polym Sci* 132:42527–42534
36. Chang Y, Pan M, Yuan J, Liu Y, Wang X, Jiang P, Wang Y, Zhong G-J, Li Z-M (2015) Morphology and film performance of phthalate-free plasticized poly(vinyl chloride) composite particles via the graft copolymerization of acrylate swelling flower-like latex particles. *RSC Adv* 5:40076–40087
37. Paulis M, Leiza JR (2010) Polymer/clay nanocomposites through emulsion and suspension polymerization. In: Mittal V (ed) *Advances in polymer nanocomposite technology*. Nova Science, New York, pp 53–101
38. Mičušík M, Reyes Y, Paulis M, Leiza JR (2010) Polymer–clay nanocomposites by miniemulsion polymerization. In: Mittal V (ed) *Polymer nanocomposites by emulsion and suspension polymerization*. Royal Society of Chemistry, London
39. Weiss CK, Landfester K (2010) Miniemulsion polymerization as a means to encapsulate organic and inorganic materials. *Adv Polym Sci* 233:185–236
40. Bourgeat-Lami E, Lansalot M (2010) Organic/inorganic composite latexes: the marriage of emulsion polymerization and inorganic chemistry. *Adv Polym Sci* 233:53–123
41. Faucheu J, Gauthier C, Chazeau L, Cavallé JY, Mellon V, Lami EB (2010) Miniemulsion polymerization for synthesis of structured clay/polymer nanocomposites: short review and recent advances. *Polymer* 51:6–17

42. Diaconu G, Micusik M, Bonnefond A, Paulis M, Leiza JR (2009) Macroinitiator and macromonomer modified montmorillonite for the synthesis of acrylic/MMT nanocomposite latexes. *Macromolecules* 42:3316–3325
43. Mičušík M, Bonnefond A, Reyes Y, Bogner A, Chazeau L, Plummer C, Paulis M, Leiza JR (2010) Morphology of polymer/clay latex particles synthesized by miniemulsion polymerization: modeling and experimental results. *Macromol React Eng* 4:432–444
44. Mballa MAM, Heuts JPA, Van Herk AM (2013) Encapsulation of non-chemically modified montmorillonite clay platelets via emulsion polymerization. *Colloid Polym Sci* 291:501–513
45. Greesh N, Ray SS (2016) Impact of non-ionic surfactant chemical structure on morphology and stability of polystyrene nanocomposite latex. *Colloid Polym Sci* 294:157–170
46. Wang S, Tian X, Sun J, Liu J, Duan J (2016) Morphology and mechanical properties of natural rubber latex films modified by exfoliated Na-montmorillonite/polyethyleneimine-G-poly (methyl methacrylate) nanocomposites. *J Appl Polym Sci* 133:1–8
47. Erdem B, Sudol ED, Dimonie VL, El-Aasser MS (2000) Encapsulation of inorganic particles via miniemulsion polymerization. II. Preparation and characterization of styrene miniemulsion droplets containing TiO₂ particles. *J Polym Sci A Polym Chem* 38:4431–4440
48. Aguirre M, Johansson Salazar-Sandoval E, Johansson M, Ahniyaz A, Paulis M, Leiza JR (2014) Hybrid acrylic/CeO₂ nanocomposites using hydrophilic, spherical and high aspect ratio CeO₂ nanoparticles. *J Mater Chem A* 2:20280–20287
49. Aguirre M, Barrado M, Iturrondobeitia M, Okariz A, Guraya T, Paulis M, Leiza JR (2015) Film forming hybrid acrylic/ZnO latexes with excellent UV absorption capacity. *Chem Eng J* 270:300–308
50. Nguyen D, Zondanos HS, Farrugia JM, Serelis AK, Such CH, Hawkett BS (2008) Pigment encapsulation by emulsion polymerization using macro-RAFT copolymers. *Langmuir* 24:2140–2150
51. Aguirre M, Paulis M, Leiza JR (2013) UV screening clear coats based on encapsulated CeO₂ hybrid latexes. *J Mater Chem A* 1:3155–3162
52. Bourgeat-Lami E, Duguet E (2006) Polymer encapsulation of inorganic particles. In: Ghosh SK (ed) *Functional coatings: by polymer microencapsulation*. Wiley-VCH, Weinheim, pp 85–152
53. Erdem B, Sudol ED, Dimonie VL, El-Aasser MS (2000) Encapsulation of inorganic particles via miniemulsion polymerization. III. Characterization of encapsulation. *J Polym Sci A Polym Chem* 38:4441–4450
54. De San Luis A, Bonnefond A, Barrado M, Guraya T, Iturrondobeitia M, Okariz A, Paulis M, Leiza JR (2017) Toward the minimization of fluorescence loss in hybrid cross-linked core-shell PS/QD/PMMA nanoparticles: effect of the shell thickness. *Chem Eng J* 313:261–269
55. Fleischhaker F, Zentel R (2005) Photonic crystals from core-shell colloids with incorporated highly fluorescent quantum dots. *Chem Mater* 17:1346–1351
56. Joumaa N, Lansalot M, Thérêt A, Elaissari A, Sukhanova A, Artemyev M, Nabiev I, Cohen JHM (2006) Synthesis of quantum dot-tagged submicrometer polystyrene particles by miniemulsion polymerization. *Langmuir* 22:1810–1816
57. González E, Bonnefond A, Barrado M, Casado Barrasa AM, Asua JM, Leiza JR (2015) Photoactive self-cleaning polymer coatings by TiO₂ nanoparticle Pickering miniemulsion polymerization. *Chem Eng J* 281:209–217
58. Bonnefond A, Gonzalez E, Asua JM, Leiza JR, Kiwi J, Pulgarin C, Rtimi S (2015) New evidence for hybrid acrylic/TiO₂ films inducing bacterial inactivation under low intensity simulated sunlight. *Colloids Surf B Biointerfaces* 135:1–7
59. Landfester K, Weiss CK (2010) Encapsulation by miniemulsion polymerization. *Adv Polym Sci* 229:1–49
60. Kobayashi S, Mullen K (eds) (2014) *Encyclopedia of polymeric nanomaterials*. Springer-Verlag, Berlin
61. Ali SI, Heuts JPA, Hawkett BS, Van Herk AM (2009) Polymer encapsulated Gibbsite nanoparticles: efficient preparation of anisotropic composite latex particles by RAFT-based starved feed emulsion polymerization. *Langmuir* 25:10523–10533

62. Costoyas A, Ramos J, Forcada J (2009) Encapsulation of silica nanoparticles by miniemulsion polymerization. *J Polym Sci A Polym Chem* 47:935–939
63. Reyes Y, Peruzzo PJ, Ferna M, Paulis M, Leiza JR (2013) Encapsulation of clay within polymer particles in a high-solid content aqueous dispersion. *Langmuir* 29:9849–9856
64. Mballa Mballa MA, Heuts JPA, Van Herk AM (2013) The effect of clay on the morphology of multiphase latex particles. *Colloid Polym Sci* 291:1419–1427
65. Nguyen D, Such CH, Hawkett BS (2013) Polymer coating of carboxylic acid functionalized multiwalled carbon nanotubes via reversible addition-fragmentation chain transfer mediated emulsion polymerization. *J Polym Sci A Polym Chem* 51:250–257
66. Huynh VT, Nguyen D, Such CH, Hawkett BS (2015) Polymer coating of graphene oxide via reversible addition-fragmentation chain transfer mediated emulsion polymerization. *J Polym Sci A Polym Chem* 53:1413–1421
67. Loiko OP, Spoelstra AB, van Herk AM, Meuldijk J, Heuts JPA (2016) An ATRP-based approach towards water-borne anisotropic polymer–Gibbsite nanocomposites. *Polym Chem* 7:3383–3391
68. Loiko OP, Spoelstra AB, van Herk AM, Meuldijk J, Heuts JPA (2016) Encapsulation of unmodified Gibbsite via conventional emulsion polymerisation using charged co-oligomers. *RSC Adv* 6:80748–80755
69. Cenacchi A, Pearson S, Kostadinova D, Leroux F, D’Agosto F, Lansalot M, Bourgeat-Lami E, Prevot V (2017) Nanocomposite latexes containing layered double hydroxides via RAFT-assisted encapsulating emulsion polymerization. *Polym Chem* 8:1233–1243
70. Aguirre M, Paulis M, Leiza JR, Guraya T, Iturrondobeitia M, Okariz A, Ibarretxe J (2013) High-solids-content hybrid acrylic/CeO₂ latexes with encapsulated morphology assessed by 3D-TEM. *Macromol Chem Phys* 214:2157–2164
71. Aguirre M, Paulis M, Barrado M, Iturrondobeitia M, Okariz A, Guraya T, Ibarretxe J, Leiza JR (2014) Evolution of particle morphology during the synthesis of hybrid acrylic/CeO₂ nanocomposites by miniemulsion polymerization. *J Polym Sci A Polym Chem* 53:792–799
72. Aguirre M, Paulis M, Leiza JR (2014) Particle nucleation and growth in seeded semibatch miniemulsion polymerization of hybrid CeO₂/acrylic latexes. *Polymer* 55:752–761
73. Garnier J, Warnant J, Lacroix-Desmazes P, Dufils PE, Vinas J, van Herk A (2013) Sulfonated macro-RAFT agents for the surfactant-free synthesis of cerium oxide-based hybrid latexes. *J Colloid Interface Sci* 407:273–281
74. Warnant J, Garnier J, van Herk A, Dufils P-E, Vinas J, Lacroix-Desmazes P (2013) A CeO₂/PVDC hybrid latex mediated by a phosphonated macro-RAFT agent. *Polym Chem* 4:5656
75. Désert A, Morele J, Taveau J-C, Lambert O, Lansalot M, Bourgeat-Lami E, Thill A, Spalla O, Belloni L, Ravaine S, et al. (2016) Multipod-like silica/polystyrene clusters. *Nanoscale* 8:5454–5469
76. Chomette C, Duguet E, Mornet S, Yammine E, Manoharan VN, Schade NB, Hubert C, Ravaine S, Perro A, Tréguer-Delapierre M (2016) Templated growth of gold satellites on dimpled silica cores. *Faraday Discuss* 191:105–116
77. Negrete-Herrera N, Putaux JL, David L, Bourgeat-Lami E (2006) Polymer/laponite composite colloids through emulsion polymerization: influence of the clay modification level on particle morphology. *Macromolecules* 39:9177–9184
78. Bon SAF, Colver PJ (2007) Pickering miniemulsion polymerization using Laponite clay as a stabilizer. *Langmuir* 23:8316–8322
79. Sheibat-Othman N, Bourgeat-Lami E (2009) Use of silica particles for the formation of organic-inorganic particles by surfactant-free emulsion polymerization. *Langmuir* 25:10121–10133
80. Colver PJ, Colard CAL, Bon SAF (2008) Multilayered nanocomposite polymer colloids using emulsion polymerization stabilized by solid particles. *J Am Chem Soc* 130:16850–16851
81. Xu Z, Xia A, Wang C, Yang W, Fu S (2007) Synthesis of raspberry-like magnetic polystyrene microspheres. *Mater Chem Phys* 103:494–499

82. Zgheib N, Putaux J-L, Thill A, D'Agosto F, Lansalot M, Bourgeat-Lam E (2012) Stabilization of miniemulsion droplets by cerium oxide nanoparticles: a step toward the elaboration of armored composite. *Langmuir* 28:6163–6174
83. Liu Y, Chen X, Wang R, Xin JH (2006) Polymer microspheres stabilized by Titania nanoparticles. *Mater Lett* 60:3731–3734
84. Chen JH, Cheng CY, Chiu WY, Lee CF, Liang NY (2008) Synthesis of ZnO/polystyrene composites particles by Pickering emulsion polymerization. *Eur Polym J* 44:3271–3279
85. Bonnefond A, Mičušík M, Paulis M, Leiza JR, Teixeira RFA, Bon SAF (2013) Morphology and properties of waterborne adhesives made from hybrid polyacrylic/montmorillonite clay colloidal dispersions showing improved tack and shear resistance. *Colloid Polym Sci* 291:167–180
86. González-Matheus K, Leal GP, Asua JM (2014) Pickering-stabilized latexes with high silica incorporation and improved salt stability. *Part Part Syst Charact* 31:94–100
87. Fischer V, Bannwarth MB, Jakob G, Landfester K, Muñoz-Espí R (2013) Luminescent and magnetoresponsive multifunctional chalcogenide/polymer hybrid nanoparticles. *J Phys Chem C* 117:5999–6005
88. Bonnefond A, Ibarra M, Gonzalez E, Barrado M, Chuvilin A, Maria Asua J, Ramon Leiza J (2016) Photocatalytic and magnetic titanium dioxide/polystyrene/magnetite composite hybrid polymer particles. *J Polym Sci A Polym Chem* 54:3350–3356
89. Gonzalez-Ortiz LJ, Asua JM (1995) Development of particle morphology in emulsion polymerization. 1. Cluster dynamics. *Macromolecules* 28:3135–3145
90. Gonzalez-Ortiz LJ, Asua JM (1996) Development of particle morphology in emulsion polymerization. 2. Cluster dynamics in reacting systems. *Macromolecules* 29:383–389
91. Gonzalez-Ortiz LJ, Asua JM (1996) Development of particle morphology in emulsion polymerization. 3. Cluster nucleation and dynamics in polymerizing systems. *Macromolecules* 29:4520–4527
92. Asua JM (2014) Mapping the morphology of polymer-inorganic nanocomposites synthesized by miniemulsion polymerization. *Macromol Chem Phys* 215:458–464
93. Reyes Y, Asua JM (2010) Modeling multiphase latex particle equilibrium morphology. *J Polym Sci A Polym Chem* 48:2579–2583
94. Stubbs J, Carrier R, Sundberg DC (2008) Monte Carlo simulation of emulsion polymerization kinetics and the evolution of latex particle morphology and polymer chain architecture. *Macromol Theory Simul* 17:147–162
95. Akhmatkaya E, Asua JM (2012) Dynamic modeling of the morphology of latex particles with in situ formation of graft copolymer. *J Polym Sci A Polym Chem* 50:1383–1393
96. Akhmatkaya E, Asua JM (2013) Dynamic modeling of the morphology of multiphase waterborne polymer particles. *Colloid Polym Sci* 291:87–98
97. Hamzehlou S, Leiza JR, Asua JM (2016) A new approach for mathematical modeling of the dynamic development of particle morphology. *Chem Eng J* 304:655–666
98. Chen YC, Dimonie V, El-Aasser MS (1992) Role of surfactant in composite latex particle morphology. *J Appl Polym Sci* 45:487–499
99. Stubbs JM, Sundberg DC (2005) A round Robin study for the characterization of latex particle morphology – multiple analytical techniques to probe specific structural features. *Polymer* 46:1125–1138
100. Gonzalez E, Tollan C, Chuvilin A, Barandiaran MJ, Paulis M (2012) Determination of the coalescence temperature of latexes by environmental scanning electron microscopy. *ACS Appl Mater Interfaces* 4:4276–4282
101. Nzudie DT (1992) Contribution a L'etude de L'interphase Des Lates "core-Shell" Par Lat RMN Du Solide a Haute Resolution. Université de Haute-Alsace, Mulhouse
102. Song M, Hourston DJ, Reading M, Pollock HM, Hammiche A (1999) Modulated differential scanning Calorimetry. Analysis of interphases in multi-component polymer materials. *J Therm Anal Calorim* 56:991–1004

103. Hourston DJ, Song M, Hammiche A, Pollock HM, Reading M (1997) Modulated differential scanning calorimetry: 6. Thermal characterization of multicomponent polymers and interfaces. *Polymer* 38:1–7
104. Tripathi AK, Tsavalas JG, Sundberg DC (2013) *Thermochimica acta* quantitative measurements of the extent of phase separation during and after polymerization in polymer composites using DSC. *Thermochim Acta* 568:20–30
105. Luo H, Scriven LE, Francis LF (2007) Cryo-SEM studies of latex/ceramic nanoparticle coating microstructure development. *J Colloid Interface Sci* 316:500–509
106. Crassous JJ, Ballauff M, Drechsler M, Schmidt U, Talmon Y (2006) Imaging the volume transition in thermosensitive core-shell particles by cryo-transmission electron microscopy. *Langmuir* 22:2403–2406
107. Geng X, Zhai MX, Sun T, Meyers G (2013) Morphology observation of latex particles with scanning transmission electron microscopy by a hydroxyethyl cellulose embedding combined with RuO₄ staining method. *Microsc Microanal* 19:319–326
108. Libera MR, Egerton RF (2010) Advances in the transmission electron microscopy of polymers. *Polym Rev* 50:321–339
109. Sawyer LC, Grubb DT, Meyers GF (2008) *Polymer microscopy* 3rd edn. Springer, New York
110. Smith RW, Bryg V (2006) Staining polymers for microscopical examination. *Rubber Chem Technol* 79:520–540
111. Midgley PA, Weyland M (2003) 3D electron microscopy in the physical sciences: the development of Z-contrast and EFTEM tomography. *Ultramicroscopy* 96:413–431
112. Tosaka M, Danev R, Nagayama K (2005) Application of phase contrast transmission microscopic methods to polymer materials. *Macromolecules* 38:7884–7886
113. Horiuchi S, Hanada T, Yase K, Ougizawa T (1999) Analysis of an interface between an immiscible polymer pair by electron spectroscopic imaging. *Macromolecules* 32:1312–1314
114. Horiuchi S, Kiyoshi Y, Kitano T, Higashida N, Ougizawa T (1997) EFTEM for the characterization of polymer blend morphologies. *Polym J* 29:380–383
115. Lieser G, Schmid SC, Wegner G (1996) Electrically conducting polymers: preparation and investigation of oxidized poly(acetylene) by EFTEM. *J Microsc* 183:53–59
116. Garcia-Meitin E, Bar G, Blackson J, Reuschle D (2008) High resolution polymer imaging using scanning transmission electron microscopy. *Microsc Microanal* 14:1380–1381
117. Horiuchi S, Yin D, Ougizawa T (2005) Nanoscale analysis of polymer interfaces by energy-filtering transmission electron microscopy. *Macromol Chem Phys* 206:725–731
118. Linares EM, Leite CAP, Valadares LF, Silva CA, Rezende CA, Galembeck F (2009) Molecular mapping by low-energy-loss energy-filtered transmission electron microscopy imaging. *Anal Chem* 81:2317–2324
119. Hofer F, Warbichler P (2005) Elemental mapping using energy filtered imaging. *Transmission electron energy loss spectrometry in materials science and the EELS atlas*. Wiley-VCH, Weinheim
120. Jeanguillaume C, Colliex C (1989) Spectrum-image: the next step in EELS digital acquisition and processing. *Ultramicroscopy* 28:252–257
121. Hunt JA, Williams DB (1991) Electron energy-loss spectrum-imaging. *Ultramicroscopy* 38:47–73
122. Kim G, Sousa A, Meyers D, Shope M, Libera M (2006) Diffuse polymer interfaces in lobed nanoemulsions preserved in aqueous media. *J Am Chem Soc* 128:6570–6571
123. Kim G, Sousa A, Meyers D, Libera M (2008) Nanoscale composition of biphasic polymer nanocolloids in aqueous suspension. *Microsc Microanal* 14:459–468
124. Yakovlev S, Libera M (2008) Dose-limited spectroscopic imaging of soft materials by low-loss EELS in the scanning transmission electron microscope. *Micron* 39:734–740
125. Drummy LF, Wang YC, Schoenmakers R, May K, Jackson M, Koerner H, Farmer BL, Mauryama B, Vaia RA (2008) Morphology of layered silicate-(NanoClay-) polymer nanocomposites by electron tomography and small-angle X-ray scattering. *Macromolecules* 41:2135–2143

126. Voorn DJ, Ming W, van Herk AM (2006) Clay platelets encapsulated inside latex particles. *Macromolecules* 39:4654–4656
127. Midgley PA, Weyland M, Yates TJV, Arslan I, Dunin-Borkowski RE, Thomas JM (2006) Nanoscale scanning transmission electron tomography. *J Microsc* 223:185–190
128. Ziese U, De Jong KP, Koster AJ (2004) Electron tomography: a tool for 3D structural probing of heterogeneous catalysts at the nanometer scale. *Appl Catal A Gen* 260:71–74
129. Mori Y, Kawaguchi H (2007) Impact of initiators in preparing magnetic polymer particles by miniemulsion polymerization. *Colloids Surf B Biointerfaces* 56:246–254

Stimuli-Responsive Latexes Stabilized by Carbon Dioxide Switchable Groups



Michael F. Cunningham, Philip G. Jessop, and Ali Darabi

Abstract Preparation of stimuli-responsive latexes whose colloidal stability can be reversibly switched using only CO₂ as a trigger is reviewed. By incorporating CO₂-responsive moieties into the formulation of an emulsion polymerization, polymer particles can be made for which stabilization originates from functional groups that are readily switched “on” (charged) and “off” (neutral) simply by adding or removing CO₂ at atmospheric pressure. The functional groups that provide colloidal stability, typically amidines or tertiary amines, can be added in various forms such as premanufactured surfactants, functional monomers, or functional, commercially available initiators. This review focuses on the preparation, behavior, and properties of these CO₂-switchable emulsion polymers. Detailed discussion is provided on how the switching behavior and latex properties are influenced by the choice of CO₂-switchable moieties and the method of their incorporation into latex particles.

Keywords CO₂-switchable • Switchable particles • Switchable surfactants

Contents

| | | |
|-----|---|-----|
| 1 | Introduction | 144 |
| 2 | CO ₂ -Switchable Surfactants | 146 |
| 3 | CO ₂ -Switchable Monomers | 147 |
| 4 | CO ₂ -Switchable Initiators | 148 |
| 5 | CO ₂ -Switchable Latexes | 149 |
| 5.1 | Switchable Surfactants | 149 |
| 5.2 | Switchable Initiators | 151 |
| 5.3 | Switchable Comonomers | 153 |
| 5.4 | Switchable Water | 154 |

| | |
|--------------------|-----|
| 6 Conclusion | 155 |
| References | 156 |

1 Introduction

Emulsion polymerization has traditionally employed surfactants that provide effective stabilization of latex particles, not only during polymerization but also during subsequent storage, transportation, and application. The stabilization mechanism can be ionic (anionic or cationic surfactants), steric (nonionic surfactants), or a combination (electrosteric stabilization, typically achieved by using a mixture of ionic and nonionic surfactants in the latex formulation). After the polymerization reaction, commercial latexes are often subjected to conditions that compromise colloidal stability, including mechanical shear (e.g., from pumps), freeze–thaw conditions, and mixing with other components (e.g., in paint formulations). Consequently, significant efforts have been spent on making many latexes highly colloidally stable. Latexes that are to be deliberately coagulated after polymerization to prepare resins only need to be stable in the reactor. Coagulation requires addition of a concentrated solution of salt and possibly acid or base, thereby creating an undesirable waste stream.

The inherent dilemma with traditional surfactants is that they are made to be as effective as possible in providing colloidal stability, yet it is frequently desirable to switch off the surfactant properties. Even for latexes to be used in coatings, the residual ionic or hydrophilic nature of the surfactant is a common problem, especially for coatings where moisture resistance is required. For example, in film-forming applications, migration of the residual surfactant has a negative effect on the properties of the final product [1–3]. Surfactant removal by washing is typically ineffective and expensive, and not economically practical for commercial processes. A potential solution to these issues is the use of “switchable surfactants,” which are surfactants whose stabilizing properties can be easily turned off by application of a trigger. It may also be valuable for some applications to be able to switch the surfactant back on. For example, commercial latexes contain about 50% water and have to be shipped to their final destination. The cost and environmental impact of shipping that much water is appreciable. With a switchable surfactant, a latex could be dewatered, shipped to its final point of use, and then reconstituted by adding water. The preparation of polymeric nanoparticles with surfaces that can be reversibly switched from charged to neutral over numerous cycles is also a subject of high interest.

Stimuli-responsive materials exhibit reversible changes in their physical or chemical properties in response to external triggers such as temperature, pH, light, or voltage [4]. In many cases, there are practical concerns with the triggers, for example, cost, environmental impact, and product contamination [5]. However, CO₂, which is a benign, inexpensive, abundant, and nontoxic trigger, has received

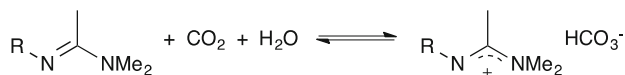


Fig. 1 CO₂-switchability of amidine-based switchable surfactants (R = C₈ to C₁₆ alkyl chain) [8]

increasing attention in recent years [6, 7]. CO₂-responsive polymers have found potential applications in areas such as latexes, gels, CO₂ capturing and monitoring, separation, encapsulation, forward osmosis, CO₂-switchable vesicles, and CO₂-switchable worm-like micelles [7].

Our first CO₂-switchable latexes were stabilized by CO₂-switchable surfactants based on alkylamidines, which could be easily switched on and off in aqueous media in the presence of CO₂ (Fig. 1) [8, 9]. Alkylamidines are protonated (switched on) by bubbling CO₂ into an aqueous surfactant solution (under only atmospheric pressure), thereby converting the alkylamidines to an amidinium bicarbonate salt. In protonated form, these molecules can effectively function as electrostatic surfactants in emulsion polymerization. When they are deprotonated (switched off) by removal of CO₂ from the system, the latex is destabilized and aggregates. Furthermore, the neutral alkylamidine is fairly hydrophobic. Removal of CO₂ from the latex is easily achieved by bubbling air, nitrogen, or any nonacidic gas through the system, or even by simply exposing the latex to air. Deprotonation by exposure of a latex to air is slower than bubbling with air, but is much faster if the latex is spread as a thin film (as is done with coatings).

A key advantage of using CO₂ as a trigger in the synthesis of CO₂-responsive latexes if multiple on/off cycles are used is that addition and removal of CO₂ occurs without salt accumulation, unlike pH-responsive latexes that use liquid acids and bases to protonate/deprotonate the switchable groups. There are, however, limitations in the use of CO₂-switchable surfactants. First, the solubility of CO₂ in water decreases with higher temperatures and, therefore, it cannot be effectively used as a trigger at atmospheric pressure at temperatures above 65°C. Running an emulsion polymerization under pressure would increase the CO₂ solubility in water and give effective switching at higher temperatures. An easier route would be to use lower temperatures with an initiator having a higher decomposition rate at low temperatures. Second, because carbonic acid is a weak acid, one needs to be cautious about using CO₂-switchable surfactants in the presence of strong acids because they irreversibly protonate the switchable groups so that they cannot be switched off.

In the following sections, we review recent progress in the development of CO₂-switchable emulsion polymers. We start by describing the use of pre-made CO₂-switchable surfactants in emulsion polymerization, and continue with a discussion of further developments based on surfactant-free routes for preparation of CO₂-switchable latexes. In these strategies using CO₂-switchable initiators and monomers, the stabilizing moieties are formed in situ in the early stages of polymerization, and therefore remain covalently bound to the particles. CO₂-responsiveness in a latex can originate from the surfactant, monomer, or initiator that contains a functional group such as a tertiary amine or amidine.

2 CO₂-Switchable Surfactants

Different types of switchable surfactants have been reported, varying in the type of trigger that is used in the switching process [10]. Examples include light-sensitive surfactants [11–15], acid/base-sensitive surfactants [16–20], and redox-sensitive surfactants [21–26]. Usually, addition of acid, base, oxidant, or reductant is required, which has an environmental impact as a result of the wastewater produced in subsequent washing steps. In the case of light-sensitive surfactants, the reaction media must be transparent [27], making them unsuitable for latexes. CO₂-switchable surfactants, a new class of stimuli-responsive surfactants, employ a simple, benign, inexpensive, and nontoxic trigger [8]. In aqueous media, pH is changed by addition of CO₂ as carbonic acid is formed. The final pH depends on the dissolved CO₂ concentration. The solubility of CO₂ in water decreases as temperature increases, and increases as pressure increases [28]. Our first switchable surfactants were long-chain alkyl amidines (Fig. 1). The removal of CO₂ to “switch off” the surfactant can be simply performed by purging with a nonacidic gas such as nitrogen, argon, or air. Conductivity measurements on CO₂-switchable surfactant solutions over repeated cycles of CO₂ and N₂ sparging confirmed the alternating protonation/deprotonation behavior (Fig. 2). Because deprotonation is an endothermic process, application of heat accelerates the deprotonation reaction. Thus, the greater the protonation enthalpy, the more heat must be supplied to switch the compound back to its neutral form. We found that amidine-based CO₂-switchable surfactants, which are readily switched on, were more difficult to switch off because of their high basicity (high pK_{aH}). We therefore developed a second generation of

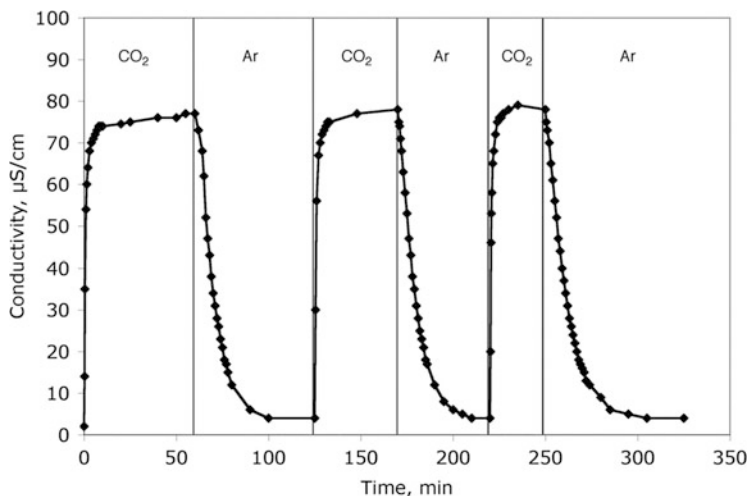


Fig. 2 Conductivity of a dimethyl sulfoxide (DMSO) solution of a switchable surfactant with $R = C_{16}H_{33}$ in Fig. 1 as a function of time during three cycles of treatment with CO₂ followed by argon [8]

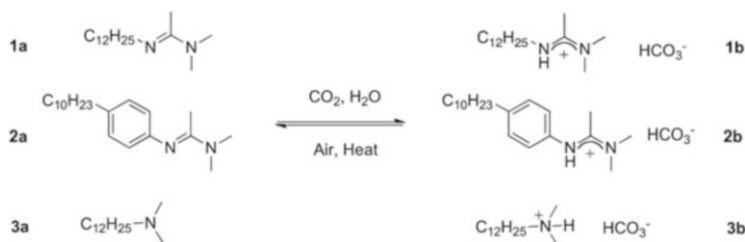


Fig. 3 Reaction of amidines and amines with CO_2 and water to form bicarbonate salts [27]

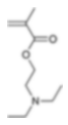
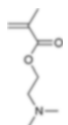
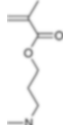
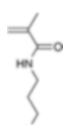
surfactants using less basic moieties, specifically aryl amidines and tertiary amines. These compounds do not switch on as quickly as the more basic alkyl amidines, but can be switched off much faster (Fig. 3). As discussed in subsequent sections, CO_2 -switchable surfactants have been used in emulsion polymerization for stabilization of the original emulsion and product latex particles.

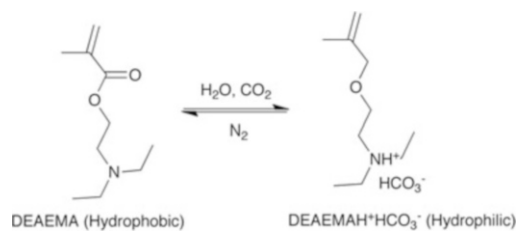
3 CO_2 -Switchable Monomers

CO_2 -switchable latexes can be prepared by incorporation of a small amount of CO_2 -switchable monomer into the formulation. The switchable monomer, being hydrophilic, is believed to copolymerize in the aqueous phase with the other hydrophobic monomers present in the formulation to yield surfactant made in situ. Ideally, most or all of the CO_2 -switchable monomer resides on the particle surface, thereby imparting switchability to the latex. Table 1 shows monomers used for the synthesis of CO_2 -responsive polymers; however, it should be noted that any monomer containing a CO_2 -switchable functional group is a potential candidate.

2-(Diethylamino)ethyl methacrylate (DEAEMA) and 2-(dimethylamino)ethyl methacrylate (DMAEMA) are the most commonly used monomers for making CO_2 -switchable latexes (Fig. 4). The pK_{aH} values of DEAEMA and the corresponding homopolymer (PDEAEMA) are 8.8 and 7.5, respectively [50]. DMAEMA has pK_{aH} values of 8.3 and 7.4 for the monomer and polymer, respectively [50]. Incorporating a small amount (not more than 1%) of DEAEMA or other switchable monomer into latex particles is typically all that is required to yield a CO_2 -switchable latex. Although the chemical structures of DEAEMA and DMAEMA are similar, they have different properties in terms of water solubility. DEAEMA and PDEAEMA are hydrophobic, but DMAEMA and PDMAEMA are hydrophilic. A good substitute for these monomers is dimethylaminopropyl methacrylamide (DMAPMAm), which is hydrophilic, CO_2 -switchable, and more hydrolytically stable.

Table 1 Summary of CO₂-switchable monomers suitable for emulsion polymerization

| Name | Structure | p <i>K</i> _{aH} monomer | p <i>K</i> _{aH} polymer | References |
|---------|---|----------------------------------|----------------------------------|-------------|
| DEAEMA |  | 8.8 | 7.5 | [20, 25–41] |
| DMAEMA |  | 8.3 | 7.4 | [29, 42–49] |
| DMAPMAm |  | 8.9–9.1 | 8.4 | [50] |
| DMAPMA |  | 9.2 | 8.8 | [50] |

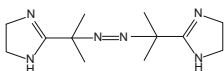
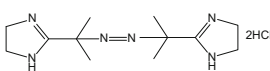
**Fig. 4** CO₂-switchability of DEAEMA

4 CO₂-Switchable Initiators

We have used the commercially available initiators 2,2'-azobis[2-(2-imidazolin-2-yl)propane]dihydrochloride (VA-044) and 2,2'-azobis[2-(2-imidazolin-2-yl)propane] (VA-061) in the preparation of CO₂-switchable latexes (Table 2). VA-061 is itself CO₂-switchable. VA-044 is not CO₂-switchable but can be converted to a CO₂-switchable form by neutralization with base to remove HCl. The 10-h half-life decomposition temperature of VA-061 is 61°C and decreases when protonated (~45°C), which makes it suitable for initiating polymerizations under a CO₂ atmosphere [56].

Although these initiators are typically used in conjunction with CO₂-switchable surfactants, the positively charged imidazole groups resulting from decomposition

Table 2 Structures of VA-044 and VA-061, and related references

| Name | Structure | References |
|--------|---|---------------------------|
| VA-061 |  | [4, 12–14, 19, 30, 51–53] |
| VA-044 |  | [27, 37, 54, 55] |

of VA-044 or protonated VA-061 are themselves effective in stabilizing latex particles. The key advantage of having a CO₂-switchable initiator is that these charged groups, which tend to reside on the particle surface, can also be switched off (and then back on if desired), thereby allowing more complete switching of the particle surface charge. By contrast, if a nonswitchable ionic initiator is used there is always residual surface charge.

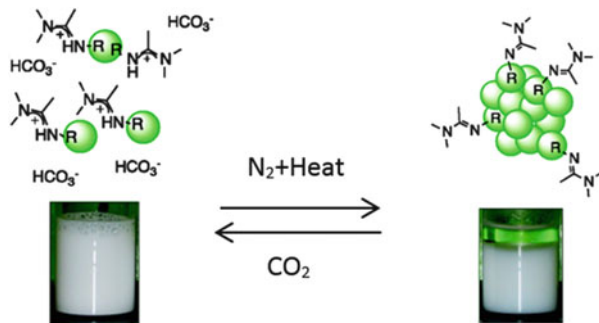
5 CO₂-Switchable Latexes

5.1 Switchable Surfactants

Alkyl amidine compounds were first used as CO₂-switchable surfactants in the emulsion polymerization of styrene and methyl methacrylate (MMA) [8, 54]. After polymerization, removal of CO₂ by bubbling of Ar at 65°C triggered aggregation of the latex. We soon realized that both initiator selection and surfactant selection were crucial factors in preparing CO₂-switchable latexes. For example, VA-044 causes permanent stability of latexes even in the absence of CO₂ because of the presence of the acid HCl, which irreversibly protonates the switchable groups [54]. (The HCl can be neutralized by addition of a strong base such as NaOH, but not by simple removal of CO₂.) We then demonstrated that these latexes could be both coagulatable and redispersible CO₂-switchable latexes (Fig. 5) [55]. Redispersion of the latexes is much easier when both initiator and surfactant are CO₂-switchable. The aggregation and redispersion of latexes were possible for several cycles without accumulation of salt [55]. Aryl amidines and tertiary amines are less basic than alkyl amidines, and as a result they are switched off much more rapidly [27]. PMMA latexes made using surfactants based on tertiary amines and aryl amidines were destabilized more easily by bubbling Ar to remove the CO₂ and had lower zeta potentials than those prepared with surfactants based on alkyl amines [27].

(*N*-Amidino)dodecyl acrylamide (DAm) was employed as a CO₂-switchable reactive surfactant for preparation of coagulatable/redispersible polystyrene (PS) latexes [4]. Redispersion of the latex was achieved by purging with CO₂, and coagulation was performed by purging with N₂ and heating to remove CO₂. However, the amidine group was reported to be partially hydrolyzed under basic

Fig. 5 Coagulation and redispersion of polystyrene latex in the presence of a CO₂-switchable surfactant and initiator [55]



conditions. These PS latexes were stable against electrolytes and could be coagulated and redispersed several times. To overcome the hydrolysis problem and simplify the synthesis steps, DMAEMA was employed in the preparation of PDMAEMA-*b*-PMMA via RAFT polymerization [36]. The diblock copolymer was used as a polymeric surfactant in the emulsion polymerization of MMA. To ensure the surfactant remained fully protonated during reaction, protonation was carried out using HCl. The resultant latex could be coagulated by addition of a small amount of base. After washing with deionized water, the latex could be redispersed and coagulated many times by addition and removal of CO₂. It was found that the latex was stable if the weight fraction of MMA (F_{MMA}) in the surfactant was lower than 58% [57].

An advantage of using polymeric surfactants is the prevention of surfactant migration in film-forming applications. When latexes are employed as film-forming polymers, physically adsorbed surfactants on the surface of the particles migrate toward the interfaces and lead to phase separation, which reduces gloss and adhesion [3]. Also, polymeric surfactants can be entrapped in pockets and increase percolation by water or increase the water sensitivity of the film. These are major drawbacks for paint and coating applications [2, 3]. Surfactants that are covalently linked to the particles cannot desorb and migrate during film formation.

CO₂-switchable PMMA and PS latexes were also prepared using commercially available *N,N*-dimethyldodecylamine (DDA), a CO₂-switchable surfactant, via miniemulsion polymerization [41]. The PMMA latexes could be aggregated by bubbling Ar at 60°C and redispersed by bubbling CO₂ at room temperature. The PS latexes were not visibly destabilized by bubbling Ar, which could be attributable to the lower density of PS (1.05 g cm⁻³) compared with PMMA (1.18 g cm⁻³) [41]. However, increasing the pH to 9 resulted in the visible aggregation of PS latexes. Higher pH results in a higher fraction of the switchable groups being deprotonated, and could be the cause of the more visible settling. (Simply removing CO₂ by sparging with Ar probably gives a lower pH than 9, meaning that more of the switchable groups remain protonated.) In a dispersion of nanoparticles composed of a DDA hydrophobic core and polyvinylformal (PVF) shell, bubbling CO₂ converted the core from hydrophobic to hydrophilic, which was the first report of preparation of water-core polymer capsules from oil/water emulsions.

One of the troublesome observations with many of the latexes we made using amidine-based switchable surfactants was that we could not reduce the particle zeta potential below about 10 mV during the switching off process, nor could we restore the zeta potential to its original value when we re-introduced CO₂. It occurred to us that the behavior and basicity of a pH-responsive group in an aqueous solution could be quite different from those on the hydrophobic surface of a particle. We therefore investigated the effect of the molecular structure of two CO₂-switchable surfactants (*N'*-dodecyl-*N,N*-dimethylacetamidinium bicarbonate, C₁₂N, and *N'*-(2-(2-(dodecyloxy)ethoxy)ethyl)-*N,N*-dimethylacetamidinium bicarbonate, C₁₂E₂N) on the coagulation and redispersion behavior of PS latexes [43]. The structure of the surfactant C₁₂E₂N (Fig. 6) provides a hydrophilic spacer that extends the amidine from the particle surface out into the aqueous phase. The zeta potential and surface coverage of PS latexes prepared with C₁₂N decreased as expected when CO₂ was removed, but did not return to the initial value when CO₂ was reintroduced to the system. However, in the case of latexes prepared with C₁₂E₂N, the initial zeta potential was recovered. Latexes with C₁₂E₂N surfactant responded more quickly and completely to N₂ and CO₂ than those with C₁₂N surfactant (Fig. 7). According to adsorption isotherms, the head groups of surface-bound C₁₂E₂N protrude into the aqueous phase, but surface-bound C₁₂N tends to lie flat against the hydrophobic surface when the switchable surfactant is neutral. Thus, when CO₂ is bubbled into the aqueous phase, the head group of C₁₂E₂N is readily protonated whereas C₁₂N is not, as a result of its effectively higher p*K*_{aH} from being in a hydrophobic environment.

5.2 Switchable Initiators

If a switchable initiator is used, surfactant is not necessarily required. We conducted surfactant-free emulsion polymerizations using only VA-061 initiator under a CO₂ atmosphere as the stabilizing moiety, finding that the latex particles could be coagulated by CO₂ removal and redispersed upon introduction of CO₂ (Fig. 8)

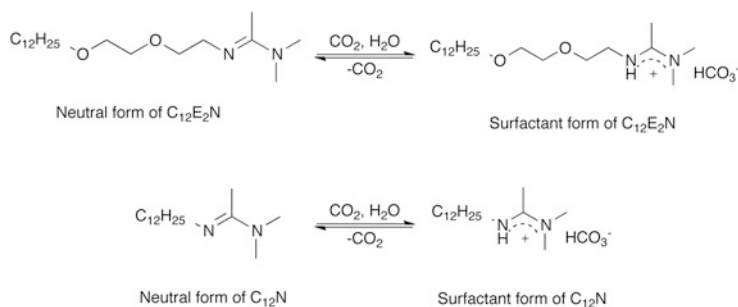


Fig. 6 Switching of surfactants C₁₂E₂N and C₁₂N between their neutral and surfactant forms [43]

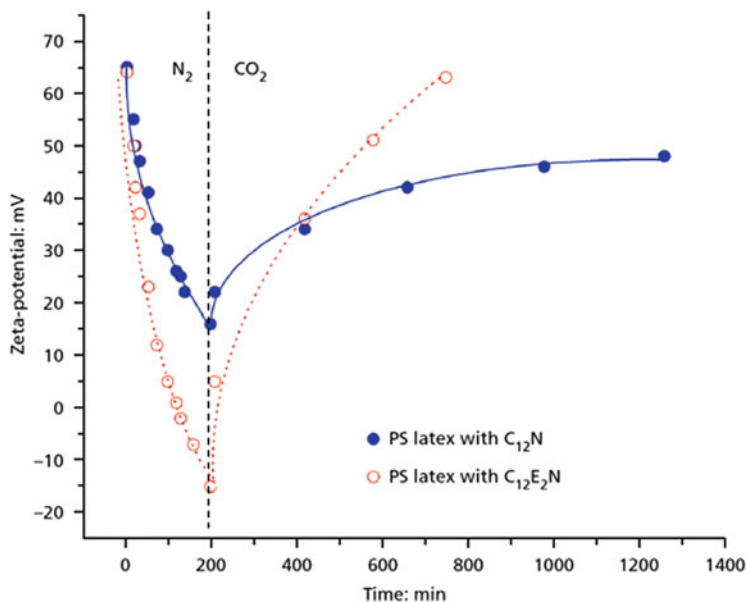


Fig. 7 The ζ potential of polystyrene particles as a function of time during destabilization using N_2 bubbling through the suspension at $80^\circ C$, followed by redispersion using CO_2 bubbling through the mixture at room temperature [43]

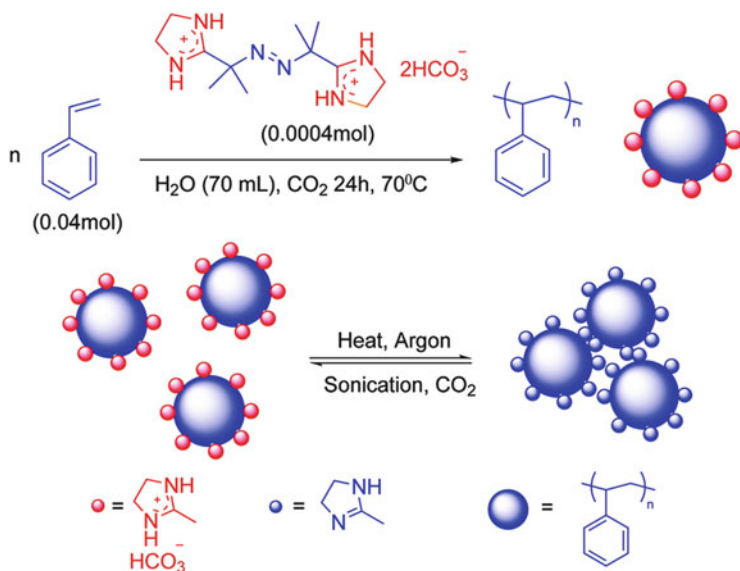


Fig. 8 Preparation of a switchable polystyrene latex and its reversible aggregation and redispersion triggered by removal and addition of CO_2 [56]

[56]. Because the imidazole groups created from VA-061 are covalently bound to the particle surface, unlike switchable surfactants, they cannot migrate or desorb, which appears to facilitate redispersion.

5.3 Switchable Comonomers

Although CO₂-responsive surfactants have proven to be effective in stabilizing latexes, they do have disadvantages. Like any traditional surfactant, they are not covalently bound to the particle surface and are therefore subject to migration on the particle surface, which can cause stability problems or eventual leaching into the environment. Because most surfactants are toxic (to aquatic species for example), leaching can be a serious concern. A preferred solution is to covalently bind the switchable groups, which improves colloidal stability and redispersibility of aggregated particles and prevents surfactant leaching.

Incorporation of a small amount of CO₂-switchable monomer that becomes covalently bound to the particles can alleviate these concerns. DEAEMA was used as a CO₂-switchable comonomer (0.54 mol% of total monomers) to prepare a CO₂-switchable and monodisperse PS latex [58]. It was found that adding a few mole percent of MMA to styrene increases the conversion considerably because MMA is more hydrophilic than styrene and produces more hydrophobic oligomers in the aqueous phase, thereby promoting particle nucleation. Hydrophilic poly (DEAEMA⁺HCO₃⁻) formed during the reaction acts as a CO₂-switchable flocculant and induces facile coagulation and redispersion of the latex [58]. After destabilization and drying, the latex could be redispersed by CO₂ bubbling and sonication (Fig. 9).

An amidine-containing styrenic monomer was synthesized and used as a CO₂-switchable comonomer in the surfactant-free emulsion polymerization of styrene [59]. Because of the use of 2,2'-azobis(2-methylpropionamidine)dihydrochloride (V-50), which is the HCl salt form of the initiator, destabilization of the latex was only possible by addition of a small amount of strong base (NaOH). However, the coagulated latex was redispersible after CO₂ bubbling followed by sonication [59]. The coagulated, filtered, and dried latex powder was redispersible using CO₂ and ultrasound.

An important concern for the redispersion of latexes is the glass transition temperature (T_g) of the polymer. Although most work described previously involved high- T_g polymers such as PS and PMMA, Zhu and colleagues were the first to consider whether CO₂-switchable, low- T_g latexes could be redispersed. Acrylic latexes with low T_g were prepared using surfactant-free emulsion polymerization (SFEP) of MMA and butyl acrylate (BA) with a small amount of DEAEMA as CO₂-switchable comonomer [60]. The T_g of the copolymer was adjusted by the MMA:BA ratio. The authors found that if the T_g is higher than room temperature, the latex is CO₂-redispersible, whereas if the T_g is lower than ambient temperature, latex particles fuse after aggregation and are not easily CO₂-redispersible.

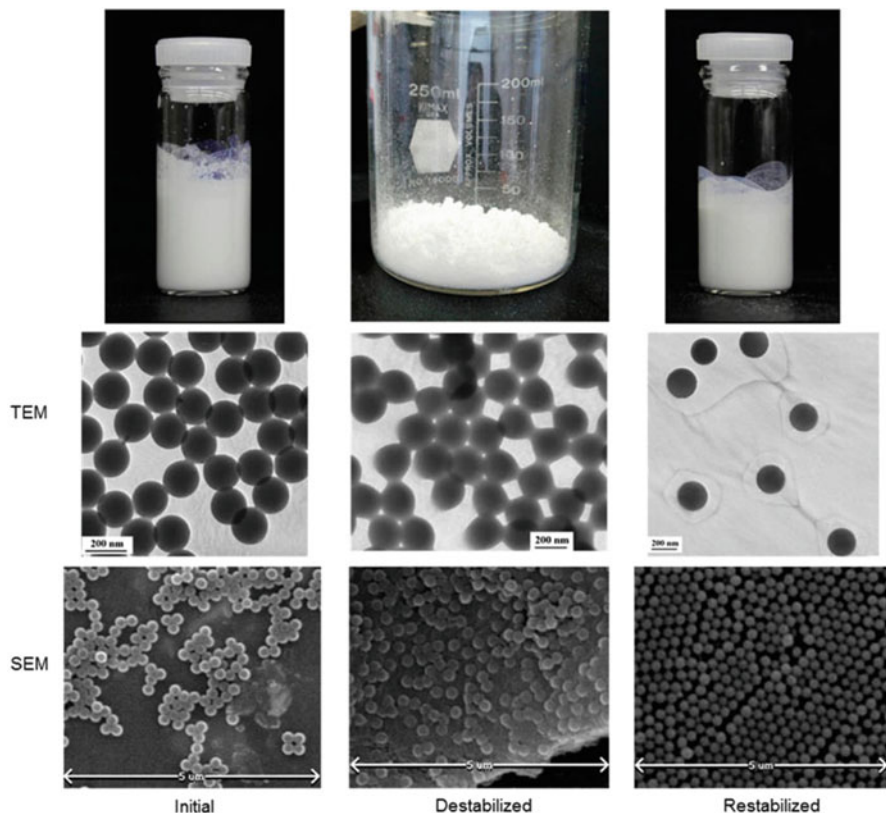


Fig. 9 Photographs and TEM and SEM micrographs of the original latex (*left*), after destabilization in the presence of PDEAEMA (*middle*), and redispersed after 10 min of sonication under CO₂ atmosphere (*right*) [58]

However, if the same low- T_g latexes are coagulated at temperatures lower than their T_g , they can be redispersed by bubbling CO₂ and using ultrasound.

Darabi et al. reported the synthesis of CO₂-switchable living polymer latexes made using nitroxide-mediated polymerization and a polymerization-induced self-assembly (PISA) process [61, 62]. A water-soluble CO₂-switchable first block of DEAEMA was made in water, followed by the addition of MMA monomer. The DEAEMA block acted as both macroinitiator and stabilizer in the SFEP process.

5.4 Switchable Water

The approaches described previously all apply to cationically stabilized latexes. We explored anionic CO₂-switchable latexes (containing carboxylic acid groups) but did not see this as a promising route. We subsequently developed an alternative

approach for anionic latexes, whereby the aqueous phase was CO₂-switchable instead of the particle surface [30]. In this method, the stability of the latex is controlled by adding a “switchable water” ionogen to the aqueous phase. With switchable water, the ionic strength of the aqueous solution can be switched between low and high values by addition and removal of CO₂. This change occurs when an amine or polyamine (the ionogen) is reversibly converted from a neutral to a bicarbonate salt by the presence of CO₂. For example, sodium dodecylsulfate (SDS) in the absence of an ionogen is not CO₂-switchable, but an aqueous solution of SDS and *N,N*-dimethylethanolamine (DMEA, an ionogen) has CO₂-switchable air/water surface tension. PS latex stabilized by SDS and containing a suitable ionogen in the aqueous phase can be aggregated by bubbling CO₂ and redispersed by bubbling Ar or air (to remove the CO₂) [30].

6 Conclusion

CO₂-switchable latexes are an innovative advance in the design of stimuli-responsive polymers. CO₂ is a safe, benign, and inexpensive trigger, and can be easily added or removed from a latex. Although much has been learned about the principles of making CO₂-switchable latexes, there remain many issues that are not well understood. The number of monomers that exhibit effective CO₂-switchability is still somewhat limited, and therefore expanding this selection would be beneficial and provide greater versatility in designing CO₂-switchable nanoparticles. Little is currently quantitatively known about the degrees of protonation/deprotonation occurring under different conditions of, for example, temperature and p*K*_{aH}, or about the role of other species that may be present in a latex (acids, bases, electrolytes). The latter is an especially important concern for commercial products such as paints and coatings, which typically contain several other components besides the latex binder. Another ongoing challenge is learning how to make low-*T*_g latexes redispersible, an important objective for materials intended to form films at lower temperatures. Hydrolysis of monomers containing tertiary amine groups can be a major problem, especially at higher temperatures. In addition to the loss of amines, the hydrolysis products are usually carboxylic acids, which can introduce negative charges that have a deleterious effect on latex stability.

There has been little study of the hydrophobicity of films made from CO₂-switchable latexes, for example using contact angle measurements. When a CO₂-switchable latex dries and forms a film, we expect that the stabilizing groups switch off and therefore become more hydrophobic, a desirable trait in many coatings where moisture resistance is important. However, this has not yet been studied. Another interesting topic is the effect of altering the rates of switching on and off. For some applications this may not be important. However, for applications such as fast-drying traffic paints, fast switching rates are desirable. Increasing the rate of switching depends largely on the p*K*_{aH} of the stabilizing groups but also on mass transfer effects such as the rate of diffusion of CO₂ or air to the switchable

sites. More generally, developing selection criteria for determining the most desirable pK_{aH} for various applications is a valuable objective.

As different applications for CO₂-switchable latexes develop, we need to acquire a better appreciation of the desirable switching traits for that application. For example, is it more important to have fast switching or more complete switching? More complete switching between the protonated and unprotonated states would give a larger change in hydrophobicity/hydrophilicity. Our new ability to make CO₂-switchable latexes and, more generally, CO₂-switchable polymer nanoparticles offers the promise of new, valuable materials and applications that have just begun to be explored.

Acknowledgments We thank the Natural Sciences and Engineering Research Council of Canada (NSERC), the Ontario Research Chairs Program (Cunningham), and Canada Research Chairs Program (Jessop) for financial support.

References

1. Shirakbari N, Ebrahimi M, Salehi-Mobarakeh H, Khorasani M (2014) Effect of surfactant type and concentration on surfactant migration, surface tension, and adhesion of latex films. *J Macromol Sci B Phys* 53:1286–1292
2. Monteiro MJ, Sjöberg M, van der Vlist J, Göttegens C (2000) Synthesis of butyl acrylate–styrene block copolymers in emulsion by reversible addition-fragmentation chain transfer: effect of surfactant migration upon film formation. *J Polym Sci A Polym Chem* 38:4206–4217
3. Aramendia E, Barandiaran E, Grade J, Blease T, Asua M (2005) Improving water sensitivity in acrylic films using surfmers. *Langmuir* 21:1428–1435
4. Zhang Q, Yu G, Wang W, Yuan H, Li B, Zhu S (2012) Preparation of N₂/CO₂ triggered reversibly coagulatable and redispersible latexes by emulsion polymerization of styrene with a reactive switchable surfactant. *Langmuir* 28:5940–5946
5. Jessop PG, Mercer SM, Heldebrant DJ (2012) CO₂-triggered switchable solvents, surfactants, and other materials. *Energy Environ Sci* 5:7240–7253
6. Lin S, Theato P (2013) CO₂-responsive polymers. *Macromol Rapid Commun* 34:1118–1133
7. Darabi A, Jessop PG, Cunningham MF (2016) CO₂-responsive polymeric materials: synthesis, self-assembly, and functional applications. *Chem Soc Rev* 45:4391–4436
8. Liu Y, Jessop PG, Cunningham MF, Eckert CA, Liotta CL (2006) Switchable surfactants. *Science* 313:958–960
9. Jessop PG (2012) Reversibly switchable surfactants and methods of use thereof. US Patent 8,283,385, 9 Oct 2012
10. Brown P, Butts CP, Eastoe J (2013) Stimuli-responsive surfactants. *Soft Matter* 9:2365–2374
11. Mirarefi P, Lee CT (2010) Photo-induced unfolding and inactivation of bovine carbonic anhydrase in the presence of a photoresponsive surfactant. *Biochim Biophys Acta* 1804:106–114
12. Zhang J, Wang S-C, Lee CJ (2009) Photoreversible conformational changes in membrane proteins using light-responsive surfactants. *J Phys Chem B* 113:8569–8580
13. Sakai K, Yamazaki R, Imaizumi Y, Endo T, Sakai H, Abe M (2012) Adsolubilization by a photo-responsive surfactant. *Colloids Surf A* 410:119–124
14. Sakai H, Aikawa S, Matsuda W, Ohmori T, Fukukita Y, Tezuka Y, Matsumura A, Torigoe K, Tsuchiya K, Arimitsu K, Sakamoto K, Sakai K, Abe M (2012) A cinnamic acid-type photo-cleavable surfactant. *J Colloid Interface Sci* 376:160–164

15. Kim I, Rabolt JF, Stroeve P (2000) Dynamic monolayer behavior of a photo-responsive azobenzene surfactant. *Colloids Surf A* 171:167–174
16. Malcolm AS, Dexter AF, Middelberg APJ (2006) Foaming properties of a peptide designed to form stimuli-responsive interfacial films. *Soft Matter* 2:1057–1066
17. Minkenberg CB, Florusse L, Eelkema R, Koper GJM, van Esch JH (2009) Triggered self-assembly of simple dynamic covalent surfactants. *J Am Chem Soc* 131:11274–11275
18. Tabor RF, Tan DD, Han SS, Young SA, Seeger ZLE, Pottage MJ, Garvey CL, Wilkinson BL (2014) Reversible pH- and photocontrollable carbohydrate-based surfactants. *Chem Eur J* 20:13881–13884
19. Tu F, Lee D (2014) Shape-changing and amphiphilicity-reversing janus particles with pH-responsive surfactant properties. *J Am Chem Soc* 136:9999–10006
20. Tang J, Lee MFX, Zhang W, Zhao B, Berry RM, Tam KC (2014) Dual responsive pickering emulsion stabilized by poly[2-(dimethylamino)ethyl methacrylate] grafted cellulose nanocrystals. *Biomacromolecules* 15:3052–3060
21. Fuhrmann K, Po A, Aeberli C, Castagner B, Gauthier MA (2013) Modular design of redox-responsive stabilizers for nanocrystals. *ACS Nano* 9:8243–8250
22. Morikawa M, Murata K, Yamada K, Kimizuka N (2013) Controlled formation of microspheres from ferrocene-derivatized amino acids in binary aqueous/organic media. *Chem Lett* 42:501–503
23. Liu X, Abbott NL (2009) Spatial and temporal control of surfactant systems. *J Colloid Interface Sci* 339:1–18
24. Zhang J, Song Y, Cronin L, Liu T (2008) Self-assembly of organic–inorganic hybrid amphiphilic surfactants with large polyoxometalates as polar head groups. *J Am Chem Soc* 130:14408–14409
25. Aydogan N, Abbott NL (2001) Comparison of the surface activity and bulk aggregation of ferrocenyl surfactants with cationic and anionic headgroups. *Langmuir* 17:5703–5706
26. Saji T, Hoshino K, Aoyagi S (1985) Reversible formation and disruption of micelles by control of the redox state of the head group. *J Am Chem Soc* 107:6865–6868
27. Fowler CI, Jessop PG, Cunningham MF (2012) Aryl amidine and tertiary amine switchable surfactants and their application in the emulsion polymerization of methyl methacrylate. *Macromolecules* 45:2955–2962
28. Cornell EA (2015) *Handbook of chemistry and physics*, 95th edn. CRC Press, Boca Raton
29. Han D, Tong X, Boissiere O, Zhao Y (2012) General strategy for making CO₂-switchable polymers. *ACS Macro Lett* 1:57–61
30. Su X, Robert T, Mercer SM, Humphries C, Cunningham MF, Jessop PG (2013) A conventional surfactant becomes CO₂-responsive in the presence of switchable water additives. *Chem Eur J* 19:5595–5601
31. Middleberg PJ, Malcolm AS, Dexter AF (2007) Peptide surfactants (Pepfactants) for switchable foams and emulsions. *Asia Pac J Chem Eng* 2:362–367
32. Dexter AF, Middelberg APJ (2007) Switchable peptide surfactants with designed metal binding capacity. *J Phys Chem C* 111:10484–10492
33. Carroll JJ, Slupsky JD, Mather AE (1991) The solubility of carbon dioxide in water at low pressure. *J Phys Chem Ref Data* 20:1201–1209
34. Su X, Fowler C, O'Neill C, Pinaud J, Kowal E, Jessop PG, Cunningham M (2013) Emulsion polymerization using switchable surfactants: a route towards water redispersable latexes. *Macromol Symp* 333:93–101
35. Wang L, Qiao W, Cao C, Li Z (2008) Synthesis and characterization of a novel double-tailed cationic surfactant. *Colloids Surf A* 320:271–274
36. Zhang Q, Yu G, Wang W-J, Li B-G, Zhu S (2012) Preparation of CO₂/N₂-triggered reversibly coagulatable and redispersible polyacrylate latexes by emulsion polymerization using a polymeric surfactant. *Macromol Rapid Commun* 33:916–921
37. O'Neill C, Fowler C, Jessop PG, Cunningham MF (2013) Redispersing aggregated latexes made with switchable surfactants. *Green Mater* 1:27–35

38. Qiao W, Zheng Z, Shi Q (2012) Synthesis and properties of a series of CO₂ switchable surfactants with imidazoline group. *J Surfactants Deterg* 15:533–539
39. Chai M, Zheng Z, Bao L, Qiao W (2014) CO₂/N₂ triggered switchable surfactants with imidazole group. *J Surfactants Deterg* 17:383–390
40. Ding Y, Chen S, Xu H, Wang Z, Zhang X, Ngo TH, Smet M (2010) Reversible dispersion of single-walled carbon nanotubes based on a CO₂-responsive dispersant. *Langmuir* 26:16667–16671
41. Zhao Y, Landfester K, Crespy D (2012) CO₂ responsive reversible aggregation of nanoparticles and formation of nanocapsules with an aqueous core. *Soft Matter* 8:11687–11696
42. Moore ER, Lefevre NA (1986) Method for shear coagulation of latex resins. US Patent 4,623,678, 18 Nov 1986
43. Su X, Jessop PG, Cunningham MF (2014) Switchable surfactants at the polystyrene–water interface: effect of molecular structure. *Green Mater* 2:69–81
44. Qian Y, Zhang Q, Qiu X, Zhu S (2014) CO₂-responsive diethylaminoethyl-modified lignin nanoparticles and their application as surfactants for CO₂/N₂-switchable Pickering emulsions. *Green Chem* 16:4963–4968
45. Tang J, Quinlan PJ, Tam KC (2015) Stimuli-responsive pickering emulsions: recent advances and potential applications. *Soft Matter* 11:3512–3529
46. Qiao W, Zheng Z, Peng H (2011) Synthesis of switchable amphiphathic molecules triggered by CO₂ through carbonyl-amine condensation. *Eur J Lipid Sci Technol* 113:841–847
47. Salentinig S, Jackson P, Hawley A (2015) Amine-functionalized CO₂ responsive triblock copolymer micelles—a small-angle X-ray scattering study. *Macromolecules* 48:2283–2289
48. Dai S, Ravi P, Tam KC (2008) pH-responsive polymers: synthesis, properties and applications. *Soft Matter* 4:435–449
49. Yan B, Han D, Boissière O, Ayotte P, Zhao Y (2013) Manipulation of block copolymer vesicles using CO₂: dissociation or “breathing”. *Soft Matter* 9:2011–2016
50. van de Wetering P, Moret EE, Schuurmans-Nieuwenbroek NM, van Steenberg MJ, Hennink WE (1999) Structure–activity relationships of water-soluble cationic methacrylate/methacrylamide polymers for nonviral gene delivery. *Bioconjugate Chem* 10:589–597
51. Carretti E, Dei L, Weiss RG (2005) Soft matter and art conservation. Rheoreversible gels and beyond. *Soft Matter* 1:17–22
52. Gil E, Hudson S (2004) Stimuli-reponsive polymers and their bioconjugates. *Prog Polym Sci* 29:1173–1222
53. Weber C, Hoogenboom R, Schubert US (2012) Temperature responsive bio-compatible polymers based on poly(ethylene oxide) and poly(2-oxazoline)s. *Prog Polym Sci* 37:686–714
54. Fowler CI, Muchemu CM, Miller RE, Phan L, O’Neill C, Jessop PG, Cunningham MF (2011) Emulsion polymerization of styrene and methyl methacrylate using cationic switchable surfactants. *Macromolecules* 44:2501–2509
55. Mihara M, Jessop PG, Cunningham MF (2011) Redispersible polymer colloids using carbon dioxide as an external trigger. *Macromolecules* 44:3688–3693
56. Su X, Jessop PG, Cunningham MF (2012) Surfactant-free polymerization forming switchable latexes that can be aggregated and redispersed by CO₂ removal and then readdition. *Macromolecules* 45:666–670
57. Zhang Q, Yu G, Wang WJ, Yuan H, Li BG, Zhu S (2013) Switchable block copolymer surfactants for preparation of reversibly coagulatable and redispersible poly(methyl methacrylate) latexes. *Macromolecules* 46:1261–1267
58. Pinaud J, Kowal E, Cunningham MF, Jessop PG (2012) 2-(Diethyl)aminoethyl methacrylate as a CO₂-switchable comonomer for the preparation of readily coagulated and redispersed polymer latexes. *ACS Macro Lett* 1:1103–1107
59. Zhang Q, Wang WJ, Lu Y, Li BG, Zhu S (2011) Reversibly coagulatable and redispersible polystyrene latex prepared by emulsion polymerization of styrene containing switchable amidine. *Macromolecules* 44:6539–6545

60. Garipey D, Zhang Q, Zhu S (2015) CO₂-redispersible polymer latexes with low glass transition temperatures. *Macromol Chem Phys* 216:561–568
61. Darabi A, Shirin-Abadi AR, Pinaud J, Jessop PG, Cunningham MF (2014) Nitroxide-mediated surfactant-free emulsion copolymerization of methyl methacrylate and styrene using poly (2-(diethyl)aminoethyl methacrylate-*co*-styrene) as a stimuli-responsive macroalkoxyamine. *Polym Chem* 5:6163–6170
62. Darabi A, Shirin-Abadi AR, Jessop PG, Cunningham MF (2015) Nitroxide-mediated polymerization of 2-(diethylamino)ethyl methacrylate (DEAEMA) in water. *Macromolecules* 48:72–80

Probing Coagulation and Fouling in Colloidal Dispersions with Viscosity Measurements: In Silico Proof of Concept



Martin Kroupa, Michal Vonka, Miroslav Soos, and Juraj Kosek

Abstract Colloidal dispersions in a flow can undergo the unwanted processes of coagulation and fouling. Prevention of these processes requires their proper understanding and the ability to monitor their extent. Currently, neither of these requirements is sufficiently fulfilled and this motivates the development of detailed models that capture the nature of the dispersion processes operating at the scale of primary colloidal particles. We model coagulation and fouling in colloidal dispersions using the dynamic discrete element method (DEM), with an interaction model accounting for particles that are elastic, adhesive, and stabilized by electrostatic charge. At the same time, the particles can adhere to the wall. Flow-field computation captures the mutual influence between particles and flow. The model also includes a pair-wise implementation of lubrication forces. The modeling results indicate that viscosity is highly sensitive to the formation of clusters, reflecting not only the larger size of clusters with increasing surface energy, but also the slower kinetics of coagulation in charge-stabilized dispersions. By contrast, viscosity is not sensitive to the attachment of particles to the wall. The mechanism of fouling determined from the simulation results comprises the initial bulk formation of clusters and subsequent dynamic wall attachment and detachment of the clusters. The presented work improves understanding of the dynamic behavior of colloidal dispersions, which is strongly relevant for industrial applications as well as for on-line monitoring and control.

The online version of this chapter (doi:[10.1007/12_2017_17](https://doi.org/10.1007/12_2017_17)) contains supplementary material, which is available to authorized users.

M. Kroupa, M. Soos (✉), and J. Kosek (✉)
Department of Chemical Engineering, University of Chemistry and Technology Prague,
Technicka 5, 16628 Prague 6, Czech Republic
e-mail: Miroslav.Soos@vscht.cz; Juraj.Kosek@vscht.cz

M. Vonka
BASF SE, Carl-Bosch-Strasse 38, 67056 Ludwigshafen am Rhein, Germany

Keywords Coagulation • Fouling • Modeling • Suspension rheology

Contents

| | | |
|-----|---|-----|
| 1 | Introduction | 162 |
| 2 | Mathematical Model | 165 |
| 2.1 | Hydrodynamics | 165 |
| 2.2 | Lubrication Forces | 167 |
| 2.3 | Structure of the Computational Domain | 167 |
| 2.4 | Nonhydrodynamic Interactions | 168 |
| 2.5 | Repulsive Particle–Wall Interactions | 168 |
| 2.6 | Adhesive Interactions | 168 |
| 2.7 | Evaluation of Viscosity | 171 |
| 2.8 | Numerical Details | 171 |
| 3 | Results and Discussion | 171 |
| 3.1 | Effect of Shear Rate | 172 |
| 3.2 | Effect of Surface Energy | 172 |
| 3.3 | Effect of Primary Particle Size | 173 |
| 3.4 | Effect of Particle Volume Fraction | 173 |
| 3.5 | Effect of Surface Potential | 174 |
| 3.6 | Adhesive Wall | 176 |
| 4 | Conclusions | 180 |
| | References | 180 |

1 Introduction

Colloidal dispersions present interesting systems from both the practical and theoretical points of view. Their practical utilization ranges from food technology through cosmetics to adhesives and paints. However, they represent a very complex system in terms of theoretical understanding, with a rich palette of physical phenomena, unexplained effects, and nontrivial relationships.

Among the most important phenomena influencing the properties of colloidal dispersions are the processes of coagulation and fouling. Coagulation refers to the bulk formation of clusters from primary colloidal particles, whereas fouling (or clogging) is the attachment of particles or clusters to a solid boundary (e.g., container walls, stirrers, or baffles). Both coagulation and fouling can be either perikinetic (i.e., induced by the thermal motion of particles) or orthokinetic (i.e., caused by the presence of flow) [1]. In the orthokinetic case, both the clusters in the bulk and those attached to the wall can break due to stress introduced by the flow. We narrow our focus to orthokinetic (i.e., shear-induced) coagulation, fouling, and breakage because these processes have a high practical relevance.

In the past two decades, a number of significant advances have improved our understanding of the mechanisms of shear-induced coagulation and breakage, and various relations are available for the kinetics of these phenomena [2–5]. However, there is still a certain disconnection between models and experiments in terms of

predicted and observed quantities. Namely, models can predict the coagulation and breakage rates together with the cluster size, even in concentrated dispersions [3, 6]. However, experimental measurements of cluster size are limited to highly diluted dispersions. On the other hand, the dynamics of coagulation can be observed by measurements of viscosity, even for concentrated dispersions [7, 8], but the theory connecting the characteristics of a colloidal dispersion undergoing coagulation and fouling to its rheological properties is still incomplete and largely relies on empirical relations [9].

The process of fouling is much less explored than coagulation. This might be caused by the fact that it is more difficult to find a well-defined system for both simulations and experiments. Although some systems, such as heat exchangers [10, 11] and membrane bioreactors [12, 13], suffering from fouling problems are relatively well documented, fouling of reactors by polymer latexes has received much less attention in the literature. The topic of particulate fouling in microchannels, including experimental and modeling studies, was thoroughly reviewed by Henry et al. The study classified the following four different stages of fouling [14]:

1. Deposition of primary particles onto the wall
2. Resuspension of primary particles or clusters from the wall
3. Coagulation (agglomeration) in the bulk flow
4. Clogging, that is, the attachment of particles or clusters to a layer that is already present on the wall

Besides the detailed description and categorization of both early and later stages of fouling, the authors introduced a new modeling approach based on the one-particle probability density function (PDF) [14]. The model takes into account interparticle forces and fluid dynamics and is able to account for wall surface roughness [15, 16]. Due to its relatively coarse level of description, this approach is suitable for industrially important cases. At the same time, it results in a certain loss of detail, which prevents thorough study of fouling mechanisms.

The authors also emphasized the necessity for the models of fouling to incorporate all the physical interactions affecting the process, namely, particle–particle, fluid–particle, fluid–surface, and particle–surface interactions [14]. Furthermore, it was pointed out that the broad range of temporal and spatial scales at which these interactions act makes the modeling of fouling a very complicated task. Several studies have attempted to fulfill these requirements. Approaches based on the solution of Navier–Stokes equations, such as the force coupling method or direct numerical simulation, treat the fluid dynamics in a detailed way [17–19]. However, the description of interparticle forces is usually simplified and the number of particles in the simulation is relatively small compared with other particle-based methods [20].

Experimentally, fouling by colloidal particles in a stirred reactor was investigated by Urrutia et al. [1]. In the perikinetic regime, the process was relatively well controlled and a monolayer of particles was mostly observed. In the orthokinetic regime, the situation was more complicated due to flow heterogeneities. The authors related their results to previous studies of bulk coagulation and coagulation

at the liquid–gas interface [21–23]. A different possibility for experimental investigation of fouling is the direct observation of deposited particles in a specially designed apparatus [24–27]. These studies represent pioneering work and their benefit is unquestionable. Nevertheless, for true understanding of the underlying mechanisms of fouling, a connection to some mechanistic model is necessary.

In aerosol systems, particle-based modeling was extensively used to simulate the deposition of particles either to walls of a channel or to fibers during filtration [20, 28–32]. For polymer latexes, such detailed modeling studies are not available. Lazzari modeled the dynamics of colloidal particle deposition using population balance equations (PBE) and identified three different regimes of deposition, which depended on the ratio of the deposition and the aggregation characteristic times [33]. However, this approach relies on identification of mechanisms that lead to deposition and the subsequent determination of the rate constants required for the PBE.

Both coagulation and fouling are strongly connected to the flow conditions and to the properties of the dispersed and the dispersing phases. The interplay between these two groups of phenomena leads to either well-stabilized systems or to coagulum formation and consequent fouling. If not controlled, these processes are responsible for large amounts of off-specification products and consequent economical losses throughout the industry. So far, industry mainly relies on empirical knowledge, whereas deeper understanding or even control of the systems is usually absent. Understanding the underpinning laws behind these interconnected phenomena is of crucial importance and this task requires a complex approach that is able to consider all the relevant phenomena, identify their relative importance, and explain the underlying mechanisms.

The present article aims at a detailed description of phenomena taking place in flowing colloidal dispersions using a model based on the discrete element method (DEM). The model incorporates a description of charge-stabilized particles that are elastic and adhesive [34]. For simulations of fouling, the elastic and adhesive interaction between the particles and the wall is considered. The mutual influence between the particles and the flow is accounted for using the two-way coupling technique. From the flow field obtained by this method, the suspension viscosity is evaluated on the basis of the balance of forces acting on the boundary of the domain. Lubrication forces, which are very important (especially in concentrated dispersions), are considered for both the particle–particle and particle–wall interactions.

This approach enables us to identify the mechanisms leading to fouling and their relative importance. Furthermore, we demonstrate that the kinetics of fouling is slower than the kinetics of coagulation and identify how it is influenced by the properties of the system. The fouling and coagulation rates obtained from these results can be directly used in the PBE modeling. The results show that coagulation has a significant effect on the viscosity of the dispersion and that changes in viscosity are related to the size and structure of clusters. On the other hand, the process of fouling does not result in any observable effect on viscosity, within the scatter naturally occurring in the results due to the dynamic nature of the system.

2 Mathematical Model

As in our previous work [6, 35], the model used in this article consists of two parts. The first part computes the flow field in the domain. This flow field is then, together with other forces and torques, used in the DEM for computation of particle dynamics. Particles in DEM are described as discrete elements. Each element is characterized by its mass (m_i), position (\mathbf{x}_i), velocity (\mathbf{v}_i), and rotation rate ($\boldsymbol{\Omega}_i$). The governing equation for the translational motion is Newton's second law:

$$\frac{d^2\mathbf{x}_i}{dt^2} = \frac{\mathbf{F}_i}{m_i}, \tag{1}$$

where \mathbf{F}_i represents the sum of all forces acting on the discrete element i . The temporal change in the rotation rate ($\boldsymbol{\Omega}_i$) is expressed as follows:

$$\frac{d\boldsymbol{\Omega}_i}{dt} = \frac{\mathbf{M}_i}{I_i}, \tag{2}$$

where \mathbf{M}_i is the sum of all torques acting on particle i and I_i is the particle momentum of inertia. For a homogeneous solid sphere, we have $I_i = \frac{2}{5}m_iR_p^2$ (particle moment of inertia around its center) and $m_i = \frac{4}{3}\pi R_p^3\rho_p$.

2.1 Hydrodynamics

The computation of hydrodynamics in the model involves both the effect of flow on the particles (i.e., the drag force and torque) and the effect of particles on the flow, including computation of the flow field. The framework for the calculation of these effects is introduced in this section.

Because particles considered in this work are of small size (under 1 μm), their Reynolds number is small, and the drag force $\mathbf{F}_{d,i}$ acting on them can be described by Stokes' law, as follows:

$$\mathbf{F}_{d,i} = 6\pi\eta_f R_p (\mathbf{v}_i^f - \mathbf{v}_i^p), \tag{3}$$

where η_f is the fluid dynamic viscosity, R_p is the radius of the particle, and \mathbf{v}_i^f and \mathbf{v}_i^p are the velocities of the fluid and particle, respectively. Buoyancy and gravity forces are neglected because the particles and fluid have the same density. The large applied shear rates cause the Peclet number to be very high and, thus, the effect of Brownian motion can be neglected. The torque on a particle caused by the local rotation of the fluid can be computed as follows [36]:

$$\mathbf{M}_i^f = \pi\eta_f(2R_p)^3 \left(\frac{1}{2} \boldsymbol{\omega}_i - \boldsymbol{\Omega}_i \right), \quad (4)$$

where $\boldsymbol{\omega}_i$ is the angular velocity of the fluid at the position of the particle center.

The effect that the particles have on the fluid is taken into account using the so-called two-way coupling between particles and fluid, which results in the modified Navier–Stokes equations in the following form [20, 37]:

$$\frac{\partial}{\partial t}(\phi_v \rho_f) + \nabla \cdot (\phi_v \rho_f \mathbf{u}) = 0 \quad (5)$$

$$\frac{\partial}{\partial t}(\phi_v \rho_f \mathbf{u}) + (\mathbf{u} \cdot \nabla)(\phi_v \rho_f \mathbf{u}) = \phi_v \eta \nabla^2 \mathbf{u} - \phi_v \nabla p - \mathbf{b}, \quad (6)$$

where ρ_f is the fluid density, \mathbf{u} is the fluid velocity, p is the pressure, \mathbf{b} is the body force exerted by particles, $\phi_v = 1 - \phi'$ is the fraction of voids, and ϕ' is the local volume fraction of particles.

For the numerical solution of Eqs. (5) and (6) we used the program OpenFOAM [38], which was coupled with the DEM model. The computational grid for the finite volume method (FVM) that is used to discretize Eqs. (5) and (6) was chosen to be regular, with cubic grid cells of size κ (length of the edge) and volume $V = \kappa^3$.

The body force $\mathbf{b}_{n,i}$, which the particle i exerts on the cell n , can be expressed as follows:

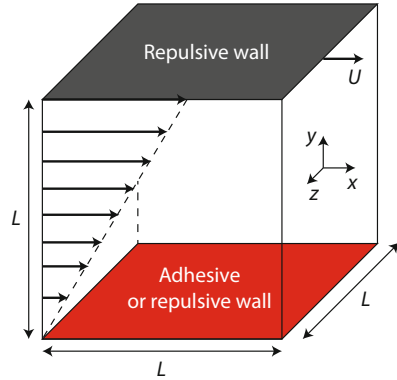
$$\mathbf{b}_{n,i} = -\frac{V_n}{V} \mathbf{F}_{d,i}, \quad (7)$$

where V_n is the volume of the subgrid cell opposite to cell n , V is the total grid cell volume, and $\mathbf{F}_{d,i}$ is the drag force acting on the i th particle. In Eq. (7), the so-called volume partitioning was used to distribute the body force of the particle onto the grid. Details of this approach are described by Marshall [20] and in our previous work [6, 35].

Determination of the local particle volume fraction ϕ' is based on the procedure of distributing the particle volume as a “cloud” around its center using a Gaussian weighting function. This procedure is described in more detail in the Supporting Information.

A discussion and validation of the hydrodynamic model [6] led to the cell size of the grid being chosen as $\kappa = 2.5R_p$. The resulting number of cubic cells is dependent on the size of the computational domain L , which (Sect. 2.3) depends on the particle volume fraction ϕ , number of particles N , and primary particle size R_p . For $\phi = 0.09$, $R_p = 125$ nm, and $N = 5,000$ there are 24 cubic cells in each spatial direction and 13,824 cells overall.

Fig. 1 Schematics of the computational domain with linear velocity profile. The *upper wall* is always repulsive, whereas the *lower wall* can be either adhesive or repulsive



2.2 Lubrication Forces

Particles immersed in a fluid affect each other through the fluid by lubrication forces [9]. These forces originate from squeezing out or sucking in the fluid when particles approach or recede, respectively. The lubrication interaction is a form of hydrodynamic interaction and, therefore, has the same origin as the framework for the computation of flow field (as described Sect. 2.1). However, because of the relatively coarse resolution of the fluid solver, the lubrication forces have to be incorporated additionally. The formulation of lubrication forces used in this work was developed by Dance and Maxey [39] and their implementation into the DEM model was thoroughly described in our previous work [35]. Additionally, we provide the necessary equations and a brief explanation in the Supporting Information.

2.3 Structure of the Computational Domain

For all simulations, we used the simple shear model of flow between two parallel plates (see Fig. 1). The upper and lower boundaries of a spatially three-dimensional box were set to represent a solid wall. The upper wall moved with velocity U and this initially created a linear velocity profile with uniform shear rate $G = \frac{U}{L}$. Later in the simulations, the velocity profile changed as a result of the presence of particles. All the remaining boundaries were considered periodic. A total of $N = 5,000$ primary particles were randomly placed into the domain of dimensions $L \times L \times L$. The actual value of L varied with the particle volume fraction ϕ and primary particle size R_p . The initial positions of primary particles were chosen such that no solid body interaction occurred at the beginning of simulations.

2.4 *Nonhydrodynamic Interactions*

The interactions between particles and between particles and the wall are crucial parts of the model for simulations of coagulation and fouling. In this section, we introduce models for all the interactions that are not related to hydrodynamics. To investigate fouling (i.e., the effect of the wall on the behavior of the system), we performed simulations for the following categories of particle–wall interactions:

Repulsive wall: Strong noncontact repulsion, with no contact tangential interactions.

Adhesive wall: Adhesive and elastic wall with contact tangential interactions and noncontact van der Waals attraction.

Note that the hydrodynamic interaction between a particle and the wall is the same for both categories. We begin with the description of the repulsive particle–wall interaction. Later, we introduce the framework for the computation of the connected noncontact and contact interactions, which is the same for both the adhesive wall and the interactions between particles.

2.5 *Repulsive Particle–Wall Interactions*

The purpose of the repulsive wall in the model is to close the system with the smallest possible effect on its behavior; therefore, we introduce a description of particle–wall interactions that is as simple as possible. For this reason, the hydration force describing a purely repulsive interaction between the particle and the wall was implemented [40]. In terms of the interaction potential energy (V_h), the hydration repulsion can be described as follows [41]:

$$V_h = \pi R_p F_0 \delta_0^2 \exp(-H/\delta_0), \quad (8)$$

where H is the particle–wall separation distance, F_0 is the hydration force constant, and δ_0 is the characteristic decay length. The values of the constants used in our model for the particle–wall interactions were $F_0 = 2 \times 10^8 \text{ N m}^{-2}$ and $\delta_0 = 3 \times 10^{-10} \text{ m}$ [35]. The interaction force (F_h) is the negative derivative of V_h with respect to separation distance (H) and is given by $F_h = -\frac{dV_h}{dH}$.

2.6 *Adhesive Interactions*

In our previous work [35], we introduced a model for the evaluation of viscosity and tested it for the most elementary system of hard sphere particles. Here, we extend these results and examine the viscosity of a suspension composed of elastic and adhesive particles. For the modeling of this system, we adopt the formulation of

normal interparticle interactions described by connection of the Derjaguin–Landau–Vervey–Overbeek (DLVO) and Johnson–Kendall–Roberts (JKR) theories. This connection was developed in our previous work [6, 34] and is briefly recalled here. The tangential forces acting between particles and between particles and the wall are described in the Supporting Information.

DLVO theory describes the noncontact interaction between electrostatically stabilized particles, which are also subject to van der Waals forces. As such, it comprises two contributions. For the van der Waals attractive potential energy ($U_{\text{vdW}}^{\text{p-p}}$) between two spherical particles of the same radius (R_p), we used the following expression [42]:

$$U_{\text{vdW}}^{\text{p-p}} = -\frac{A_H}{6} \left\{ \frac{2R_p^2}{h^2 + 4hR_p} + \frac{2R_p^2}{(h + 2R_p)^2} + \ln \left[1 - \left(\frac{2R_p}{h + 2R_p} \right)^2 \right] \right\}, \quad (9)$$

where h is the separation distance such that $h = u - 2R_p$, where u is the distance between centers of the two particles. The quantity $A_H^{\text{p-p}}$ is the Hamaker constant of the particle–particle interaction.

The potential energy ($U_{\text{vdW}}^{\text{p-w}}$) between the particle and the wall is described as follows [42]:

$$U_{\text{vdW}}^{\text{p-p}} = -\frac{A_H^{\text{p-w}}R_p}{6H} \left[1 + \frac{H}{2R_p + H} + \frac{H}{R_p} \ln \left(\frac{H}{2R_p + H} \right) \right], \quad (10)$$

where $A_H^{\text{p-w}}$ is the Hamaker constant of the particle–wall interaction. The electrostatic repulsive potential energy (U_{ele}) of two colloidal particles can be expressed as follows [42]:

$$U_{\text{ele}} = 2\pi\epsilon_0\epsilon_rR_p(\psi)^2 \ln(1 + \exp(-\kappa h)), \quad (11)$$

where ϵ_0 is the vacuum permittivity, ϵ_r is the relative permittivity of the medium, ψ is the surface potential of the particles (assumed to be constant in the model), and κ is the reciprocal of the Debye length κ^{-1} . Electrostatic stabilization is not considered for the particle–wall interaction.

The resulting DLVO potential energy (U_{DLVO}) is obtained by the following summation:

$$U_{\text{DLVO}} = U_{\text{vdW}} + U_{\text{ele}}. \quad (12)$$

The corresponding interaction force (F_{DLVO}) is the negative derivative of U_{DLVO} with respect to separation distance (h) and is given by $F_{\text{DLVO}} = -\frac{dU_{\text{DLVO}}}{dh}$.

JKR theory describes the interaction of adhesive, elastic solid bodies. The adhesive force in JKR theory is assumed to act only within the flattened contact region. The equations for JKR theory used in this work were proposed by Johnson et al. [43]. We use the implementation of Marshall [20]. The equations are valid generally for spheres with radii R_p^i and R_p^j . The so-called effective radius (R) is

defined as $R = 1 / \left(\frac{1}{R_p^i} + \frac{1}{R_p^j} \right)$. For contact of the particle with the wall, the radius R_p^j becomes infinite. When no external force is acting on the particles and the force equilibrium is reached, we can define the equilibrium radius of the contact area (a_0) as follows:

$$a_0 = \left(\frac{9\pi\gamma R^2}{E} \right)^{1/3}, \quad (13)$$

where γ denotes the surface energy (as discussed later in this section) and E is the effective Young's modulus, given by the following expression:

$$\frac{1}{E} = \frac{1 - \nu_i^2}{E_i} + \frac{1 - \nu_j^2}{E_j}, \quad (14)$$

where E_i and E_j are the Young's moduli and the quantities ν_i and ν_j are the Poisson's ratios of the two interacting bodies. The following equation for the (nonequilibrium) radius of the contact area (a) is implicit [20]:

$$h = 6^{1/3} \delta_C \left[2 \left(\frac{a}{a_0} \right)^2 - \frac{4}{3} \left(\frac{a}{a_0} \right)^{1/2} \right], \quad (15)$$

where the critical overlap (δ_C) is given by the following equation:

$$\delta_C = \frac{a_0^2}{2(6)^{1/3} R}. \quad (16)$$

Finally, the normal force (F_{ne}) between two colliding particles can be obtained from the following equation:

$$\frac{F_{ne}}{F_C} = 4 \left(\frac{a}{a_0} \right)^3 - 4 \left(\frac{a}{a_0} \right)^{3/2}, \quad (17)$$

where the critical force (F_C) is given by the following:

$$F_C = 3\pi\gamma R. \quad (18)$$

The quantity F_C corresponds to the maximum adhesive force that can occur between particles described by JKR theory. The direct relation between F_C and the surface energy (γ) represents a powerful possibility to use both theoretical predictions of γ or mimic a specific system based on atomic force microscopy (AFM) colloidal probe measurements [44, 45]. Detailed discussion about this choice, together with a description of the connection between DLVO and JKR theories, can be found in our previous article [34].

2.7 Evaluation of Viscosity

The viscosity of the suspension is evaluated from the balance of forces acting on the upper wall. The model system is set correspondingly to the basic physical phenomena taking place in a standard rotational viscometer. The detailed procedure is described in our previous work [35].

2.8 Numerical Details

The dynamics in the two parts of the model occur on different time scales and, therefore, different time steps are required for each part. Following the guidelines of Marshall [20], the time step for particle motion was set as $\Delta t_p = 1 \times 10^{-10}$ s and the time step for the fluid dynamics was set as $\Delta t_F = \frac{1}{100G}$, where $G = \frac{U}{L}$ is the shear rate. The numerical issues are more thoroughly elaborated in our previous work [6, 34].

For integration of the resulting system of ordinary differential equations Eqs. (1) and (2), we used the solver LSODE from ODEPACK [46].

3 Results and Discussion

Similar to the description of the model, the presented results are divided into two parts. The first part (Sects. 3.1–3.5) focuses on the bulk behavior of an adhesive suspension with various degrees of stabilization and, for this case, both the walls in the computational domain are repulsive. In the second part (Sect. 3.6), the lower wall is adhesive and the particles and clusters can attach to it. Constant parameters of the simulations are summarized in Table 1. The values of studied parameters are stated in the figure captions.

Table 1 Values of model parameters used in the simulations

| Quantity | Value | Name |
|------------------------|--------------------------|--------------------------------|
| A_H | 1.3×10^{-20} J | Hamaker constant |
| E | 1.6 GPa | Young's modulus |
| ν | 0.2 | Poisson's ratio |
| ρ_p | 1,000 kg m ⁻³ | Particle density |
| μ_{eff} | 0.5 | Effective friction coefficient |
| θ^{crit} | $\pi/4$ | Critical rolling angle |
| η_F | 1×10^{-3} Pa s | Fluid dynamic viscosity |
| ρ_F | 1,000 kg m ⁻³ | Fluid density |
| T | 293.15 K | Absolute temperature |

3.1 Effect of Shear Rate

For the simulations of coagulation and breakage, the first investigated parameter was the shear rate G . In Fig. 2, we show its effect on the size of clusters (represented as the root-mean-squared radius of gyration) and the suspension viscosity and their dependence on the normalized time. The clusters start to grow after a certain induction period, because the particles need to approach each other from the originally dispersed state. The effect of various parameters on the cluster size and its dynamic development is discussed elsewhere in much more detail [6].

In contrast to the presence of a lag period for the growth of cluster size, the viscosity starts to increase immediately from the beginning of the simulation. This is caused by the fact that the initial condition of the calculation represents a flow field undisturbed by the presence of particles. Therefore, there is an induction period, during which the dynamics of the viscosity time development is not realistic. Such behavior was also observed for the simpler system of hard spheres [35].

3.2 Effect of Surface Energy

The dynamic development of the system shows that both the cluster size and the viscosity reach a steady value after a certain period of time. This value corresponds to the state of dynamic equilibrium resulting from the interplay between the coagulation and breakage of clusters [6]. The steady state value decreases with the applied shear rate, which is shown in Fig. 3a together with the effect of surface energy γ . This quantity represents the strength of adhesion between the primary particles and it is therefore not surprising that the cluster size increases with

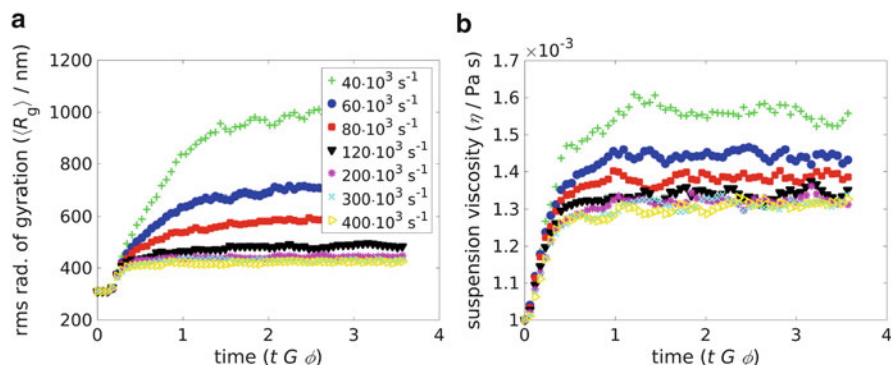


Fig. 2 (a) Root-mean-square radius of gyration and (b) viscosity as a function of dimensionless time for different values of shear rate. The legend is the same for both (a) and (b). The values of parameters were $\phi = 0.09$, $R_p = 400 \text{ nm}$, $\gamma = 0.1 \text{ mJ m}^{-2}$, and $\psi = 0 \text{ mV}$

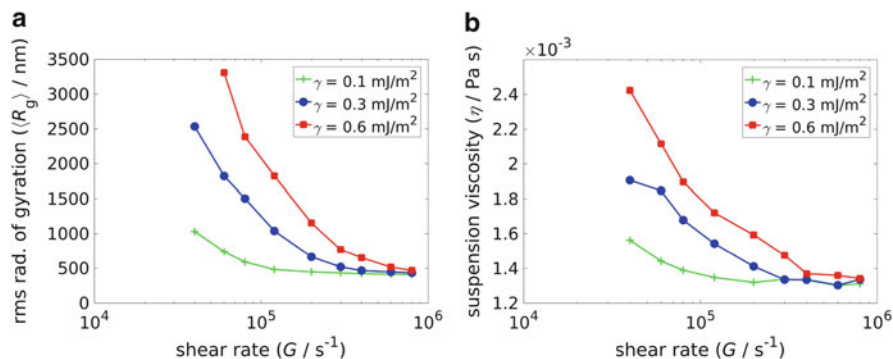


Fig. 3 Steady-state (a) root-mean-square radius of gyration and (b) viscosity as a function of shear rate for different values of surface energy γ . The values of parameters were $\phi = 0.09$, $R_p = 400 \text{ nm}$, and $\psi = 0 \text{ mV}$

increasing γ . Interestingly, a very similar behavior is observed in the plot relating viscosity to the shear rate (Fig. 3b), suggesting that there is a relation between cluster size and viscosity. These results are the quantification of various experimental observations that used viscosity measurements to observe coagulation (i.e., cluster growth) in stabilized systems in a qualitative way [7, 8]. Using our model, the increase in viscosity can be directly related to the increase in cluster size.

3.3 Effect of Primary Particle Size

The particle size affects the relative importance of the forces in the system. This results in the relative size of clusters being larger for smaller primary particles, as can be seen in Fig. 4a and in our previous work [6]. This effect clearly translates to the viscosity of the suspension (see Fig. 4b) and suggests that the viscosity of a coagulating suspension might be dependent not only on the size of clusters, but also on the size of the primary particles.

3.4 Effect of Particle Volume Fraction

It can be seen from Fig. 5 that, although there is an observable effect of cluster size on the suspension viscosity that results in the shear-thinning behavior, the effect of the particle volume fraction is even stronger. This result is relevant for the handling and processing of colloidal latexes, because it shows that their viscosity is affected by several system properties, such as the volume fraction of solids, shear rate, particle size, and surface energy. This dependency is in direct contrast to the

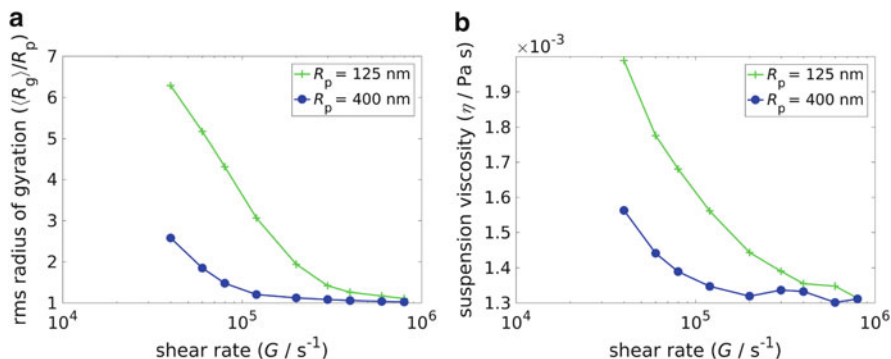


Fig. 4 Steady-state (a) root-mean-square radius of gyration (normalized) and (b) viscosity as a function of shear rate for different values of primary particle size R_p . The values of parameters were $\phi = 0.09$, $\gamma = 0.1 \text{ mJ m}^{-2}$, and $\psi = 0 \text{ mV}$

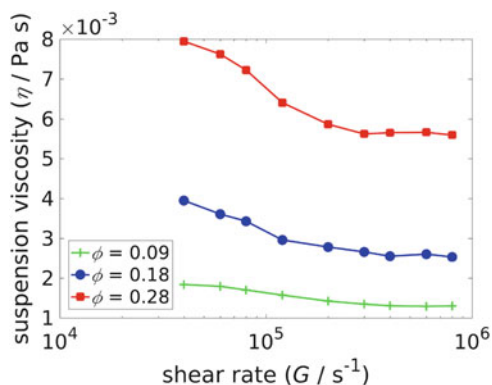


Fig. 5 Steady-state viscosity as a function of shear rate for different values of particle volume fraction ϕ . The values of parameters were $\gamma = 0.1 \text{ mJ m}^{-2}$, $R_p = 125 \text{ nm}$, and $\psi = 0 \text{ mV}$

suspensions of hard spheres (noninteracting particles), where the effect of the particle volume fraction dominates [35].

3.5 Effect of Surface Potential

The simulations we have considered so far were for a system without an energy barrier between the particles (i.e., for surface potential $\psi = 0 \text{ mV}$). Setting a nonzero value of ψ opens a whole new dimension of behavior rich with various nontrivial phenomena. The time development of cluster size and viscosity is shown in Fig. 6. It is clearly observable that the presence of an energy barrier significantly affects the dynamics of the system. For small values of ψ , the time developments of

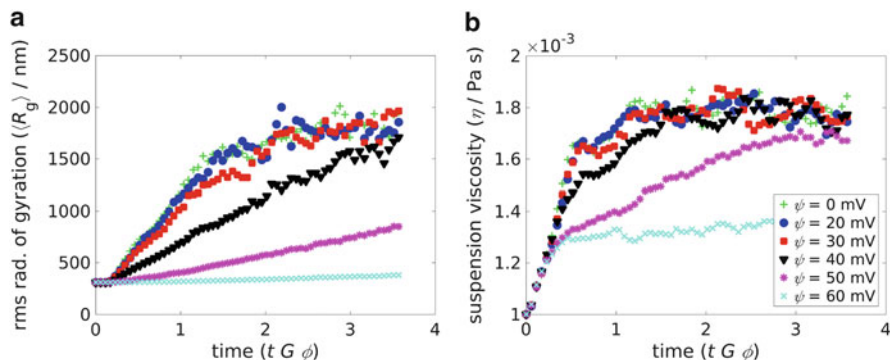


Fig. 6 (a) Root-mean-square radius of gyration and (b) viscosity as a function of time for different values of surface potential ψ . The legend is the same for both (a) and (b). The values of parameters were $\phi = 0.09$, $R_p = 400$ nm, $\gamma = 0.3$ mJ m $^{-2}$, and $G = 60,000$ s $^{-1}$

both $\langle R_g \rangle$ and η follow similar trends (Fig. 2), but increased stabilization causes much a slower increase in both these quantities with time. Although the dynamics is different, it is clearly visible that the curves for both the cluster size and viscosity eventually reach the same steady-state value. This can be observed for cases that reach the steady state within the timescale of the simulation. Note that the energy barrier acts only as kinetic stabilization and does not alter the equilibrium properties of the system, although it dramatically influences the timescale of the phenomena.

To generalize these trends, in Fig. 7 we plot the shear-rate dependence of the cluster size, viscosity, and number of particles in clusters. These plots do not represent steady-state values, because the dynamics for large values of ψ is too slow to be captured by the model within a reasonable computational time. Instead, we show the state of the system at (normalized) time $tG\phi = 3.57$ (i.e., at the end-time of simulations in Fig. 6). The system shows relatively complicated behavior, with a maximum occurring in the dependence of all the quantities on the shear rate. This complex dependence highlights the need to understand the details of the dynamic behavior of colloidal dispersions. When such a plot is constructed for the typical timescale of a process under investigation, it reveals dynamic information about the possible state of the dispersion handled in the process.

In Fig. 7d, we plot the characteristic time of coagulation as a function of the shear rate. Let us first focus on the green curve for a destabilized system ($\psi = 0$ mV). The slope of the curve in the double logarithmic plot (i.e., the exponent of the power-law scaling) is close to -1 , which suggests that the dynamics is governed purely by the flow. With increasing values of ψ , the slope of the curve starts to change rapidly at low values of the shear rate. This indicates that, in this region, in addition to flow dynamics, the energy barrier strongly influences the dynamics of coagulation. The influence of the energy barrier presents a generalization of our previous findings, which revealed a power-law scaling of t_c with G , with the

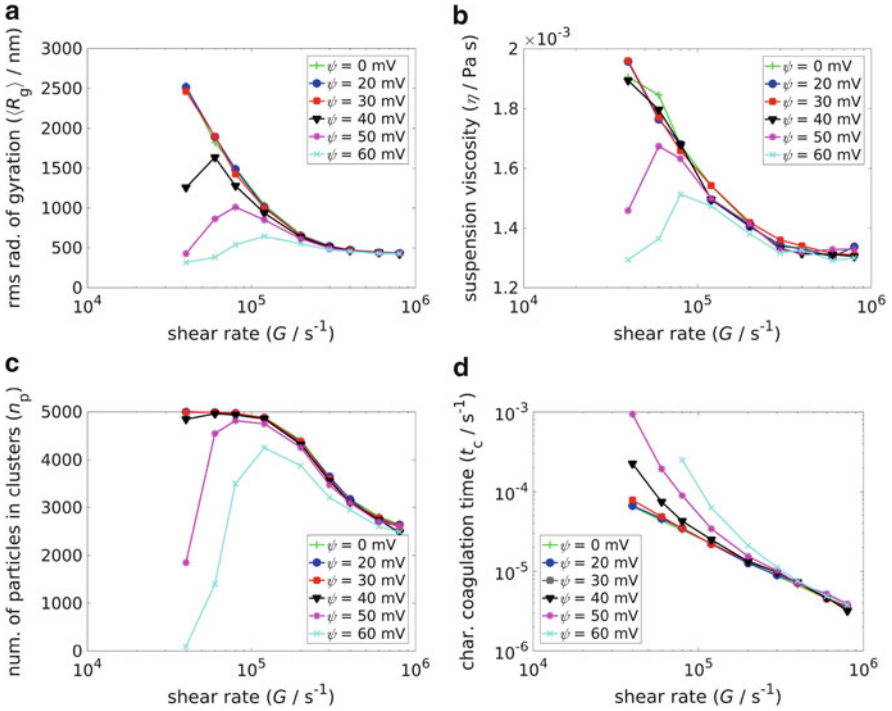


Fig. 7 (a) Root-mean-square radius of gyration, (b) viscosity, (c) number of particles in clusters, and (d) characteristic coagulation time as a function of shear rate for different values of surface potential ψ . (a–c) represent the state of the system at time $tG\phi = 3.57$ (i.e., at the end-time of simulations in Fig. 6). The values of parameters were $\phi = 0.09$, $R_p = 400$ nm, and $\gamma = 0.3$ mJ m $^{-2}$

exponent being much smaller than -1 for highly stabilized systems. Here, these results were extended and related to the limit of a destabilized system.

3.6 Adhesive Wall

Here, we move from a system with both repulsive walls to a system in which only the upper wall is repulsive and the lower wall is adhesive. As a consequence of this change, the particles and clusters can attach to the lower wall. This can be observed in Fig. 8, which shows snapshots from the end of two simulations with particles on the wall. These snapshots show that completely different results are obtained for different applied shear rates G . For the lower shear rate of $G = 80 \times 10^3$ s $^{-1}$, a number of large clusters are formed in the system (green color) and a considerable fraction are attached to the wall (red color). On the other hand, for $G = 800 \times 10^3$ s $^{-1}$, many particles remain in a dispersed state (blue color) and only a few are attached to the wall.

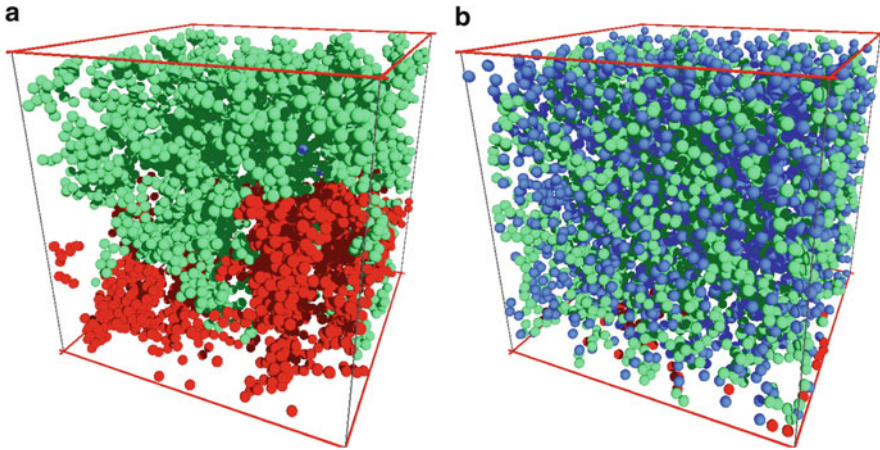


Fig. 8 Snapshots from simulations with the adhesive wall for dispersions under (a) low shear ($G = 80 \times 10^3 \text{ s}^{-1}$) and (b) high shear ($G = 800 \times 10^3 \text{ s}^{-1}$). *Blue* particles are dispersed particles, *green* are coagulated, and *red* are attached to the wall (both directly and indirectly). The values of parameters were $\phi = 0.09$, $\gamma = 0.1 \text{ mJ m}^{-2}$, and $R_p = 125 \text{ nm}$

These qualitative observations are quantified in Fig. 9a as the dependence of the number of particles in clusters (green) or attached to the wall (red) on time for the two different values of shear rate. Apart from the above-mentioned differences, there are two other interesting phenomena. First, there is a significant difference between the dynamics of coagulation (i.e., the formation of clusters) and the dynamics of fouling (i.e., the attachment of particles to the wall). Although the number of particles in clusters quickly reaches a steady state for both values of G , there is a time delay before the particles start to attach to the wall. Second, the number of particles attached to the wall shows a large scatter compared with bulk behavior. This is because there are large clusters attaching to and detaching from the wall during the course of the simulation. The maximum number of wall-attached particles is plotted in Fig. 9b as a function of shear rate. Two types of particle behavior can be observed in the system. Either the particles are all attached to the wall at low shear rates, or very few particles are attached at high shear rates. The transition between these two regimes is rapid.

From the differences in the dynamics of cluster formation and wall attachment, it can be concluded that the characteristic time of fouling is much longer than the characteristic time of coagulation, as shown in Fig. 10. This suggests that the mechanism of fouling in simple shear flow consists of two phases. First, bulk coagulation takes place. Subsequently, the attachment of clusters to the wall creates a particle layer, which sticks to the wall and starts the fouling on the wall. The attached clusters can break and only some particles stay on the wall, which leads to a large fluctuation in the number of wall-attached clusters (also observable in Fig. 9).

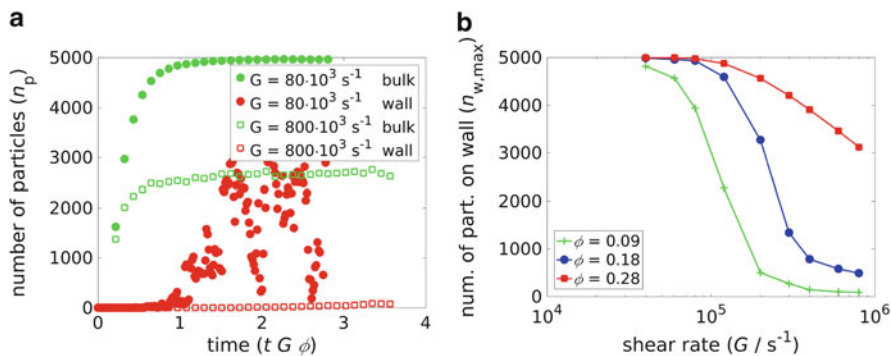


Fig. 9 (a) Number of particles in clusters and attached to the wall as a function of time. (b) Number of particles attached to the wall as a function of shear rate for different values of particle volume fraction ϕ . The values of parameters were $\phi = 0.09$, $\gamma = 0.1 \text{ mJ m}^{-2}$, and $R_p = 125 \text{ nm}$

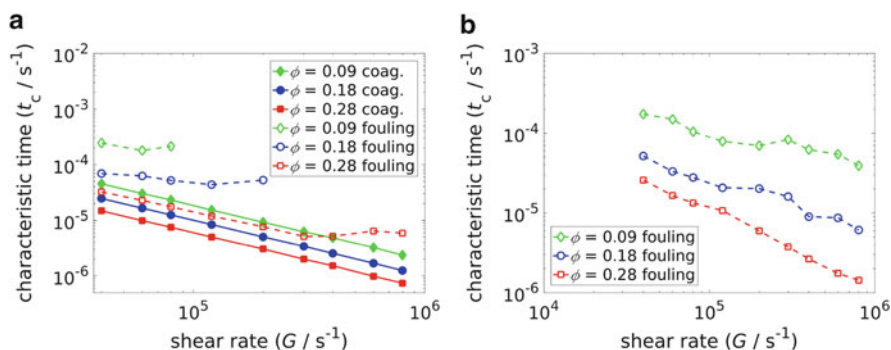
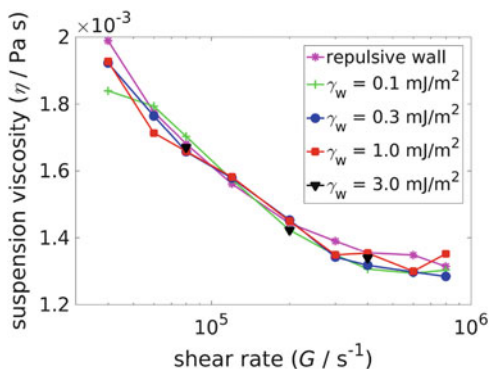


Fig. 10 (a) Characteristic time of coagulation and fouling as a function of the shear rate for different values of particle volume fraction ϕ . Coagulation time was evaluated as the time needed for n_p or n_w to reach $n_{\text{crit}} = \frac{N}{3}$ particles, either in aggregates or attached to the wall. (b) The same case with $n_{\text{crit}} = \frac{N}{100}$. The values of parameters were $\gamma = 0.1 \text{ mJ m}^{-2}$ and $R_p = 125 \text{ nm}$

Another interesting aspect follows from the comparison of Fig. 10a, b. These plots show the characteristic time of fouling for the same simulation, but evaluated using a different value of the parameter n_{crit} , which represents the number of wall-attached particles used for determination of the characteristic time. The solid lines (representing coagulation) have steeper slopes than the broken lines (representing fouling) at high values of G , demonstrating that the processes of fouling and coagulation follow different mechanisms (see also Fig. 9). Namely, although a small number of particles attach to the wall relatively quickly and stay attached even for large values of shear rate, the buildup of a larger layer takes longer and is more sensitive to shear rate.

Although the number of particles attached to the wall changes significantly with different conditions, the strength of adhesion of the particles to the wall appears insignificant. This is clearly visible in Fig. 11, which shows no appreciable effect on

Fig. 11 Suspension viscosity as a function of the shear rate for different values of the surface energy of the particle–wall interaction γ_w . The values of parameters were $\phi = 0.09$, $\gamma = 0.1 \text{ mJ m}^{-2}$, and $R_p = 125 \text{ nm}$



viscosity of changing the value of the surface energy of the particle–wall interaction. These results indicate that, unlike coagulation, fouling has only negligible effect on the suspension viscosity in the simple-shear flow for the timescale region accessible by the model.

Following the mechanism of fouling described, a cluster attached to the wall detaches after a certain period. But, this detachment is often connected with the breakage of the cluster and a small part of the original cluster can stay attached to the wall. Another cluster might collide with these wall-attached particles and the process repeats. In this sense, the adhesive wall only contributes to the coagulation and breakage that already occur in the system and does not introduce any additional dissipation that would translate into an increase in viscosity. Another explanation relies on the fact that the values of the surface energy for both the particle–particle and particle–wall interactions are much smaller than the theoretical values that can be found in the literature [42]. However, this is a necessary condition for us to observe the trends presented here within the temporal and spatial scales of the model. For a greater number of adhesive particles, the formed clusters would span the whole domain and no scaling of cluster size would be observed.

Another mechanism could also be present, such as the plastic deformation or partial sintering that is responsible for tighter attachment of particles to the wall in real processes. This mechanism is not present in the current model formulation.

Overall, the big advantages of the present modeling approach are the possibility to identify mechanisms taking place in colloidal dispersions and the ability to gain insight into these processes. However, these results are difficult to test experimentally in a direct way. A possible indirect form of validation could be to use the PBE modeling approach [33], which relies on the identification of mechanisms leading to fouling and the estimation of rate constants. Information on both of these can be obtained directly from our model. Subsequently, the outcome of the PBE model can be compared with experimental results at a reactor scale, such as those in a recently published study of reactor fouling by colloidal latexes [1].

4 Conclusions

The processes of coagulation and fouling in stabilized colloidal dispersions were modeled using the discrete element method. Coagulation (i.e., the formation of clusters in the bulk) was shown to be much faster than fouling (i.e., the attachment of primary particles or clusters to the wall). However, the kinetics of coagulation is highly affected by the degree of stabilization, in the sense that more stable latexes retain their dispersed state for a longer time. The viscosity evaluated from the model was shown to be sensitive to this delay in the cluster growth. Moreover, the relation between viscosity and cluster size was also observed for the effect of various parameters, such as the primary particle size and surface energy. These findings are promising for the concept of using viscosity measurement as a probe for the determination of dispersion properties. On the other hand, fouling did not have any observable effect on the dispersion viscosity in the simulations that were performed in simple shear flow. A different type of flow can lead to different results, and the issue remains an open question. In this study, the mechanism of fouling in simple shear flow was revealed by a thorough analysis. The mechanism consists of the dynamic attachment and detachment of clusters to and from the wall. Therefore, the presence of an adhesive wall only contributes to the coagulation and breakage that already take place in the system and does not result in an increase of viscosity. The results of this study represent an advance in theoretical understanding of the field of colloidal science. The observed sensitivity of viscosity to dispersion properties is also relevant for industrial applications. It contributes to the usage of first principle models in areas where only empirical knowledge was used up to now.

Acknowledgement The authors are grateful for the support provided by EC SPIRE project RECOBA (H2020-636820) and by Czech Science Foundation (GACR) project 16-22997S. Financial support from specific university research (MSMT No 20-SVV/2016) is gratefully acknowledged.

References

1. Urrutia J, Pea A, Asua JM (2016) Reactor fouling by preformed latexes. *Macromol React Eng* 11(1):1600043. doi:[10.1002/mren.201600043](https://doi.org/10.1002/mren.201600043)
2. Soos M, Moussa AS, Ehrl L, Sefcik J, Wu H, Morbidelli M (2008) Effect of shear rate on aggregate size and morphology investigated under turbulent conditions in stirred tank. *J Colloid Interface Sci* 319:577–589
3. Zaccone A, Soos M, Lattuada M, Wu H, Baebler MU, Morbidelli M (2009) Breakup of dense colloidal aggregates under hydrodynamic stresses. *Phys Rev E Stat Nonlinear Soft Matter Phys* 79:061401
4. Harada S, Tanaka R, Nogami H, Sawada M (2006) Dependence of fragmentation behavior of colloidal aggregates on their fractal structure. *J Colloid Interface Sci* 301:123–129
5. Conchuir BO, Harshe YM, Lattuada M, Zaccone A (2014) Analytical model of fractal aggregate stability and restructuring in shear flows. *Ind Eng Chem Res* 53:9109–9119

6. Kroupa M, Vonka M, Soos M, Kosek J (2015) Size and structure of clusters formed by shear induced coagulation: modeling by discrete element method. *Langmuir* 31:7727–7737
7. Guery J, Bertrand E, Rouzeau C, Levitz P, Weitz DA, Bibette J (2006) Irreversible shear-activated aggregation in non-Brownian suspensions. *Phys Rev Lett* 96:198301
8. Zaccone A, Gentili D, Wu H, Morbidelli M (2010) Shear-induced reaction-limited aggregation kinetics of Brownian particles at arbitrary concentrations. *J Chem Phys* 132:134903
9. Mewis J, Wagner N (2012) *Colloidal suspension rheology*; Cambridge series in chemical engineering. Cambridge University Press, Cambridge
10. Visser J, Jeurnink TJM (1997) Fouling of heat exchangers in the dairy industry. *Exp Thermal Fluid Sci* 14:407–424
11. Bansal B, Chen XD (2006) A critical review of milk fouling in heat exchangers. *Compr Rev Food Sci Food Saf* 5:27–33
12. Bouhabila E, Ben Aim R, Buisson H (2001) Fouling characterisation in membrane bioreactors. *Sep Purif Technol* 22-23:123–132
13. Delgado S, Villarroel R, Gonzalez E (2008) Effect of the shear intensity on fouling in submerged membrane bioreactor for wastewater treatment. *J Membr Sci* 311:173–181
14. Henry C, Minier JP, Lefevre G (2012) Towards a description of particulate fouling: from single particle deposition to clogging. *Adv Colloid Interf Sci* 185:34–76
15. Henry C, Minier JP, Lefevre G, Hurisse O (2011) Numerical study on the deposition rate of hematite particle on polypropylene walls: role of surface roughness. *Langmuir* 27:4603–4612
16. Henry C, Minier JP, Lefevre G (2012) Numerical study on the adhesion and reentrainment of nondeformable particles on surfaces: the role of surface roughness and electrostatic forces. *Langmuir* 28:438–452
17. Agbangla GC, Climent E, Bacchin P (2014) Numerical investigation of channel blockage by flowing microparticles. *Comput Fluids* 94:69–83
18. Agbangla GC, Bacchin P, Climent E (2014) Collective dynamics of flowing colloids during pore clogging. *Soft Matter* 10:6303–6315
19. Dupuy M, Xayasenh A, Duval H, Waz E (2016) Analysis of non-Brownian particle deposition from turbulent liquid-flow. *AIChE J* 62:891–904
20. Marshall JS (2009) Discrete-element modeling of particulate aerosol flows. *J Comput Phys* 228:1541–1561
21. Peters J, Heller W (1970) Mechanical and surface coagulation. 2. Coagulation by stirring of alpha-FeOOH-sols. *J Colloid Interface Sci* 33:578
22. Heller W, Peters J (1970) Mechanical and surface coagulation. 1. Surface coagulation of alpha FeOOH sols. *J Colloid Interface Sci* 32:592
23. De Lauder WB, Heller W (1971) Mechanical and surface coagulation. 5. Role of solid-liquid interface and of turbulence in mechanical coagulation. *J Colloid Interface Sci* 35:308
24. Sjollema J, Busscher HJ (1990) Deposition of polystyrene particles in a parallel plate flow cell. 1. The influence of collector surface-properties on the experimental deposition rate. *Colloids Surf* 47:323–336
25. Georgieva K, Dijkstra DJ, Fricke H, Willenbacher N (2010) Clogging of microchannels by nano-particles due to hetero-coagulation in elongational flow. *J Colloid Interface Sci* 352:265–277
26. Kumar D, Bhattacharya S, Ghosh S (2013) Weak adhesion at the mesoscale: particles at an interface. *Soft Matter* 9:6618–6633
27. Mustin B, Stoeber B (2016) Single layer deposition of polystyrene particles onto planar polydimethylsiloxane substrates. *Langmuir* 32:88–101
28. Li SQ, Marshall JS, Liu GQ, Yao Q (2011) Adhesive particulate flow: the discreteelement method and its application in energy and environmental engineering. *Prog Energy Combust Sci* 37:633–668
29. Boor BE, Siegel JA, Novoselac A (2013) Monolayer and multilayer particle deposits on hard surfaces: literature review and implications for particle resuspension in the indoor environment. *Aerosol Sci Technol* 47:831–847

30. Chen S, Liu WW, Li SQ (2016) Effect of long-range electrostatic repulsion on pore clogging during microfiltration. *Phys Rev E* 94:063108
31. Yue C, Zhang Q, Zhai ZQ (2016) Numerical simulation of the filtration process in fibrous filters using CFD-DEM method. *J Aerosol Sci* 101:174–187
32. Shahzad K, D'Avino G, Greco F, Guido S, Maffettone PL (2016) Numerical investigation of hard-gel microparticle suspension dynamics in microfluidic channels: aggregation/fragmentation phenomena, and incipient clogging. *Chem Eng J* 303:202–216
33. Lazzari S (2016) Modeling simultaneous deposition and aggregation of colloids. *Chem Eng Sci* 155:469–481
34. Kroupa M, Vonka M, Kosek J (2014) Modeling the mechanism of coagulum formation in dispersions. *Langmuir* 30:2693–2702
35. Kroupa M, Vonka M, Soos M, Kosek J (2016) Utilizing the discrete element method for the modeling of viscosity in concentrated suspensions. *Langmuir* 32:8451–8460
36. Crowe C, Sommerfeld M, Tsuji Y (1998) *Multiphase flows with droplets and particles*. CRC, Boca Raton
37. Marshall JS (2007) Particle aggregation and capture by walls in a particulate aerosol channel flow. *J Aerosol Sci* 38:333–351
38. The OpenFOAM Foundation OpenFOAM open source software. The OpenFOAM Foundation, London. www.openfoam.org. 2017
39. Dance SL, Maxey MR (2003) Incorporation of lubrication effects into the force-coupling method for particulate two-phase flow. *J Comput Phys* 189:212–238
40. Israelachvili J (2010) *Intermolecular and surface forces*. Elsevier Science, Amsterdam
41. Cowley AC, Fuller NL, Rand RP, Parsegian VA (1978) Measurement of repulsive forces between charged phospholipid bilayers. *Biochemistry* 17:3163–3168
42. Hunter RJ (2001) *Foundations of colloid science* 2nd edn. Oxford University Press, Oxford
43. Johnson KL, Kendall K, Roberts AD (1971) Surface energy and contact of elastic solids. *Proc R Soc A* 324:301–313
44. Schmitt FJ, Ederth T, Weidenhammer P, Claesson P, Jacobasch HJ (1999) Direct force measurements on bulk polystyrene using the bimorph surface forces apparatus. *J Adhes Sci Technol* 13:79–96
45. Hodges CS, Cleaver JAS, Ghadiri M, Jones R, Pollock HM (2002) Forces between polystyrene particles in water using the AFM: pull-off force vs particle size. *Langmuir* 18:5741–5748
46. Netlib ODEPACK library. <http://www.netlib.org/>. 2017

Monitoring of Vinyl Acetate–Ethylene Processes: An Industrial Perspective



Eric Frauendorfer, Muhammad Babar, Timo Melchin,
and Wolf-Dieter Hergeth

*Dedicated to Prof. Dr. H.-U. Moritz on the occasion of his
65th birthday.*

Abstract Monitoring of vinyl acetate–ethylene (VAE) processes plays a crucial role in achieving high process efficiency in industry while ensuring process safety and the needed product quality. Different methods are applied along the process chain, which includes production of the VAE polymer dispersion in high pressure reactors, degassing of the product back to atmospheric pressure, storage and shipping, and spray drying of the polymer to create a dispersible polymer powder. Properties of interest to monitor on a routine basis can be process related, such as heat output and conversion, or product related, such as total solids, viscosity, pH, particle size distribution, moisture content, and chemical composition. Other techniques can also be used to gain further knowledge of the process (e.g., mixing behavior) and of the product (e.g., polymer structure, volatile organic compounds, and biostability). Different monitoring techniques are discussed, focusing on their applicability in the industrial process under consideration.

Keywords Online analytics • Polymerization • Process monitoring • Vinyl acetate-ethylene copolymer

Contents

| | | |
|---|-----------------------------------|-----|
| 1 | Introduction | 184 |
| 2 | Method Overview | 187 |
| | 2.1 Sampling Considerations | 187 |
| | 2.2 Calorimetry | 189 |

| | | |
|-----|------------------------|-----|
| 2.3 | Optical Methods | 193 |
| 2.4 | Acoustic Methods | 199 |
| 2.5 | Chromatography | 202 |
| 2.6 | NMR | 204 |
| 2.7 | Other Methods | 205 |
| 2.8 | Biocontamination | 207 |
| 3 | Conclusion | 209 |
| | References | 209 |

1 Introduction

Significant opportunities exist today for improving the cost of manufacturing and quality assurance by using process analytical technology. This field has grown significantly in recent decades due to an increasing appreciation of the value of data collected during production, paired with the falling cost of sensors, data management (including sensor integration), and computational power. The horizon has been expanded from simple process measurements such as temperature, pressure, and pH to devices that can measure chemical composition and other physical attributes as well as phase states and fluidics. Instruments commonly employed include optical and nuclear magnetic resonance (NMR) spectrometers, gas chromatographs, and acoustic instruments. This paper analyzes the value delivered and challenges posed by various types of online analyzer technologies when applied to a vinyl acetate–ethylene (VAE) manufacturing process.

Monitoring instrumentation can be used for different target settings along the process (Fig. 1), in-line, at-line, or on-line, to measure parameters defined as attributes of interest. The aim of monitoring is to accomplish at least one of the following targets:

- (1) Ensure needed product quality and quality consistency by process monitoring (detect variations/changes)
- (2) Process control, to run the process closer to limiting thresholds in a safe way, thus increasing process efficiency and product quality
- (3) Detect and act upon process equipment changes, such as reactor fouling, and the maintenance status of the equipment
- (4) Deepen scientific understanding of the process itself, building up mechanistic knowledge of how process factors affect the product and process performance
- (5) Avoid sample extraction, potentially improving work safety and use of personnel resources
- (6) Avoid the need for specially trained personnel for analytical work

VAE processes are complex and multifactorial systems. Traditional one-factor-at-a-time experiments do not necessarily address interaction between products and process variables. Experiments conducted during product and process development can serve as building blocks of knowledge that grow to accommodate a higher

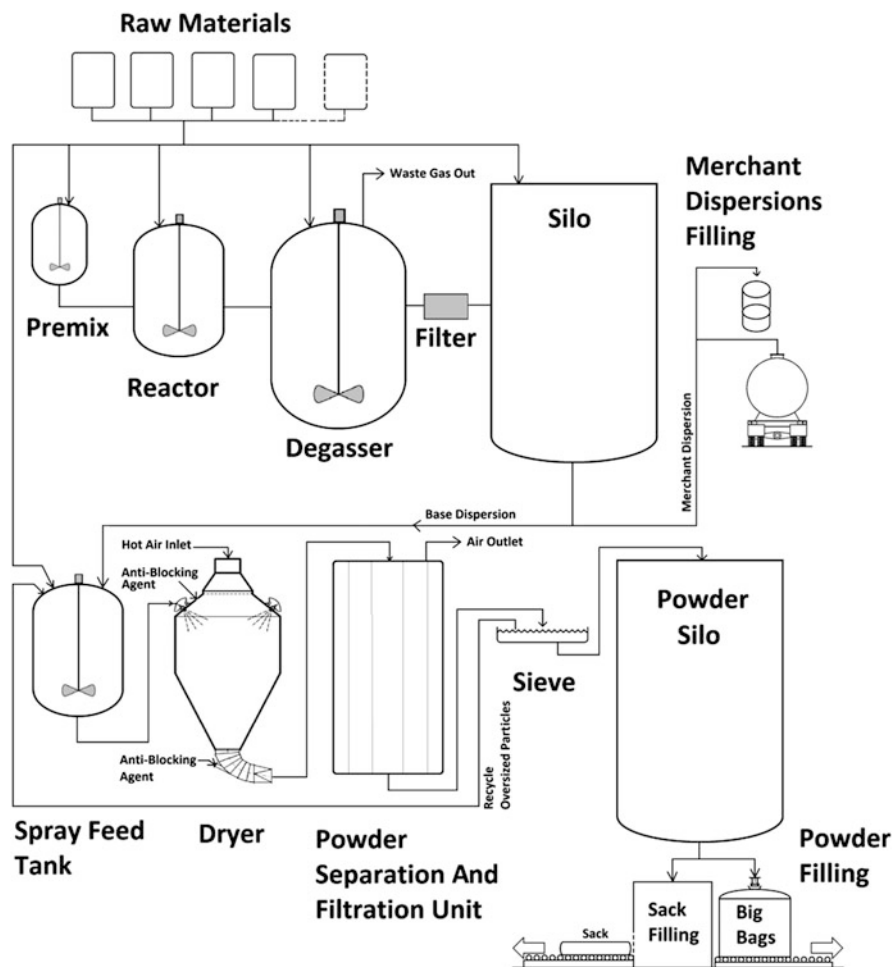


Fig. 1 The VAE process consists of (1) polymerization in the reactor (20–80 m³ at ~80°C and ~80 bar); (2) degassing of product back to atmospheric pressure; (3) filtration, storage, and shipping of dispersion; (4) spray drying; and (5) storage and shipping of powder. Different process monitoring methods can be used during the process and are described in the text

degree of complexity with time. A knowledge base can be of most benefit when it consists of scientific understanding of the relevant multifactorial relationships (e.g., between process and quality attributes). It is beneficial to use multivariate mathematical approaches, such as statistical design of experiments, response surface methodologies, process simulation, and pattern recognition tools in conjunction with knowledge management tools. Methodological experiments based on statistical principles of orthogonality, reference distribution, and randomization provide

effective means of identifying and studying the effect and interaction between product and process variables.

Multivariate data acquisition and data analysis tools are usually advanced software packages that aid collection of raw data and statistical analysis of that data. A multivariate analysis enables the building and real-time execution of multidimensional mathematical models, the input being the signal from process analyzers/sensors and the output being the quality attributes required for a specific process (viscosity, molecular mass distribution, etc.)

After the relationship between a critical quality attribute and process parameter has been established and any statistical models developed, the next step is to control the process in real time. This is accomplished by conditioning the signal coming from the process analyzer and generating an output to a controller configured to modify the process parameter in such a way that critical quality attributes remain within specified limits at all times. This is the most crucial step in ensuring that real-time quality assurance is met. Such monitoring allows manufacturers to produce product with consistent quality and helps to reduce waste and overall costs.

VAE polymerizations usually take place at 20–120 bar. Accordingly, any sensor installed in the high pressure part of the process must be constructed to withstand these conditions. Furthermore, as fouling of the reactor occurs over time, it might be necessary to use a high-pressure cleaning system (high-pressure jet of cleaning solution such as water) directed at the inner surfaces of the reactor. The local pressure of the jet, focused on a very small surface area, can easily exceed the above-mentioned pressure ranges and should be taken into account when selecting a sensor and/or its installation location. Systems to (automatically) retract the sensor from the reactor during this time are a viable safeguard option. The seal of the sensor is also important, because it might potentially be the source of a chemical breach that could lead to formation of an explosive atmosphere in the plant. The same applies for sample extraction, where the sampling stream might have to be depressurized for downstream analysis. Degassing of the sample, formation of foam, etc., might hinder the feasibility of such an extraction, as might a change in the sample itself as a result of the depressurization step.

Another challenge is representative sampling of the product, because segregation phenomena can occur in the product stream, at the sampling site, or during extraction and transport of a sample. In addition to the representativeness of the sample, the repeatability and reproducibility of analysis also have to be taken into account.

Installation of new on-line sensors in high-pressure vessels can be an expensive and lengthy process if the pressure containment structure is modified (e.g., another port installed) and the vessel must be reapproved by the authorities. This is avoided in the majority of cases, also because VAE reactors normally include a cooling jacket. A possible installation of sensors might use pipelines directly adjacent to the reactor (e.g., before outlet valves and peering into the reactor) and thus avoid a change to the reactor wall.

The on-line use of traditional process data (temperature, pressure, feed, etc.) with mathematical methods (soft sensors) for reaction profile tracing and

installation of sensors in downstream processes (pipeline to the degasser, in the degasser, or after the degasser) might provide the necessary data for monitoring the process, avoiding a change to the high-pressure system.

2 Method Overview

2.1 Sampling Considerations

Obtaining a representative sample on which to perform measurements can be challenging. Often, small samples (compared with the bulk mass) have to be analyzed at, or extracted from, a certain point in the process. The error deriving from small sample size can be counteracted by increasing the number of samples analyzed, but that does not change the possibility that the samples themselves might not represent the bulk material (base population) as a result of discriminatory processes before the point of sample presentation, or during extraction, handling, or even measurement. This is especially true for powder flows, including VAE powders created by spray drying of VAE dispersions and then pneumatically transferred to silos, where segregation can occur as a result of differences in particle size, morphology, mass, density, chemical composition (e.g., moisture), or electrostatic properties [1–5]. Figure 2 shows the effect of such processes on the particle size distribution of different samples of the same VAE powder. The samples were taken from a powder flow at the bottom of the spray dryer by different means (flute and hook probe) and from the final (bulk) powder and analyzed via light scattering using a Beckman Coulter LS13320 device.

When comparing multiple samples, the sampling is called “accurate” when it is free from bias (i.e., the error of sampling is a random variable about the true mean). Sampling is deemed “precise” when the error variation is small, irrespective of whether the mean is the true mean or not [6]. It should be clear that the sampling process includes all steps, from sample extraction (or presentation if on-line) and sample transportation (or signal conveying) to the processing, measurement, and documentation of results. Each step can influence the result, especially if manual steps are involved [7, 8]. Measurement system analysis approaches encompass all relevant aspects of assessing sampling quality [9] (but not necessarily how well the samples represent the bulk material).

Furthermore, sample presentation can have an influence on the measurement result (e.g., temperature) or, in the case of VAE powders, on the bulk density at the sensor (e.g., for elemental X-ray fluorescence or microwave moisture measurements). Again, using several measurement points and averaging results can be a necessary step.

As an alternative to extraction of a sample, a partial stream of the product might be analyzed using a by-pass. This can facilitate the cleaning and maintenance of sensors as the by-pass can be closed at both ends using valves. Flow of the product

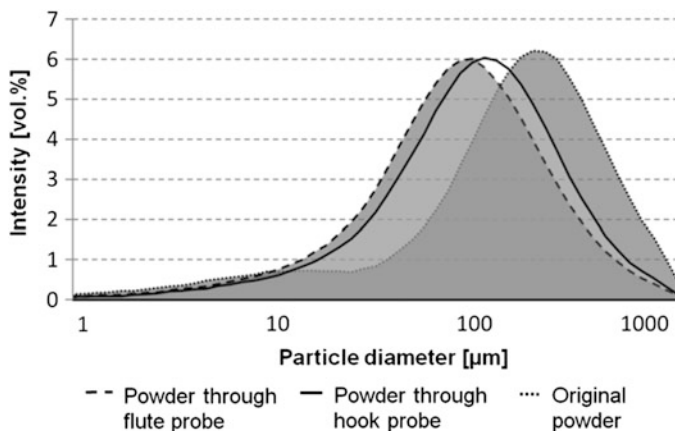


Fig. 2 Different particle size distributions resulting from different powder sample extraction techniques

into the by-pass should be thoroughly analyzed because the product flowing at the pipe wall might be different from that flowing in the center, or product might be segregated by the stream going into the by-pass. The same applies to insertion of probes into product streams [10] and orientation of the sensors in relation to the stream (i.e., how the sample flows onto the sensor surface). For VAE dispersions, it might be useful to set the angle of the surface of a spectroscopic sensor slightly away from the direction of the incoming stream, so that the sample at the sensor window is continuously being exchanged and the surface is being kept clean by the flow. Other sensors might need steady and constant flows (e.g., rotary on-line viscometers) or steady flows (e.g., needing a certain length of straight pipe in front of the sensor).

Extraction of a sample might be necessary if no equivalent on-line technique is available or dilution is needed; example are gas chromatography (GC) and laser diffraction particle sizing.

With high-pressure reaction systems, it is difficult to deal with small sampling lines that might clog. Furthermore, waste disposal can make sample extractions difficult, as a certain robustness is needed in an industrial environment to ensure system reliability and cost effectiveness.

An example of a working system with sample extraction and multiple analysis techniques is the system for automatic continuous online monitoring of polymerization reactions (ACOMP) developed at Tulane University (New Orleans, LA). A small stream of reaction mixture is continuously withdrawn from the reactor, continuously diluted with solvent from a reservoir, and pumped through several detectors that measure parameters such as multiangle light scattering, refractive index, viscosity, and conductivity [11–16].

2.2 Calorimetry

A particularly versatile method for monitoring polymerization reactions, and one of inherent on-line nature, is process calorimetry [17–20]. The information accessible from either heat flux or heat balance approaches is the heat of polymerization, which is linked to monomer conversion. Polymerization reactions, especially VAE emulsion polymerizations, are generally highly exothermic, providing significant spread in the reactor T_r and jacket T_j temperatures over time. The temperature sensor is the most important sensor applied in process calorimetric measurements. Temperature is always monitored in industrial polymerization processes, but for calorimetric application the accuracy and calibration stability of the temperature sensors must be high, with low error and noise in relation to the heat flow being measured. A broad overview of the advantages and disadvantages of contact and noncontact sensors is given in a report by Fonseca et al. [18].

According to Fonseca et al., techniques suitable for polymerization calorimetry can be generally divided into heat flow (HF) methods, heat balance (HB) methods, and power compensation calorimetry (PCC) [18]. Each technique comes with its inherent challenges for implementation in production-scale reactors. HF methods require knowledge of the overall heat transfer coefficient U and the reactor heat exchange area A (Eq. 1). The HB approach does not depend on this information but requires additional temperature measurements (Eq. 2) and lacks responsivity to T_j changes. Both HF and HB methods require careful consideration of heat introduced to the reactor by feeds (Q_{inflow}), losses Q_{loss} , and changes in the reactor volume in semibatch operation. In the following equations, m_r is the reactor mass, $C_{p,r}$ the total reactor heat capacity, and Q_{stir} the heat dissipated by stirring:

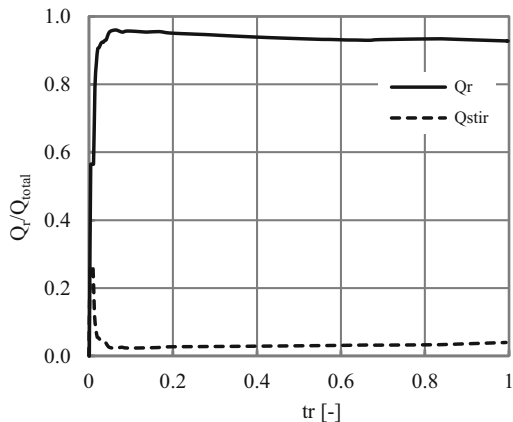
$$Q_{r,\text{hf}} = UA(T_r - T_j) + m_r C_{p,r} \frac{dT_r}{dt} - Q_{\text{inflow}} - Q_{\text{stir}} + Q_{\text{loss}} \quad (1)$$

$$Q_{r,\text{hb}} = F_j C_{p,j} (T_{j,\text{in}} - T_{j,\text{out}}) + m_r C_{p,r} \frac{dT_r}{dt} - Q_{\text{inflow}} - Q_{\text{stir}} + Q_{\text{loss}} \quad (2)$$

The PCC principal is straightforward but not suitable for production-scale reactors. Here, constants T_j and T_r , controlled with an electric heater, are defined. As the polymerization progresses, the electric power necessary to maintain the selected reactor temperature is controlled. Thus, the electric power profile is proportional to the heat of polymerization. However, the method requires constant T_j and a heater surface area that is not influenced by deposit formation. Furthermore, electric heating is not feasible for ton-scale reactors or process monitoring, especially because significant differences between T_j and T_r are required for fast heat removal and high space–time yields.

HF calorimetry is a technique that has been intensively discussed in the literature [21, 22] and has shown its power through comparison with external and internal complementary analytics [21, 23–26]. The technique is especially sensitive to fast reaction dynamics because the temperatures necessary for calculation of the heat of

Fig. 3 Contribution of heat of reaction and stirrer heat dissipation with respect to the total heat detected at the end of a vinyl acetate emulsion polymerization as function of the reduced polymerization time t_r .



polymerization only depend on T_j and T_r . In consequence, it is crucial to know the relevant heat exchange area A and the overall heat transfer coefficient U , which determine the heat conduction process as function of time (Eq. 1). Further terms in the HF balance equation account for the accumulated heat of the reactor content, heat losses from radiation and conduction, losses associated with reflux condensers if used, and heat introduced by energy dissipation during stirring. In industrial-scale reactors, heat radiation losses can be neglected because of the surface-to-volume ratio, but stirrer-induced energy dissipation must be included. This contribution can range from 5% for a reaction mixture of low viscosity to 10% for a high viscosity mixture, with respect to the determined chemical heat (compare Fig. 3) [27].

In semibatch reactions, which are commonly used for VAE polymerization, additional care must be taken with regard to heat introduced by input of initiators, additives, and monomers. For polymerization reactions, the main challenges are changes in the heat exchange area A and the heat transfer coefficient U . The heat exchange area can vary significantly for semibatch reactions, with only 10% of the final reaction mass localized in the initial load of the reactor. It is also affected significantly by formation of wall deposits within a single batch or a campaign of several batches. A typical example of polymer fouling is given in Fig. 4. The increase in thermal resistance as a result of deposits can be calculated in analogy to heat exchange theory. The ratio of instantaneous and initial thermal resistance after chemical cleaning yields information about the fouling behavior in a semibatch campaign. It is assumed in this qualitative analysis that deposits are only formed on the reactor side and not on the jacket side.

The dramatic change in thermal resistance in a semibatch campaign also illustrates that determination of parameters U and A is defined by continuous variation, even for the same product and recipe. Calibration is needed to account for changes in viscosity, heat capacity, and the overall heat transfer coefficient as functions of polymerization time. It is possible to apply calibration stages before and after reaction, using on-line parameter estimation techniques that make use of the conversion dependence on U or temperature oscillation techniques for continuous

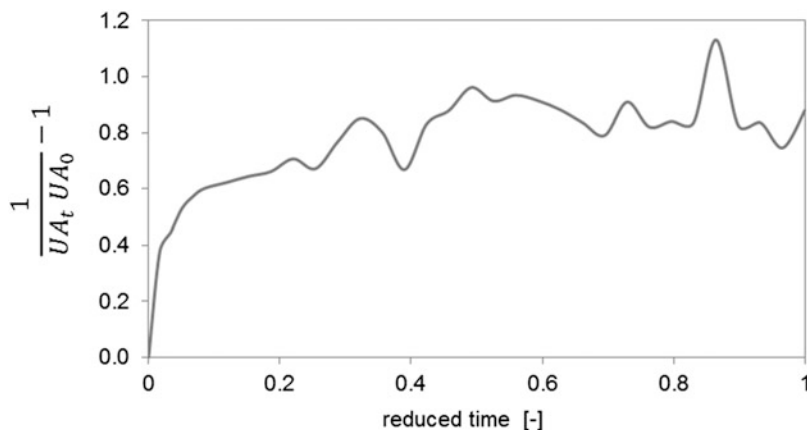


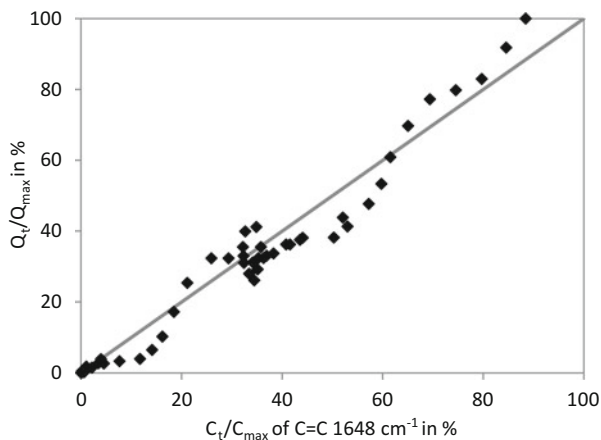
Fig. 4 Qualitative change in UA as a function of the reduced production time in a VAE emulsion polymerization semibatch campaign. The increase in the heat transfer resistance is described as the ratio of the initial resistance at start of the campaign UA_0 to the actual heat transfer resistance at time t

UA estimation [21, 22, 28]. BenAmor et al. developed a solution to the UA problem in semibatch emulsion terpolymerizations of styrene, butyl acrylate (BA), and methyl methacrylate (MMA) by using a sample-free cascade observer technique [28]. However, care must be taken in baseline selection and determination of the heat of polymerization [26]. All of the mentioned techniques are suitable for laboratory- and pilot-scale reactors. For industrial-scale equipment, HF methods are not as easy to implement, especially because of the UA dilemma.

A method that is easier to implement in production is HB calorimetry. In this case, no information about UA is needed. Instead, the reactor jacket inlet $T_{j,in}$ and outlet $T_{j,out}$ temperatures, as well as the cooling medium heat capacity $c_{p,j}$ and mass flow F_j , are used for calculation of the heat of polymerization. This kind of approach is independent of changes in A , U , and heat transfer properties of the reaction medium. The bigger the reactor, the higher the possible $\Delta T_{j,in-out}$ and thus the better the performance of the HB method. However, large $\Delta T_{j,in-out}$ can only be achieved with long residence times of the cooling medium in the jacket and, thus, small mass flow. This leads to low responsiveness of the reactor system and large time constants, which can be overcome by improved design of the cooling system [21]. Although the HB method does not offer the same dynamics as the HF method, it is the method of choice in industrial-scale reactors. Typical applications of calorimetry in VAE polymerization are process safety evaluation, process control, and quality control. In safety evaluation, calorimetry is used at laboratory and pilot scales to determine relevant safety parameters such as time to maximum rate, adiabatic temperature rise, and cooling capacity.

Although calorimetry in general is a very useful tool in process control, it is inherently restricted to univariate data output. It is not possible to obtain instantaneous monomer conversion profiles directly in multimonomer reactions unless

Fig. 5 Comparison of normalized heats of polymerization and Raman monomer concentration as a function of polymerization time (*diagonal*). The reaction heat was normalized to the final heat of reaction in HF calorimetry; the Raman signals are normalized to the initial concentration of vinyl acetate



kinetic models or additional reaction data are applied to the gathered heat profiles [24, 25]. Industrial recipes usually consist of more than two monomers and more than one feed. Hergeth et al. [23] demonstrated that combining calorimetry and spectroscopic methods such as near-infrared (NIR) or Raman spectroscopy provides deeper understanding of the emulsion polymerization processes of vinyl acetate (VAc). This is not only useful for scientific reasons, but also for routine monitoring of monomer conversion profiles in production. Similar investigations were conducted by Elizalde et al. [24, 25] for VAc/BA and BA/MMA. They obtained excellent agreement between off-line gravimetric, on-line Raman, and calorimetric analyses for the overall monomer conversion profiles. This observation was verified for the solution polymerization of VAc in isopropanol in a pilot-scale reactor setup, with sufficient agreement between Raman and calorimetric data (see Fig. 5).

For instantaneous conversion profiles under starved conditions in the BA/MMA system, better agreement with off-line data from GC measurements was obtained with Raman spectroscopy. Analysis of instantaneous monomer conversion under starved feed conditions remains a challenge for both spectroscopic and calorimetric methods at the industrial reactor scale. This is also true for the finishing steps, where residual monomer levels are significantly below 2 wt% and need to be reduced to less than 200 ppm in postpolymerization or with equivalent monomer reduction methods. In postpolymerization, calorimetry fails as a monitoring tool for HB and HB analysis because the heat of residual polymerization is very low compared with energy dissipation by stirring.

2.3 Optical Methods

Optical spectroscopy covers the wavelength range from ultraviolet (UV, $\lambda > 10$ nm) to the far-infrared (FIR, $\lambda \approx 1$ mm). The experimental setup utilizes typical light sources (e.g., lamps, lasers), light detectors (e.g., photomultipliers, charge-coupled devices), optical elements (e.g., monochromators, mirrors, gratings, filters, lenses), and fibers. Electromagnetic wave spectroscopy with short (e.g., X-rays) and long (e.g., microwaves) wavelengths requires completely different technological instrumentation. Optical spectroscopic measurement in absorption or emission mode can be carried out in a transmission, transfection, reflection, or scattering setup [29]. In turbid or highly scattering media such as polymeric dispersions and powders, attenuated total reflection (ATR) and fiber-optic-based evanescent wave spectroscopy (EWA), both focusing on analysis of surfaces and thin layers, are the setups of choice for on-line absorption measurements, and Raman reflection spectroscopy for emission mode analysis. A thorough overview of optical spectroscopic techniques for on-line process analytics with respect to selectivity, sensitivity, and robustness under industrial constraints has been published [30].

2.3.1 Infrared Spectroscopy

Mid-Infrared Spectroscopy

Mid-infrared (MIR) spectroscopy is the standard workhorse for chemical composition analysis in almost all analytical laboratories in chemical companies around the world. In contrast to its extensive use on the bench, MIR spectroscopy has never found its way into pilot and plant reactor applications in industry for on-line polymerization monitoring because of important restrictions on MIR light transmission: (1) Fiber lengths for the MIR wavelength range are limited because of their absorption properties. (2) Fibers are expensive and too fragile for installation in a plant environment. (3) Mirror optics to transmit the light are also too delicate, and are prone to dust contamination. For VAE emulsion systems, the strong water absorption in the MIR region interferes with spectral features of interest that change during the reaction. Nevertheless, there are a few academic papers dealing with in-situ MIR polymerization monitoring [31–34] utilizing ATR technology. The Mettler-Toledo ReactIR[®] instrument platform [35] enables study of reaction initiation, progress, and safety, especially for solution polymerizations under laboratory conditions.

Near-Infrared Spectroscopy

Absorption bands in the near-infrared (NIR) arise from overtones and combinations of fundamental vibrations, making them weaker and much more complex compared

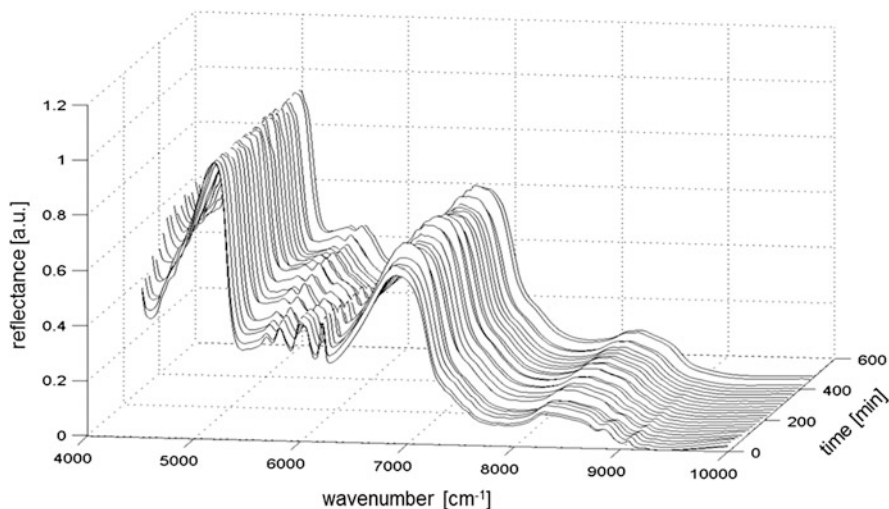


Fig. 6 NIR spectra evolution during emulsion copolymerization

with MIR absorption bands. However, combined with appropriate mathematics, NIR spectroscopy is well established in industry for quality control of educts and products and for monitoring chemical reactions, including polymerizations [36]. The peculiarities of NIR spectroscopy for on-line monitoring of reactions have been discussed elsewhere [18, 27].

The installation of in-situ NIR equipment (either with transflection or ATR probes) is straightforward, even in pressurized vessels, pipes, or by-passes in an industrial environment. Before turning on the process application, effort has to be spent on calibrating the NIR device with the results of at least one independent analytical measurement, and on developing mathematical models for spectrum analysis. Calibration transfer between different NIR instruments is always a major challenge. Never underestimate the time, manpower, and cost of continuing calibration checks and mathematical model maintenance for a running application.

In addition to monitoring the progress of a polymerization reaction in terms of overall and individual monomer conversion, as well as polymer generation or solids content (Fig. 6), NIR spectra can be exploited to extract information on the molecular weight [37, 38] and particle size [39, 40] of the polymeric emulsion. Under certain conditions, varying particle sizes might be directly visible in the raw NIR spectra, making the calibration mathematics relatively straightforward and simple, especially for final product emulsions (Fig. 7).

From an industrial VAE point of view, the time and effort needed for sample extraction and conditioning to obtain calibration data by off-line particle sizing is prohibitive for NIR on-line particle size monitoring over the whole reaction run. However, particle size information inherently present in the NIR spectra is always integrated into the “Golden Batch” soft sensor framework to observe reaction runs [23].

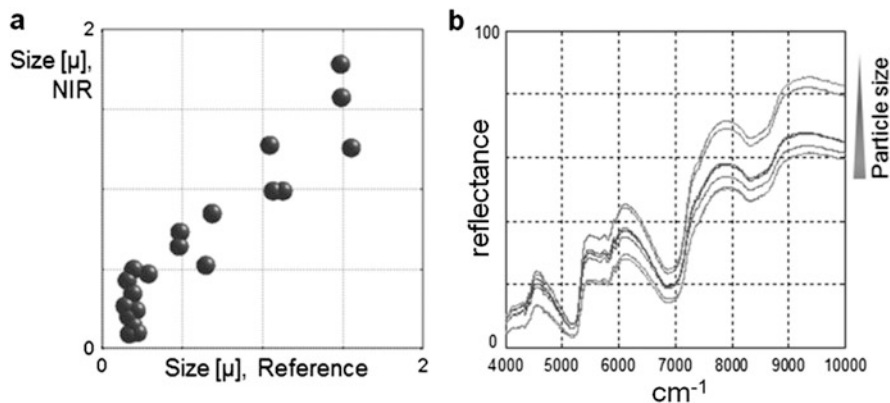


Fig. 7 NIR particle sizing of final VAE product emulsions: (a) size from NIR spectra correlated with the reference method (static light scattering), and (b) examples of NIR spectra of dispersions with different overall particle sizes

NIR molecular weight calibration is also not appropriate for industrial VAE radical polymerization processes because the molecular weight distribution (1) is very broad and dominated by molecules of the order of 100 kDa, and (2) does not change significantly during most of the reaction run, except at the very beginning and the very end. Unfortunately, slight VAE crosslinking at the end of the reaction (i.e., under monomer starved conditions), which governs final material properties, is more or less NIR invisible.

The implementation of NIR-based on-line moisture measurement of polymeric powders has been described in detail elsewhere [42]. The residual moisture level of polymeric powders is an important parameter in control of the spray drying process, and crucial for the flow properties and long-term applicability of the powder (Fig. 8).

Raman Spectroscopy

The on-line method of choice for obtaining specific chemical information about a free-radical polymerization run is Raman spectroscopy, which is an emission-mode optical technique typically installed in a confocal backscattering setup (i.e., almost reflection). Raman scattering (complementary to IR) occurs for nonpolar molecular vibrations, with polarizability being modulated by the vibration. Therefore, double and triple bonds in monomers and polymers are strong Raman scatterers. Despite the extreme weakness of the effect, Raman spectral band intensities are proportional to the number of corresponding molecules, enabling very simple concentration determination. Raman spectroscopy is oblivious to water, thus making it an ideal tool for study of aqueous systems such as VAE emulsions [43, 44].

Laboratory equipment is still dominated by Fourier-transform (FT) Raman instruments, whereas most on-line Raman installations are based on dispersive

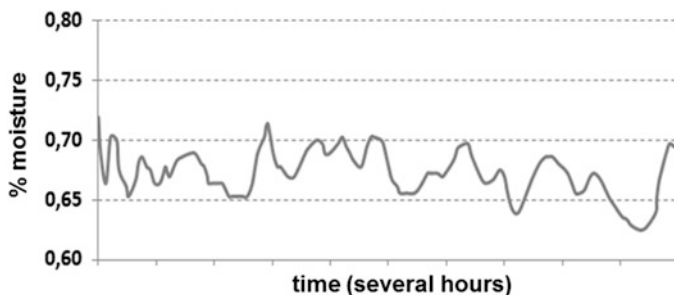


Fig. 8 On-line NIR measurement of moisture in polymeric powders

optical components and confocal excitation/collection optics interfaced to charge-coupled device or charge injection device detectors via optical fibers. For cost reasons and Raman quantum efficiency, HeNe laser excitation at 633 nm is preferred for industrial pilot and plant applications. Technical grade chemicals may show some fluorescence at 633 nm excitation caused by impurities. Excitation with the long-wave light of diode lasers at 785 nm reduces fluorescence at the expense of considerably less Raman quantum efficiency (λ^{-4} dependency). Care has to be taken with respect to the incident laser light intensity at the focal point within a reaction mixture, which might be prone to rapid reaction or even explosion upon strong illumination and heating. Restrictions on laser light intensity may apply for certain reacting systems.

Raman double bond peak positions of vinyl and diene monomers are in the 1,600–1,650 cm^{-1} wavenumber range (Table 1). Most peaks are well separated from each other, thus enabling selective monitoring of individual comonomer concentrations and their conversion to (co)polymer [23, 45] (Fig. 9). Combination of the monomer-specific Raman result with the overall calorimetry signal gives a comprehensive view of polymerization progress.

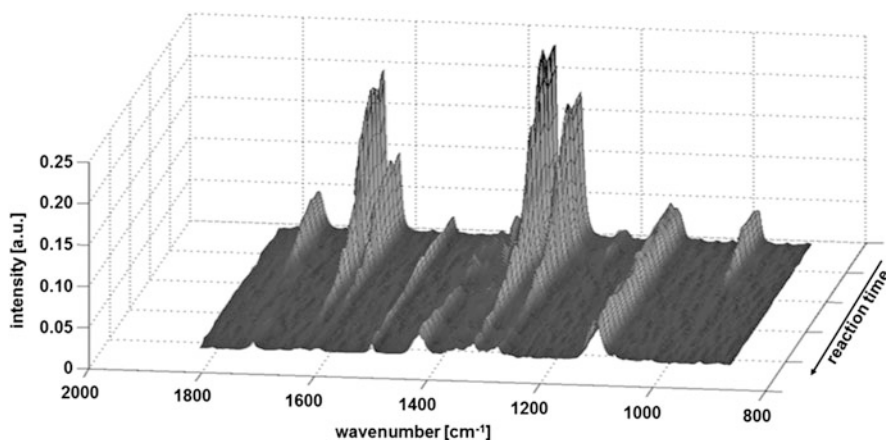
Residual monomer determination close to the reaction end by means of Raman spectroscopy can be beneficial for optimizing cycle time in a polymerization plant, even though the lower detection limit of monomers by Raman is orders of magnitude higher than by conventional GC [45]. Because of the scattering nature of the Raman effect, the signal contains particle size specifics in disperse systems [46]. So far, no report on industrial utilization of this information for reaction monitoring purposes has been published.

As known from textbooks, some vibrational bands in the IR or Raman spectrum (i.e., their band position) are sensitive to the polarity of the surroundings. Band shift [45] and band shape [46] analysis can give additional insights into monomer conversion and partitioning.

Recent development of low resolution spectrometers, tiny matchbox format instruments, handheld devices, and disposables for surface enhanced Raman spectroscopy have paved the way for massive implementation of Raman spectroscopy in the polymer industry, all the way from quality control to reaction monitoring.

Table 1 Double bond Raman lines of vinyl acetate, ethylene, and some potential comonomers

| Monomer | $\nu(\text{C}=\text{C})$ (cm^{-1}) |
|---------------------|---|
| Vinyl acetate | 1,648 |
| Ethylene | 1,623 ^a |
| Vinyl chloride | 1,607 |
| Butyl acrylate | 1,638 |
| Ethylhexyl acrylate | 1,637 |
| VeOVA 9/10 | 1,646 |
| Vinyl sulfonate | 1,619 |

^aPeak shift depending on pressure**Fig. 9** Raman spectra of vinyl acetate–ethylene emulsion copolymerization

2.3.2 Other Optical Spectroscopy

Typical instrumentation for ultraviolet/visible (UV/VIS) spectroscopy is very simple, robust, and inexpensive. UV/VIS spectroscopy is highly sensitive but not very informative, because there are only a few very broad absorption peaks in the wavelength region. Absorption features in the UV range are dominated by water absorption in aqueous mixtures such as VAE emulsions and, therefore, not very selective. In the VIS spectral range, light attenuation is dominated by particulate scattering rather than absorption in disperse systems. Thus, light scattering techniques are standard methods for particle sizing in laboratory and plant environments.

The quantum efficiency of fluorescence events is several orders of magnitude higher than for the Raman effect. Therefore, fluorescence spectroscopy is a well-established on-line technology for bioprocess monitoring [47]. However, in an industrial polymerization reactor, nonspecific impurities in commercial grade ingredients generate most of the fluorescence signal. To the best of our knowledge, there is no published report dealing with emulsion polymerization monitoring in industry by means of fluorescence spectroscopy.

The Terahertz (THz) hype has triggered some activity in industrial laboratories. However, THz spectroscopy is not feasible for aqueous emulsion systems because of the very strong water absorption in that spectral range. At the moment, THz is still a curiosity in the chemical industry, but may have future potential for quality control and reception inspection of educts, as well as predelivery check of products.

2.3.3 Photon Density Wave Spectroscopy

Recently, photon density wave (PDW) spectroscopy has been developed as a process analytical tool for monitoring chemical reactions in highly scattering media such as emulsions. In contrast to optical spectroscopic techniques, PDW does not analyze wavelength-dependent spectral features. Modulated laser light of a fixed VIS or NIR wavelength, with varying modulation frequencies, illuminates a certain volume of the highly scattering medium through an optical fiber, generating photon density waves. Light-collecting fibers at several different distances from the illuminating fiber and interfaced to detectors measure the phase shift and amplitude of the multiply scattered and transmitted light from the source. Both the phase and amplitude of the detected light are governed by the chemical composition of all the particulate matter within the medium. Analysis in terms of light scattering theory gives access to the concentration of components and particles and particle sizes [48, 49].

PDW is able to detect changes in an emulsion polymerization system from the very beginning until final monomer conversion. All the typical events of the process, including monomer emulsification, initiator feed, initiator decomposition (i.e., radical generation), monomer feed, monomer consumption, other component feeds, particle growth, and particle aggregation lead to characteristic changes in the scattering and absorption coefficients, enabling comprehensive reaction monitoring.

The probe head of the device is tightly sealed for pressures up to some tens of bars. Fouling at the fiber tips does not interfere with the measurements, making the PDW technique suitable for industrial application, even in the plant environment (Fig. 10).

In contrast to PDW, diffusing wave spectroscopy (DWS) [50] has never made the transfer from academia to industry because problems appear when the particle-interaction contribution to the particle diffusion becomes stronger. Systems with solid contents of up to 60% can be difficult to measure and are limited to a particle diameter range of 100–3,000 nm.

Some other commercially available techniques for particle sizing in disperse systems, such as particle vision and measurement (PVM), focused beam reflectance measurement (FBRM), and optical coherence tomography (OCT), are not suitable for VAE polymerization monitoring over the whole run because of their blindness to particles in the submicron range, where the important limited agglomeration of polyvinyl alcohol (PVOH) stabilized particles occurs.

Fig. 10 Developmental PDW probe head with central light-emitting glass fiber and several light-capturing glass fibers located at different distances from the emitting fiber



One approach to measurement of particle sizes in undiluted dispersions (up to about 40 wt%) is the fiber optic quasi-elastic light scattering (FOQELS) approach (Brookhaven). The sensor uses two optical fibers, one emitting visible light from a laser diode and one collecting the scattered light at 153° . Both fibers are aligned to look through a window into the process (or cuvette) and the signal is analyzed with dynamic light scattering (DLS) techniques [51]

2.4 Acoustic Methods

Ultrasound methods suitable for reaction monitoring include ultrasonic velocity measurements, ultrasonic absorption (spectroscopy), and acoustic emission recording. Ultrasonics are nondestructive, noninvasive, inherently safe, extremely fast with respect to response times, and easy to use (data interpretation might be a different story). Piezoelectric transducers can both generate and detect ultrasonic waves, and therefore act as emitters and receivers in an application. The typical frequency range of ultrasonic transducers for reaction monitoring is 1–10 MHz.

2.4.1 Ultrasound Velocity

The velocity of sound in water is in the 1,500 m/s range and slightly depends on temperature, whereas the velocity in VAc increases from 1,150 m/s (monomer at 20°C) to 1,853 m/s (polymer at 20°C) during the course of polymerization because of changes of its compressibility and density. Therefore, sound velocity is very sensitive for chemical and physical changes in the reacting system (Fig. 11).

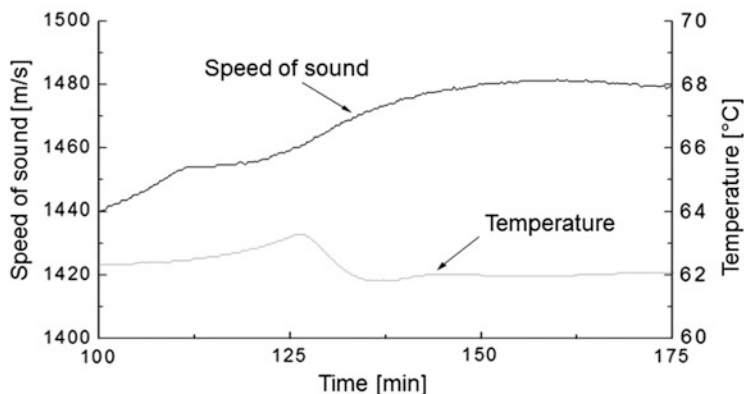


Fig. 11 Ultrasound velocity and mixture temperature during the course of emulsion polymerization

Appropriate model calculations based on individual component contributions to the “overall” sound velocity enables almost immediate determination of monomer conversion and total solids.

Ultrasonic polymerization monitoring by velocity measurements has a long tradition in academia (e.g., [52, 53]), but only a few (temporary) monitoring applications in the polymer industry have been mentioned publicly. Transducer fouling is always a major issue for plant installations. Gas bubbles stirred into the mixture of an atmospheric polymerization may hamper ultrasonic reaction monitoring completely.

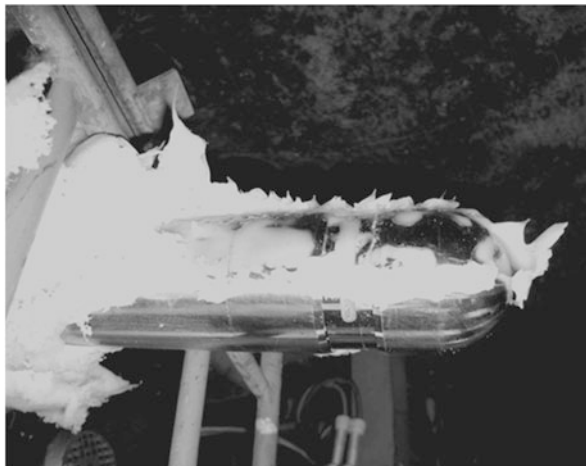
Most industrial ultrasonic velocity devices are simply installed to measure concentrations, densities, and, in some rare cases, medium velocities in tanks or tubes either with transducers inserted into the medium or clamped onto their exterior walls.

2.4.2 Ultrasound Absorption (Spectroscopy)

Sound attenuation in a reacting mixture might be caused by many different loss mechanisms, a few of which are intrinsic, thermal, and viscous losses; scattering effects; and relaxation processes. The only effect of some importance for polymer reaction monitoring is sound scattering in particulate mixtures, which is useful for particle sizing. The typical size range of particles detectable by ultrasonic extinction is microns to millimeters, with strongly decreasing sensitivity in the submicron region.

For on-line measurement, the reacting mixture has to be pumped through a narrow slit between the transducers, which causes some shear stress to the latex. Especially for PVOH-stabilized VAE latexes, the final particle size distribution is achieved by a limited agglomeration step during the course of polymerization,

Fig. 12 Sympatec OPUS ultrasound extinction probe with fouling. The shear forces generated in the reactor during dispersion polymerization around the probe created a fast buildup of polymer, thus hindering successful measurement



which is accompanied by shear instability that causes severe fouling at the ultrasonic probe (Fig. 12).

2.4.3 Acoustic Emission

In contrast to sound velocity and attenuation measurements, acoustic emission (AE) is a passive technique that involves listening to acoustic events (i.e., noise) originating from the system. Root causes for acoustic emissions can be gas bubbling, crack initiation and propagation, hard particles bumping into each other and into reactor or tube walls, etc.

Soft VAE particles reacting in an emulsion polymerization tank do not create any noise upon collision with each other or with walls. An extraordinary source of acoustic emissions in mixtures is gas bubbling during depressurization at the reaction end. Continuous noise stemming from motors, stirrers, pumps, seals, gears, and transmission changes accompanies the rising level of reactor filling and increasing viscosity of the latex. In the long run, this noise is indicative of the performance of all the mechanical devices interfaced to the reactor. Hence, it could be used as an indicator for predictive maintenance actions.

AE is an interesting effect for continuously monitoring the anticaking material added to the spray drying process for VAE latexes [41] (Fig. 13). The ultrasonic noise level is almost proportional to the amount of hard anticaking material added to the soft polymer particles upon drying. The size, shape, and density of the hard particles may have an influence on the AE power spectrum.

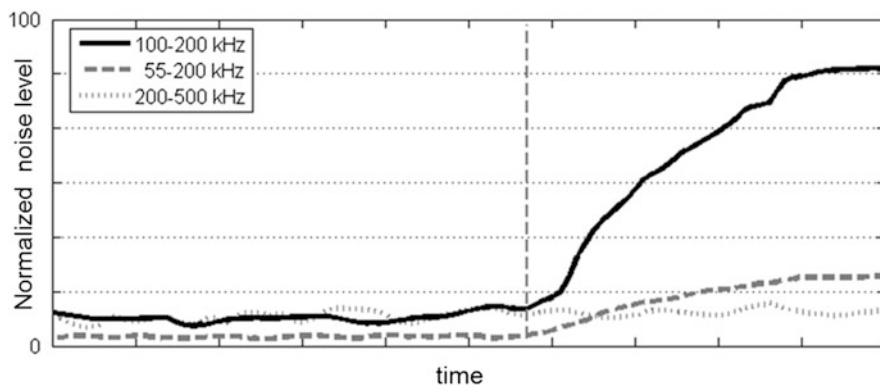


Fig. 13 Acoustic emissions generated by particles of anticaking agent added into a VAE dispersion spray dryer

2.5 Chromatography

One of the most frequently used methods for determination of residual monomer concentration in polymerization reactions is GC. Either injection or headspace methods can be used for analysis. Protocols for at- or off-line measurement of complex compositions are well established and implemented in daily production processes. Injection methods require sample dilution, solvent extraction, and (sometimes) addition of an external standard, whereas headspace techniques need additional information on the partitioning of the monomer between particle, droplet, water, and gas phase. Use of the more elaborate full evaporative headspace technique avoids the need to know the monomer partitioning. Forcing the monomer into the gas phase through full evaporation of the sample needs time and temperature. It is possible to achieve that within a 5 min time frame, as demonstrated by Chai et al. for MMA latexes [54]. However, GC methods are limited in terms of process control strategies because of the unavoidable time lags between sampling, pretreatment, analysis, and data output. For quality control there are no such constraints so that at-line GC and other chromatographic techniques such as size exclusion chromatography (SEC) and high-pressure liquid chromatography can be applied for molecular weight quantification of by-products and volatile organic compounds (VOCs) in general.

Use of GC techniques in monitoring of industrial emulsion polymerization processes requires a carefully designed sampling process. Sampling can be carried out via a direct transfer line from the reactor, a single or (multi)loop, or a by-pass system. Except for direct analysis of the reactor gas phase, every sampling technique offers challenges with respect to flocculation, demixing, clogging of pipes, and consistency in the pretreatment procedures. Two publications describe workaround solutions to cope with the threat of deposition in the sampling line or loops [55, 56]. However, every improvement adds complexity to the monitoring system, which is not desired for start operation procedures.

A straightforward example of a simple by-pass system is analysis of the waste gas composition after degassing in VAE emulsion copolymerization. The degassing step covers the transfer from the reaction vessel to a post-treatment vessel under simultaneous pressure release. If no integrated recovery system is available, this waste gas stream, containing monomers and VOCs, is transferred to a flare and analyzed by in-line GC. The target information is the composition of the flare feed, for better control of the burning process and monitoring of emissions. The ongoing miniaturization of GC equipment could lead to lab-on-a-chip solutions specifically designed for predefined VOC determination, which is possible today for VOC analysis in water samples [57]. At-line and off-line GC methods provide significant advantages in terms of handling, maintenance, and implementation costs compared with on-line monitoring approaches. Furthermore, other on-line techniques such as spectroscopy and calorimetry can often provide enough information (e.g., on residual monomer concentration) with simpler sampling techniques; thus, off-line data acquisition via GC is often the approach of choice in VAE production.

For use in polymerization, the main challenges with chromatography techniques are sampling and the required dilution step. The dilution process needs to cover chemical quenching of the polymerization, external standard addition if required, dilution with water or solvents by a factor of approximately 1,000 for high solid products [58], and homogenization of the modified sample. The described dilution and sampling issue has been the focus of a number of works with similar strategies [13, 14, 58]. An interesting approach to the sampling and dilution dilemma is offered by Reed and coworkers [59–62]. Here, a continuous and small stream of the product is introduced to the “front end,” which also covers the dilution and mixing step [13]. The small lag times and continuous nature of the sampling process have proven the potential of ACOMP to give insights into reaction mechanisms and kinetics or as a data source for process control purposes [13, 14, 58]. In general, ACOMP offers the possibility of a multidetector approach combining several techniques, such as DLS, SEC, GC, and low field NMR. SEC methods have been especially used in ACOMP for on-line molar mass monitoring in different reactor operation modes and for controlled radical polymerization and free-radical emulsion polymerization [13, 14, 58, 63].

For determination of molar mass, SEC or gel permeation chromatography (GPC) with a calibration or multidetection approach are commonly used with a thermodynamically good solvent [64]. SEC methods usually require a filtration step for removal of the nonsoluble polymer fraction and have further constraints, which are summarized elsewhere [64]. Thus, implementation requires routine replacement of the filters. A solution to the filtration issue is offered by the family of field-flow fractionation (FFF) techniques. A recent example of the power of off-line FFF techniques in determination of molar mass and gel content was given by Pasch et al. [64]. However, the samples were dried and dissolved to a total concentration of 7 mg mL^{-1} , which is a dilution factor of 80 for a high solid dispersion. For on-line process monitoring, drying of the polymer prior to measurement is not possible; therefore, water is present at a similar concentration to the polymer. Sweetman et al. used capillary hydrodynamic fractionation (CHDF) and GPC for simultaneous

analysis of particle size distribution and molar mass during semibatch emulsion polymerization of BA and VAc [65]. Although the analysis was conducted off-line, CHDF offers the same potential in combination with sampling techniques as other chromatographic techniques because it requires dilution to 0.1–5% solids and can be operated in a continuous way [65]. The method relies on a full laminar flow profile in a capillary, which enables fractionation of particles by size. As a result of Brownian motion of the particles radial to the direction of flow, smaller particles approaching the capillary wall more closely are retained by the lower flow velocity in the proximity of the wall. The fractionation efficiency is a function of the particle size, viscosity of the eluent, capillary geometric properties, and flow rate. However, CHDF is not used for on-line particle sizing in VAE polymerization due to the restriction to particle sizes $\ll 1 \mu\text{m}$ and the tendency for capillary blocking.

2.6 NMR

Although NMR spectroscopy has become a workhorse technique for polymer characterization and synthesis chemistry, it is not as frequently used in on-line industrial process analytics [66]. Its versatility in the analysis of polymer composition and structural features has been demonstrated [67–69] as well as its application in hyphenated in- and on-line measurements [70–74]. On-line applications of low-, mid-, and high-field NMR remain research techniques [68, 69, 75–77] used, for example, in determination of kinetic parameters [18, 78]. The capabilities of ^1H low-field and $^1\text{H}/^{13}\text{C}$ solid-state NMR in emulsion polymerization of BA and copolymerization with MMA have been successfully demonstrated [76, 79, 80]. However, their industrial implementation as standard process analytics techniques still faces challenges.

In addition to mid- and low-field NMR, which are also suitable for direct quantification with spectral resolution, time domain NMR is a robust, easy to implement alternative [71, 81]. In general, relaxometry measurements provide easy and fast determination of transverse (T_2) and longitudinal (T_1) relaxation rates, both dominated by inter- and intramolecular fluctuations in homonuclear dipolar interactions [82]. Both time constants refer to measurable changes in magnetization in the z -direction $M_z(T_1)$ or xy -plane $M_{xy}(T_2)$ as function of the time interval t [66]. Equations (3) and (4) give the fundamental functions for both relaxation process, with M_0 and $M_{xy,0}$ being the magnetization of thermal equilibrium in z and the component of magnetization in the xy -plane. In an on-line loop setup with stopped or continuous flow [67, 75, 82, 83], the more sensitive time T_2 can yield information about changes in proton mobility and, thus, on solids and the viscosity of the reaction mass. However, care must be taken with design of the loop setup. The influence of T_1 on the polarization process needs to be considered thoroughly because magnetization increases exponentially with T_1 and determines the flow rate and residence time in the magnetic field before analysis [66, 71, 72]. Furthermore, temperature and mass flow control is essential to avoid

concentration and temperature inhomogeneities and, thus, fluctuation in the thermal equilibrium magnetization [66].

$$M_z(t) = M_0 \left(1 - e^{-\frac{t}{T_1}}\right) \quad (3)$$

$$M_{xy}(t) = M_{xy,0} e^{-\frac{t}{T_2}} \quad (4)$$

In VAE polymerization, additional challenges arise for implementation of on-line NMR systems. Polymerization pressure and explosion protection need to be considered and require special design and encapsulation of the equipment. Furthermore, polymer deposits and shear-induced viscosity fluctuations can lead to significant over- or underestimation of process variables in a loop system. In at- or off-line applications, time domain-NMR (TD-NMR) has already been used for monitoring solid content in VAE emulsions. Figure 14 shows a representative example of a solids content calibration curve for free induction decay (FID) experiments using a biexponential function for determination of T_2 (Eq. 5).

$$I(t) = A_1 e^{-\frac{t}{T_{2,1}}} + A_2 e^{-\frac{t}{T_{2,2}}} \quad (5)$$

2.7 Other Methods

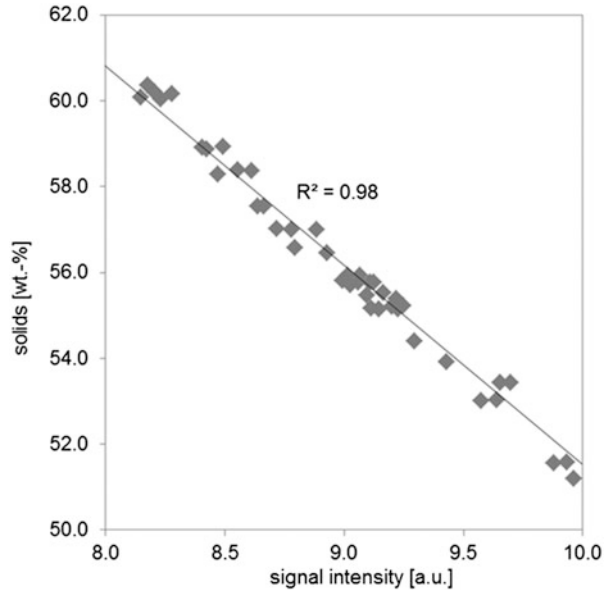
2.7.1 Conductometry

An affordable method for on-line monitoring of polymerization processes is the conductometric approach, if the relation between ion concentration and conductivity is known. The conductivity sensor can respond to changes in the concentration of ionic surfactants in emulsion polymerization reactions, capturing surfactant dynamics in the media, which can be related to changes in the surface area of the polymer particle phase, and therefore also particle nucleation and/or coagulation phenomena. Additionally, conductivity measurements can give information about emulsion polymerization kinetics [84, 85]. Examples of emulsion polymerizations are given in the literature [85–88].

2.7.2 Industrial Process Tomography

Industrial process tomography solutions can be based on many different technologies, including so-called hard-field tomography applications, where the direction of travel of energy waves from the power source is constant (e.g., using ionizing radiation in X-ray tomography). In soft-field tomography, the input signal distribution is influenced by the traversed material, like electrical impedance tomography (EIT) and electrical capacitance tomography (ECT) [89]. Electrical resistance

Fig. 14 Ratio of fast and slow amplitudes (A_1/A_2) from biexponential fitting of T_2 relaxation curves



tomography (ERT) is a variant of EIT, in which the real component of the electrical impedance is the main property of the medium analyzed [90, 91].

VAE dispersions have a conductivity of about 1–2 mS/cm, opening the path to reliable ERT measurements, which enable visualization of three-dimensional conductivity distributions within the process unit in real time. This can, for example, also give information on degassing processes and foam formation in VAE processes, where the dispersion has to be depressurized from the reactor into a degassing vessel. Another viable method could be the ultrasound pulse echo approach [92].

All these methods are nondestructive and some are noninvasive (e.g., ECT). Gathering information from the vessel content (be it a reactor, pipe, or column) can help improve understanding of mixing and hydrodynamics, as well as separation and transportation processes (including the formation of foam). It can also help in validation of computational fluid dynamics simulations. A simple way to obtain information from the inside of the process is the use of conductivity measurements at different locations in the system, if the added feeds exhibit different conductivities. Figure 15 shows the conductivity signal created by adding a tracer into a VAE reaction system directly at a feed inlet, the middle of the reactor, and the bottom of the reactor. The broadness of the signal flank can be used to characterize the mixing behavior of the reactor.

ECT can be used to analyze the three-dimensional multiphase flows in gas/solid conveyor systems, helping to understand material distribution and plug flows. If a model relating the dielectric permittivity to the bulk density is known, the average solids distribution can be extracted from a cross-sectional image [93], which could make the method interesting for VAE dispersion spray drying processes.

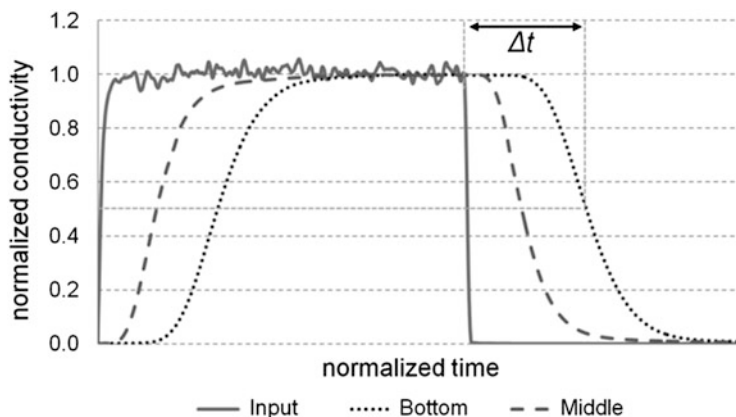


Fig. 15 Conductivity measurements at different locations of a VAE reactor after addition of a highly conductive tracer

2.7.3 Dielectric Spectroscopy

Dielectric spectroscopy (DS) is based on the measurement of the dielectric properties of materials (e.g., dielectric permittivity), giving information about different molecular motions and relaxation processes. DS can cover a wide range of frequencies (10^{-5} – 10^{11} Hz), enabling analysis of molecular events such as electronic, displacement, orientation, and interfacial polarization and motion of charge carriers [18, 94]. The method has found a large range of applications in research on rechargeable batteries, chemical sensors, fuel cells, and electrochromic display devices and, in general, is used for analysis of electroactive polymers [95, 96].

If a chemical reaction changes the rate of motion and polarization of molecules, affecting the dielectric response of the mixture, then DS can be a viable method for monitoring the reaction [18, 29]. The molecular dynamics of different poly(vinyl acetate) (PVAc)-containing blends can also be analyzed using DS [97, 98]. Application of DS to VAE systems are mainly focused on development and analytical topics. For example, the interfacial interactions and dynamics of samples with different amounts of PVAc adsorbed on silica particles was analyzed using dielectric methods and FTIR spectroscopy [99].

2.8 Biocontamination

Polymer emulsions can be vulnerable to biocontamination. Over the last few decades, the growing number of regulations on biocides and restrictions on the availability of biocidal molecules has created a challenging situation. The only way to minimize risks is to combine the use of suitable biocide packages with stringent plant hygiene and the necessary monitoring tasks.

Although it is safe to assume that the VAE dispersion is sterile after the polymerization process in the reactor, post-adds and downstream processes could re-introduce biocontaminants such as yeasts or bacteria.

One major aspect of plant hygiene is the control and treatment of raw materials (especially those that are used after the main polymerization step, including process water) to avoid introduction of biocontaminants into the system. Furthermore, pipes, storage vessels, product vessels (including tank trucks), and retained samples must be controlled.

Process water should be treated and chlorinated. If initial contamination of the water (e.g., from wells) is high, an initial UV-based treatment can be effective in lowering the level of contamination. The main treatment step is chlorination of the water. Monitoring and control of chlorination (with gaseous chlorine or hypochlorite) in VAE dispersion plants is usually done on-line via photometric/colorimetric or amperometric systems [100, 101]. Former systems often used *N,N*-diethyl-1,4-phenylenediamin (DPD), which is oxidized to give a red color that is quantified either photometrically or, commonly, off-line using comparison color cards. The latter systems have the advantage of not needing a regular supply of DPD, but need complex calibrations, including the effect of pH and temperature. These on-line measurements provide regular values, but can only measure water from one (or a few close-by) sampling point(s). Additional monitoring of the chloride concentration in samples from other points along the process is essential, because the concentration of active chloride might be diminished downstream if biomaterial is present.

The measurement of biocontaminants can be done using traditional techniques for cultivating samples (e.g., on agar plates). This plating requires 3–7 days for the necessary precision.

Faster techniques have been designed (e.g., enzyme-linked immunosorbent assays) that can provide results within a few hours, including sample processing, but need specialized personnel and individualized design of the method for a specific species or family thereof. One viable method that can be used by plant personnel is an adenosine triphosphate (ATP) fluorescence test, which presents a signal according to the presence of ATP molecules [102], but only gives a rough indication of contamination for VAE dispersions.

Another on-line monitoring method is the detection of CO₂ created through metabolism of the organism. Glass electrodes can be used for solutions or infrared sensors for the gas phase. Tests in VAE dispersion filled closed bulk containers showed that such sensors could measure the CO₂ level as required. The sensor had a measuring range of up to 1,000 ppm with $\pm 0.5\%$ accuracy and used a filament lamp to measure the CO₂ IR adsorption and a reference IR band. Tests in a VAE plant dispersion silo (see Fig. 16) showed the signal to be strongly influenced by air balancing with the atmosphere (through wash bottles for biohygiene) and incoming new product and additives.

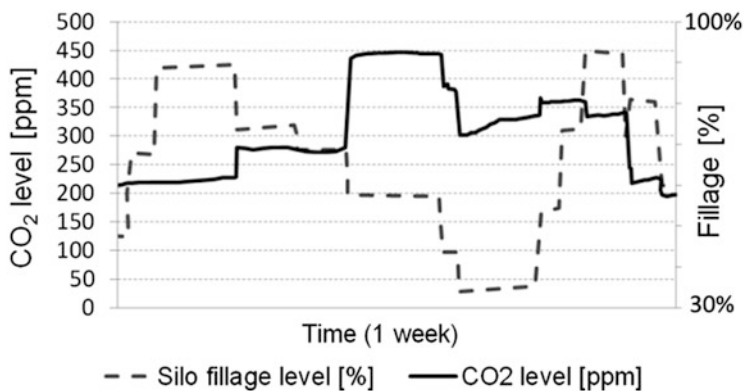


Fig. 16 CO₂ measurements in a VAE dispersion silo show fluctuations resulting from infrastructure influences (change of product level in the vessel)

3 Conclusion

Many different sensor types are available for measuring properties of interest in VAE processes at-line and on-line. The high pressure nature of VAE reactors, changes in properties of the reactor contents during reaction (e.g., through particle formation and aggregation), and the tendency for fouling at reactor walls limits the industrial choice to robust sensors (e.g., spectroscopic probes). The installation of sensors in legacy high-pressure equipment is limited by the availability of ports, as changes to the physical structure of the vessel is avoided if possible. Therefore, gathering on-line data from the reaction itself is not always feasible, and the installation of downstream sensors the only option. In general, sensors that can measure a property directly in undiluted samples are preferred (e.g., photon density wave spectroscopy for particle sizing) because the properties of the product sample might change through dilution. Sample extraction from the reaction system is a viable possibility, if clogging of the line, detrimental effects of depressurization and, possibly, dilution, do not play a role. It is, therefore, necessary to individually assess products for their robustness to extraction and dilution steps, and appraise sensors concerning their ease of installation and robustness to fouling.

References

1. Gy P (2004) Part IV: 50 years of sampling theory – a personal history. *Chemom Intell Lab Syst* 74:49–60
2. Petersen L, Minkkinen P, Esbensen KH (2005) Representative sampling for reliable data analysis, theory of sampling. *Chemom Intell Lab Syst* 77:261–277
3. Smith PL (2008) An introduction to general sampling: reducing bias and variation in bulk sampling. *J GXP Compliance* 12(4):60–65

4. Smith PL (2008) Error and variation in bulk material sampling. *J GXP Compliance* 12 (5):69–76
5. Smith PL (2009) Q & A on sampling bulk materials. *J GXP Compliance* 13(1):67–73
6. Allen T (2003) Powder sampling and particle size determination. Elsevier, London
7. Muzzio FJ, Goodridge CL, Alexander A, Arratia P, Yang H, Sudah O, Mergen G (2002) Sampling and characterization of pharmaceutical powders and granular blends. *Int J Pharm* 250(1):51–64
8. Muzzio FJ, Robinson P, Wightman C, Brone D (1997) Sample practices in powder blending. *Int J Pharm* 155(2):153–178
9. Chrysler, Ford, General Motors (2010) Measurement system analysis 4th edn. Automotive Industry Action Group, Southfield
10. Apley QJ, Cliff WC, Creer JM (1984) Sampling device for withdrawing a representative sample from single and multi-phase flows. Patent US 4,442,720 A
11. Enohnyaket P, Kreft T, Alb AM, Drenski MF, Reed WF (2007) Determination of molecular mass during online monitoring of copolymerization reactions. *Macromolecules* 40:8040
12. Alb AM, Paril A, Çatalgil-Giz H, Giz A, Reed WF (2007) Evolution of composition, molar mass, and conductivity during the free radical copolymerization of polyelectrolytes. *J Phys Chem B* 111:8560
13. Alb AM, Reed WF (2008) Simultaneous monitoring of polymer and particle characteristics during emulsion polymerization. *Macromolecules* 41:2406–2414
14. Alb AM, Reed WF (2009) Online monitoring of molecular weight and other characteristics during semibatch emulsion polymerization under monomer starved and flooded conditions. *Macromolecules* 42:8093–8101
15. Kreft T, Reed WF (2009) Predictive control of average composition and molecular weight distributions in semibatch free radical copolymerization reactions. *Macromolecules* 42 (15):5558–5565
16. Reed WF, Alb AM (eds) (2013) Monitoring polymerization reactions: from fundamentals to applications. Wiley, Hoboken
17. Moritz H-U (1989) Polymerization calorimetry – a powerful tool for reactor control. In: Reichert KH, Geisler W (eds) *Polymer reaction engineering*. VCH, Weinheim, pp 248–266
18. Fonseca GE, Dubé MA, Penlidis A (2009). *Macromol React Eng* 3:327
19. Landau RN (1996) Expanding the role of reaction calorimetry. *Thermochim Acta* 289 (2):101–126
20. Gesthuisen R, Krämer S, Niggemann G, Leiza JR, Asua JM (2005) Determining the best reaction calorimetry technique: theoretical development. *Comput Chem Eng* 29:349–365
21. Esposito M, Sayer C, de Araújo PHH (2010) In-line monitoring of emulsion polymerization reactions combining heat flow and heat balance calorimetry. *Macromol React Eng* 4:682–690
22. Tietze A, Ludtke I, Reichert K-H (1996) Temperature oscillation calorimetry in stirred tank reactors. *Chem Eng Sci* 51:3131–3137
23. Hergeth WD, Jaeckle C, Krell M (2003) Industrial process monitoring of polymerization and spray drying processes. *Polym React Eng* 11:663
24. Elizalde O, Azpeitia M, Reis MM, Asua LM, Leiza JR (2005) Monitoring emulsion polymerization reactors: calorimetry versus Raman spectroscopy. *Ind Eng Chem Res* 44:7200–7207
25. Elizalde O, Leiza JR, Asua JM (2004). *Macromol Symp* 206:135–148
26. Lamb DJ, Fellows CM, Morrison BR, Gilbert RG (2005) A critical evaluation of reaction calorimetry for the study of emulsion polymerization systems: thermodynamic and kinetic aspects. *Polymer* 46:285–294
27. Frauendorfer E, Wolf A, Hergeth W-D (2010) Polymerization online monitoring. *Chem Eng Technol* 33:1767–1778
28. BenAmor S, Colombié D, McKenna T (2002) Online reaction calorimetry. Applications to the monitoring of emulsion polymerization without samples or models of the heat-transfer coefficient. *Ind Eng Chem Res* 41:4233–4241

29. Hergeth W-D (2011) On-line monitoring of chemical reactions. Ullmann's encyclopedia of industrial chemistry 7th edn. Wiley-VCH, Weinheim, pp 345–398
30. Kessler RW, Kessler W, Zikulnig-Rusch E (2016) A critical summary of spectroscopic techniques and their robustness in industrial PAT applications. *Chem Ing Tech* 88:710–721
31. Chatzi EG, Kammona O, Kiparissides C (1997) Use of a midrange infrared optical-fiber probe for the on-line monitoring of 2-ethylhexyl acrylate/styrene emulsion copolymerization. *J Appl Polym Sci* 63:799–809
32. Hua H, Dube MA (2001) Terpolymerization monitoring with ATR-FTIR spectroscopy. *J Polym Sci Part A Polym Chem* 39:1860–1876
33. Roberge S, Dube MA (2007) Inline monitoring of styrene/butyl acrylate miniemulsion polymerization with attenuated total reflectance/Fourier transform infrared spectroscopy. *J Appl Polym Sci* 103:46–52
34. Schuchardt P, Siesler HW (2017) Real-time analysis of the polymerization kinetics of 1,4-butanediol and 4,4'-diphenylmethanediisocyanate by fiber-coupled Fourier transform infrared spectroscopy. *Anal Bioanal Chem* 409:833–839
35. Mettler-Toledo (2017) FTIR spectroscopy with in situ reaction monitoring. Mettler-Toledo, Columbia. http://www.mt.com/us/en/home/products/L1_AutochemProducts/ReactIR.html. Accessed 17 Feb 2017
36. Santos AF, Silva FM, Lenzi MK, Pinto JC (2005) Monitoring and control of polymerization reactors using NIR spectroscopy. *Polym-Plast Technol Eng* 44:1–61
37. Cherfi A, Fevotte G, Novat C (2002) Robust on-line measurement of conversion and molecular weight using NIR spectroscopy during solution polymerization. *J Appl Polym Sci* 85:2510–2520
38. Sheibat-Othman N, Fevotte G, Peycelon D, Egraz J-B, Asua J-M (2004) Control of polymer molecular weight using near infrared spectroscopy. *AIChE J* 50:654
39. Reis MM, Araujo PHH, Sayer C, Guidici R (2003) Correlation between polymer particle size and in-situ NIR spectra. *Macromol Rapid Commun* 24:620–624
40. Reis MM, Araujo PHH, Sayer C, Guidici R (2004) In situ near-infrared spectroscopy for simultaneous monitoring of multiple process variables in emulsion copolymerization. *Ind Eng Chem Res* 43:7243–7250
41. Frauendorfer E, Hergeth W-D (2016) Prozessanalytik bei der zerstäubungstrocknung – beispiele und herausforderungen. *Chem Ing Tech* 88:777–785
42. Schrader B (1995) Infrared and Raman spectroscopy: methods and applications. VCH, Weinheim
43. Elizalde O, Leiza JR (2009) Raman application in emulsion polymerization systems. In: Amer MS (ed) *Raman spectroscopy for soft matter applications*. Wiley-Blackwell, New York, pp 95–144
44. Frauendorfer E, Hergeth W-D (2017) Industrial application of Raman spectroscopy for control and optimization of vinyl acetate resin polymerization. *Anal Bioanal Chem* 409:631–636
45. Reis MM, Araujo PHH, Sayer C, Guidici R (2003) Evidences of correlation between polymer particle size and Raman scattering. *Polymer* 44:6123–6128
46. Hergeth W-D, Codella PJ (1994) Monomers in polymer dispersions. Part IV: partition of acrylonitrile in rubber latex as studied by Raman spectroscopy. *Appl Spectrosc* 48:900–903
47. Anton F, Lindemann C, Hitzmann B, Reardon KF, Scheper T (2010) Fluorescence sensors for bioprocess monitoring. In: Flickinger MC (ed) *Encyclopedia of industrial biotechnology: bioprocess, bioseparation, and cell technology*. Wiley, New York, pp 2482–2491
48. Hass R, Reich O (2011) Photon density wave spectroscopy for dilution-free sizing of highly concentrated nanoparticles during starved-feed polymerization. *Chem Phys Chem* 12:2572–2575
49. Hass R, Munzke D, Reich O (2010) Inline-partikelgrößenmesstechniken für suspensionen und emulsionen. *Chem Ing Tech* 82:477–490
50. Maret G (1997) Diffusing-wave spectroscopy. *Curr Opin Colloid Interface Sci* 2:251–257

51. Singha N (2001) Use of fiber optics quasi-elastic light scattering (FOQELS) in the particle sizing of polymer lattices. *Kaut Gummi Kunstst* 54(3):97–100
52. Hauptmann P, Dinger F, Säuberlich R (1985) A sensitive method for polymerization control based on ultrasonic measurements. *Polymer* 26:1741–1744
53. Hergeth W-D, Starre P, Schmutzler K, Wartewig S (1988) Polymerizations in the presence of seeds: 3. Emulsion polymerization of vinyl acetate in the presence of quartz powder. *Polymer* 29:1323–1328
54. Chai X-S, Hou QX, Schork FJ (2004) Determination of residual monomer in polymer latex by full evaporation headspace gas chromatography. *J Chromatogr A* 1040(2):163–167
55. Leiza JR, de la Cal JC, Montes M, Asua JM (1993) Online monitoring of conversion and polymer composition in emulsion polymerization systems. *Process Control Qual* 4 (3):197–210
56. Noel LFJ, Brouwer ECP, van Herk AM, German AL (1995) On-line gas chromatography and densimetry to obtain partial conversions of both monomers in emulsion copolymerization. *J Appl Polym Sci* 57:245
57. Zhou M, Lee J, Zhu H, Nidetz R, Kurabayashi K, Fan X (2016) A fully automated portable gas chromatography system for sensitive and rapid quantification of volatile organic compounds in water. *RSC Adv* 6:49416–49424
58. McAfee T, Leonardi N, Montgomery R, Siqueira J, Zekoski T, Drenski MF, Reed WF (2016) Automatic control of polymer molecular weight during synthesis. *Macromolecules* 49:7170–7183
59. Reed WF, Drenski MF, From PCT Int. Appl (2016) Systems and methods for control of polymer reactions and processing using automatic continuous online monitoring. Patent WO 2016054138 A1 20160407
60. Reed WF, From PCT Int. Appl (2016) Device and method for changing solution conditions in serial flow. Patent WO 2016061024 A2 20160421
61. Reed WF, Drenski MF, From PCT Int. Appl (2016) Systems and methods for predicting and controlling the properties of a chemical species during a time-dependent process. Patent WO 2016118507 A1 20160728
62. Reed WF, From PCT Int. Appl (2017) Scheduling analysis and throughput of macromolecular solutions based on light scattering measurements. Patent WO 2017015499 A1 20170126
63. Rosenfeld C, Serra C, O'Donohue S, Hadziioannou G (2007) Continuous online rapid size exclusion chromatography monitoring of polymerizations – CORSEMP. *Macromol React Eng* 1:547–552
64. Maka AC, Williams RP, Pasch H (2016) Field flow fractionation for the size, molar mass, and gel content analysis of emulsion polymers for water-based coatings. *Macromol Chem Phys* 217:2027–2040
65. Sweetman SJ, Immanuel CD, Malik TI, Emmett S, Williams N (2008) Simultaneous controllability of PSD and MWD in emulsion polymerisation. *Macromol React Eng* 2:382–397
66. Colnago LA (2014) Why is inline NMR rarely used as industrial sensor? Challenges and opportunities. *Chem Eng Technol* 37(2):191–203
67. Ibbett RN (ed) (1993) *NMR spectroscopy of polymers*. Blackwell Academic & Professional, Glasgow
68. Hofmann M, Herrmann A, Ok S, Franz C, Kruk D, Saalwächter K, et al. (2011) Polymer dynamics of polybutadiene in nanoscopic confinement as revealed by field cycling ^1H NMR. *Macromolecules* 44:4017–4021
69. Mujtaba A, Keller M, Ilisch S, Radosch HJ, Thurn-Albrecht T, Saalwächter K, et al. (2012) Mechanical properties and cross-link density of styrene-butadiene model composites containing fillers with bimodal particle size distribution. *Macromolecules* 45:6504–6515
70. Rántzsch V, Wilhelm M, Guthausen G (2016) Hyphenated low-field NMR techniques: combining NMR with NIR, GPC/SEC and rheometry. *Magn Reson Chem* 54:494–501
71. Dalitz F, Cudaj M, Maiwald M, Guthausen G (2012) Process and reaction monitoring by low-field NMR spectroscopy. *Prog Nucl Magn Reson Spectrosc* 60:52–70

72. Singh K, Blümich B (2016) NMR spectroscopy with compact instruments. *Trends Anal Chem* 83:12–26
73. Cudaj M, Guthausen G, Hofe T, Wilhelm M (2011) SEC-MR-NMR: online coupling of size exclusion chromatography and medium resolution NMR spectroscopy. *Macromol Rapid Commun* 32:665–670
74. Cudaj M, Guthausen G, Hofe T, Wilhelm M (2012) Online coupling of size-exclusion chromatography and low-field ^1H NMR spectroscopy. *Macromol Chem Phys* 213:1933–1943
75. Harbou EV, Behrens R, Berje J, Brächer A, Hasse H (2016) Studying fast reaction kinetics with online NMR spectroscopy. *Chem Ing Tech* 89:369–378. doi:10.1002/cite.201600068
76. Dewel M, Vogel N, Weiss CK, Landfester K, Spiess HW, Münnemann K (2012) Online monitoring of styrene polymerization in miniemulsion by hyperpolarized ^{129}Xe NMR spectroscopy. *Macromolecules* 45:1839–1846
77. Sans V, Porwol L, Dragone V, Cronin L (2015) A self optimizing synthetic organic reactor system using real-time in-line NMR spectroscopy. *Chem Sci* 6:1258–1264
78. Vargas MA (2010) online low-field ^1H NMR spectroscopy: monitoring of emulsion polymerization of butyl acrylate. *Macromolecules* 43:5561–5568
79. Landfester K, Spiegel S, Born R, et al. (1998) On-line detection of emulsion polymerization by solid-state NMR spectroscopy. *Colloid Polym Sci* 276:356
80. Landfester K, Spiess HW (1998) Characterization of interphases in core – shell latexes by solid-state NMR. *Acta Polym* 49:451–464
81. Adams A (2016) Analysis of solid technical polymers by compact NMR. *Trends Anal Chem* 83:107–119
82. Meyer K, Kern S, Zientek N, Guthausen G, Maiwald M (2016) Process control with compact NMR. *Trends Anal Chem* 83:39–52
83. Foley DA, Bez E, Codina A, Colson KL, Fey M, Krull R, et al. (2014) NMR flow tube for online NMR reaction monitoring. *Anal Chem* 86:12008–12013
84. Santos AF, Lima AL, Pinto JC, Graillat C, McKenna TF (2003) Online monitoring of the evolution of the number of particles in emulsion polymerization by conductivity measurements. I. Model formulation A. *J Appl Polym Sci* 90(5):1213–1226
85. Farshchi F, Santos AF, Othman S, Hammouri H, McKenna TF (2004) Monitoring of emulsion polymerization using conductimetry coupled with calorimetry. In: 8th international workshop on polymer reaction engineering, Hamburg, 3–6 October 2004
86. Santos AF, Lima EL, Pinto JC, Graillat C, McKenna TF (2004) On-line monitoring of the evolution of number of particles in emulsion polymerization by conductivity measurements. II. Model validation. *J Appl Polym Sci* 91(2):941–952
87. Graillat C, Santos A, Pinto JC, McKenna TF (2004) On-line monitoring of emulsion polymerisation using conductivity measurements. *Macromol Symp* 206:433–442
88. Zhao F (2011) Online conductivity and stability in emulsion polymerization of n-butyl methacrylate. Theses and Dissertations. Paper 1276, Lehigh University, Bethlehem
89. Ye Z, Yang CL, Ma L, Wei HY, Banasiak R, Soleimani M (2013) Volumetric soft field and hard field tomography: MIT, ECT, EIR, cone beam CT. In: 7th World Congress on Industrial Process Tomography
90. Sharifi M, Young B (2013) Electrical resistance tomography (ERT) applications to chemical engineering. *Chem Eng Res Des* 91(9):1625–1645
91. Fransolet E, Crine M, L’Homme G, Toye D, Marchot P (2002) Electrical resistance tomography sensor simulations: comparison with experiments. *Meas Sci Technol* 13:1239–1247
92. McClements DJ, Fairley P (1991) Ultrasonic pulse echo reflectometer. *Ultrasonics* 29(1):58–62
93. Jaworski A, Dyakowski T (2001) Application of electrical capacitance tomography for measurement of gas-solids flow characteristics in a pneumatic conveying system. *Meas Sci Technol* 12:1605–1616
94. Runt JS, Fitzgerald JJ (eds) (1997) Dielectric spectroscopy of polymeric materials. Fundamentals and applications. American Chemical Society, Washington

95. Scrosati B (ed) (1993) Applications of electroactive polymers. Chapman and Hall, London
96. Gray FM (1991) Solid polymer electrolytes – fundamentals and technological applications. VCH, New York
97. Zardalidis G, Floudas G (2012) Pressure effects on the dynamic heterogeneity of miscible poly(vinyl acetate)/poly(ethylene oxide) blends. *Macromolecules* 45:6272–6280
98. Madouly SA, Mansoor AA, Abdou NY (2007) Molecular dynamics of amorphous/crystalline polymer blends studied by broadband dielectric spectroscopy. *Eur Polym J* 43:1892–1904
99. Füllbrandt M, Purohit PJ, Schönhals A (2013) Combined FTIR and dielectric investigation of poly(vinyl acetate) adsorbed on silica particles. *Macromolecules* 46(11):4526–4632
100. Jensen JN, Johnson JD (1989) Specificity of the DPD and amperometric titration methods for free available chlorine: a review. *J Am Water Works Assoc* 81(12):59–64
101. Rice EW, Baird R, Eaton AD (eds) (1992) Standard methods for the examination of water and wastewater. American Public Health Association, Washington
102. Udenfriend S (ed) (1969) Florescence assay in biology and medicine. Academic, London

Index

A

- Acetoacetoxyethyl methacrylate (AAEM), 112
- Acoustic emission, 201
- 2-Acrylamido-2-methyl propane sulfonic acid (AMPS), 120
- Adenosine triphosphate (ATP) fluorescence test, 208
- Adhesive wall, 168, 176
- Alkylamidines, 145
- Allyl methacrylate (AMA), 113
- Atom transfer radical polymerization (ATRP), 6, 116, 117
- Attenuated total reflection (ATR), 193
- Automatic continuous online monitoring of polymerization reactions (ACOMP), 188
- Azobis[2-(2-imidazolin-2-yl)propane] (VA-061), 148
- Azobis[2-(2-imidazolin-2-yl)propane] dihydrochloride (VA-044), 148
- Azobis(2-methylpropionamidine) dihydrochloride (V-50), 153

B

- BA-*co*-AA-*co*-AMPS, 120
- Bancroft's rule, 30
- Biocontamination, 207
- Boltzmann distribution, 93, 95, 98
- Boltzmann effect, 81
- Butylacrylate-methylmethacrylate-acrylic acid copolymer latexes, 95

C

- Cadmium sulfide (CdS), 122, 123
- Calorimetry, 127, 189–196, 203
- Capillary hydrodynamic fractionation (CHDF), 203
- Carbon dioxide, supercritical, 46, 65
- CdSe/ZnS quantum dots (QDs), 120
- CeO₂, 120
- Chalcogenide/polymer hybrid, magnetoresponsive, 123
- Coagulation, 161
- Coatings, 2, 11, 46, 105–109, 116, 121, 132, 144, 155
 - adhesives, 11
 - UV-blocking, 120
- Colloidal interactions, 79, 83
- Comonomers, switchable, 153
- Composites, 105
- Conductometry, 205
- Core-shell particles, 107
- CO₂-switchable groups, 143
- Counterions, association, 79
- Critical micelle concentration (CMC), 34, 35

D

- Debye-Hückel parameter, 83
- Deryaguin-Landau-Verwey-Overbeek (DLVO) theory, 79–83, 92, 100, 169, 170
- Dielectric spectroscopy (DS), 207
- 2-(Diethylamino)ethyl methacrylate (DEAEMA), 147

Diethyl-1,4-phenyldiamin (DPD), 208
 Diffusing wave spectroscopy (DWS), 198
 Diffusion, 45
 2-(Dimethylamino)ethyl methacrylate (DMAEMA), 147
 Dimethylaminopropyl methacrylamide (DMAPMAm), 147
 Dimethyldodecylamine (DDA), 150
 Discrete element method (DEM), 161, 164
 Dispersed systems, 45
 Dispersion polymerization, 45
 (N-Amidino)dodecyl acrylamide (DAm), 149
 Dodecyl-*N,N*-dimethylacetamidinium bicarbonate, 151
N'-(2-(2-(Dodecyloxy)ethoxy)ethyl-*N,N*-dimethylacetamidinium bicarbonate, 151
 Droplet formation, 23
 forced, 25
 spontaneous, 30
 Drug delivery, 109

E

Efficiency, 1, 9, 58, 119, 184
 Elastomer latex, fluorinated, 87
 Electrical capacitance tomography (ECT), 205
 Electrical double layer (EDL), 80
 Electrical impedance tomography (EIT), 205
 Electrolyte dissociation equilibrium, 82
 Emulsification, spontaneous, 30–41
 Emulsion polymerization, 1, 23, 80, 143, 189
 Encapsulation, 115–123, 132–134, 145, 205
 Evanescent wave spectroscopy (EWA), 193

F

Fiber optic quasi-elastic light scattering (FOQELS), 199
 Flocculant, CO₂-switchable, 153
 Focused beam reflectance measurement (FBRM), 198
 Fouling, 161–180, 184–190, 198–201, 209
 Free-radical polymerization (FRP), 3, 45–54, 73, 195
 Fuchs stability ratio, 79, 80

G

Gibbsite, 120
 Gouy–Chapman theory, 85
 Graphene oxide, 121

H

Hamaker relation, 83
 Heat exchangers, 163
 Hexafluoropropylene (HFP), 61
 High-angle annular dark field (HAADF) cryo-STEM image, 130
 High-pressure liquid chromatography (HPLC), 202
 Hogg–Healy–Fuersteneau expression, 83
 Hollow latex particles, 109
 Hydration, 80–100, 168
 Hydrodynamics, 165
 Hydroxymethyl methacrylate (HEMA), 109

I

Initiators, CO₂-switchable, 148
 Interaction energy barrier, 80

J

Johnson–Kendall–Roberts (JKR) theory, 169

K

Kinetic rate constants, 56
 Kolmogorov length, 26

L

Latexes, 5, 32, 80, 105, 143, 163, 200
 CO₂-switchable, 149
 stimuli-responsive, 143
 Layered double hydroxide (LDH), 117
 LDPE, 11
 Lubrication forces, 167

M

Magnetite, 121, 123
 Magneto-responsive, 123
 Mathematical modeling, 1, 13, 105, 165
 Membrane bioreactors, 163
 Methacrylic acid (MAA), 111
 Methacryloxymethyltriethoxysilane (MMS), 120
 Methylacryloyloxyl-2-hydroxypropyl perfluorooctanoate (FGOA), 108
 Mid-infrared (MIR) spectroscopy, 193
 Miniemulsion polymerization, 1, 10, 116
 Modeling, 45, 161
 Monomers
 CO₂-switchable, 147

- residual, 8
- Montmorillonite, 116
- Morphologies
 - composite latex particles, 123
 - flower-like, 113
 - nonequilibrium, 111
- Multi-angle laser light scattering (MALLS), 30

- N**
- Nanoparticles, 2, 111–134, 144, 150, 155
 - CO₂-switchable, 155
- Navier–Stokes equations, 163, 166
- Near-infrared (NIR) spectroscopy, 193
- Nitroxide-mediated polymerization, 154

- O**
- Online analytics, 183
- Optical coherence tomography (OCT), 198

- P**
- Particles
 - morphology, 1, 6, 105
 - switchable, 143
 - volume fraction, 86–91, 166, 173, 178
- Particle size distribution (PSD), 7, 14
- Particle vision and measurement (PVM), 198
- P(BA-*co*-MMA)/P(BA-*co*-MMA-*co*-acrylate-dodecafluoroheptyl methacrylate-*co*-AA), 113
- P(BA-*co*-MMA)/P(BA-*co*-MMA-*co*-DFMA-*co*-AA), 115
- P(BA-*co*-S)/NaMMT, 121
- PBA/PVC, 115
- PDEAEMA, 147
- PDMAEMA-*b*-PMMA, 150
- Perfluoropolyether (PFPE)-based carboxylate, 87
- Photocatalytic coatings, 116
- Photon density wave (PDW) spectroscopy, 198
- Physicochemical process interplay, 79
- Pickering stabilization, 120
- P(MA-*co*-BA)/LDH, 118
- P(MMA-BA-MAAEGDMA)/P(MMA-St-MAA)/P(St-DVB), 110
- P(MMA-*co*-BA-AA)/CeO₂, 119
- P(MMA-*co*-BA-*co*-SA)/TiO₂, 122
- P(MMA-*co*-BA)/Gibbsite/(AA-*co*-BA), 118
- PMMA/PS/MMT, 118
- Poisson–Boltzmann equation, 85
- Polyacrylate/polyacrylate, fluorinated, 108
- Polyacrylate/PS, 110
- Polyacrylate/PU, 108
- Polyethylene wax dispersions, micronized, 11
- Polymer hybrids, 105
- Polymer–inorganic particles, 115
- Polymerization
 - dispersion, 45
 - emulsion, 23
 - induced self-assembly (PISA), 154
 - miniemulsion, 1
 - precipitation, 45
 - radical, 45
- Poly(methacrylate-*co*-methacrylic acid)/poly(methacrylic acid-*co*-*N*-isopropylacrylamide), 109
- Poly(methacrylic acid-*co*-*N*-isopropylacrylamide), 110
- Polystyrene (PS), 26, 27, 33, 37, 112, 149
 - magnetite/CdS, 122
 - SiO₂, 120
 - switchable, 152
 - TiO₂/magnetite, 122
- Poly(styrene-*co*-butyl acrylate) [P(*S-co*-BA)], 109
- Poly(styrene-*co*-butyl acrylate)/poly(styrene-*co*-butyl acrylate), crosslinked, 108
- Polyurethane, 10, 109
- Polyvinyl alcohol (PVOH), 198
- Poly(vinyl alcohol) (PVA), 39
- Poly(vinyl chloride) (PVC), 69
- Polyvinylformal (PVF), 150
- Population balance equations (PBE), 164
- Power compensation calorimetry (PCC), 189
- Precipitation polymerization, 45
- Probability density function (PDF), 163
- Process efficiency, 1
- Process monitoring, 183
- P(*S-co*-DVB)/P(MMA-*co*-DVB)/CdSe/CdS, 119
- P(*S-co*-MA)/CeO₂, 119
- PVAc/PVOH/MMT, 118
- P(VC-*co*-AAEM)/PS, 112, 114
- P(VDF-*co*-MA), 120
- P(VDF-*co*-MA)/CeO₂, 119

- Q**
- Quantum dots (QD), 2, 116, 119

- R**
- Radicals
 - concentration profiles/termination, 5

Radicals (*cont.*)

- entry/exit, 1, 3, 5
- polymerization
 - controlled, 6, 13, 14, 45, 116, 203
 - free, 3, 45–54, 73, 195

Raman spectroscopy, 195

Reactors, continuous, 10

Redox initiators, 8

Repulsive wall/barrier, 80, 87, 168, 171, 176

Reversible addition–fragmentation chain transfer (RAFT) polymerization, 6

Rheology, suspension, 161

S

Sanchez–Lacombe equation, 66

Shear, 26–28, 61, 73, 144, 162, 201

- mechanical, 144

- rate, 62, 165, 167, 171–178

- stress, 200

Size exclusion chromatography (SEC), 203

Smith–Ewart population balance, 5

Snowman-like hybrid particles, 120

Sodium styrene sulfonate (NaSS), 12

Stability model, generalized, 79

Styrene, 4, 5, 13, 30, 36–40, 48, 91, 112, 120, 133, 153, 191

- acrylate copolymer latex, 91

- divinyl benzene (DVB), 120

Surface charge, 79–101, 149

Surface energy, 161, 172, 180

Surface potential, 83, 85, 87, 97–101, 169, 174

Surfactant adsorption equilibrium, 81

Surfactant-free emulsion polymerization (SFEP), 153

Surfactants, 4, 10–14, 28–40, 46–49, 65–70, 79–102, 120, 127, 143–156, 205

- acid/base-sensitive, 146

- adsorption, 79

- CO₂-switchable, 143

- ionic, 205

- light-sensitive, 146

- redox-sensitive, 146

- toxicity, 153

Surfmers, 12, 14, 123

Suspension rheology, 161

Switchable particles, 143

T

Thermodynamics, 23

TiO₂, 121–123

Toxicity, 116, 153

Transition metals

- early, 11

- late, 11, 14

Transport, parameters, 58

U

Ultrasound absorption (spectroscopy), 200

Ultrasound pulse echo, 206

Ultrasound velocity, 199

UV/VIS spectroscopy, 197

V

VA-044, 148, 149

VA-061, 148, 149, 151, 153

Vinyl acetate–ethylene copolymer, 11, 183

Vinylbenzyl phosphonyl diethyl ester, 120

Vinyl chloride (VC), 48, 61, 69, 73, 112

Vinylidene fluoride (VDF), 61

Vinylimidazole (VI), 61

Vinyl-pyrrolidone (VP), 61

Viscosity, 7, 13, 26, 46, 111, 124, 171, 183, 186, 201, 205

Volatile organic compounds (VOCs), 8, 202, 203

W

Water, switchable, 154

Z

Zeta potential, 40, 80, 149, 151

ZnO, 119, 121, 133